Discovering the Missing Population of AGN Pairs with *Chandra*

by

Adi Foord

A dissertation submitted in partial fulfillment
of the requirements for the degree of
Doctor of Philosophy
(Astronomy and Astrophysics)
in The University of Michigan
2020

Doctoral Committee:

Assistant Professor Kayhan Gültekin, Chair
Associate Professor Julie Comerford
Associate Professor Elena Gallo
Dr. Edmund Hodges-Kluck
Professor Timothy McKay
Professor Jon Miller

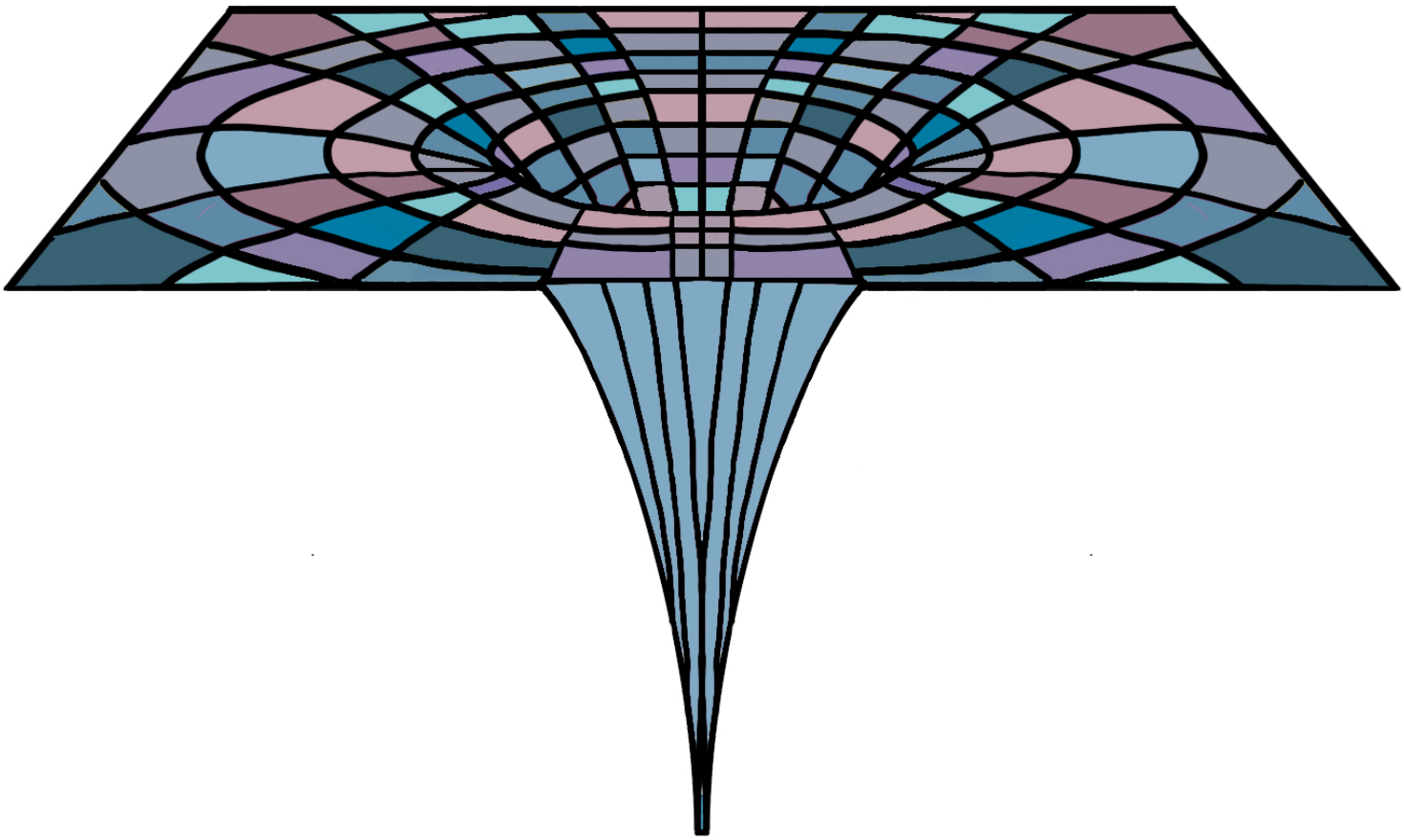

Adi Foord

foord@umich.edu

ORCID iD: 0000-0002-1616-1701

To the OG Dr. Foords, my parents, who worked incredibly hard to become the first-generation Ph.D.s of both their families. I am honored to join the Dr. Foord squad.

ACKNOWLEDGEMENTS

First, thank you to Mike. I'm lucky to have such an incredible life partner. I couldn't have survived the stressful parts of this process without your love, support, and late-night cookie and calzone deliveries. You keep me grounded and constantly remind me of the bigger picture – I'm so excited for all of our future adventures. Thank you to my wonderful cats, Simcoe and Freddie, who let me hug and pet them while eating said cookies and calzones, and acting like they don't mind.

Thank you my wonderful family – Ima, Abba, Dani, and Careen. You've been my biggest cheerleaders since Day 1, and you always pretend to read my papers when I email them to you. Abba, thank you for your constant support, and sitting through all of my dry runs for talks since middle school. Ima, thank you for serving as inspiration as an intelligent and creative scientist who is always pushing the limits.

Thank you to Kayhan. You treated me like an equal, and you gave me the space to ask questions and pursue creative ideas. With your endless support, I've grown into a better scientist. Thank you to my thesis committee, for your thoughtful input throughout the years, and for supporting my career as either co-authors, mentors, and/or colleagues. Also, thank you for agreeing to read the following 220 pages of text.

Thank you to Keren, who supplied me with pounds of chocolate during the most stressful moments. You continuously give me the confidence to be my colorful-self in this field, and you serve as inspiration for what I one day hope to become. Thank you to Jessie, Edmund, and Vivienne, who have acted as mentors throughout much of my career, and continue to

support me from afar.

Thank you to my wonderful friends Tina and Alex, who have cheered me on since we were floor-mates freshman year of college. You've supported me through the many hurdles and brick walls I've needed to climb over, while also celebrating all of my successes and achievements.

Thank you to the friends I've made while at Michigan: Allison, Aleksandra, Erin, Kamber, Renee, Traci, Larissa, Kevin, and all of the graduate students. I feel lucky to have been able to pursue a Ph.D. in this department. I will never forget the many, *many*, hours we've spent together – either laughing or commiserating – I was able to finish this dissertation with your love.

TABLE OF CONTENTS

LIST OF FIGURES

Figure

LIST OF TABLES

Table

ABSTRACT

Although the first supermassive black hole (SMBH) was observed over 100 years ago, the details regarding how they form, evolve, and impact their surroundings remain active topics of research. In fact, only over the past 5 years has the existence of black holes been confirmed via the advent of detectors such as the Advanced Laser Interferometer Gravitational Wave Observatory (LIGO) and the Event Horizon Telescope (EHT). From an observational perspective, although all massive galaxies are thought to harbor nuclear SMBHs, the observability is dependent on the accretion activity. The activity of accreting SMBHs, or Active Galactic Nuclei (AGN), is expected to evolve with time and is likely a function of the ability to efficiently channel gas inflow to the galactic center. Many black hole feeding mechanisms exist, such as gravitational instabilities in galaxies that are barred or nucleated, gas dynamic processes involving multiple black holes, and major galaxy interactions. To further complicate the matter, it is possible that more than one mechanism plays a role at any given time. However, analyzing which SMBHs are active, and why, is vital to understanding various feedback processes and how the growth of a SMBH and its host galaxy are tied. In this dissertation, I present various analyses that are all focused on studying the activity of SMBHs in various environments. Specifically, I have studied a population of AGN in nucleated galaxies to analyze how nuclear star clusters affect SMBH activity (Chapter 2), and a binary AGN candidate (two SMBHs that are gravitationally bound; Chapter 3) that did not appear to be undergoing any major merger. However, the majority of my dissertation focuses on detecting and analyzing AGN pairs, ("dual AGN", if the SMBHs are not yet gravitationally bound). Despite the importance of dual AGN to wide-ranging astrophysical fields such as galaxy formation and gravitational waves, the rate of dual AGN has yet

to be accurately measured. Yet, the rate of dual AGN can inform us of the role galaxy mergers play in triggering AGN, timescales for post-merger SMBHs to sink to the center of the potential well, as well as merger-related feedback physics. Dual AGN that are widely separated relative to the instrument PSF and have near unity flux ratios are easy to identify, however dual AGN with small separations and/or flux ratios can only be distinguished from a single AGN with advanced statistical analysis. As a result, very few dual AGN have been confirmed. Thus, I've developed a tool called `BAYMAX` (Bayesian Analysis of Multiple AGN in X-rays), that quantitatively evaluates whether a given source in a *Chandra* observation is composed of a single or multiple point sources, using a Bayesian framework. With `BAYMAX`, I am methodically expanding the known population of multiple AGN systems (Chapters 5 and 6), while learning more about their preferential environments via multi-wavelength (Optical, IR, and X-ray) analyses.

CHAPTER I

Introduction

Supermassive black holes (SMBHs) represent the most massive singularities in space-time, with masses upwards of 1 million solar masses. Since the 18th century, objects whose gravitational fields are too strong for light to escape were hypothesized[1] (Michell 1784; Laplace 1799), and the first modern solution of general relativity that would characterize a black hole quickly followed (Schwarzschild 1916). However, only over the past 5 years (nicely coinciding with my time in graduate school) has the existence of black holes been confirmed. On September 14, 2015 the Advanced Laser Interferometer Gravitational Wave Observatory (LIGO) detected the gravitational signal produced by the collision of two stellar mass black holes (Abbott et al. 2016). As the first gravitational signal ever detected on Earth, it represented one of the strongest pieces of evidence for the existence of black holes. In particular, the waveform matched the predictions of general relativity for a gravitational wave emanating from the inward spiral and merger of a pair of black holes close to 36 and 29 solar masses (Abbott et al. 2016). In the supermassive realm, on April 10, 2019, images were released from the Event Horizon Telescope (EHT) which showed the "shadow", or the event horizon, of a supermassive black hole lying in the heart of nearby galaxy M87 (Event

[1]It is worth mentioning the exceedingly long title of Rev. John Michell's paper: "On the Means of Discovering the Distance, Magnitude, &c. of the Fixed Stars, in Consequence of the Diminution of the Velocity of Their Light, in Case Such a Diminution Should be Found to Take Place in any of Them, and Such Other Data Should be Procured from Observations, as Would be Further Necessary for That Purpose".

Horizon Telescope Collaboration et al. 2019). The event horizon represents the surface beyond which gravity is so strong that nothing that crosses it, even light, can return. These two monumental measurements have confirmed the analytical solution first found by Karl Schwarzschild in 1916: black holes exist.

However the details regarding how they form, evolve, and impact their surroundings remain active topics of research. Current outstanding questions, with controversial results, are: (i) "Where and how do they grow and evolve?"; and (ii) "Is there any significant interplay between their activity and their environments?" Below I outline previous work addressing these points, before discussing current and future work which will help further our understanding on the nature of SMBH activity.

1.1 Supermassive Black Hole Detection Through the Electromagnetic Spectrum

In order to study SMBHs and their environments, you must first find them. After over 50 years of research, we believe that most massive galaxies harbor nuclear supermassive black holes in their nuclei (e.g., Richstone et al. 1998; Kormendy & Ho 2013), and the observability is dependent on the accretion activity. As SMBHs are inherently void of light (i.e., "black") within the event horizon, most detections are based on evidence of hot gas and dust surrounding *actively accreting SMBHs*, or active galactic nuclei ("AGN"). These detection techniques vary from photometric evidence to spectroscopy, and span a wide range of wavelengths. The basis of these diagnostics relies on the unique emission expected around a supermassive black hole; in particular, supermassive black holes have distinctive non-thermal spectral energy distributions (SED), high luminosity densities, and different variability timescales than expected from an ensemble of stars. With this information, scientists have designed numerous techniques to search for accretion around supermassive black holes. Below, I go into more detail on a small subset of photometric and spectroscopic AGN diagnostics using op-

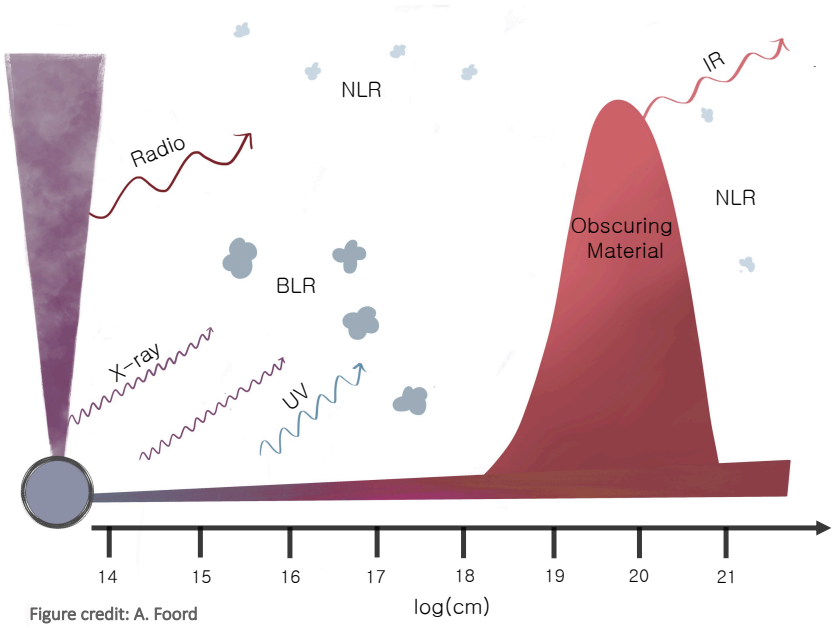

Figure 1.1: A diagram of a SMBH, with various regions of emission, and the corresponding wavelengths, highlighted.

tical, infrared, and X-ray emission, that are directly associated with the research presented in later chapters.

1.1.1 Optical

Historically, optical telescopes and detectors made the first detections of super massive black holes. NGC 1068 was the first, although the origin of emission was unknown at the time. NGC 1068 was singled out due to "peculiar" broad emission features, which we now know to be the AGN's broad emission lines (Fath 1913; Slipher 1917)[2]. In 1943, Carl Seyfert expanded on this analysis to a larger sample of spiral galaxies, and similarly found broadened emission features that a parent sample of "normal" galaxies did not contain. Soon, optical counterparts were found for a new class of extragalactic, luminous, radio sources (Baade & Minkowski 1954), that were discovered to have non-stellar spectra (and thus, appropriately named quasi-stellar radio sources or "quasars"; Schmidt 1963; Greenstein & Matthews 1963;

[2]As V.M. Slipher wrote: "..the extremely high radial velocity, and peculiar disk-like images of the emission lines, the high scale spectrogram brings out what had not been recognized before — that the hydrogen lines spread farther into the fainter parts of the nebula then do the nebulium lines".

Schmidt & Matthews 1964), similar to the samples studied by Seyfert ("Seyfert" galaxies). As time went on, it became clear that the spectra of this new class of sources varied; for example, "Seyfert 2" galaxies lack broad emission lines, but instead have strong, narrow forbidden lines that can not be produced by ionization from normal stars. Eventually Seyferts and quasars were grouped under the same name – Active Galactic Nuclei (a term first coined by Burbidge 1970, however they were yet to be attributed to SMBHs[3]).

We now believe the spectral features seen in Seyfert galaxies are due to the presence of a massive black hole sitting in the galactic nucleus (see Figure 1.1). Seyfert 1 galaxies have both broad (implying gas velocities of 1000–5000 km/s) and narrow (implying gas velocities of 500–1000 km/s) emission lines superimposed on one another, while Seyfert 2 galaxies have only narrow-line features. While the broad emission features are thought to originate from high density gas (where electron density $n_{\rm e} \approx 10^9$ cm^{-3}) very close to the nucleus ("broad-line region", or BLR), the narrow-line features are though to originate from low density ($n_{\rm e} \approx 10^3 - 10^6$ cm^{-3}) gas clouds at larger distances ("narrow-line region", or NLR). Many optical surveys look for these distinctive features when creating samples of AGN. Broad optical emission lines such as Hα and Hβ with widths implying velocities upwards of 1000 km/s are sure sign-posts for AGN activity. This can be better understood using a simple virial argument. Assuming a self-gravitating, spherical distribution of gas:

$$M \approx v^2 r / G \tag{1.1}$$

where the total enclosed mass M, can be estimated from the nucleus radius r (< 10 pc, an upper-limit set by space-based spatial resolution[4]), and the velocity dispersions, v, are measured from the widths of the optical emission lines (of the order 10^3 km s^{-1}). Thus,

[3]From Burbidge 1970, speaking about the observed broad hydrogen lines in Seyfert galaxies: "Since these velocities are much larger than the escape velocity, unless there is an exceedingly large mass concentration [which can be ruled out at least in the case of NGC 1068] the large widths were thought to give fairly direct evidence for large scale mass loss.."

[4]The size of the BLR is best constrained via reverberation mapping, or measuring emission-line time delays, which is outside the scope of this simple example.

the mass within 10 pc can be inferred to be in the range $M \approx 10^{9\pm1} M_{\odot}$, a scenario that is incompatible with most theories besides the presence of a SMBH.

Strong narrow-line emission from "forbidden" lines (like [N II] or [O III]) are expected due to high-energy photons originating from the nucleus. In particular, narrow-line ratios (such as [O III]/Hβ) are often used to help distinguish between Seyfert-like galaxies from other types of emission-line galaxies – as the ratio of flux from forbidden lines to hydrogen recombination lines are expected to be higher for nuclei with AGN versus those with star forming regions (e.g., Baldwin et al. 1981; Kewley et al. 2001; Kauffmann et al. 2003). However, it is not possible to unambiguously distinguish different nuclei from one another on the basis of a single flux ratio from any pair of lines – but various types of objects can be distinguished by considering the intensity ratio of *two* pairs of lines (where the relative strengths of various lines are a function of the shape of the ionizing continuum, which can be used to distinguish between, i.e., a blackbody and power-law ionizing spectra). The most common line ratios used are [O III]/Hβ and [N II]/Hα, where both are necessary in order to cleanly identify AGN (for example, star forming galaxies with low metallicities are expected to have a high ratio of [O III] to Hβ, similar to an AGN, but low [N II]/Hα). These diagrams are commonly known as"BPT" diagrams ("Baldwin, Phillips, and Terlevich", the authors who first attempted the narrow emission-lines classification scheme; Baldwin et al. 1981), and an example is shown in Figure 1.2.

However, the detectablility of optical emission lines will be affected by various factors such as dilution by starlight, which reduces the equivalent width of spectral lines and the visibility of non-thermal emission in the optical range. These effects are amplified at moderate to high redshifts, where star formation is expected to be higher and optical emission lines are redshifted into NIR spectral bands. Additionally, optical emission is susceptible to obscuration from gas and dust in the line of sight. For example, environments with higher ($>10^{22}$ cm^{-2}) column-densities along the line-of-sight can result in optical absorption of $A_V > 5$, extinguishing almost all UV - NIR light.

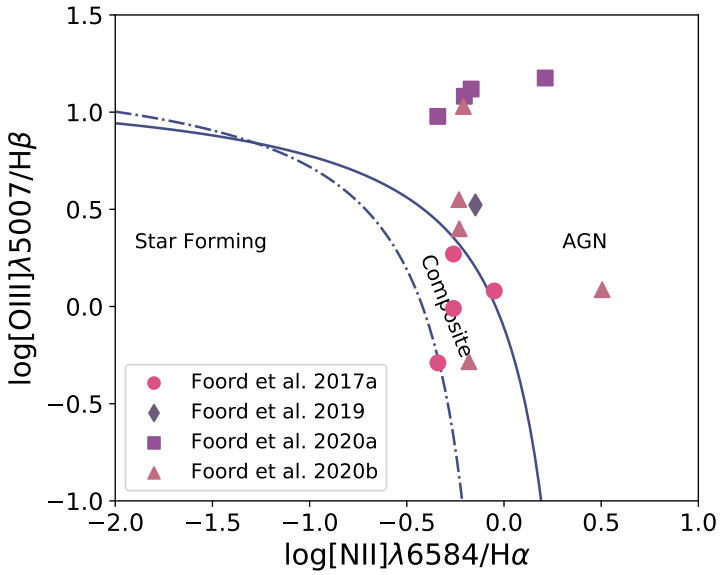

Figure 1.2: BPT optical spectroscopic line ratio diagrams for various X-ray identified AGN analyzed in Foord et al. (2017a, 2019, 2020), where blue lines represent the Kewley et al. (2001) (solid) and Kauffmann et al. (2003) (dot-dashed) demarcations, which separate different sources of photoionization. The X-ray identified AGN span a range of luminosities and Eddington ratios, and only the brightest are classified as "AGN" via the BPT diagnostics.

1.1.2 Infrared

A large contribution to the bolometric luminosity of AGN comes from the infrafred (IR) spectral band ($f = 10^{12} - 10^{14.5}$ Hz, or $1 - 3000$ μm). In particular, for Seyfert galaxies and low-luminosity AGN, the IR contribution is complex and due to multiple thermal components. The IR emission comprises three main spectral components − thermal radiation from dust in a compact region near the AGN ("torus"); thermal dust continuum associated with star formation or starburst activity (resulting in emission lines from polycyclic aromatic hydrocarbons and continuum features); and line emission from molecular, atomic, and ionic species (Soifer et al. 2008). The thermal radiation associated with stellar activity dominates mostly at longer wavelengths ($\lambda > 10$ μm) while that from the AGN dominates between $2 - 10$ μm (see Fig. 1.3). Because the thermal spectral energy distribution from the torus is a result of reprocessed energy from the enclosed AGN, analyzing mid-IR spectra allows one to indirectly measure AGN activity. This is especially useful for objects that have heavily

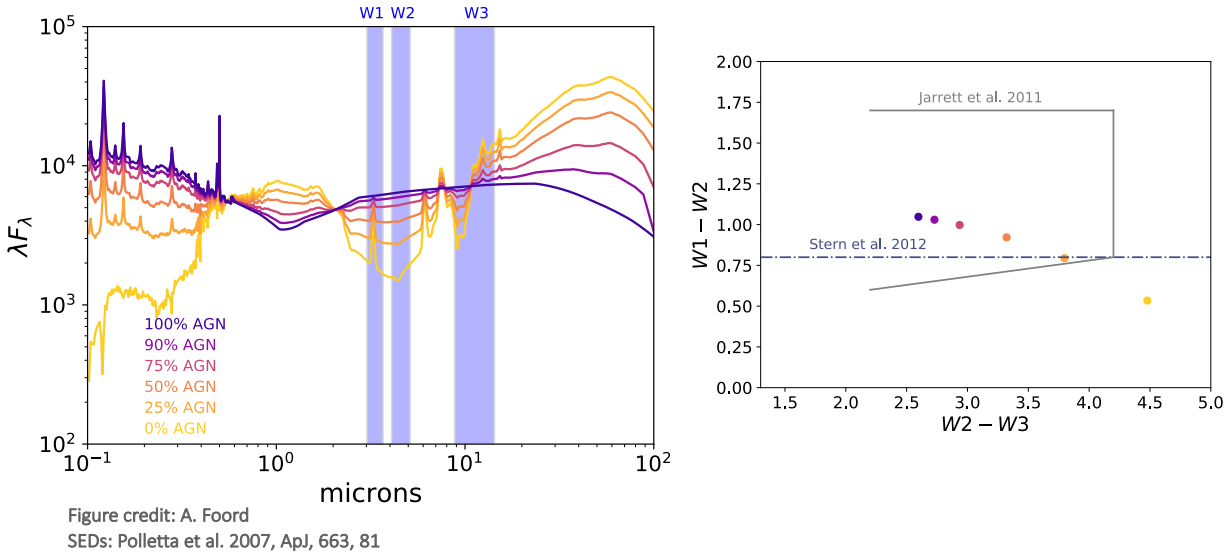

Figure 1.3: An example of mid-IR AGN color selection. A starburst galaxy's SED (*left*) will change shape as a function of increasing fractional contribution from an AGN, which will change the measured magnitude of flux, as detected in various *WISE* filters (shown in blue). Various mid-IR color-cuts and "wedges" (*right*) have been defined to effectively select galaxies with luminous, obscured, AGN.

obscured, dusty, regions (such as galaxy mergers) where direct measurements of emission via optical light may not be possible.

Historically, the IR band coverage has been relatively limited, with respect to optical, due to only a small subset of the spectral region being accessible from the ground. However, with the advent of many space-based IR observatories such as NASA's *Spitzer Space Telescope* and *Wide-Field Infrared Survey Explorer* (*WISE*), and ESA's *Herschel Space Observatory*, an unprecedented amount of legacy IR imaging and spectroscopic data has been collected for over a million AGN[5]. Studies of mid-IR colors are used to identify types of luminous obscured AGN (see, e.g., Stern et al. 2012). Mid-IR selection of AGN relies on distinguishing AGN spectra from the stellar spectra of galaxies (see Fig. 1.3). In particular, luminous and obscured AGN will sit in different locations on mid-IR color-color diagrams, and various color cuts and "wedges" on these diagrams have been defined to cleanly select AGN. Criteria were

[5]The next milestone for space-based IR telescopes will be the *James Webb Space Telescope*, mainly focusing on the near infrared (operating between 0.6 and 27 μm), and set to launch in $t = t_c + \xi$ years (where t_c is the current date and ξ represents a random number uniformly in domain $(0, t_{H_0})$)

first developed based on photometry via the Infrared Array Camera (IRAC; Fazio et al. 2004) on board *Spitzer*, such as the "Lacy wedge" (Lacy et al. 2004, 2007), the "Stern wedge" (Stern et al. 2005), and untitled color cuts with non-eponymous authors (Messias et al. 2012). These were extended to *WISE* when the instrument launched in 2009 (Jarrett et al. 2011; Stern et al. 2012; Mateos et al. 2012; Assef et al. 2013). Through many studies, galaxies hosting bolometrically dominant AGN have become identifiable using various *WISE* filters ($W1 = 3.4\mu$m, $W2 = 4.6\mu$m, $W3 = 12\mu$m), up to large ($z = 3.5$) redshifts (Jarrett et al. 2011; Stern et al. 2012). However, IR selection techniques are most powerful for (i) obscured and (ii) luminous AGN. Dilution by the host galaxy will cause bluer $W1 - W2$ colors, making less powerful AGN not identifiable using simple *WISE* color criteria.

1.1.3 X-rays

With increasing frequency, one begins to probe the innermost regions of the central engine of the AGN. It is believed that UV photons produced from the thermal spectrum of the accretion disk are scattered to higher energies via interactions with relativistic elections. These relativistic electrons are believed to reside above the accretion disk ("corona"; Haardt & Maraschi 1993). The spectrum — usually plotted as N_E (photons cm^{-2} s^{-1} keV^{-1}) = $AE^{-\Gamma}$ — has an approximate power-law shape with power-law index $\Gamma = 1.8$ (Corral et al. 2011). Because the temperature of the disk and the relativistic electrons' energy distribution are limited, the inverse Compton spectrum should have a high-energy cutoff (extending up to a few hundred keV). The X-ray spectrum is also expected to undergo reprocessing through absorption. The hard X-rays can irradiate the dense, cold, disk material, giving rise to a high-energy bump in the 20-100 keV band ("Compton hump") as well as fluorescence iron lines near $\sim$6.4 keV (see, e.g., Fabian et al. 2000). Thus, by detecting and analyzing the X-ray emission of a source, one can verify its origin. With all X-ray analyses, one must be wary of other sources of X-ray emission. In particular, X-ray binaries (XRBs; systems of neutron star or solar mass black holes accreting material from a nearby companion star)

and the hot ionized interstellar medium (ISM) are the main contributors to the total X-ray output of normal (i.e., not containing an AGN) star forming galaxies. While emission from the hot ISM appears diffusely spread throughout the galaxy, X-ray binaries are bright compact sources, the true AGN-mimicking culprits. In particular, because the accretion physics between these other compact objects is similar (but scaled down) to SMBHs, their X-ray spectra have many similar qualities.

Analyzing emission lines near $\sim$6.4 keV (the iron line is actually a doublet comprising the $K_{\alpha 1}$ and $K_{\alpha 2}$ lines at 6.404 and 6.391 keV) can probe the spacetime and disk dynamics near the black hole, and constrain many characteristics of a compact object system. Although both XRBs and AGN can exhibit fluorescence iron lines, the equivalent widths (EW; the line flux divided by the continuum flux at the line energy) should differ, as the emission is generally thought to originate from matter in an accretion disk rotating around the compact object (see Fabian et al. 2000 for a review of AGN X-ray spectra, as well as Miller et al. 2002; Miller 2007; Miller et al. 2013 for a review of XRB X-ray spectra). While most XRBs with detected fluorescence iron lines have $EW < 30$ eV, AGN X-ray spectra have fluorescence iron lines with equivalent widths between $50 - 300$ eV (Mushotzky et al. 1993), corresponding to velocities of orders tens of thousands of kilometers per second. However, for shallower datasets, where low-resolution spectra don't show evidence of iron lines, it becomes much more difficult to discern between AGN and XRBs on spectral shape alone. In particular, SMBHs and XRBs have similar non-thermal X-ray spectra, regardless of accretion state (soft/high or hard/low). Although type 1 X-ray bursts can be used to identify systems with neutron stars (an effect of thermonuclear runaway of hydrogen and helium on the neutron star surface), X-ray binaries with stellar black holes are not expected to undergo these events.

Thus, although a detailed analysis of the X-ray spectrum can give insight on characteristics of the system, there exist many degeneracies between supermassive black hole and XRB spectra. Although these degeneracies can be further untangled with sufficient timing studies (i.e, quasi-periodic oscillation studies) one of the easiest methods is to find sufficiently (and

consistently) bright X-ray sources. In general, X-ray point sources with X-ray luminosities between 2−7 keV above 10^{40} erg s^{-1} are *highly likely* to be due to accretion onto a SMBH. This idea is simply shown by the following: the potential energy of a mass m a distance r from a central mass of mass M is $U = GMm/r$. The rate at which the potential energy of infalling material can be converted to radiation (or, the luminosity accretion, L_{acc}) is given by:

$$L_{acc} \approx \frac{dU}{dt} = \eta \frac{GM}{r} \frac{dm}{dt} = \eta \frac{GM\dot{M}}{r}, \tag{1.2}$$

where $\dot{M}$ is the mass accretion rate. Because of the uncertainty associated with how much of the accretion energy falls into the black hole (adding to its mass) versus how much is radiated, η is included to represent how efficient the accreted mass is converted into radiation. Substituting the Schwarzschild radius $R_S = 2GM/c^2$ (which is the event horizon for a non-rotating black hole) into Eq. 1.2:

$$L_{acc} \approx \eta \dot{M} c^2. \tag{1.3}$$

We can make a few assumptions. For an average AGN SED, the 2−7 keV luminosity can be assumed to be ∼10% of the bolometric luminosity, such that $L_{acc} = 10^{41}$ erg s^{-1}. Assuming a very low value of $\eta = 0.007$ (the efficiency of hydrogen fusing to helium) the accretion rate would be $\dot{M} \approx 10^{-6}$ $M_\odot$ yr^{-1}, over 10^4 times higher than the typical order of magnitude for accretion rates in neutron star X-ray binaries. Pairing a more reasonable guess for the accretion efficiency of $\eta \sim 0.1$ (see, e.g, Raimundo et al. 2012) with luminosities associated with more luminous AGN ($L = 10^{47}$ erg s^{-1}), the rate at which mass is processed in the source can exceed 20 $M_\odot$ yr^{-1}! Furthermore, assuming that the systems are radiating at less than the Eddington limit[6], accreting masses exceeding 10^9 $M_\odot$ are required. With white dwarfs and neutron stars subjected to upper limits on their masses of $1.4M_\odot$ and $3M_\odot$, *only supermassive black holes are plausible candidates for these X-ray bright objects in galactic*

[6]The Eddington limit (or luminosity) is the radiative luminosity at which the gravitational force inward matches the radiative force outwards: $L_{edd} = \frac{4\pi c G M m_p}{\sigma_T}$. Here, m_p is the mass of photon and σ_T is the Thomson scattering cross-section.

nuclei[7]. Indeed, studies on populations of nearby XRBs and AGN have shown that the majority of nearby AGN have $L_X > 10^{40}$ erg s^{-1} (Lehmer et al. 2010, 2019; Foord et al. 2017a).

Similar to the IR waveband, space-based telescopes are required for high-sensitivity X-ray observations. *Uhuru*, the first X-ray telescope on an orbiting satellite was launched in 1970, and was followed by other proportional counter detector systems such as NASA's *HEAO-1*. A major leap forward occurred with *HEAO-2* (later named *Einstein*), launched in 1978, which was the first orbiting X-ray telescope to use Wolter-geometry grazing incidence mirrors (Wolter 1952). Unlike the earlier proportional counter detector systems, this allowed for X-ray imaging, and many successful X-ray instruments followed (ROSAT, ASCA, RXTE). X-ray satellites that are currently taking data in the $2-10$ keV range today include: NASA's *Chandra X-ray Observatory* ($0.2-10$ keV), ESA's *XMM-Newton* mission ($0.2-10$ keV), and NASA's *Neil Gehrels Swift Observatory* ($0.3-150$ keV), each with their own unique strengths. With $0.8''$ angular resolution, *Chandra* provides the highest spatial resolution of X-ray images to date.

While sensitive X-ray surveys are quite powerful at identifying even low-luminosity AGN, such surveys are not sensitive to heavily obscured AGN. In particular, if nearby absorbing matter has column densities exceeding $N_H \approx 1.5 \times 10^{24}$ cm^{-2}, the value corresponding to unity optical depth for Compton scattering (and thus known as "Compton thick" sources), the lower energy X-rays are readily absorbed and scattered. However, heavily obscured AGN are the ideal targets for mid-IR diagnostics. This illustrates that synergies between X-ray and mid-infrared surveys can be used to help identify populations of AGN over a large range of Eddington luminosity. Optical photometric surveys are the most heavily biased, with a sensitivity largely restricted to the least obscured, most luminous AGN.

[7]However, an important caveat are ULXs, as well as regions with extreme star bursts, which should be taken into account for sources with $L_X < 10^{41}$ erg s^{-1}.

1.2 Effective feeding mechanisms

The activity of AGN is expected to evolve with time (i.e., Brandt & Alexander 2010), and is likely a function of the ability to efficiently channel gas inflow to the galactic center. Many black hole feeding mechanisms exist, such as gravitational instabilities in galaxies that are barred or nucleated (galaxies that host a massive nuclear star cluster, Naiman et al. 2015), gas dynamic processes involving the presence of multiple black holes (Begelman et al. 1980), and major galaxy interactions (Alonso et al. 2007). To further complicate the matter, it is possible that more than one mechanism plays a role at any given time. Regardless of the feeding mechanism, during periods of active accretion they likely serve as an important driver of galaxy evolution. This is supported by the various SMBH-galaxy scaling relations (e.g., Kormendy & Ho 2013), where the mass of the SMBHs appear to be fundamentally linked to large scale properties of the host galaxy, such as the stellar velocity dispersion and total bulge mass. Thus, analyzing which SMBHs are active, and why, is vital to understanding various feedback processes and how the growth of a central SMBH and its host galaxy are tied.

1.2.1 SMBH activity in nucleated galaxies

Up to 80% of galaxies with stellar mass $M_* < 10^{10} M_\odot$ host a massive nuclear star cluster (NSC; Côté et al. 2006; Georgiev & Böker 2014). NSCs are the densest known stellar concentrations in our Universe, with typical half-light radii of several parsecs and masses ranging between $10^5 - 10^8 M_\odot$ (Böker et al. 2004; Walcher et al. 2005). Theoretical work suggests that the presence of an NSC can provide a favorable environment for the formation and/or growth of massive black holes (Stone et al. 2017). In particular, it has been suggested that runaway tidal capture processes occurring in NSCs can form a $10^{2-3} M_\odot$ SMBH seed that grows via tidal disruption events to larger sizes (Miller & Davies 2012; Gnedin et al. 2014; Stone et al. 2017). In addition to facilitating the formation of a SMBH, recent star formation in NSCs has been theorized to enhance the SMBH feeding rates. Because NSCs

are comparable in mass (or, even more massive) with respect to the central SMBH, they can significantly alter the gas flow and provide an efficient mechanism for funneling gas toward the central black hole (Naiman et al. 2015). These effects in nucleated galaxies may be further enhanced during galaxy mergers.

Observationally, various studies have been carried out to measure if the presence of a NSC affects the activity of a central SMBH (Seth et al. 2008; Foord et al. 2017a). This is done by comparing the "active fraction" (the percentage of galaxies in a given sample that host AGN) of nucleated galaxies to non-nucleated galaxies. The largest observational study to date is presented in Seth et al. (2008), where the active fraction was determined from a sample of 75 nucleated galaxies with suitable optical spectroscopic data from either the Sloan Digital Sky Survey (SDSS) or the Palomar Survey (Filippenko & Sargent 1985). Here, AGN were identified using BPT diagnostics (see §1.1.1), and they concluded that the measured active fraction of nucleated galaxies ($\sim 10\%$) was consistent with the galaxy population as a whole.

However, as discussed in §1.1, optical emission line ratio diagnostics are arguably best-suited to probing high-luminosity, unobscured, AGN; as a result, optical AGN population studies are necessarily incomplete. Thus, Foord et al. (2017a) expanded on this analysis by searching for low-luminosity AGN (down to X-ray luminosities of 10^{38} erg s^{-1}) in nucleated galaxies via a uniform, luminosity-limited X-ray survey. The sample consisted of 51 nucleated Virgo early-types (for which results were first reported in Gallo et al. 2008, 2010; Miller et al. 2012a) and 47 nucleated late-types. Having measurements for two different types (late-type and early-type) of nucleated galaxy samples allowed for an additional comparison between the active fraction of nucleated early- versus late-types, the latter which are home to bluer NSCs and arguably larger gas reservoirs. After correcting for contamination to the nuclear X-ray signal from bright X-ray binaries and accounting for the different stellar mass distributions, Foord et al. (2017a) found no statistically significant difference in the active fraction of early-type versus late-type nucleated galaxies, while across the whole sample, the active fraction

was found to be consistent with the galaxy population as a whole (as concluded in Seth et al. 2008). More details on this analysis are presented in Chapter II.

1.2.2 SMBH activity via mergers

Galaxy mergers are thought to be a key process behind the various SMBH-galaxy scaling relations, by a combination of merging repeatedly with each other (Jahnke & Macciò 2011), triggering feedback processes from the central AGN (Hopkins et al. 2006), or triggering star formation that quenches the AGN's fuel supply (Sobral et al. 2015). However, the connection between AGN triggering and galaxy mergers remains poorly understood, even though AGN are likely key players in the evolution of massive galaxies. In particular, there is an ongoing debate regarding whether or not galaxy-galaxy interactions are responsible for, or even correlated with, AGN activity.

Theoretically, there are many reasons to expect a link between gas-rich, similar-mass mergers and the accretion of material onto at least one of the black holes (e.g., Volonteri et al. 2003; Hopkins et al. 2005). Tidal forces between galaxies can introduce gravitational torques that effectively dissipate the specific angular momentum of material from the large-scale gas reservoirs and transport significant quantities down to scales in which SMBHs can accrete (Barnes & Hernquist 1991a; Di Matteo et al. 2008; Anglés-Alcázar et al. 2017a).

Yet, observationally, contending results have led to uncertainty in whether AGN triggering is dependent on environment. It has been shown that luminous, dust-obscured, SMBHs around $z = 1$ are likely to have their accretion triggered by galaxy interactions (Urrutia et al. 2008; Glikman et al. 2015; Treister et al. 2012; Fan et al. 2016), while other studies have found no AGN-merger connection at the highest luminosities (Schawinski et al. 2012; Villforth et al. 2014). Contrasting results have similarly been found for nearby ($z < 1$) galaxies: evidence supporting a correlation between merging and AGN has been found by many studies (e.g., Koss et al. 2010; Ellison et al. 2013; Satyapal et al. 2014; Weston et al. 2017), while others conclude large-scale merger signatures do not appear to correlate with

the presence of an AGN. It is likely that these contradictory results are due to the variability of the AGN activity during the lifetime of the merger, as the AGN may not be 'on' during the entire merger event. In particular, these types of studies are usually carried out by selecting large samples of AGN, and comparing the host galaxy characteristics of the AGN to non-AGN systems. However, AGN activity is a *stochastic* process that is thought to vary on timescales far shorter (from hours to Myr) than changes related to larger-scale processes occurring on the galactic scale (such as morphology, and star-formation; >100 Myr). This variability can diminish significant correlations between the measured SMBH accretion and star-formation (Hickox et al. 2014) and/or stellar mass (Yang et al. 2017). On top of this, the activity of AGN is likely obscuration and merger-stage dependent (Kocevski et al. 2015; Koss et al. 2016; Weston et al. 2017). Consequently, past measurements were likely complicated by (1) AGN variability, (2) the difficulty in measuring higher-redshift mergers, and (3) the obscuration and merger-stage dependency of AGN activity. Therefore, one of the best ways to analyze the possible ties between merger environments and SMBH activity is to study systems with *unique observational flags of merger-driven SMBH growth* - or, dual AGN.

Standard galaxy formation assumes that galaxies merge, their SMBHs form a dual SMBH system—a pair of SMBHs in a single galaxy with separations $< 10\,\mathrm{kpc}$ but gravitationally unbound—and then a binary ($< 1\,\mathrm{kpc}$) SMBH system, eventually hardening and coalescing. The dynamical evolution of a pair of massive black holes in the violently relaxed core of a newly merged galaxy proceeds through several stages:

(1) The captured hole sinks toward the centre of the stellar distribution on the dynamical friction time scale: $t_{df} \approx 2$ Gyr $\left(\frac{r_i}{5\mathrm{kpc}}\right)^2 \frac{\sigma}{200\ \mathrm{kms}^{-1}} \frac{10^8 M_\odot}{M}$. Here, r_i is the initial distance of the SMBH from the center of the galaxy, σ is the circular speed of the SMBH, and M is the mass of the SMBH. For typical values, the inspiral time is only 2 Gyr, and any $10^8 M_\odot$ black hole sitting within ∼10 kpc of the center of a typical galaxy will spiral to the center within a Hubble time. These inspiral times are expected to be even shorter for eccentric orbits,

where the SMBH can pass through higher density regions with stronger drag forces (Binney & Tremaine 1987).

(2) When the SMBHs become close enough to feel each other's potential, they will become gravitationally bound. This should occur when the mass of stars enclosed in the separation between the two objects is of the order of the binary mass. For an isothermal sphere, this amounts to a mutual separation of $a \sim \frac{G(M_1+M_2)}{\sigma^2}$, where M_1 and M_2 are the masses of each SMBH. At this point, dynamical friction acts on the SMBH pair as if they were a single object, without affecting the relative motion of each SMBH and thus is ineffective in extracting angular momentum from the binary.

(3) As the binary orbit shrinks, the relative orbital velocity of the two black holes grows and eventually exceeds the velocity dispersion σ of stars in the galaxy (i.e., when $a \ll \frac{GM}{\sigma^2}$, or $a \ll 10\mathrm{pc}\ \frac{(\mathrm{M_1+M_2})}{10^8 M_\odot}\left(\frac{200\mathrm{kms}^{-1}}{\sigma}\right)^2$). The binary can now be classified as "hard". The main mechanism of energy loss is through interactions with the nearby stellar and gaseous environment of the galactic nucleus, where further hardening at sub-parsec scales can proceed via 3-body scattering of background stars. Interactions with stars in the host galaxy can drive the SMBH binary to semi-major axes as small as a few milliparsecs. However, only a small fraction of the stars in the core interact strongly with the SMBH pair, and the region of phase space with small enough angular momentum is called the "loss cone". The mass of stars in the loss cone shrinks as the binary semi-major axis decreases and eventually may become smaller than the black-hole masses. Here, the binary can empty the loss cone, and further shrinkage of the semi-major axis can stall ("the final parsec problem"). However, torques from triaxial potentials can re-fill the loss cone (Gualandris et al. 2017), as well as interactions with a third supermassive black hole (Ryu et al. 2018; see Chapter VI).

(4) If the binary semi-major axis shrinks far enough, gravitational radiation takes over as the dominant cause of orbital decay. The binary system will coalesce under the influence of gravitational radiation in $t_{gr} = 5.81\ \mathrm{Myr}\ \left(\frac{a}{0.01\mathrm{pc}}\right)^4 \left(\frac{10^8 M_\odot}{M_1+M_2}\right)^3 \frac{(M_1+M_2)^2}{M_1 M_2}$.

If sufficient gas is available, the SMBH pairs at each stage may be actively accreting and

can be classified as "dual AGN" and "binary AGN". AGN pairs are signposts of ongoing galaxy mergers and are the observational progenitors of the loudest gravitational wave (GW) events in the Universe. Analyzing the dual and binary AGN population is imperative to understanding which environmental dependencies are linked with AGN activity, as well the expected GW event rate detectable with Pulsar Timing Arrays (PTAs; Mingarelli 2019).

1.3 The search for AGN pairs

The frequency of galaxy mergers in our observable Universe implies that multi-AGN should be relatively common. The galaxy merger fraction with separations < 1 kpc by $z = 0.25$ is predicted to be between $\sim$6% and 10% (Hopkins & Quataert 2010a), and recent cosmological simulations predict that >30% of dual AGN systems have subsequent merger events with a tertiary AGN. However, the sample size of confirmed multi-AGN systems remains small (see Fig. 1.4).

Confirmation of dual AGN systems requires spatially resolving each individual AGN; beyond $z > 0.05$ high-resolution imaging is necessary, which can be accomplished with both radio or X-ray observations. Radio observations can resolve radio-emitting cores on the smallest spatial scales, and a handful of binary AGN have been detected using radio observations (where the angular resolution is on milliarcsec scales, corresponding to < parsec-scale separations for nearby galaxies; see Rodriguez et al. 2006; Rosario et al. 2010; Tingay & Wayth 2011; Fu et al. 2011, 2015; Deane et al. 2014; Gabányi et al. 2014; Wrobel et al. 2014a,b; Müller-Sánchez et al. 2015; Kharb et al. 2017). However this technique is only efficient for radio-loud AGN ($\approx$ 15% of the AGN population; Hooper et al. 1995), and AGN can only be differentiated from jet components at radio frequencies if they are compact and have flat or inverted spectral indices (see, e.g., Burke-Spolaor 2011; Hovatta et al. 2014). Indeed, this is further complicated by the fact that regions of intense starbursts can mimic both compactness and brightness temperatures of AGN; thus complementary IR data may be necessary to properly classify the source (see, e.g., Varenius et al. 2014)

Few telescopes possess the necessary resolution, and as a result, most observational evidence for AGN pairs primarily relies on indirect detections. Below, I go into more detail regarding popular techniques to search for binary and AGN systems.

1.3.1 Binary AGN

For the direct detection of a binary AGN ($a \lesssim 100$ pc), it is almost necessary to use radio observations. Such small separations become impossible to resolve with *Chandra* beyond a distance of $\sim$4 Mpc. The closest AGN pair candidate identified using two resolved point sources with *Chandra* is NGC 3393 (Fabbiano et al. 2011) with a projected separation of $\sim$ 150 pc ($\sim 0\farcs6$). However, this source has been contested as potentially spurious (Koss et al. 2015). With the Very Large Baseline Interferometer (VLBI, with typical *milli-arcsecond* scale angular resolution) one can directly resolve AGN pairs with projected linear separations as small as $\sim$one parsec in the local Universe and $\sim$10 parsec at any redshift. The smallest separated binary AGN to date was discovered with the VLBI, 0402+379, with an estimated separation of only 7.3 parsec (Maness et al. 2004; Rodriguez et al. 2006; Bansal et al. 2017). However, a severe limitation of this approach is that only a minority of AGN ($< 10\%$ of the population), are strong (i.e. at least mJy-level) radio emitters (Ivezić et al. 2002). Therefore, with VLBI observations alone, it is only possible to prove the AGN nature of a candidate dual source if both companions are radio AGN.

Thus, many indirect detection techniques have been developed to search for binary AGN. A popular method involves looking for periodic variability in the optical flux, which may be expected from accretion via a circumbinary disk (e.g., D'Orazio et al. 2013; Farris et al. 2015b,a). Well-known quasars that have been identified as binary AGN candidates via time-domain techniques include PG 1302-102 (Graham et al. 2015) and PSO J334.2028+01.4075 (Liu et al. 2015). In particular, assuming the variability timescale of the optical flux traces the orbital period of the system, separations of $a = 0.01$ pc and $a = 0.006$ pc were deduced for PG 1302-102 and PSO J334.2028+01.4075. However, these techniques came under scrutiny in

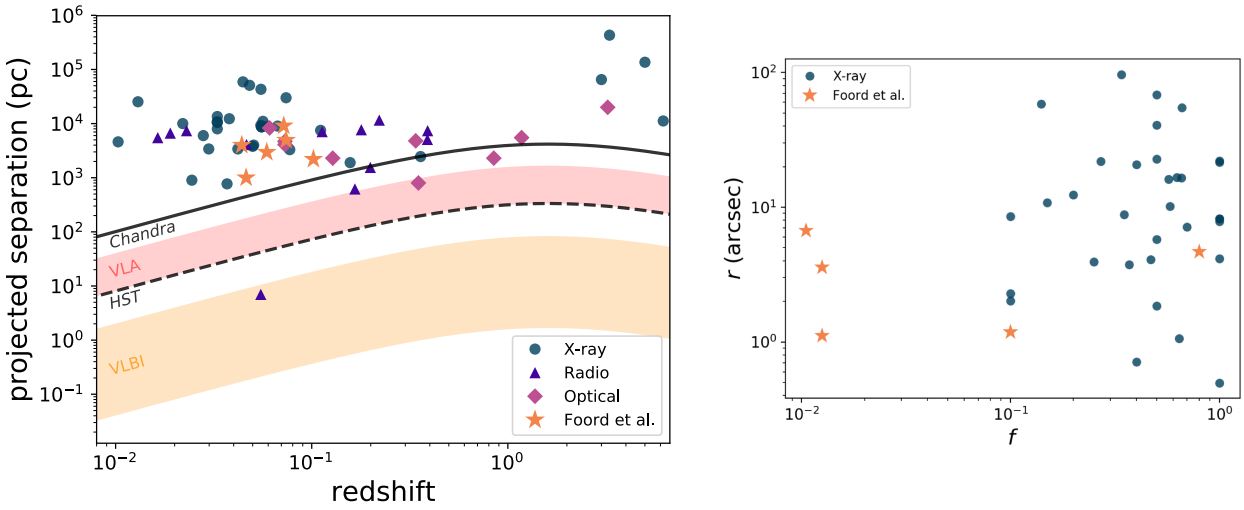

Figure 1.4: The projected separations and redshifts of dual AGN candidates from the literature (*left*) and the angular separation (r) versus count ratio (f, defined as the ratio of the number of counts associated with the secondary AGN versus the primary AGN) of the X-ray detected dual AGN candidates (*right*). Dual AGN candidates are detected either via X-ray (blue circles), radio (purple triangles), or optical (pink diamonds) observations, and the angular resolution of various telescopes are overplotted. The X-ray detections discovered using `BAYMAX` are shown in gold stars. The closest separated systems are detected via radio, while most dual AGN candidates have been found using X-rays and have separations >1 kpc. With `BAYMAX`, I am beginning to probe the low count-ratio / small-separation population of dual AGN, previously undetected using other techniques.

Vaughan et al. (2016), where they showed that sinusoidal variations are difficult to distinguish from stochastic (i.e., "red noise") processes when less than 5 cycles are detected. In response, Liu et al. (2016) tested the persistence of PSO J334.2028+01.4075's light-curve fluctuations using an extended baseline analysis composed of both archival and new data, and a simple sinusoidal model was *disfavored* for the optical flux variations. In Chapter III, I present an analysis on the multi-wavelength emission of PSO J334.2028+01.4075, to robustly identify its true accretion nature (Foord et al. 2017b).

1.3.2 Dual AGN

One of the most popular methods of indirectly finding dual AGN candidates is via double-peaked narrow line emission regions (e.g., Zhou et al. 2004; Gerke et al. 2007; Comerford

et al. 2009, 2011, 2012, 2013; Liu et al. 2010b; Wang et al. 2009; Ge et al. 2012; Fu et al. 2012). Double-peaked narrow lines can be a result of a dual AGN system during the period of the merger when their narrow line regions are well-separated in velocity. The system can display two sets of narrow line emission regions, such as [O III], where the separation and width of each peak will depend on parameters such as the distance between the two AGN. However, the optical regime alone is insufficient to confirm a dual AGN candidate, because of ambiguity in interpretation of the observed double-peaked NLRs. For example, bipolar outflows and rotating disks can also can produce the double-peaked emission feature (e.g., Greene & Ho 2005; Rosario et al. 2010; Müller-Sánchez et al. 2011; Smith et al. 2012; Nevin et al. 2016). Indeed, follow-up observations using high-resolution imaging and spatially resolved spectroscopy have found that many double-peaked dual AGN candidates are most likely single AGN (Shen et al. 2011; Fu et al. 2012; Comerford et al. 2015). On top of this, it has been shown that many dual AGN, over a wide range of physical separations, are not identifiable using optical emission line diagnostics, most likely due to optical extinction and dilution by star formation (see, e.g., Koss et al. 2012).

The most efficient method to directly detect emission associated with dual AGN is to use X-ray observations via *Chandra*. As detailed in §1.1.3, X-rays are able to penetrate through most levels of obscuration, and above a given luminosity threshold ($\sim 10^{40}$ erg s^{-1}), X-ray point-like emission is highly likely to be associated with accretion onto a SMBH (Lehmer et al. 2010; Foord et al. 2017a; Lehmer et al. 2019). However, the detection of the most closely separated pairs is limited by the instrument's Point Spread Function (PSF). Even with *Chandra*'s superior angular resolution (where the half-power diameter of *Chandra*'s Advanced CCD Imaging Spectrometer, ACIS, is $\sim 0\farcs8$ at $\sim$1 keV), systems with physical separations less than 1 kpc become difficult to resolve beyond $z \geq 0.05$. As a result, fewer than $\sim$40 dual AGN have been confirmed to date (Rubinur et al. 2018), where the majority have separations larger than 1 kpc (see Fig. 1.4), resulting in limited studies on their activity and environments.

For example, there is no well-constrained measurement of the fraction of dual AGN. The rate of dual AGN at low redshifts has been estimated to be anywhere from $\sim 0.1\%$ (at ~ 1 kpc, Liu et al. 2011b) to as high as 7% (Koss et al. 2012). On top of this, AGN observability is expected to increase as a function of angular separation between the SMBHs (e.g., Goulding et al. 2018; Capelo et al. 2017; Barrows et al. 2017a). Recent observations of moderately nearby ($z < 0.1$), mildly separated (< 5 kpc) systems find the fraction of dual AGN to be as high as 40% (Barrows et al. 2017a). The large range of values for the rate of dual AGN in the literature is a direct result of (i) incomplete/inhomogeneous samples and (ii) sensitivities to only the largest separations and count ratios. In particular, samples that have been identified via radio and/or optical diagnostics are systematically incomplete, and large X-ray samples have been created via low angular resolution instruments such as *Swift*.

1.4 Pushing the limits of *Chandra* to expand the population of dual AGN

For my dissertation, I have developed a `PYTHON` tool `BAYMAX` (**B**ayesian **A**nal**Y**sis of **M**ultiple **A**GN in **X**-rays) that allows for a quantitative and rigorous analysis of whether a source in a given *Chandra* observation is more likely composed of one or two X-ray point sources (Foord et al. 2019, 2020). `BAYMAX` is capable of detecting dual X-ray point source systems with low flux ratios between the secondary and primary AGN, as well with angular separations smaller than *Chandra*'s half-power diameter. I briefly review the Bayesian framework below, but refer the reader to Chapters IV, V, and VI for more details.

A Bayesian approach combines all available information (using prior distributions and likelihood models) to infer the unknown model parameters (posterior distributions). Bayes Theorem implies:

$$\underbrace{\frac{P(M_2 \mid D)}{P(M_1 \mid D)}}_{\text{Posterior odds}} = \underbrace{\frac{P(D \mid M_2)}{P(D \mid M_1)}}_{\text{Bayes factor}} \times \underbrace{\frac{P(M_2)}{P(M_1)}}_{\text{Prior odds}}, \tag{1.4}$$

where the posterior odds represents the ratio of the dual point source model (M_2) vs. the single point source model (M_1) given the data D. The Bayes factor ($\mathcal{B}$) quantifies the evidence of the data for M_2 vs. M_1, and the prior odds represents the prior probability ratio of M_2 vs. M_1. Specifically, the Bayes factor is the ratio of the marginal likelihoods:

$$\mathcal{B}_{2/1} = \frac{\int P(D \mid \theta_2, M_2) P(\theta_2 \mid M_2) d\theta_2}{\int P(D \mid \theta_1, M_1) P(\theta_1 \mid M_1) d\theta_1}, \tag{1.5}$$

representing the ratio of the plausibility of observed data D, given two different models, and parameterized by the parameter vectors θ_2 and θ_1. Under the assumption that M_2 and M_1 are a priori equally probable, the Bayes factor directly represents the posterior odds. Thus the Bayes factor is dependent on two components — the likelihood density, $P(D \mid \theta_j, M_j)$, and the prior density, $P(\theta_j \mid M_j)$ (see Fig. 1.5). BF with values >1 or <1 signify whether M_2 or M_1, respectively, is more likely (I analyze false positive space to define a "strong" BF for a given observation; more detail is given in Chapters IV and V).

Combining `BAYMAX` with other complementary multi-wavelength observations, I am beginning to find the missing population of dual AGN and measuring which factors affect and enhance their activity (Foord et al. 2019, 2020). In particular, results with `BAYMAX` have been populating the low count-ratio (f, defined as the ratio between the number of counts associated with the secondary AGN versus the primary AGN) and low-separation regime of the dual AGN population; given the low number of counts associated with the secondary (< 10), these systems were previously undetected (see Fig.1.6).

1.5 Dissertation Overview

Chapter II outlines an analysis studying AGN activity in nucleated galaxies. In this chapter, I show that the activity of nucleated galaxies is consistent with activity of non-nucleated galaxies; furthermore the activity is consistent between late-type (spiral) and early-type (elliptical) galaxies. This study has been published in the Astrophysical Journal.

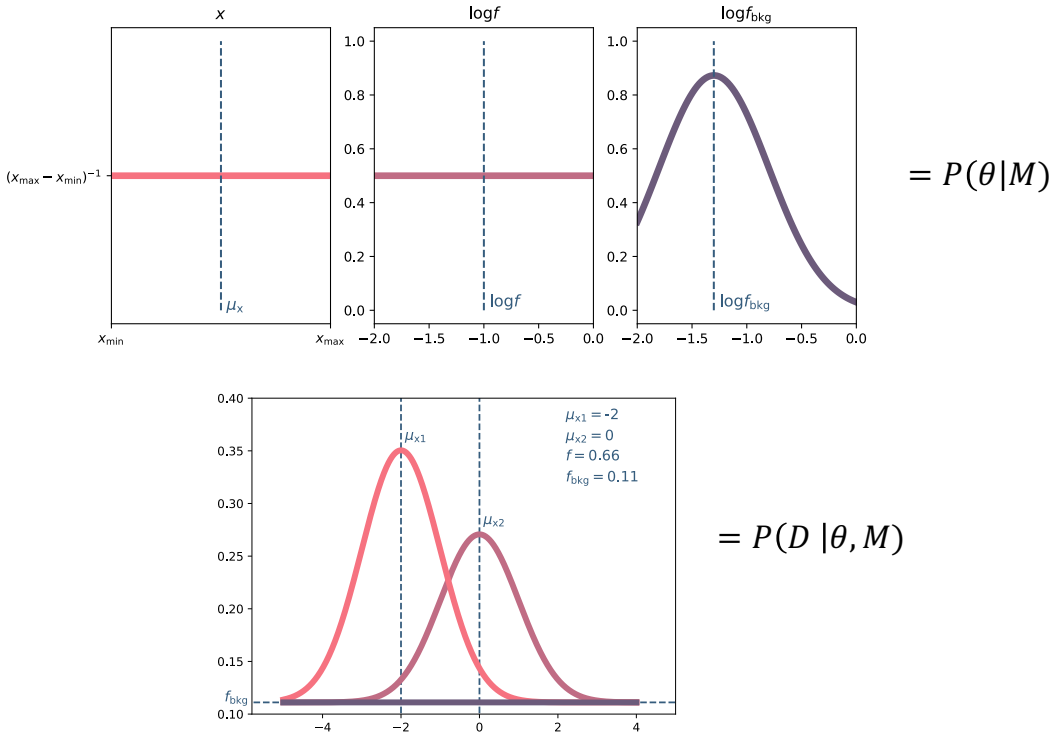

Figure 1.5: Examples of prior densities for standard parameters (such as sky x location, count ratio between the secondary and primary, f, and fraction of background counts, $f_{\rm bkg}$) and likelihood densities for a dual point source model evaluated at specific parameter values.

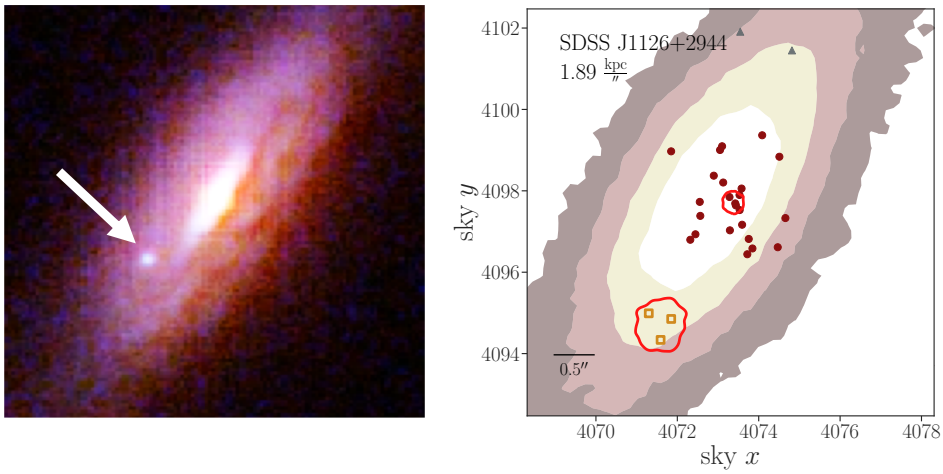

Figure 1.6: Stacked *HST* F160W (red), F814W (green), and F438W (blue) image of SDSS J1126, a dual AGN analyzed by `BAYMAX` in Foord et al. (2020). `BAYMAX` strongly favors the dual point source model. White arrows points to location of secondary AGN. *Right:* The 0.5–8 keV *Chandra* dataset, with 68% confidence intervals (red lines) for the best-fit sky x and sky y positions for a primary and secondary AGN. Counts most likely associated with the primary/secondary are denoted by circles/squares. Contours of the *HST* F160W observation are overplotted.

Chapter III presents a multi-wavelength study of a binary-AGN candidate, PSO J334.2028 +01.4075. This quasar was first identified as a binary AGN candidate due to the variability of its optical flux. I analyzed the first targeted X-ray observation of the quasar, and analyzed the multi-wavelength SED in order to better understand the accretion nature. I show that the emission is consistent with accretion onto a single AGN. This study has been published in the Astrophysical Journal

Chapter IV reviews the first analysis carried out via `BAYMAX`, where I analyzed the lowest-mass dual AGN candidate to date, SDSS J0914+0853. SDSS J0914+0853 was first targeted as a dual AGN candidate based on shallow, archival, *Chandra* imagining. When binned and smoothed, the observation appeared to be extended in the north-west direction, with a separation between two X-ray peaks of $0\farcs35$. Combining this shallow observation with an additional, deeper, *Chandra* dataset, I confirmed that the dual AGN candidate was, in fact, likely a single AGN. This study has been published in the Astrophysical Journal.

Chapter V describes an analysis of 12 dual AGN candidates via `BAYMAX`. Each of these AGN were targeted as dual AGN candidates based on double peaked narrow [O III] emission lines in their optical spectra. They each received follow-up observations with *Chandra*, where I found that 4 of the 12 systems are likely dual X-ray point sources, 1 of which is a dual AGN. Analyzing their X-ray spectra as well as complementary *HST* photometric data, I found that the dual AGN may prefer closely separated (i.e., between the galactic nuclei) and gas-rich environments, in agreement with computational predictions. This study has been published in the Astrophysical Journal.

Chapter VI presents the first systematic search for triple AGN in *Chandra* observations. Analyzing 7 nearby ($0.059 < z < 0.078$) triple galaxy mergers with existing archival *Chandra* and SDSS DR16 observations, the goal is to measure the nearby triple AGN density as well as compare environmental parameters across each single, dual, and triple AGN discovered. With `BAYMAX`, I conclude that 1 triple merger system in our sample has no AGN; 1 triple merger system is composed of a single AGN; 4 triple merger systems in our sample are

dual AGN, *all of which are new discoveries*; and I confirm one triple AGN system, SDSS J0849+1114. This study is currently in preparation to be submitted to the Astrophysical Journal for publication.

Finally, Chapter 7 concludes by summarizing the work presented in this dissertation and discussing future directions of the field of AGN pairs.

CHAPTER II

AGN Activity in Nucleated Galaxies as Measured by *Chandra*

2.1 Preface

Results in this chapter were published in: *Foord, A., et. al 2017a. AGN Activity in Nucleated Galaxies as Measured by Chandra. The Astrophysical Journal, Volume 841, Issue 1, article id. 51* and are reproduced here with minor style revisions by permission of the American Astronomical Society under the non-exclusive right of republication granted to authors.

2.2 Abstract

Motivated by theoretical expectations that nuclear star clusters (NSCs) in galactic centers may provide a favorable environment for super-massive black holes to form and/or efficiently grow, we set out to measure the fraction of nearby nucleated galaxies that also host an Active Galactic Nucleus (AGN). We targeted a distance-limited sample of 98 objects with the *Chandra X-ray Telescope*, down to a uniform X-ray luminosity threshold of $\sim 10^{38}$ erg s^{-1}. The sample is composed of 47 late-types and 51 early-types, enabling us to further investigate the active fraction as a function of galactic morphology. After correcting for contamination to the nuclear X-ray signal from bright X-ray binaries, we measure an

active fraction f=11.2%$^{+7.4}_{-4.9}$ (1σ C.L.) across the whole sample, in agreement with previous estimates based on an heterogeneous combination of optical, X-ray and radio diagnostics, by Seth et al. (2008). After accounting for the different stellar mass distributions in our samples, we find no statistically significant difference in the active fraction of early- vs. late-type nucleated galaxies, with f=10.6%$^{+11.9}_{-4.9}$ and 10.8%$^{+11.3}_{-6.3}$, respectively. For the early-type nucleated galaxies, we are able to carry out a controlled comparison with a parent sample of non-nucleated galaxies covering the same stellar mass range, finding again no statistically significant difference in the active fraction. Taken at face value, our findings suggest that the presence of a NSC does not facilitate nor enhance accretion-powered emission from a nuclear super-massive black hole. This is true even for late-type nucleated galaxies, home to bluer NSCs and arguably larger gas reservoirs.

2.3 Introduction

While all massive galaxies are thought to harbor nuclear supermassive black holes (SMBHs; e.g. Kormendy & Ho 2013), observational evidence for SMBHs becomes slim, and increasingly hard to acquire, for galaxies with stellar mass $M_* \lesssim 10^{10}\ M_\odot$. On the other hand, up to 80% of galaxies with $M_* \lesssim 10^{10}\ M_\odot$ host a massive nuclear star cluster (NSC; Côté et al. 2006; Georgiev & Böker 2014), with nearby early-type galaxies exhibiting a smooth transition from nuclear light deficits to nuclear light excess with decreasing galaxy mass (Côté et al. 2007; Turner et al. 2012). NSCs are the densest known stellar concentrations in our universe, with typical half-light radii of several parsecs and masses ranging between $10^5 M_\odot$ – $10^8 M_\odot$(Böker et al. 2004; Walcher et al. 2005). The resolution of the *Hubble Space Telescope* (HST) has allowed for detailed studies on the properties and occurrence rates of NSCs (e.g. Carollo et al. 1997, 1998, 2002; Böker et al. 2002, 2004; Walcher et al. 2005, 2006; Côté et al. 2006; Turner et al. 2012; Leigh et al. 2012; Georgiev & Böker 2014; Georgiev et al. 2016).

In a seminal work, Ferrarese et al. (2006) studied a large sample of nearby early-type galaxies and proposed that, as one moves down the mass function, NSCs take over from

SMBHs as the main mode of compact mass aggregation in galactic nuclei. This however, does not imply that SMBHs and NSCs must be mutually exclusive, as exemplified by the nucleus of our own Milky Way (Schödel et al. 2009), as well as many others (e.g., Seth et al. 2008; Graham & Spitler 2009; Gallo et al. 2010; Neumayer & Walcher 2012; Georgiev & Böker 2014). In fact, theoretical work suggests that the presence of a NSC can provide a favorable environment for the formation and/or growth of massive black holes. For example, Stone et al. (2017) suggest that runaway tidal capture processes occurring in NSCs can form a 10^{2-3} $M_{\odot}$ SMBH seed which then grows via tidal disruption events to larger sizes (see Miller & Davies 2012 and Gnedin et al. 2014 for earlier arguments on these same lines). An interesting case, where the above formation scenario does not seem to apply is Henize 2-10, where a NSC seems to be forming independently around a massive central black hole with stellar mass $M_{*} \lesssim 10^{7}$ $M_{\odot}$ (Reines et al. 2011; Nguyen et al. 2014; Arca-Sedda et al. 2015). Co-evolution between the NSC and SMBH in systems such as Henize 2-10 could occur during galaxy mergers, as modeled by Hopkins & Quataert (2010a,b). In addition to facilitating the formation of a SMBH, recent star formation in NSCs could enhance the SMBH feeding-rates, and thus the expected active fraction[1] (Baldassare et al. 2014; see Naiman et al. 2015 for a discussion on NSCs enhancing SMBH feeding-rates during galaxy mergers). This effect would be even more pronounced in the nuclei of late-types, home to larger gas reservoirs. From a different angle, Antonini et al. (2015) investigate the occurrence of NSCs and SMBHs (regardless of their accretion-powered activity level) using semi-analytical galaxy formation models (see also Antonini & Merritt 2012; Antonini 2013). Among galaxies of all types, they find that the local fraction of systems containing both a NSC and SMBH ranges between a few up to 25% for host galaxy stellar masses between $10^{9} M_{\odot}$ – $10^{11} M_{\odot}$ (see their figure 7), with the early-types having a somewhat higher fraction. These occupation values may represent upper limits to the measurable active fraction, allowing a comparison with observational results.

[1]Here defined as the measured fraction of galaxies hosting an Active Galactic Nucleus (AGN) down to some arbitrarily defined accretion luminosity.

The most complete observational study to date on the coexistence of NSCs and actively accreting SMBHs is presented in Seth et al. (2008), where they inspect a sample of 176 nucleated galaxies spanning all galaxy types. Of these, 75 had suitable optical spectroscopic data with either the Sloan Digital Sky Survey (SDSS) or the Palomar Survey (Filippenko & Sargent 1985); a fraction of the remaining objects had heterogeneous X-ray or radio coverage. Seth et al. (2008) find that, of the nucleated galaxies with optical spectroscopic data, 10% are classified as AGN based on the standard optical emission line ratio BPT ("Baldwin, Phillips, & Terlevich") diagram (Baldwin et al. 1981; Kewley et al. 2006), with an additional 15% falling in the AGN-star forming composite region. From this, they conclude the *active fraction of nucleated galaxies is consistent with the galaxy population as a whole.*

In this chapter, we search for the presence of low-luminosity AGN (i.e. weakly accreting SMBHs) in nucleated galaxies by means of a uniform, luminosity limited X-ray survey. Whereas optical emission line ratio diagnostics are arguably best suited at probing Eddington-ratios in excess of 10^{-3}, high spatial resolution X-ray imaging within ~ 30 Mpc affords AGN detectability down to two orders of magnitude deeper Eddington ratios, granted a careful assessment of the X-ray binary contamination (see, e.g. Gallo et al. 2010). In what follows, we report on a comparative analysis of 2 samples of nearby nucleated galaxies, both targeted with the *Chandra X-ray Telescope* down to a limiting luminosity of 10^{38} erg sec^{-1}. The first sample consists of 51 nucleated Virgo early-types (for which results were first reported in Gallo et al. 2008, 2010, Miller et al. 2012a); the second sample consists of 47 nucleated late-types, drawn from Seth et al. (2008) as described below. Our aims are two-fold: (i) to measure the overall active fraction down to a uniform limiting luminosity, and compare it with the active fraction as measured for a parent sample of non-nucleated systems over a comparable stellar mass range; (ii) to compare the active fraction as measured for nucleated early- vs. late-types. The former goal addresses whether the presence of a NSCs enhances the likelihood of there being an actively accreting SMBH; the latter will help us determine the effect of its several-pc scale environment, if any, on SMBH feeding.

2.4 Sample Selection and Data Analysis

Out of 176 galaxies that compose the initial Seth et al. (2008) sample of nucleated galaxies, 51 are Virgo early-type; those were observed by *Chandra* as part of a large Cycle 8 program (AMUSE-Virgo; Proposal ID: 08900784, PI: Treu); the results were presented in Gallo et al. (2008, 2010). The remaining objects are late-type galaxies spanning distances between 4 and 40 Mpc. Out of those, we culled a sub-sample of objects (i) within $\simeq$20 Mpc; (ii) face-on, and (iii) located more than $\pm30^{\circ}$ off the galactic plane, so as to minimize local and Galactic absorption. Visual inspection of optical data was used to determine the inclination of each galaxy. This yields 47 late-type galaxies. The distance cut was chosen to ensure that the planned X-ray luminosity detection threshold would match that of the Virgo early-type sample that were previously targeted by *Chandra*. In the following, we report on the new results on the late-type galaxies.

Out of 47 objects, 18 had sufficiently deep archival data. We targeted the remaining 29 galaxies in Cycle 16 (Proposal ID:16620343, PI: Gallo, hereafter C16 sample). Each C16 galaxy was placed on the back-illuminated S3 chip of the Advanced CCD Imaging Spectrometer (ACIS) detector, with exposure times ranging from 1–5 ks, chosen in order to achieve a uniform 3σ point-like source detection threshold of 10^{38} erg s^{-1}. Typical exposure times for the archival subsample are longer than those of the C16 data, with the highest exposure being 90 ks for NGC 5879. For archival sources with multiple visits, we prioritize the observation with the target being closer to the aim-point. In the case of multiple observations with comparable aim-points, we prioritize the shortest exposure, again to match the sensitivity of the C16 data.

We follow a similar data reduction for the late-type galaxies as described in previous X-ray studies of the AMUSE-Virgo/Field surveys (Gallo et al. 2008, 2010; Miller et al. 2012b,a; Plotkin et al. 2014; Miller et al. 2015), using the Chandra Interactive Analysis of Observations (`CIAO`) v4.8. We first correct for astrometry, preferentially cross-matching the *Chandra*-detected point-like sources with the Sloan Digital Sky Survey Data Release

9 (SDSS DR9) catalog, and using the U.S. Naval Observatory's USNO-B1 catalog for all other galaxies outside of the SDSS footprint. The *Chandra* sources used for cross-matching are detected by running `wavdetect` on the reprocessed level 2 event files. We require each matched pair to be less than 2 arsec from one another, and a minimum of 3 matches for an image to be astrometrically corrected. Seventeen of the late-type galaxies are astrometrically corrected, all with shifts less than $0\farcs5$. Of those, 82% use the SDSS DR9 catalog and 18% use the USNO-B1 catalog.

We then correct for background flaring by removing intervals where the background rate was found to be 3σ above the mean level. We rerun `wavdetect` on the filtered 0.5–7 keV data to generate a list of X-ray point sources using wavelets of scales 1, 1.5, and 2.0 pixels using a 1.5 keV exposure map, and set the detection threshold significance to 10^{-6} (corresponding to one false detection over the entire S3 chip). Source position errors are calculated as the quadratic sum of the positional uncertainty for the X-ray source (discussed in Garmire et al. 2000), the uncertainty in the optical astrometry ($< 0\farcs1$ for both SDSS and USNO-B1), and the uncertainty in the X-ray bore-sight correction.

Next, we screen each image for diffuse X-ray emission following the methodology presented in Plotkin et al. (2014) (albeit contamination from hot, free-free emitting gas is expected to be small in our sample of nucleated late-types). We first generate the (source-free) galaxies' X-ray surface brightness profiles in the 0.5–7 keV band. This is done with annuli centered on the optical center of the galaxy and extending to a radius of R_{25}, defined as the radius where the surface brightness drops to 25 mag arcsec^{-2} (R_{25} values are tabulated in Liu et al. 2011b and Georgiev & Böker 2014). The background surface brightness, c_{bk}, is determined by taking the median value from 4 circular regions outside each galaxy's R_{25} value. A galaxy is classified as having diffuse emission if the inner (i.e., within R_{25}) surface brightness profile exceeds $3\times c_{bk}$. Two archival galaxies, NGC 4030 and NGC 5879, meet this criterion (not surprisingly, both belong to the high-end tail of the sample's mass distribution, with stellar masses $\log(M/M_\odot)$ of 10.9 and 10.0, respectively, and also have longer

exposures times, of 14 and 90 ks, respectively). For these two objects, we restrict our X-ray point source search to energies between 2-7 keV, where diffuse gas typically contributes less than 5% of the total X-ray emission, and rerun `wavdetect` using a 4.5 keV exposure map.

For each galaxy we search for an X-ray point source within 2″ of the nominal, SDSS-listed optical center (2″ corresponds to 95% of the encircled energy radius at 1.5 keV for ACIS). Counts are extracted from a 2″ radius circular region centered on the optical center position/X-ray source center (in the case of non detection/detection, respectively), using a source-free annulus with inner radius of 20″ and outer radius of 30″ for background extraction. Source net count rate and flux values (or upper limits) are determined using the `CIAO` script `srcflux` assuming an absorbed powerlaw spectrum ("xspowerlaw.pow1" and"xsphabs.abs1") with photon index $\Gamma = 1.8$, and using the tool `colden`[2] to evaluate the neutral hydrogen column density towards each object. Out of 47 late-type galaxies, 5 are associated with a statistically significant, point-like, nuclear X-ray source. The nuclear X-ray luminosity values and upper limits are shown in Table 2.1, while more detailed information about the 5 detections are given in Table 2.2.

2.5 Origin of the nuclear X-ray Emission

2.5.1 X-ray binary luminosity assessment

We will now focus on the 5 late-type galaxies with nuclear X-ray detections in order to assess the physical nature of the emission. Based on the $\log N$–$\log S$ relation presented in Rosati et al. (2002), the probability that any of the detected X-ray sources can be attributed to a background object within the *Chandra* Point Spread Function (PSF) varies between 10^{-3}–10^{-4}, and is thus deemed negligible. The X-ray luminosities of the detected nuclei range between $0.2 - 1 \times 10^{39}$ erg sec^{-1}. While nuclear X-ray luminosity in excess of 10^{40} erg sec^{-1} can be comfortably attributed to AGN emission (see, e.g., Lehmer et al. 2010), here,

[2] `Colden` uses the National Radio Astronomy Observatory (NRAO) dataset supplied by Dickey & Lockman (1990).

Table 2.1: Nucleated late-type galaxy properties

Galaxy	obsID	Type	Exposure (ks)	Distance (Mpc)	$\log M_*$ ($\log M_\odot$)	$\log L_X$ ($\log$(erg s^{-1}))
(1)	(2)	(3)	(4)	(5)	(6)	(7)
NGC 300	16028 (A)	Scd	63.84	1.9	9.3	< 35.4
NGC 337a	16976 (C16)	SABd	3.20	14.3	9.4	< 38.36
NGC 406	16977 (C16)	Sc	4.70	17.5	9.7	< 38.35
NGC 428	16978 (C16)	SABm	2.97	15.9	9.8	< 38.36
NGC 1042	12988 (A)	SABc	30.00	18.0	10.0	38.34
ESO 548-G29	16979 (C16)	SABb	3.70	16.2	9.56*	< 38.76
ESO 418-8	16980 (C16)	SABd	3.12	14.1	9.4	< 38.35
NGC 1483	16981 (C16)	SBbc	2.26	12.6	9.1	< 38.26
NGC 1493	7145 (A)	SBc	9.24	11.3	9.6	38.68
NGC 1688	16982 (C16)	SBc	2.03	13.4	9.5	< 38.40
NGC 1892	16983 (C16)	Sc	2.56	15.2	9.6	< 38.37
NGC 2082	7838 (A)	SBb	5.07	15.3	9.8	< 38.10
NGC 2104	16984 (C16)	SBm	2.63	12.8	9.1	< 38.35
UGC 4499	16985 (C16)	Sd	2.17	12.6	8.7	< 38.36
NGC 3423	16346 (A)	Sc	47.02	14.7	9.9	< 37.34
NGC 3455	16986 (C16)	SABb	4.35	16.9	9.5	< 38.35
NGC 3501	16987 (C16)	Sc	4.55	17.4	9.56*	< 38.28
NGC 3782	16988 (C16)	Scd	4.94	13.6	9.56*	< 38.37
NGC 3906	16989 (C16)	SBcd	4.50	16.9	9.3	< 38.36
NGC 3913	7856 (A)	Scd	4.70	17.1	9.4	< 37.65
NGC 3949	16990 (C16)	Sbc	3.39	14.6	9.9	< 38.27
NGC 4030	11670 (A)	Sbc	14.86	21.1	10.9	< 37.94
NGC 4144	16991 (C16)	SABc	1.05	7.2	9.0	< 38.22
NGC 4183	16992 (C16)	Sc	3.58	16.2	9.6	< 38.35
NGC 4204	7092 (A)	SBd	1.99	13.9	9.56*	< 38.49
NGC 4206	16993 (C16)	Sbc	2.00	11.3	9.5	< 38.38
NGC 4299	7834 (A)	SABd	5.07	16.8	9.3	< 38.07
NGC 4411b	7840 (A)	SABc	4.89	19.1	9.6	< 38.31
NGC 4487	16994 (C16)	Sc	2.82	14.7	9.8	39.07
NGC 4496a	16995 (C16)	SBd	2.72	15.0	9.7	< 38.48
NGC 4517	16996 (C16)	Sc	4.06	16.5	10.6	< 38.34
NGC 4618	7147 (A)	SBm	9.11	10.7	9.6	< 37.52
NGC 4625	7098 (A)	SABm	7.10	11.7	9.4	< 38.27
NGC 4701	7148 (A)	Sc	9.04	11.1	9.3	< 37.56
NGC 5023	16997 (C16)	Sc	1.02	5.4	8.7	< 38.18
NGC 5068	7149 (A)	Sc	6.67	8.7	10.0	< 36.51
UGC 8516	16998 (C16)	Sc	3.64	16.7	9.3	< 38.35
NGC 5585	7150 (A)	SABc	5.32	10.5	9.4	< 37.12
NGC 5879	2241 (A)	Sbc	88.77	15.0	10.0	38.55
NGC 6239	16999 (C16)	SBb	4.25	16.9	9.6	< 38.28
IC 5052	17000 (C16)	SBcd	1.02	6.0	9.1	< 38.10
IC 5256	17001 (C16)	SBd	1.39	9.9	9.56*	< 38.32
NGC 7424	3495 (A)	Sc	23.24	10.8	9.6	< 37.11
NGC 7690	17002 (C16)	Sb	4.43	18.2	9.8	39.05
UGC 12732	17003 (C16)	SABm	2.18	12.3	9.56*	< 38.35
ESO 241-G06	17004 (C16)	SBm	1.54	17.3	9.56*	< 38.35
NGC 7793	3954 (A)	Scd	47.75	3.9	9.6	< 36.16

Note. – Columns: (1) Galaxy name; (2) observation ID, denoted as Cycle 16 data (C16) or archival data (A); (3) filtered exposure time in seconds, after correcting for background flares in `CIAO`; (4) morphological type of host galaxy; (5) distance, in Mpc, taken from Seth et al. (2008); (6) stellar mass of the host galaxy in $M_\odot$, taken from Seth et al. (2008); (7) nuclear X-ray luminosity between 0.3 and 7 keV, in erg s^{-1}.

$*$ - denote galaxies with no available V-band data. Galactic mass is taken to be the median value of our late-type sample.

Table 2.2: X-ray detections for nucleated late-types

Galaxy	Optical α (J200)	Optical δ (J200)	α (J200)	δ (J200)	δ	X-ray counts
(1)	(2)	(3)	(4)	(5)	(6)	(7)
NGC 1042	2:40:23.99	-8:26:01.1	2:40:23.959 (0.12)	-8:26:00.57 (0.12)	0.6	23 (4.8)
NGC 1493	3:57:27.47	-46:12:39.2	3:57:27.454 (0.10)	-46:12:38.55 (0.10)	0.6	48 (6.9)
NGC 4487	12:31:04.48	-8:03:13.8	12:31:04.497 (0.12)	-08:03:12.48 (0.12)	0.8	17 (4.1)
NGC 5879	15:09:46.663	+57:00:00.67	15:09:46.725 (0.08)	+57:00:00.64 (0.08)	0.2	140 (11.8)
NGC 7690	23:33:02.542	-51:41:54.11	23:33:02.528 (0.13)	-51:41:54.44 (0.13)	0.3	17 (4.1)

Note. – Units of right ascension are hours, minutes, and seconds, and units of declination are degrees, arcminutes, and arcseconds. Columns: (1) Galaxy name; (2) and (3): R.A. and Dec. of optical center; (4) and (5): R.A. and Dec. of X-ray nucleus with the positional uncertainty on the centroid position given in parenthesis, in arcseconds; (6) δ between optical center and X-ray nucleus, in arcseconds; (7) nuclear X-ray source net counts extracted between 0.3 and 7 keV, with errors in parenthesis.

the inferred values warrant a careful assessment of the contamination from bright X-Ray Binaries (XRBs) to the *Chandra* PSF (see Gallo et al. 2008, 2010; Miller et al. 2012a for further discussion). Our assessment of the origin of the detected nuclear X-ray emission will depend on the number of central ($<2''$) X-ray binary sources expected from the entire late-type sample. To this end, we first estimate the *total*, expected X-ray luminosity due to XRBs for each of our 47 late-type galaxies. More specifically, the X-ray Luminosity Function (XLF) of Low-Mass X-ray Binaries (LMXBs) is known to be set by the galaxy cumulative star formation history, and thus scales with the total stellar mass of the galaxy, M_* (Ghosh & White 2001; Grimm et al. 2002; Gilfanov 2004; Kim & Fabbiano 2004; Humphrey & Buote 2008), whereas the High-Mass X-ray Binary (HMXB) XLF traces recent star formation within the galaxy (Sunyaev et al. 1978; Grimm et al. 2003; Lehmer et al. 2010; Mineo et al. 2012), and its normalization depends on the galaxy's Star Formation Rate (SFR).

We start by adopting the analytic prescription by Lehmer et al. (2010), who built on the above mentioned, previous investigations to carry out a systematic assessment of the different possible contributions to the total X-ray luminosity of nearby galaxies, including LMXBs and HMXBs, as well as diffuse emission from hot gas. For a given M_* and SFR, the total, 2–10 keV luminosity from XRBs ($L_{\rm XRB}^{\rm gal}$) can be expressed as:

$$L_{XRB}^{gal} = \alpha M_* + \beta SFR, \tag{2.1}$$

with best fitting parameters $\alpha = (9.05 \pm 0.37) \times 10^{28}\,\mathrm{erg\,s^{-1}}\,M_{\odot}^{-1}$ and $\beta = (1.62 \pm 0.22) \times 10^{39}\,\mathrm{erg\,s^{-1}}(\,M_{\odot}\,\mathrm{yr^{-1}})^{-1}$.

Stellar masses were taken from Seth et al. (2008) and were derived using galaxy colors and the M/L relations presented in Bell et al. (2003) (errors are on the order of 0.15 dex). The formalism presented in Bell et al. (2005) was adopted to estimate SFRs, where the 12μm (f_{12}), 25μm (f_{25}), 60μm (f_{60}), and 100μm (f_{100}) flux density values from the IRAS Faint Source Catalog (Moshir & et al. 1990) were employed to estimate the total infrared luminosity, L_{IR}, for each galaxy, following Perault (1987) (see also Sanders & Mirabel 1996). We use Wide-field Infrared Survey Explorer (WISE) data and IR color diagnostics (after Jarrett et al. 2011, Stern et al. 2005) to test for a possible contribution from the central SMBH to the IR luminosity for our 5 detections. We find that none of our sources fall within the AGN parameter space empirically identified by Jarrett et al. (2011), implying that the above SFRs are likely unaffected by the presence of a central SMBH (this is not surprising, considering the extremely low Eddington ratios we are operating at).

Five late-type galaxies (NGC 3423, NGC 3501, NGC 4183, NGC 5023, and UGC 12732) have no IRAS coverage, and we estimate their SFRs via 70 μm measurements from the *Spitzer* Multiband Imaging Photometer (MIPS; for conversion measurements between MIPS and IRAS filters see Terrazas et al. 2016); 1.4 GHz measurements from the Very Large Array (VLA; for conversion measurements between 1.4 GHz and total IR emission see Bell et al. 2003); and Hα measurements from the Hα Galaxy Survey (see James et al. 2004), preferentially in that order.

Finally, multiple distances are available in the literature for each galaxy, including Seth et al. (2008), Georgiev & Böker (2014), Böker et al. (2002), and Carollo et al. (1997, 1998, 2002), with the study by Seth et al. (2008) using Virgo infall-corrected velocities from Hyperleda and redshift-independent indicators listed in NED[3]. We compared the distances published in Seth et al. (2008) to those published in Georgiev & Böker (2014) and the ear-

[3]https://ned.ipac.caltech.edu/

lier publications, and find that the values agree with one-another with an expected scatter and no systematic shifts. Thus, for the purpose of drawing a fair comparison between the late and early-type sample, we adopt the distances published in Seth et al. (2008) (we verified, however, that our results are qualitatively insensitive to the distance source choice). Distances and stellar masses for each host galaxy can be found in Table 2.1.

2.5.2 Nuclear X-ray binary contamination

In order to estimate possible contamination to the *Chandra* PSF, we (i) estimate the *fractional* contribution to $L_{\rm XRB}^{\rm gal}$ (Eq. 2.1) to the actual, detected nuclear X-ray signal, and (ii) estimate the total number of expected central ($< 2''$) XRBs in our late-type sample. Values of the fractional contribution of $L_{\rm XRB}^{\rm gal}$ for each galaxy allows us to derive the proper normalization constants when calculating the expected number of central XRBs. Regarding point (i), we first convert the estimated $L_{\rm XRB}^{\rm gal}$ into (0.5-7) keV luminosities using webPIMMS[4] for a power law spectrum with $\Gamma = 1.8$. In order to estimate the mean XRB luminosity in the nucleus, we follow the methodology presented in Alfvin et al. (2016) and assume that the total $L_{\rm XRB}^{\rm gal}$ is distributed according to the optical light profile.

Most of our late-type galaxies with a detected X-ray nucleus have Wide-Field Planetary Camera 2 (WFPC2) observations in the Hubble Legacy Archive (HLA)[5], where we use observations taken with the well-calibrated F606W /F814W filters. For those with no WFPC2 observations (NGC 3501, NGC 4144, NGC 4183, NGC 4206, and IC 5052) we use ACS F606W/F814W imaging. With the Image Reduction and Analysis Facility (`IRAF`) software, we mask out bright foreground stars in the field of view and use `ds9` to extract the radial profiles of each galaxy's surface brightness. We integrate the light profiles out to R_{25} to calculate the total luminosity of the galaxy and estimate the fraction that is contained within the central $2''$. The radial surface brightness profiles for the 5 late-type detections, analyzed in `IRAF` via `ELLIPSE`, are shown in Figure 2.1. To assess for errors introduced by using

[4]heasarc.gsfc.nasa.gov/cgi-bin/Tools/w3pimms/w3pimms.pl
[5]http://hla.stsci.edu/

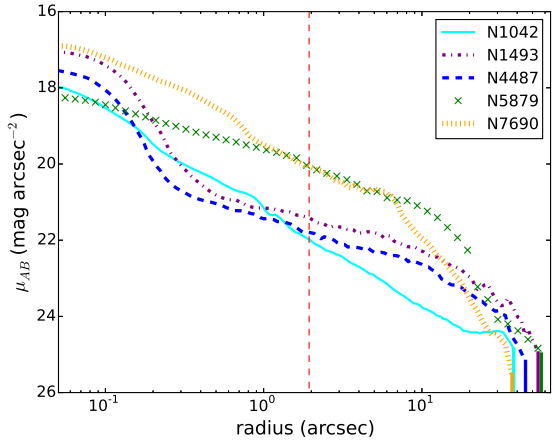

Figure 2.1: Radial surface brightness profiles of the 5 late-type galaxies with detected nuclear X-ray emission, projected along the semi-major axis. Profiles were extracted from HLA images in the F606W (NGC1042, NGC 4487, NGC 5879, and NGC 7690) and F814W filter (NGC 1493). The red vertical dashed line marks 2″. For each galaxy, the solid vertical line at the end of the profile marks the extent of R_{25}. Error bars are < 0.1 mag.

different filters, we compare the fractional luminosity values (within 2″) between the F606W and F814W radial profiles for a handful of nearby galaxies with observations available in both bands and find the difference consistently lower than 0.4%. The X-ray luminosity due to XRBs within the central 2″ is obtained by multiplying the 0.5-7 keV total X-ray binary luminosity, $L_{\rm XRB}^{\rm gal}$, by the galaxy's respective fractional value as estimated above. The fractions range from 0.5 – 9.8%, with nuclear XRB luminosities, $L_{\rm XRB}^{n}$ between $3{\times}10^{35}$ up to $\sim$ $3{\times}10^{38}$ erg s^{-1}.

Regarding point (ii), we then estimate the total number of expected central ($< 2''$) XRBs in our late-type sample. For each galaxy we calculate N(>L), where for our non-detections N is defined as the number of expected central XRBs with luminosities greater than or equal to the sensitivity threshold ($L \geq 10^{38}$ ergs s^{-1}) and for our 5 detections, N is defined as the number of expected central XRBs with luminosities greater than or equal to the detected central X-ray luminosity ($L \geq L_X$). We assume the nuclear XRB luminosity is due to a distribution of both LMXBs and HMXBs that follow the XLFs presented in Gilfanov (2004) and Grimm et al. (2003): $dN/dL = {\rm K}_1 L^{-\alpha 1} + {\rm K}_2 L^{-\alpha 2}$, where for our given luminosity

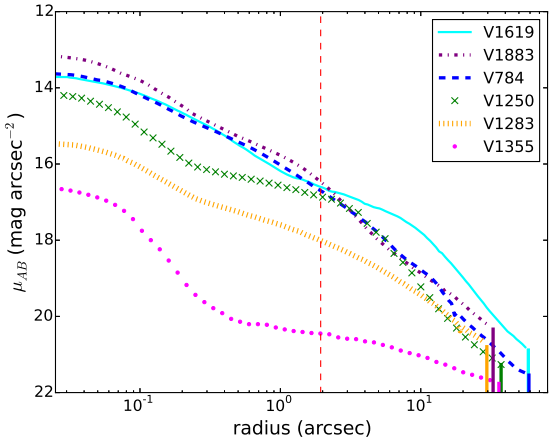

Figure 2.2: Radial surface brightness profiles of the 6 early-type Virgo galaxies with detected nuclear X-ray emission, projected along the semi-major axis. Profiles were extracted from HST ACS F850LP images. Demarcations are the same as presented in Figure 2.1.

range $\alpha 1 = 1.8$ and $\alpha 2 = 1.61$. The normalization constants K_1 and K_2 are derived from the expected fractional XRB luminosity (see Eq. 2.1). We build a distribution of expected nuclear XRBs from the entire late-type group by sampling through each galaxy 10^6 times and randomly pulling a value, x, from a Poisson distribution centered on N. If $x \geq 1$, we count x XRBs from the central $2''$ for a given galaxy. Furthermore, we assign each XRB an X-ray luminosity via inverse transform sampling from the galaxy's cumulative distribution. This process allows us to measure the most likely number of central XRBs from our sample as well as calculating the probability that, at a given luminosity, each of our central detections are SMBHs ($P_{\rm SMBH}$). Following this methodology, the most likely number of total, central, XRBs in the late-type sample is projected to be $\sim$1.4, with probabilities $P_{\rm SMBH}$ for our five detections ranging from 94.4 to 98.1%.

To allow for a proper comparison between the late-type sample considered above and the companion early-type sample targeted by *Chandra* as part of the AMUSE-Virgo program, we carry out the same steps as described in the previous sub-section for the early-type galaxies (specifically, we wish to carry out a direct comparison for the XRB contamination, which was

Table 2.3: Nucleated early-type galaxies with X-ray detections

Galaxy	Distance (Mpc)	$\log M_*$ ($\log M_\odot$)	$\log L_X$ ($\log(\mathrm{erg\ s^{-1}})$)
(1)	(2)	(3)	(4)
VCC1619	15.49	10.2	38.68
VCC1883	16.60	10.4	38.35
VCC784	15.85	10.3	38.62
VCC1250	17.62	10.2	38.73
VCC1283	17.38	10.1	38.54
VCC1355	16.90	9.4	38.58

Note. – Columns: (1) Galaxy name; (2) distance, in Mpc; (3) total galactic stellar mass, in $\log M_\odot$; (4) nuclear X-ray luminosity between 0.3 and 7 keV, in erg $\mathrm{s^{-1}}$. All values are taken from Gallo et al. (2010).

addressed somewhat differently by Gallo et al. 2010[6]). All of the 51 nucleated early-types have dual-band (F475W & F850LP) HST Advanced Camera for Surveys (ACS) imaging data, as part of the ACS Virgo Cluster Survey (Côté et al. 2006); 6 out of 51 were found to have a nuclear X-ray source (Gallo et al. 2010; see Table 2.3).

The radial surface brightness profiles of the six detections are shown in Fig 2.2. We assess for errors introduced by using different instruments/filters between the late-type and early-type radial profiles by comparing the fractional luminosity values (within $2''$) between the WFPC2 and ACS observations. We find that the fractional luminosity in the F814W band is consistently 1.36 times greater than the fractional luminosity in the F850LP band, and thus multiply all F850LP fractions by this value. This fractional value is then multiplied by the estimated $L_{\mathrm{XRB}}^{\mathrm{gal}}$ in order to estimate the expected XRB luminosity from the central $2''$. We note that SFRs for this sample — and hence the HMXB contribution to the total X-ray luminosity — are expected to be negligible. We checked the validity of this assumption by calculating the SFR for VCC1250, the bluest galaxy, and indeed found the corresponding HMXB contribution to $L_{\mathrm{XRB}}^{\mathrm{gal}}$ to be negligible, where the $\mathrm{SFR}_{V1250} \approx 0.08\ M_\odot\ \mathrm{yr^{-1}}$ contributed $< 8\%$ of the total luminosity expected from XRBs). We thus ignore the β term

[6]Gallo et al. (2010) estimated the probability of XRB contamination for the nucleated Virgo galaxies using the XLF of globular clusters, as presented by Sivakoff et al. (2007). This was motivated by the stellar number density of NSCs being arguably closer to that of globular clusters than the field; however, this approach requires knowledge of the clusters' $g - z$ colors, and hence dual band, g and z-equivalent HST imaging data, which are not available for our sample of early types.

in Equation 2.1 for the early-type galaxies. In general, the early-type galaxies are found to contain a larger portion of the total light within the central $2''$ than the late-type sample, and thus have higher expected $L^n_{\rm XRB}$, with fractions ranging from 1.2–45.3%, and 0.5–7 keV $L^n_{\rm XRB}$ values between 7×10^{35}–$1.7 \times 10^{38}\,{\rm erg\,s^{-1}}$.

We follow the same methodology as the late-types to estimate (i) the number of expected central XRBs and (ii) the probabilities that the 6 early-type detections are SMBHs. For our non-detections we define N as the number of expected central XRBs with luminosities greater than or equal to the average sensitivity threshold ($L \geq 3{\times}10^{38}$ ergs s^{-1}; see Gallo et al. 2010) and for the 6 detections we define N as the number of expected central XRBs with luminosities greater than or equal to the detected central X-ray luminosity ($L \geq L_X$). Here, we assume the nuclear XRB luminosity is solely due to a distribution that follows the XLF of LMXBs Gilfanov (2004): $dN/dL = {\rm K}L^{-\alpha}$, where the slope for our given luminosity range is $\alpha = 1.8$ and the normalization constant K is derived from the expected nuclear luminosity of XRBs. We find that the most likely number of total, central, XRBs in the early-type sample is projected to be consistent with 1, with probabilities $P_{\rm SMBH}$ for the six detections ranging from 90.1 to 92.7% (see Table 2.4).

We combine the results from the late- and early-type XRB contamination analysis. The total number of nuclear XRBs follows a Poisson distribution, for which we find a most likely value of 3. The likelihood of detecting at least 11 SMBHs is $< 3\%$, and at the 3σ (99.7%) confidence level 3 of our 11 detections are SMBHs.

2.6 Active Fraction

The probability-weighted X-ray detections discussed above can be employed to estimate the active fraction of nearby nucleated galaxies, down to a uniform X-ray luminosity threshold, and as a function of morphological class. Before comparing the active fractions between the late-type and early-type samples, we determine whether the two distributions are consistent with being drawn from the same mass distributions by using a weighting function.

Table 2.4: XRB Contamination

Galaxy	$\log L^{n}_{\rm XRB}$ ($\log$(erg s^{-1}))	$P_{\rm SMBH}$ (%)
(1)	(2)	(3)
N1042	37.76	94.40
N1493	36.96	96.90
N4487	37.10	98.07
N5879	37.62	96.10
N7690	37.99	98.10
V1619	37.71	92.70
V1883	38.02	90.10
V784	38.23	92.00
V1250	38.10	92.70
V1283	37.73	91.80
V1355	36.65	92.00

Note. – Columns: (1) Galaxy name; (2) XRB luminosity between 0.3 to 7 keV expected in central 2″, in erg s^{-1}; (3) probability that source is a SMBH instead of an XRB. *Top*: late-type sample; *Bottom*: early-type sample.

We follow the procedures outlined in Miller et al. (2012a), and Baldassare et al. (2014): the two samples are represented as a sum of Gaussians and we use a weighting function, defined as the ratio of the late-type distribution to the early-type distribution, to draw a subsample from the early-type distribution that has the same number of galaxies and mass distribution as the late-type sample (see Figure 2.3). We draw 500 such subsamples and find that, on average, they contain 5.5 objects with nuclear X-ray point sources, corresponding to $10.8\%^{+11.3}_{-6.3}$. For the late-type sample, we found five our of 47 objects objects to have nuclear X-ray detections, corresponding to $10.6\%^{+11.9}_{-4.9}$. Poisson statistics show that for an expected value of five active nuclei, there is a 38% chance of finding six or more active nuclei in a sample of 47. This argues for no statistically significant difference in the nucleation fraction of the early- and late-type samples. Across both morphological types, we find the active fraction to be $11.2\%^{+7.4}_{-4.9}$.

2.6.1 Regression Analysis

In the following we explore a possible relation between the galaxy stellar mass, M_*, and the central X-ray luminosity, L_X. Values for M_* are derived from the galaxy's absolute

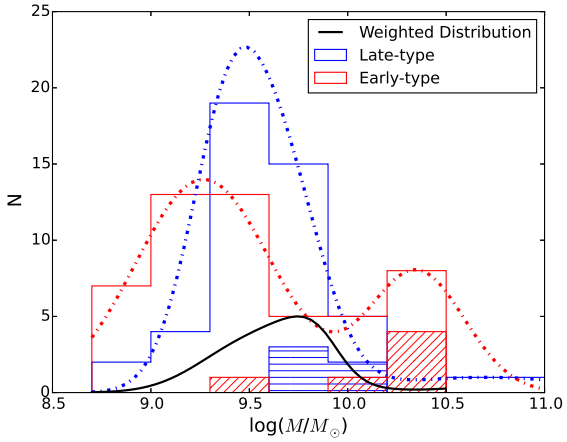

Figure 2.3: Stellar mass distributions of the late- (open blue histogram) and early-type (open red histogram) samples. The distribution of galaxies with central X-ray detections are shown for both as histograms with diagonal (early-type) and horizontal (late-type) hatching. Each sample has been fit with multiple Gaussians. The weighted distribution, defined as the ratio of the late-type distribution to the early-type distribution, is shown as a black curve. This is used to draw a subsample of the early-type galaxies with the same number and mass distribution as the late-type sample, allowing for a proper comparison of the active fraction between different morphological types.

luminosity (L_B), thus the M_*–L_X relation is similar to the L_B–L_X relation, which has been seen in nearby early-type galaxies (Pellegrini 2010). As well, a relation between M_*–L_X can be reflective of a possible relation between M_{BH}–L_X due to the correlation between M_* and M_{BH}. Similar analyses have been carried out for the AMUSE surveys, where a statistically significant correlation has been found between nuclear X-ray luminosity and host stellar mass (Miller et al. 2012b,a). For the AMUSE-Field galaxies, Miller et al. (2012b) find a slope in the M_*–L_X plane of $\beta = 0.71 \pm 0.10$, which is consistent with a non-zero value at a 3-σ level. The tendency for the X-ray luminosity to increase less rapidly than M_* can be interpreted as lower-mass galaxies being more X-ray luminous per unit stellar mass, however the large scatter ($\sim$0.7) allows for alternative explanations.

Motivated by the results of the AMUSE surveys, we assess the presence of a quantitative relation of the form:

$$\log L_X - 38.2 = \alpha + \beta \times (\log M_* - 9.52), \tag{2.2}$$

where the variables are centered on the median values of the measured nuclear X-ray luminosity and host stellar mass for our combined sample of early and late-type nucleated systems. We use the Bayesian linear regression code `linmix_err.pro`, by Kelly (2007), which incorporates both uncertainties and censoring to determine the best-fit parameters. Similar to Miller et al. (2012b), our errors are taken to be 0.1 dex on $\log(L_{\rm X})$, associated with the uncertainty in the distance. Our errors are taken to be 0.18 on $\log(M_*)$; this is derived by adding in quadrature the error of 0.15 dex found in Seth et al. (2008) and the scatter of 0.1 dex in M/L as presented in Bell et al. (2003). First, we treat every X-ray detected nucleus as indicative of an accreting SMBH, regardless of XRB contamination (i.e., we take $P_{\rm SMBH}$=100% for all of the detected nuclei). To ensure uniform censoring, we set all of the upper limits below $\log(L_{\rm X}) = 38.0$ (from deeper, archival exposures) to a value of 38. We find the median values of the intercept, slope, scatter and Pearson correlation coefficient to be: $\alpha = -1.50 \pm 0.35$, $\beta = 1.67 \pm 0.42$, $\sigma = 0.90 \pm 0.20$, and $r = 0.62 \pm 0.11$ (median values are taken from 10,000 draws of the posterior distributions, and the 1σ errors quoted are calculated as the 16th and 84th percentiles). Figure 2.4 shows the distribution of $\log L_{\rm X}$ vs. $\log M_*$ for our complete sample with the "best fit" line shown in red. Although the intrinsic scatter is large, the Pearson correlation value of 0.6 suggests a statistically significant correlation ($r = 0.6$ for 98 points corresponds to a p value < 0.01 given the sample size).

A valid concern, however, has to do with the ability of `linmix_err.pro` to recover an intrinsic correlation when dealing with a large fraction of upper limits, rather than detections (i.e., 89% of the data points, in our case). In order to assess this, following Kelly (2007) we start from the same stellar mass distribution as our data and simulate a random distribution of $L_{\rm X}$ that follows the above mentioned relation: $\log L_{\rm X} - 38.2 = -1.50 + 1.67 \times (\log {\rm M}_* - 9.52)$, with an intrinsic scatter of 0.9, and Pearson correlation value of 0.62, as shown in the left panel of Figure 2.5. We then run `linmix_err.pro` on the simulated points, adopting

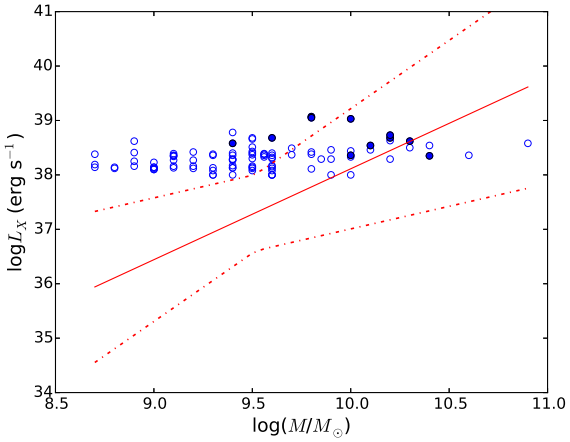

Figure 2.4: Measured nuclear X-ray luminosities, $L_{\rm X}$, as a function of host galaxy stellar mass, M_*, for our full sample of late and early-type galaxies (98 systems). Filled circles mark detections and open circles mark upper limits. Error bars are taken to be 0.1 dex for both $L_{\rm X}$ and M_*. The "best-fitting relation" from our Bayesian linear regression analysis is shown as a solid red curve, with the dotted lines corresponding to 2σ error bars. Here, 1σ error bars correspond to the 16th and 84th percentiles of the posterior distributions.

progressively higher X-ray luminosity detection thresholds values to lower the detection fraction, down to the limiting case of only 11% of the data resulting into detections, shown in the right panel of Figure 2.5. For this case, Figure 2.6 shows the full posterior distributions of β, σ, and r recovered by `linmix_err.pro`, compared to the "true" values, indicated by the solid red vertical line. In spite of the very high fraction of upper limits, the median values of the parameters' posterior distributions agree within 2σ with the "true" values.

Finally, in order to incorporate the results of our XRB contamination assessment into the correlation analysis we follow the probabilistic method described by Alfvin et al. (2016), i.e., we run `linmix_err.pro` 200 times, probabilistically varying whether each X-ray nucleus is treated as an upper limit or a detection according to the probabilities estimated in the previous Section (see Table 2.4). We find that the distribution of slopes is consistent with $\beta = 1.67 \pm 0.42$, but the uncertainties do not rule out a zero slope.

As a consistency check on the fitting, we stacked the data for late-type galaxies, using the de-flared data in the 0.5–7.0 keV band and applying the diffuse-gas corrections where

appropriate. Since not all of the galaxies are astrometrically corrected, we use a detection cell $5''$ across instead of the $2''$ cell quoted above. We adopted bins of $9.0 \leq \log M_* < 9.5$, $9.5 \leq \log M_* < 10.0$, and $10.0 \leq \log M_* < 10.5$, in which we measure $L_X = 0.2 \pm 0.1 \times 10^{38}\,\mathrm{erg\,s^{-1}}$, $L_X = 1.0 \pm 0.2 \times 10^{38}\,\mathrm{erg\,s^{-1}}$, and $L_X = 3.5 \pm 0.6 \times 10^{38}\,\mathrm{erg\,s^{-1}}$, respectively. These errors incorporate the systematic error in L_X and M_*.

Assuming that black holes follow a L_X–M_* relation with some scatter, which is the same assumption used in the fitting above, we find that the three bins rule out a non-zero slope at greater than 3σ. The high-mass bin only has several galaxies, so the effect of intrinsic scatter may be severe. However, if we ignore it, the remaining two average luminosities are still inconsistent at greater than 3σ. There is also a large variance in the individual exposure times, but when omitting the longest exposures a non-zero slope is ruled out at greater than 3σ.

We examined the effect of XRB contamination on the average luminosities following the procedure outlined above to assess how many counts are likely from undetected XRBs. The effect is most pronounced in the lowest mass bin, where there are only nine total counts and we expect at least this many about 30% of the time. Indeed, the luminosity in this bin is consistent with that expected from XRBs, since for the exposure-weighted average mass in this bin we expect $L_X < 2 \times 10^{37}\,\mathrm{erg\,s^{-1}}$. In contrast, there are only a few galaxies in the high-mass bin and there are two strong detections with low odds of being XRBs (see above). Even if one of these detections is an XRB, the residual luminosity is greater than 3σ above that in the low-mass bin.

Compared to the regression analysis above, stacking uses more information about the number of counts above background but sacrifices information about the stellar mass distribution. The consistency of these approaches in finding a non-zero $L_X - M_*$ slope implies that this result is real and not an artifact of a particular scheme.

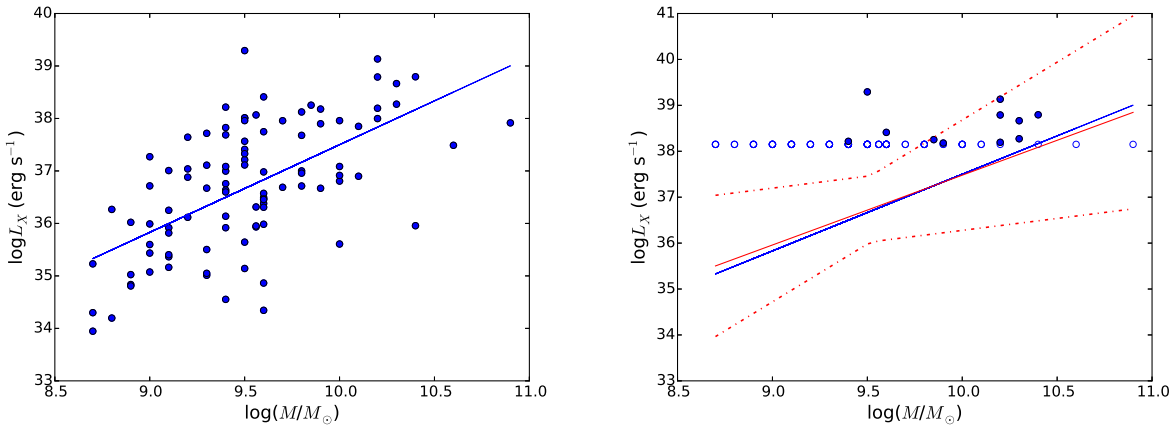

Figure 2.5: A simulated sample of nucleated galaxies (*left*) with the same stellar mass distribution as our nucleated galaxy sample and the best-fit relation recovered by `linmix_err.pro` (*right*) where a luminosity detection threshold of $\log(L_{\rm X})$=38.15 is chosen such that the nuclear X-ray detection fraction matches that of our sample (11%). *Left*: Starting from the same stellar mass distribution as our nucleated galaxy sample, we simulate a random distribution of $L_{\rm X}$ that follows the relation: $\log L_{\rm X} - 38.2 = -1.50 + 1.67 \times (\log M_* - 9.52)$ (shown as a solid blue line), with an intrinsic, uniform scatter of 0.9, and Pearson correlation value of 0.62. *Right*: To match the actual nuclear X-ray detection fraction of our sample (i.e., 11%), a luminosity detection threshold of $\log(L_{\rm X})$=38.15 is chosen, so that all data points below that value turn into upper limits. The solid red line represents the "best-fitting" relation recovered by `linmix_err.pro` (with dotted lines corresponding to 2σ error bars), to be compared to the "true" relation (blue solid line). As also shown in Figure 2.6, the median value of the slope posterior distribution for the 11% detection fraction data set is consistent with the "true" slope to within 2σ.

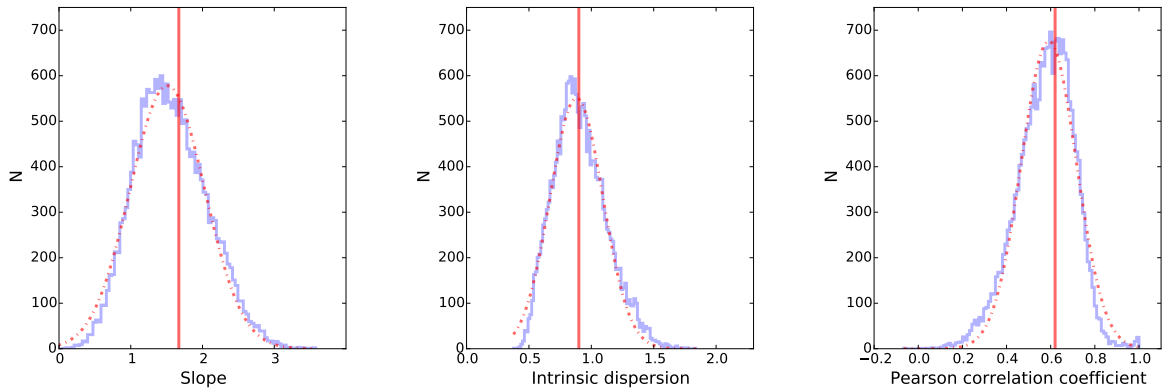

Figure 2.6: The posterior distributions of the slope, intrinsic scatter, and the linear correlation coefficient for the simulated data points shown in the right panel of Figure 2.5 (11% detection fraction) are plotted here in purple, and fit with Gaussian distributions (red dashed curves). For comparison, the *true* values of the slope, scatter and correlation coefficient, corresponding to the simulated data in the left panel of Figure 2.5 are shown as vertical red lines. The "true" values are consistent with the medians of the purple posterior distributions at the 2σ level, indicating that the regression analysis is robust even for detection fractions as low as $\sim 10\%$.

2.6.2 Nuclear star cluster compactness

One of the most recent, comprehensive studies on nucleated late-type galaxies is presented in Georgiev & Böker (2014), where 224 spiral galaxies with NSCs were thoroughly analyzed via *HST* observations. They find that all of the well-resolved (S/N $>$ 30) NSCs with known AGN in their sample appear more compact than the parent nucleated sample (see figure 12 in their paper). They interpret this as compact, excess flux in the F606W filter due to Hα emission produced by weak AGN activity and/or star formation. 34 of our 47 late-type galaxies were included in their study, including 3 (NGC 1042, NGC 1493, and NGC 4487) of the 5 objects that we identified as active via X-ray analyses. One of the objects, NGC 1042, was recognized as an AGN by Georgiev & Böker (2014) based on results from Shields et al. (2008), but was not included in their compactness study due to S/N $<$ 30 (NGC 1493 and NGC 4487 were excluded from their parent sample for similar reasons). Here, we extend their analysis by plotting the 3 objects on the same size-luminosity plot (r_{eff} vs. M_V) as in

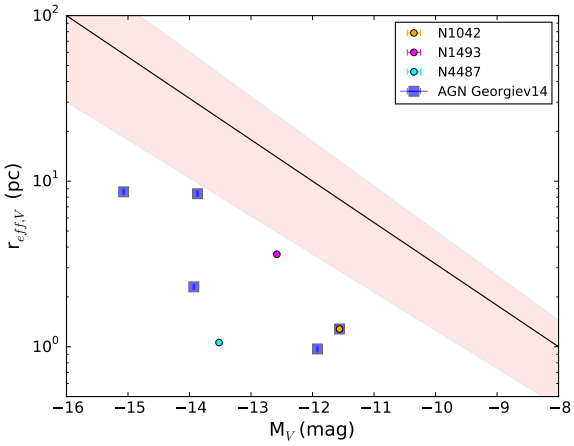

Figure 2.7: Effective V-band radius versus V-band magnitude for the 3 late-type detections from our sample that are included in the catalogue presented in Georgiev & Böker (2014) – NGC 1042 (orange circle with blue square), NGC 1493 (pink circle) and NGC 4487 (cyan circle). The size-luminosity relation for the NSCs in the catalogue of spiral galaxies analyzed in Georgiev & Böker (2014) is shown in black, with region of error shown in red: log r_{eff} = -2.0±0.2 – 0.25±0.01 M_V. Blue squares denote the galaxies with known AGN in Georgiev & Böker (2014). NGC 1042 was recognized as an AGN by Georgiev & Böker (2014) but was not included in their compactness study due to S/N < 30 (NGC 1493 and NGC 4487 were excluded from their parent sample for similar reasons). Error bars on M_V are < 0.1 mag. We find that our nucleated galaxies with AGN tend to have more compact effective radii at a given luminosity.

Georgiev & Böker (2014) (see Figure 2.7). All 3 objects lie below the best-fit relation found in Georgiev & Böker (2014). We confirm the trend that nucleated galaxies with AGN tend to have more compact effective radii at a given luminosity, possibly caused by the presence of a weak AGN and/or a younger stellar population that is more concentrated than the surrounding NSC stars.

2.7 Summary and Discussion

In this work, we report on *Chandra* observations of a distance-limited sample of 98 galaxies known to harbor NSCs, with the aim to characterize the incidence and intensity of the AGN (or rather, weakly accreting SMBH) population down to a uniform X-ray detection threshold of 10^{38} erg s^{-1}, i.e. comparable to Eddington limit for a stellar mass object. From

a theoretical standpoint, a somewhat higher active fraction can be expected in nucleated galaxies (i.e., compared to non-nucleated galaxies over the same mass range), due to the NSC facilitating either the *formation* of a nuclear SMBH, its *feeding*, or a combination of the two. Naively assuming a roughly constant mass accretion rate onto the SMBH, the former scenario would result into a higher fraction of active galaxies among nucleated vs. non-nucleated. At the same time, the latter scenario, with enhanced fueling, can be expected to be more relevant for nucleated late-types, home to bluer NSCs and thus enhanced gas reservoir for black hole accretion (Antonini et al. 2015; Naiman et al. 2015; Gnedin et al. 2014; Muratov & Gnedin 2010; see, however, Antonini et al. 2015).

The data set presented here is comprised of new *Chandra* data for 47 late-types, plus archival data for 51 early-types (Gallo et al. 2010; Miller et al. 2012b,a), enabling us to (i) improve on previous measurements of the nucleated galaxy active fraction (e.g., Seth et al. 2008) by adopting a uniform criterion for identifying and measuring accretion-powered emission; (ii) carry out a morphology-dependent analysis, which in turn could break the degeneracy between an intrinsically higher fraction of nucleated galaxies actually hosting SMBHs vs. an enhancement in the fueling of such SMBHs, likely resulting into a higher active fraction for the late-type sample.

With respect to point (i), after accounting for X-ray binary contamination to the nuclear X-ray signal, we estimate an active fraction of $11.2\%^{+5.0}_{-7.3}$ across the whole sample. This is in broad agreement with previous estimates by Seth et al. (2008). A more detailed comparison with their results is warranted in order to compare the diagnostics power of high resolution X-ray imaging observations vs. different wavelengths/methods. Our sample of 98 objects represents a distance-limited sub-sample drawn from the original Seth et al. (2008) sample; for these 98 nucleated galaxies, they present uniform optical diagnostics, in the form of BPT optical emission line ratios, for 53 objects. Only 2 out of 53 (i.e., NGC 5879 and NGC 4411B) are identified as active (with six more, namely NGC 1042, NGC 3423, NGC 4206, NGC 4517, VCC 1619, NGC 4625 identified as composite). By comparison, we identify 7 out

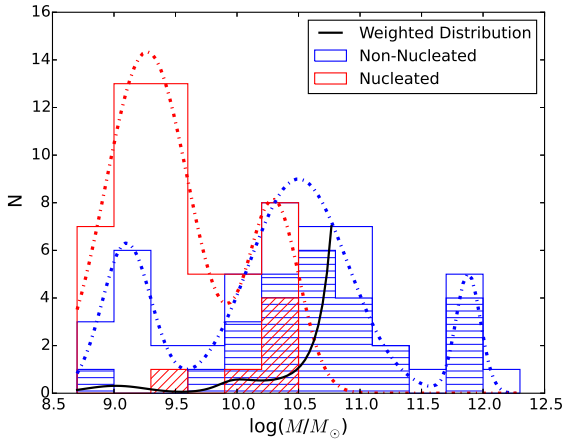

Figure 2.8: Stellar mass distributions of the 100 Virgo early-types targeted as part of the Virgo Cluster Survey, 51 of which are nucleated (red open histogram) while 49 are not (blue open histogram). The distribution of galaxies with central X-ray detections are shown for both as histograms with diagonal (nucleated) and horizontal (non-nucleated) hatching. Each sample has been fit with multiple Gaussians. The weighted distribution, defined as the ratio of the non-nucleated distribution to the nucleated distribution, is shown as a black curve. This is used to draw a sub-sample of nucleated galaxies with the same number and mass distribution of the non-nucleated sample within the mass range $8.7 < \log(M/M_\odot) < 10.5$, allowing for a proper comparison of the active fraction between nucleated and non-nucleated systems.

53 as likely AGN (NGC 1042[7], NGC 5879, VCC 784, VCC 1250, VCC 1283, VCC 1619, and VCC 1883; notice, however, that we do not detect NGC 4411B in X-rays). While recognizing that our assessment of X-ray binary contamination does not take into account potential differences in the X-ray binary XLF between nucleated and non-nucleated galaxies, this direct comparison suggests that in the nearby universe, *Chandra* observations are superior to standard emission line ratio diagnostics to identify low-level SMBH accretion. We close this comparison by noting that the 10 per cent active fraction quoted by Seth et al. (2008) stems from a sample of 75+ galaxies with (non-uniform) spectral coverage. Additional AGN were identified through archival X-ray observations, with *ROSAT, XMM-Newton, Chandra*, as well as radio observations. Overall, the two galaxies that were identified by Seth et al. as actively accreting via X-ray diagnostics have stellar masses slightly below the mean mass of the 7 optical galaxies found to host AGN via BPT diagnostics (i.e., $\log(M/M_{\odot})= 10.3$ & 10.2, vs. $\log(M_{\rm mean}/M_{\odot}) = 10.4$).

With respect to point (ii), as discussed in Section 4, after accounting for the different mass distributions, we find no statistically significant difference in the active fraction among nucleated late and early-types ($10.8\%\ ^{+11.3}_{-6.3}$ vs. $10.6\%\ ^{+11.9}_{-4.9}$, respectively).

Recently, Antonini et al. (2015) employed semi-analytical models to make predictions about the rate of coexistence of NSCs and SMBHs in local galaxies, regardless of activity level. Among the simulated nucleated galaxies with stellar mass $< 10^{10} M_{\odot}$, the early-types are predicted to have a larger SMBH *occupation* fraction than late-types (the reader is referred to figure 7 in their paper). Assuming the occupation model presented in Antonini et al. (2015) is correct, the similar AGN fractions observed in early- vs. late-type samples suggests that late type galaxies may more efficiently fuel their SMBHs.

The overall active fraction for our nucleated sample is also consistent with the well known 10% active fraction often quoted for the general population, albeit across a much larger dy-

[7]Shields et al. (2008) report on follow-up optical spectroscopy of NGC 1042 using the TWIN spectrograph at the Calar Alto 3.5 m telescope (with 3" wide extraction region for consistency with the SDSS fiber aperture), and conclude that the source is indeed an AGN.

namical range in galaxy mass, redshift, as well as accretion-luminosity sensitivity (e.g, Ho et al. 1997; Kewley et al. 2006). However, in the light of the well known trend of increasing apparent active fraction with host stellar mass (due to the ability to probe progressively lower Eddington ratios towards higher masses), a more meaningful comparison is one between nucleated vs. non-nucleated galaxies across comparable stellar (and hence, black hole) mass ranges, and down to a uniform accretion luminosity threshold. This can be accomplished by looking at the 100 early-type galaxies that comprise the ACS Virgo cluster survey (51 nucleated, 49 non-nucleated), and for which we also have uniform *Chandra* coverage (by comparison, we lack a parent sample of non-nucleated late-type with uniform *Chandra* coverage). On average, the non-nucleated sample has a stellar mass of $\log(M/M_{\odot}) = 10.3$ that spans between $8.7 < \log(\mathrm{M/M_{\odot}}) < 12.3$, while the nucleated sample has a lower average stellar mass of $\log(M/M_{\odot}) = 9.5$ that ranges between $8.7 < \log(\mathrm{M/M_{\odot}}) < 10.5$. Thus, we follow the same approach as described in Section 2.6 in order to carry out a mass-weighted comparison of the active fraction between the nucleated and non-nucleated Virgo galaxies within the mass range $8.7 < \log(\mathrm{M/M_{\odot}}) < 10.5$ (see Figure 2.8). On average, the nucleated subsample has 4 objects with nuclear X-ray point sources, corresponding to an active fraction of $15\%^{+20}_{-10}$. The non-nucleated subsample has 10 objects with nuclear X-ray point sources, corresponding to an active fraction of $38\%^{+38}_{-18}$. Poisson statistics show that for an expected value of 10 nucleated galaxies, there is a 3% chance of finding 4 or fewer objects. Thus, the nucleated subsample is measured to have a marginally lower active fraction than the non-nucleated sample; this supports our conclusion that nucleated galaxies do not appear to have enhanced AGN fractions.

The main results and implications of this work can be summarized as follows:

1. After correcting for contamination to the nuclear X-ray signal from bright X-ray binaries and accounting for the different stellar mass distributions, we find no statistically significant difference in the active fraction of early- vs. late-type nucleated galaxies, with f=$10.6\%^{+11.9}_{-4.9}$ and $10.8\%^{+11.3}_{-6.3}$. Across the whole sample, we measure an active fraction f=$11.2\%^{+7.4}_{-4.9}$ (1σ

C.L.), in agreement with previous estimates by Seth et al. (2008). For the early-type nucleated galaxies we carry out a controlled comparison with a parent sample of non-nucleated galaxies and find no statistically significant difference in the active fraction. We conclude that nucleated galaxies do not appear to have enhanced AGN fractions.

2. We investigate a relationship between the host galaxy stellar mass, M_*, and the central X-ray luminosity, L_X of the form: $\log L_X - 38.2 = \alpha + \beta \times (\log M_* - 9.52)$. We find the most-likely values for the y-intercept, slope, intrinsic scatter, and Pearson correlation coefficient to be: α = -1.50 $\pm$ 0.35, β = 1.67 $\pm$ 0.42, σ = 0.90 $\pm$ 0.20, and r = 0.62 $\pm$ 0.11. When we incorporate XRB contamination into our analysis, no statistically significant relation is found between the contamination-weighted X-ray luminosities and inferred host stellar masses.

3. We extend the size-luminosity analysis analyzed in Georgiev & Böker (2014) by adding three late-type detections from our sample that are included in their catalogue: NGC 1042, NGC 1493, and NGC 4487. We confirm the general trend that nucleated galaxies with AGN tend to have more compact effective radii at a given luminosity, possibly caused by the presence of a weak AGN and/or a younger stellar population that is more concentrated than the surrounding NSC stars.

We close by noting that, at the luminosity levels we are operating, a careful assessment of the X-ray binary contamination to the nuclear X-ray signal is crucial in order to draw meaningful conclusions. In the absence of a quantitative prescription for the XLF of NSCs, our methodology, which admittedly relies on XLFs established for the non-nuclear regions of nearby galaxies, may indeed underestimate such contribution. If this is the case, however, the active fractions quoted in this work are somewhat over-estimated, further strengthening our conclusion that the presence of a NSC does not favor nor enhance AGN activity.

We thank our referee, Anil Seth, for his constructive and thorough suggestions that improved this chapter. Support for this work was provided by the National Aeronautics and Space Administration through Chandra Award Number GO5-16082X issued by the Chandra

X-ray Observatory Center, which is operated by the Smithsonian Astrophysical Observatory for and on behalf of the National Aeronautics Space Administration under contract NAS8-03060.

CHAPTER III

A Multi-wavelength Analysis of Binary-AGN Candidate PSO J334.2028+01.4075

3.1 Preface

Results in this chapter were submitted to the Astronomical Journal as *Foord, A., et. al 2017b. A Multi-wavelength Analysis of Binary-AGN Candidate PSO J334.2028+01.4075. The Astrophysical Journal, Volume 851, Issue 2, article id. 106* and are reproduced here with minor style revisions by permission of the American Astronomical Society under the non-exclusive right of republication granted to authors.

3.2 Abstract

We present analysis of the first *Chandra* observation of PSO J334.2028+01.4075 (PSO J334), targeted as a binary-AGN candidate based on periodic variations of the optical flux. With no prior targeted X-ray coverage for PSO J334, our new 40 ksec *Chandra* observation allows for the opportunity to differentiate between a single or binary-AGN system, and if a binary, can characterize the mode of accretion. Simulations show that the two expected accretion disk morphologies for binary-AGN systems are (i) a "cavity," where the inner region of the accretion disk is mostly empty and emission is truncated blueward of the wavelength associated with the temperature of the innermost ring, or (ii) "minidisks", where there is

substantial accretion from the cirum-binary disk onto one or both of the members of the binary, each with their own shock-heated thin-disk accretion system. We find the X-ray emission to be well-fit with an absorbed power-law, incompatible with the simple cavity scenario. Further, we construct an SED of PSO J334 by combining radio through X-ray observations and find that the SED agrees well with that of a normal AGN, most likely incompatible with the minidisk scenario. Other analyses, such as locating the quasar on IR color-color diagrams and analyzing the quasar mass predicted by the fundamental plane of black hole activity, further highlight the similarity of PSO J334 with respect to normal AGN. On the multi-wavelength fronts we investigated, we find no evidence supporting PSO J334 as a binary-AGN system, though our analysis remains insensitive to some binary configurations.

3.3 Introduction

Classical hierarchical galaxy evolution predicts galaxies to merge (e.g., White & Rees 1978), allowing any central supermassive black holes (SMBH) to assemble into binary active galactic nuclei (AGN) systems (Volonteri et al. 2003). The galaxy merger can serve as one possible avenue of growth for the central black holes, and it is expected to end with the coalescence of the two black holes as a result of the emission of gravitational waves (see Begelman et al. 1980). The new SMBH will have a different mass and spin (Rezzolla et al. 2008) and can receive a gravitational recoil large enough to kick it out of the merged host galaxy (e.g., Volonteri et al. 2008; Baker et al. 2008; Merritt et al. 2004; Lousto & Zlochower 2013). As powerful sources of gravitational waves and a likely influence on the BH occupation fraction of galaxies, binary SMBHs are important systems to study.

The process of black hole merging can be broken into distinct phases. Here, we reorganize the original phases presented in Begelman et al. (1980) to emphasize details important to our analysis: (1) the galaxy merger phase, where the two central black holes sink to the center and a bound black hole pair forms with semimajor axis a; (2) the final parsec phase, where the black hole binary system may or may not stall at a separation of $0.1 \leq a \leq 1.0$

pc as a result of ejecting all the stars in its loss cone. This phase is referred to as the "final parsec problem" (Milosavljević & Merritt 2003a,b) and many potential solutions have been theorized (e.g., Yu 2002; Escala et al. 2005; Berczik et al. 2006; Mayer et al. 2007; Dotti et al. 2007; Berentzen et al. 2009; Cuadra et al. 2009; Lodato et al. 2009; Khan et al. 2013); (3) the circum-binary accretion phase, where circum-binary accretion is expected as a result of the typical accretion disk size being larger than the binary separation a (see Milosavljević & Phinney 2005); (4) the gravitational wave phase, where the binary is sufficiently hardened and gravitational waves carry energy from the system until the binary merges (see Peters 1964); and (5) the post-merger phase, where the new black hole has a different mass and spin (Rezzolla et al. 2008), possibly leading to a recoil large enough to displace or eject the black hole from the galaxy center (Volonteri et al. 2008; Baker et al. 2008; Merritt et al. 2004; Lousto & Zlochower 2013).

"Dual-AGN" are usually defined as a pair of AGN with kilo-parsec scale separations (i.e., phase 1; see Comerford et al. 2009), while a "binary-AGN" is a pair of BHs that are gravitationally bound with typical separations $a < 100$ pc (i.e., phase 2 & 3; see Bansal et al. 2017 for the first resolved binary-AGN candidate with a separation of ~ 7.3 pc). Such a system becomes impossible to resolve with *Chandra* beyond a distance of $\sim$4 Mpc. For example, the closest dual-AGN candidate identified using two resolved point sources with *Chandra* is NGC 3393 (Fabbiano et al. 2011) with a projected separation of $\sim$150 pc ($\sim 0\farcs6$). However, this source has been contested as potentially spurious (e.g., Koss et al. 2015).

Thus many indirect detection techniques have been developed to search for signs of binary-AGN. One such method involves looking for periodic variability in the optical flux via time-domain observations, a possible result of accretion via a circum-binary disk (e.g., D'Orazio et al. 2013; Farris et al. 2015b,a). Perhaps the strongest case of a candidate binary-AGN, OJ 287, was identified by its variable luminosity and has exhibited regular optical outbursts with $\sim$12 year period (Lehto & Valtonen 1996). However, OJ 287 is not the typical binary system, as the fluctuations in its lightcurve have been modeled as the

secondary SMBH periodically intercepting the primary SMBH's accretion disk (Valtonen et al. 2008 and references therein). Such a model can result from a configuration where there is a considerable misalignment between the orbital plane of the secondary SMBH and the accretion-disk plane of the primary SMBH.

Other quasars have been identified as binary-AGN candidates via time-domain techniques, such as PG 1302−102 (Graham et al. 2015) and PSO J334.2028+01.4075 (hereafter PSO J334; Liu et al. 2015). PG 1302−102 was identified as a binary-AGN based on the periodic variability of the optical flux on an observed timescale of ∼1,884 days, corresponding to a separation of $a \sim 0.01$ pc (Graham et al. 2015). Further, it was argued that the variability of the light curve could be explained by relativistic Doppler boosting from an unequal-mass binary (D'Orazio et al. 2015). Similarly, PSO J334, at a redshift of $z = 2.06$, was identified as a potential binary system based on periodic variation of the optical flux on an observed timescale of ∼542 days, corresponding to a separation $a \sim 0.006$ pc (Liu et al. 2015). However, recently Vaughan et al. (2016) have shown that the data presented on PG 1302-102 and PSO J334 are not strong enough to support the model of a binary-AGN system. Specifically, they find that sinusoidal variations are difficult to distinguish from a stochastic ("red noise") process when the number of cycles is ≤ 2, and that at least ∼5 cycles are needed to confirm a true periodic trend in lightcurves. In response, Liu et al. (2016) tested the persistence of PSO J334's periodic lightcurve fluctuations using an extended baseline analysis composed of both archival and new data. This new analysis disfavors a simple sinusoidal model for PSO J334 over a baseline of 5 cycles. Yet, the true nature of PSO J334 remains in question. Recent Karl Jansky Very Large Array (VLA) and Very Long Baseline Array (VLBA) coverage presented in Mooley et al. (2017) further supports that PSO J334 is a binary black hole system, as the quasar was found to be lobe-dominated with a twisted radio structure, a possible result of a precessing jet.

Perhaps the best way to discern between the binary and single-AGN models is to use multi-wavelength observations. With no prior targeted X-ray coverage for PSO J334, our

new 40 ksec *Chandra* observation allows for a complete multi-wavelength description of the quasar. Specifically, combining archival data with our new observations may enable us to differentiate between a single or binary-AGN system, and if a binary, can possibly characterize the mode of accretion. If PSO J334 is a binary system with separation $a = 28R_S$ (where $R_S = 2GM/c^2$ is the Schwarzchild radius for a BH with mass M; Liu et al. 2016) we expect that the binary is well into the gravitational-wave dominated regime, where circum-binary accretion is likely. The mode of circum-binary accretion will depend on the current state of the system. For example, if the specific angular momentum of the streams is small compared to the specific angular momentum at the innermost stable circular orbit (ISCO), the streams will flow directly into the SMBHs (see Gültekin & Miller 2012, Tanaka & Haiman 2013, Tanaka 2013, Gold et al. 2014, Roedig et al. 2014). However, this scenario is expected for SMBHs with very small separations. For all other binary systems, accretion disks form around each SMBH ("minidisks"), extending to a tidal truncation radius that is expected to be less than $\sim a/2$ (Paczynski 1977, also see Roedig et al. 2014 for the dependency of the truncation radius on mass ratio q).

For further-evolved binaries, the timescale to fully accrete the minidisks can be smaller than the gravitational-wave timescale; in this scenario the mini-disks will be drained before the two SMBHs merge. Here we may expect a cavity between the circum-binary disk and the SMBHs, as the inner regions of the accretion disk are mostly void of gas. The cavity model and the minidisk model are expected to manifest differently in the observational data. For example, one can look at the X-ray spectrum to search for the presence of streams from the circum-binary disk accreting onto the minidisk (e.g., Roedig et al. 2014; Farris et al. 2015b,a). Further, the radio–X-ray AGN spectral energy distribution (SED) can be used to search for abnormalities, such as "notches" in the SED expected from minidisks (however, see Leighly et al. 2016 for a critical perspective on possible "notches" in the SED of Mrk 231), or the presence of a cavity (see Milosavljević & Phinney 2005). Here we present a multi-wavelength analysis of PSO J334, discovered in the FIRST Bright Quasar Survey (Becker et al. 2001),

in order to infer its true accretion nature. In the following analysis we assume a standard ΛCDM cosmology of $\Omega_\Lambda = 0.7$, $\Omega_M = 0.3$, and $H_0 = 70$ km s^{-1}.

3.4 X-ray Data Analysis

We targeted PSO J334 in Cycle 17 (Proposal ID:17700741, PI: Gültekin). The quasar was placed on the back illuminated S3 chip of the Advanced CCD Imaging Spectrometer (ACIS) detector, with an exposure time of 40 ks. The exposure time was chosen in order to achieve a 3σ point-like source detection, based on an upper-limit calculated from a previous *XMM-Newton* slew survey observation where no emission consistent with the position of PSO J334 was detected, and assuming emission from an active black hole with $L \geq 10^{-3}$ $L_{\rm Edd}$ with mass $\log(M/M_\odot) = 9.1$ (Liu et al. 2016; Mooley et al. 2017). Our 40 ks exposure is not sensitive to the ∼542 day optical period found by Liu et al. (2016). Further, our observation is not sensitive to any quasi-periodic signal associated with the decay time from gravitational waves.

We follow a similar data reduction as described in previous X-ray studies analyzing active fractions (Gallo et al. 2008, 2010; Miller et al. 2012b,a, 2015; Plotkin et al. 2014; Foord et al. 2017a), using the Chandra Interactive Analysis of Observations (`CIAO`) v4.8. We first correct for astrometry, cross-matching the *Chandra*-detected point-like sources with the Sloan Digital Sky Survey Data Release 9 (SDSS DR9) catalog. The *Chandra* sources used for cross-matching are detected by running `wavdetect` on the reprocessed level 2 event file. We require each matched pair to be less than $2''$ from one another and have a minimum of 3 matches. Our final astrometrically-corrected image has a shift less than $0\farcs5$. We then correct for background flaring by removing intervals where the background rate was found to be 3σ above the mean level, resulting in the removal of a 197 second interval. We then rerun `wavdetect` on filtered 0.5 to 7 keV data to generate a list of X-ray point sources. We use wavelets of scales 1, 1.5, and 2.0 pixels using a 1.5 keV exposure map, and set the detection threshold significance to 10^{-6} (corresponding to one false detection over the entire S3 chip).

We identify the quasar as an X-ray point source $\sim 0\farcs4$ from the nominal, SDSS-listed optical center ($2''$ corresponds to 95% of the encircled energy radius at 1.5 keV for ACIS).

All errors evaluated in this chapter are done at the 95% confidence level and error bars quoted in the following section are calculated with Monte Carlo Markov Chains via the XSPEC tool `chain`.

3.4.1 Spectral Fitting

The quasar's net count rate and flux value are determined using XSPEC, version 12.9.0 (Arnaud 1996). Counts are extracted from a circular region with radius of $2''$ centered on the X-ray source center, using a source-free annulus with inner radius of $20''$ and outer radius of $30''$ for the background extraction. We fit the spectrum between 0.3 and 7 keV with an absorbed red-shifted power-law (`phabs*zphabs*zpow`; hereafter Model 1) where we fix the Galactic hydrogen column density (the photoelectric absorption component `phabs`) to a value[1] of 3.5×10^{20} cm^{-2}. As a result of being in the low-count regime, we implement the Cash statistic (`cstat`; Cash 1979) and a minimum of 1 count per bin in order to best assess the quality of our model fits. We find the best-fit parameters intrinsic $N_H = 0.91^{+4.84}_{-0.89} \times 10^{22}$ cm^{-2} and $\Gamma = 2.02^{+0.83}_{-0.39}$, with an observed 2–10 keV flux of $3.20^{+0.9}_{-1.1} \times 10^{-14}$ erg cm^{-2} s^{-1}, or rest-frame 2–10 keV luminosity of $9.40^{+1.4}_{-1.1} \times 10^{44}$ erg s^{-1} at $z = 2.06$ (assuming isotropic emission). K-corrections are not applied to the *Chandra* data, as we directly measure the flux density from the spectrum. In Figure 3.1, we show the X-ray spectrum of PSO J334 along with the best-fit XSPEC model.

We add a line component to the *Chandra* spectrum (`phabs*zphabs*(zpow+zgaus)`) to investigate the presence of an Fe K-α line (seen as a slight excess compared to the model at observed-frame 2 keV in Fig. 3.1). Allowing the line energy to vary, a gaussian component is best-fit at rest-frame $6.2^{+1.2}_{-4.4}$ keV. We find that the addition of this Fe K-α line is not statistically significant (as is evident from the uncertainties on the line energy) most likely a

[1]We evaluate the neutral hydrogen column density using values from the Leiden/Argentine/Bonn (LAB) Survey of Galactic HI (Kalberla et al. 2005) via WebPIMMS.

result of the spectrum only having 196 counts. Further, the placement of the emission line is near a strong drop in effective area of the ACIS-S3 chip, which complicates the study of a potential line. While the Fe K-α line is not statistically significant, we fix the rest-frame energy to 6.4 keV and the width of the line $\sigma = 0$ keV, and calculate an equivalent width (EW) of 0.22 keV with a 3σ upper limit of 0.55 keV.

We test for the presence of two accretion disks by fitting a broken power-law to the spectrum (`phabs*zphabs*bknpo`; Model 2). Such a spectrum may originate from a binary system where both SMBHs are accreting with their own minidisk. We model the spectrum with a broken power-law in order to avoid the degeneracies that exist in parameter-space for a double power-law model. To properly compare Model 2 to a single disk system, we also fit the spectrum with a broken power-law but tie the two photon index values to one-another (i.e, $\Gamma_1 = \Gamma_2$; Model 3). We note this approach produces best-fit parameters consistent with best-fit parameters of Model 1. We conduct an F-test to investigate the significance of Model 2 with respect to Model 3, and find an f-value of 0.25 (with probability value $p = 0.78$). At a 95% confidence level, we conclude that the spectrum does not need an additional photon index to explain its shape. We note that these results are not necessarily indicative of a single-AGN system, as it is difficult to disentangle two power-laws without predominant spectral features, such as Fe K-α lines at different velocities (a non-negligible scenario, see Eracleous et al. 2012; Popović 2012; Jovanović et al. 2016; Simić & Popović 2016 for more details of emission lines in binary-AGN).

We calculate the X-ray hardness ratio (HR) of PSO J334, defined as (H-S)/(H+S) where S and H are the soft (0.5–2.0 keV) and hard (2.0–8.0 keV) X-ray band net counts detected by *Chandra*. The HR is found to be $\sim$-0.40, consistent with the expected value for an AGN with $N_H \simeq 10^{22}$ cm^{-2} and $z \simeq 2.06$ (e.g. Wang et al. 2004).

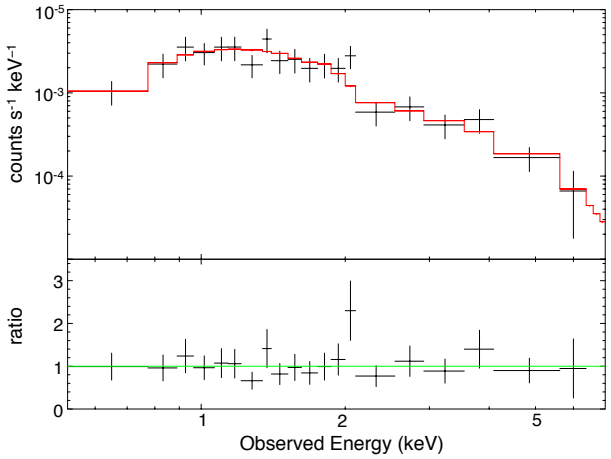

Figure 3.1: The observed 0.3 – 7.0 keV *Chandra* spectrum of PSO J334 (*top*) with the ratio of the data to the continuum model (*bottom*). The spectrum of PSO J334 is shown in black, where the data have been folded through the instrument response. We fit the spectrum with the model `phabs*zphabs*zpow`, fixing the Galactic absorption and redshift parameters at $N_H = 3.5\times\ 10^{20}$ cm^{-2} and $z = 2.06$. The best-fit model is shown in red, where intrinsic $N_H = 0.91^{+4.84}_{-0.89} \times 10^{22}$ cm^{-2} and $\Gamma = 2.02^{+0.83}_{-0.39}$. We calculate an observed 2–10 keV flux of $3.20^{+0.9}_{-1.1}\times\ 10^{-14}$ erg cm^{-2} s^{-1}, or rest-frame 2–10 keV luminosity of $9.40^{+1.4}_{-1.1}\times\ 10^{44}$ erg s^{-1} at $z = 2.06$ (assuming isotropic emission). All errors are evaluated at the 95% confidence level. We find that at a 95% confidence level, the spectrum does not need an additional power-law to explain the data. The spectrum has been rebinned for plotting purposes.

3.5 The Spectral Energy Distribution

In the following section we construct a spectral energy distribution of PSO J334, by combining radio to X-ray observations, and compare it to standard non-blazar AGN SEDs presented in Shang et al. (2011). For all K-corrections, we adopt the $K(z)$ relation as presented in Richards et al. (2006).

3.5.1 Radio

PSO J334 has archival spectroscopy from the FIRST Bright Quasar Survery (FBQS), and has recently been re-observed by the VLA as part of the Caltech-NRAO Stripe 82 Survey (Mooley et al. 2016). Further, Mooley et al. (2017) present VLBA observations of PSO J334 at 7.40, 8.67, and 15.37 GHz, respectively. Two VLBA components are resolved — a South East and a North West component. Both the compactness and the inverted radio spectrum of the South East component (possibly due to synchrotron self-absorption) suggest that it is the "core" from which the North West component has been ejected. For the purposes of constructing the SED, we use the VLBA integrated flux density values for the South East component (see table 3 in Mooley et al. 2017). K-corrections for the radio data points are implemented assuming a spectral index $\alpha = -0.3$ with a dispersion 0.2 (where $F_\nu \propto \nu^{-\alpha}$). The value for α is taken from Stocke et al. (1992), and represents the radio slope of the average quasi-stellar object (QSO) SED, which includes contributions from both the core and lobes.

3.5.2 Infrared

For the infrared regime we use archival *Wide-field Infrared Survey Explorer* (*WISE*) from the AllWISE Source Catalog (Cutri et al. 2013), as well as stacked archival J- and K-band data from the UKIRT InfraRed Deep Sky Survey (UKIDSS; Lawrence et al. 2007). For the *WISE* data we use observations taken in the W1, W2, and W3 bands, where the quasar was detected with a SNR > 3.0. We correct for Galactic extinction using the dust map

from Schlafly & Finkbeiner (2011), where $E(B-V) = 0.0401$. K-corrections are applied assuming a spectral index $\alpha = -1.0$ with a dispersion of 0.2, calculated from the average 1–10 μm spectral index for the AGN sample presented in Shang et al. (2011).

3.5.3 Optical

PSO J334 has archival g-, r-, i-, and z-band data from the Pan-STARRS1 Medium Deep Survey (PS1 MDS; Kaiser et al. 2010), V-band data from the Catalina Real-time Transient Survey (CRTS; Drake et al. 2009), and archival u-, g-, r-, i-, and z-band data from the Sloan Digital Sky Suvey (SDSS). For the purposes of constructing our SED, we use magnitudes extracted from deep stacked images in the g-, r-, i-, and z-bands from PS1 MDS (Liu et al. 2015, 2016). Similar to the IR regime, we correct for Galactic extinction using the dust map from Schlafly & Finkbeiner (2011). For the PS1 MDS K-corrections, we follow Liu et al. (2015) and assume a spectral index $\alpha = -0.5$ with a dispersion of 0.3 (also see Elvis et al. 1994; Vanden Berk et al. 2001; Ivezić et al. 2002).

3.5.4 Ultraviolet

PSO J334 has u-band data from the Canada-France-Hawaii Telescope (CFHT; Heinis et al. 2016b,a; Liu et al. 2016) and archival *Galaxy Evolution Explorer* (*GALEX*) data in both the FUV and NUV bands. Further, the quasar has *GALEX* Time Domain Survey data in the NUV, taken to analyze possible periodic variations in the UV lightcurve (Gezari et al. 2013; Liu et al. 2015, 2016). For our SED we use magnitudes derived from deep stacked u-band CFHT data and the archival FUV and NUV *GALEX* data. To account for Galatic absorption in the CFHT data we use the dust map from Schlafly & Finkbeiner (2011), while for the *GALEX* observations we use FUV and NUV extinction values listed in Yuan et al. (2013). As all data points are shortward of the Lyα emission line, we apply K-corrections using the spectral index $\alpha = -1.57$ and a dispersion of 0.17 (Telfer et al. 2002; Richards et al. 2006).

3.5.5 The Multi-wavelength SED

In Fig. 3.2 we present the rest-frame multi-wavelength SED of PSO J334 in νL_ν (erg s^{-1}) versus frequency (Hertz), assuming a luminosity distance $d_L = 16.1$ Gpc at $z = 2.06$. We search for any abnormalities in the SED by comparing our data to the composite non-blazar AGN SEDs presented in Shang et al. (2011). The composite SEDs are based on a sample of 85 optically bright non-blazar quasars, composed of 27 radio-quiet and 58 radio-loud quasars. Most objects in the sample have quasi-simultaneous UV/optical data, while radio, IR, and X-ray data are obtained from either the literature or new observations. Both the radio-quiet and radio-loud composite SEDs are overplotted with PSO J334's data in Fig. 3.2. We normalize the flux density of our data to rest-frame $\lambda = 2000$ Å for comparison to the standard AGN SEDs. The luminosities for each rest-frame frequency are listed in Table 3.1.

A simple comparison between the data and the Shang et al. (2011) SEDs shows a good agreement between PSO J334's emission and that of a radio-quiet AGN. The classical definition of radio-quiet quasars are AGN that have $R = f(5\text{ GHz})/f(4400\text{ Å}) < 10$, where $f(5$ GHz) is the rest-frame flux density at 5 GHz and $f(4400$ Å) is the rest-frame flux density at 4400 Å (Kellermann et al. 1989). Above $R = 10$, AGN are usually classified as radio-loud. Results from Becker et al. (2001) identify PSO J334 as a radio-loud quasar, with $R \sim$200. We use the new 7.40 GHz observations of the South East component of PSO J334 from Mooley et al. (2017), where the resolution has increased from the previous FBQS observations, and derive an R value of ~ 17 (similar to Becker et al. 2001, we assume the radio spectrum follows $f \propto \nu^{-0.5}$ to extrapolate the rest-frame 5 GHz flux density). Although PSO J334 is technically defined as a radio-loud AGN, $R \sim 17$ is decidedly between the radio-loud sample SED from Shang et al. (2011) (where the median $R \sim 1600$) and the radio-quiet sample SED (where the median $R \sim 0.3$). Besides the radio regime, there is substantial overlap between PSO J334's SED and the Shang et al. (2011) data at all other wavelengths.

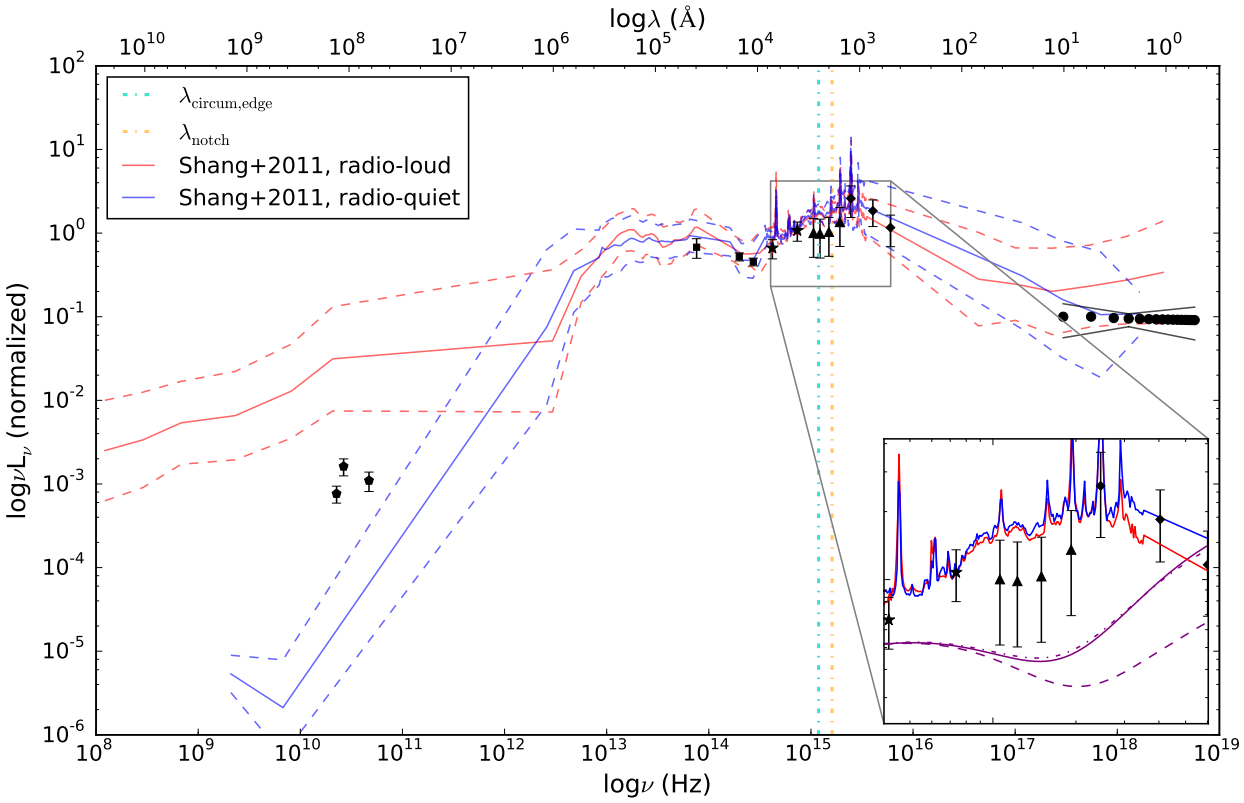

Figure 3.2: Rest-frame multi-wavelength SED of PSO J334, where radio data are from the VLA (black hexagons), IR data are from *WISE* (black-filled squares) and UKIDSS (black-filled stars), optical data are from Pan-STARRS1 (black-filled triangles) , UV data are from CFHT and *GALEX* (black-filled diamonds), and X-ray data is from *Chandra* (black-filled circles). Errors on data points are evaluated at the 95% confidence level. We overplot the composite non-blazar AGN SEDs presented in Shang et al. (2011), for both radio-loud (red line) and radio-quiet (blue line) AGN (1σ error bars are denoted by dashed lines). We normalize the flux density of our data to rest-frame $\lambda = 2000$ Å. We indicate $\lambda_{\rm circum,edge} = 2500$ Å, the wavelength that corresponds to the emission emitted at the inner-edge of a possible circum-binary accretion disk at $R_{\rm circum,edge} = 2a$ (assuming blackbody radiation), with a cyan dot-dashed line. If PSO J334 were consistent with the cavity model, we do not expect much emission at wavelengths with energies higher than $\lambda_{\rm circum,edge}$. We also indicate the predicted center wavelength for a notch at $\lambda_{\rm notch} = 1900$ Å, predicted to range between 500 Å and 7000 Å for a mass ratio $0.3 < q < 1.0$. If PSO J334 were consistent with the minidisk model, we expect a dip in the thermal continuum in this region. The inset shows how the SED is expected to change with the addition of a notch, where we use the analytical calculations derived in Roedig et al. (2014) to illustrate a notched SED with i) $q = 1.0$, $f_1 = f_2 = 0.5$ (purple solid curve), ii) $q = 0.3$, $f_1 = 0.45$, $f_2 = 0.55$ (purple dash-dot curve, and iii) $q = 0.1$, $f_1 = 0.92$, $f_2 = 0.08$ (purple dashed curve). The continuum for the notch is estimated by approximating the Shang et al. (2011) SED between 500 Å and 7000 Å in log space with a straight line. We note that although PSO J334 appears to be better aligned with the radio-quiet sample, the quasar is technically considered to be radio-loud with $R \sim 17$.

Table 3.1: Spectral Energy Density Values

Filter or Detector (1)	Telescope or Survey (2)	logν (log(Hz)) (3)	logνL$_\nu$ (log(erg s^{-1})) (4)
...	VLBA	10.35	-3.12 ± 0.11
...	VLBA	10.42	-2.80 ± 0.11
...	VLBA	10.67	-2.96 ± 0.13
W3	*WISE*	13.88	-0.02 ± 0.13
W2	*WISE*	14.30	-0.14 ± 0.05
W1	*WISE*	14.44	-0.20 ± 0.05
J	UKIDSS	14.62	-0.03 ± 0.13
K	UKIDSS	14.87	0.18 ± 0.13
z	PS1 MDS	15.03	0.15 ± 0.29
i	PS1 MDS	15.18	0.14 ± 0.29
r	PS1 MDS	15.09	0.16 ± 0.29
g	PS1 MDS	15.28	0.28 ± 0.29
u	CFHT	15.40	0.56 ± 0.23
NUV	*GALEX*	15.61	0.21 ± 0.22
FUV	*GALEX*	15.78	0.41 ± 0.19
ACIS-S3	*Chandra*	17.68–18.38	$-0.87^{+0.06}_{-0.05}$

Note. – Columns: (1) filter or detector; (2) telescope, denoted as the Very Large Baseline Array (VLBA); the *Wide-field Infrared Survey Explorer* (*WISE*); the UKIRT InfraRed Deep Sky Survey (UKIDSS); the Pan-STARRS1 Medium Deep Survey (PS1 MDS); the Canada-France-Hawaii Telescope (CFHT); the *Galaxy Evolution Explorer* (*GALEX*); and the *Chandra X-ray Observatory* (3) rest-frame frequency assuming a redshift of $z = 2.06$, in units of Hz. The *Chandra* frequency range corresponds to the rest-frame energy range of 2–10 keV; (4) extinction- and K-corrected luminosity assuming a luminosity distance d_L =16.1 Gpc, in units of erg s^{-1}. Values have been normalized to the luminosity at rest-frame $\lambda = 2000$Å. Error bars are evaluated at the 95% confidence level. Please see Section 3.5 for details on extinction values and K-corrections applied.

3.6 Results and Discussion

Past studies of PSO J334 have revealed various results regarding the accretion mode of the quasar, as analyses in different wavelength regimes have suggested both single- and binary-AGN systems. PSO J334 was first targeted as a binary-AGN candidate based on periodic variation of the optical flux (Liu et al. 2015). Assuming that the rest-frame period of the quasar variability traced the orbital period of the binary, a binary separation of ~ 0.006 pc was estimated. However, recently Vaughan et al. (2016) have shown that sinusoidal variations are difficult to distinguish from a stochastic process when the number of cycles

is ≤ 2; they conclude that at least $\sim$5 cycles are needed to confirm a true periodic trend in lightcurves. Searching for sinusoidal variations in candidate binary-AGN lightcurves is complicated by the fact that binary-AGN are likely to show both periodic and stochastic variations. This is a result of regular quasar variability overlapping with any modulation resulting form being in a binary system. More complex analyses will be necessary for future studies of candidate binary-AGN lightcurves, as it is still relatively uncertain how to best model quasar noise power spectra.

Liu et al. (2016) confirmed that the data disfavored a simple sinusoidal model using an extended baseline analyses composed of both new and archival data in optical and UV. However, most recently Mooley et al. (2017) have re-established the idea of PSO J334 being a binary-AGN system via new VLA and VLBA observations. The central radio "core" of the quasar was found to have an elongation position angle (PA) twisted by $\sim 39^{\circ}$ with respect to the elongation PA measured by the VLA on kiloparsec scales. Such twists have been modeled in 3C 207 as a result of a precessing jet, possibly due to the orbital motion associated with binary-AGN (see Hough 2013). However, if the jet axis is close to our line of sight, the PAs may appear amplified as projected onto the plane of the sky. Such a scenario may be relevant to PSO J334, which has been identified as a Type I quasar via broadened CIV (1549 Å) and Mg II (2798 Å) lines (Liu et al. 2015, 2016; Mooley et al. 2017).

With no prior targeted X-ray coverage for PSO J334, our new 40 ksec *Chandra* observation allows for a complete multi-wavelength description of the quasar. Specifically, combining radio–X-ray observations enables us to differentiate between a single or binary-AGN system, and if a binary, can possibly characterize the mode of accretion. Simulations show that the two most basic types of accretion disk morphologies for binary-AGN systems are a "cavity", where the inner region of the accretion disk is mostly empty and emission is truncated blueward of the wavelength associated with the temperature of the innermost ring, or "mini-disks", where there is substantial accretion onto one or both of the members of the binary, each with their own shock-heated thin-disk accretion system. In the following section we will

discuss the implications of our *Chandra* observation and investigate the possibility of PSO J334 being a binary-AGN in terms of the cavity and mini-disk models.

3.6.1 The Null Hypothesis: PSO J334 is a single-AGN

We first consider analyses which are used to identify normal AGN. Due to the high redshift of PSO J334 standard emission line diagnostics, including narrow emission line ratios (e.g., Kewley et al. 2006) or broad Hα emission (e.g., Greene & Ho 2005), are redshifted into the near-infrared where archival spectroscopic data are not available. However, the good agreement between PSO J334's SED and the non-blazar AGN SEDs presented in Shang et al. (2011) strongly suggests a single-AGN system.

We compute the IR colors of PSO J334, as IR colors are often used as a tool to identify AGN (Jarrett et al. 2011; Stern et al. 2012), although red IR colors can also be produced when dust is heated by recent star formation. Specifically, we determine the position of PSO J334 on a *WISE* color–color plot to (i) determine whether it meets the AGN IR criteria, and (ii) determine if there are any abnormalities in its placement with respect to a normal AGN. We compare PSO J334's *WISE* colors to the "AGN box" empirically defined by Jarrett et al. (2011), which is based on the colors of quasi stellar objects (QSOs) and Seyfert galaxies with redshift out to $z \sim 2$. With $W1 - W2 = 1.13 \pm 0.11$ and $W2 - W3 = 3.26 \pm 0.27$, PSO J334 has IR colors located within the AGN box of Jarrett et al. (2011) and does not seem to have any IR color abnormalities compared to other QSOs at similar redshifts. However, it is not clear if binary-AGN would differ from a standard AGN in IR color-color diagrams (see Ellison et al. 2017 for an example where a candidate dual-AGN has *WISE* colors consistent with a standard AGN).

Secondly, our *Chandra* observations allows us to look at the location of PSO J334 on the Fundamental Plane of Black Hole Activity (FP) — an empirical relationship between the black hole mass, 5 GHz luminosity L_{5GHz}, and 2–10 keV luminosity L_X. Gültekin et al. (2009a) fit a relation to be used as an estimation for black hole mass based on observations

of L_X and L_{5GHz} of the form:

$$\log\left(\frac{M}{10^8 M_\odot}\right) = 0.19 + 0.48\log\left(\frac{L_{5\mathrm{GHz}}}{10^{38}\,\mathrm{erg\,s^{-1}}}\right) - 0.24\log\left(\frac{L_X}{10^{40}\,\mathrm{erg\,s^{-1}}}\right). \quad (3.1)$$

Whether or not the local FP relation is appropriate for high accretion rate AGN remains a topic of debate. For example, Gültekin et al. (2009a) studied a sample of AGN with dynamical black hole mass estimates and uniform analysis of archival *Chandra* data, and confirmed that the inclusion of high-accretion rates sources, such as Seyfert galaxies, increased the intrinsic scatter about the FP. However, other analyses reflect that the FP may be applicable for high accretion-rate sources (e.g., Panessa et al. 2007; Gültekin et al. 2014). Recognizing the caveats of such an analysis, we use the results of Gültekin et al. (2009a) to calculate the projected mass of the system and compare it to the measured total mass of the system, which we take to be $\log(M/M_\odot) = 9.1$ (Liu et al. 2016; Mooley et al. 2017). Binary-AGN with small mass ratios may result in offsets from the FP if the secondary is the main accretor — the mass calculated via the FP relation may be smaller compared to mass of the entire system, reflecting that the coupled X-ray/Radio emission stems from the less massive secondary. However, because of the large scatter on the calculated mass via the FP relation of ~ 1 dex, this approach is only sensitive to the more extreme mass ratio values, e.g. $q \leq 0.01$. We find that the mass projected from the FP relation of Gültekin et al. (2009a) is consistent, within the error bars, with the entire mass of the system.

3.6.2 Binary-AGN models

3.6.2.1 A Cavity in the Circum-binary Disk

If PSO J334 were consistent with the cavity model, the radiation that a normal disk would radiate within the inner edge of the circum-binary disk, $R_{\mathrm{circum,edge}}$, will be missing. The exact values of the temperatures we deduce below depend on details regarding the micro-physics of the system; here we make rough estimates using a standard accretion disk

model. Assuming a thin-disk model, a mass ratio not much less than unity (e.g., $q > 0.01$), and an inner edge located at $R_{\rm circum,edge} \simeq 2a$ (Milosavljević & Phinney 2005), the temperature at the inner edge of the circum-binary disk is given by: $T_{\rm circum,edge} \simeq 1.96 \times 10^4 \left[\dot{m}\left(\eta/0.1\right)^{-1} M_8^{-1} \left(a/100R_G\right)^{-3}\right]^{1/4}$ K (Roedig et al. 2014). Here, $\dot{m}$ is the accretion rate in Eddington units, η is the accretion efficiency, M_8 is the total mass of the binary in units of $10^8 M_\odot$, and a is the separation between the two BHs in units of gravitational radius R_G ($R_G = GM/c^2$). In the case of a cavity, we do not expect much emission at temperatures above $T_{\rm circum,edge}$. We note that this temperature is not predicted to change late into the evolution of the binary where the orbital time becomes smaller than the inflow time of the circum-binary disk, a scenario that may be very relevant to PSO J334 given the calculated separation between the SMBHs listed in Liu et al. (2016).

To calculate $T_{\rm circum,edge}$ we consider the parameters $\eta = 0.1$, $\log(M/M_\odot) = 9.1 \pm 0.3$ (Mooley et al. 2017), and $a = 28 \pm 14 R_S = 56 \pm 28 R_G$ (Liu et al. 2016). We calculate the accretion rate in Eddington units as $\dot{m} = \dot{M}/\dot{M}_{\rm Edd} \approx \dot{M}[3 \times 10^{-8}(M/M_\odot) M_\odot {\rm yr}^{-1}]^{-1} \approx 0.26 \pm 0.1$. Here $\dot{M} = L_{\rm bol}/(\eta c^2)$, where $L_{\rm bol}$ is the bolometric luminosity of the circum-binary accretion disk and is determined from the quasar bolometric luminosity corrections presented in Runnoe et al. (2012), using the quasar's continuum flux density at $\lambda = 3000$ Å presented in Liu et al. (2016).

$T_{\rm circum,edge}$ is found to be $\simeq 11000 \pm 4000$ K, or a cut-off wavelength $\lambda_{\rm circum,edge} \simeq 2500^{+1600}_{-700}$ Å assuming blackbody radiation from the circum-binary accretion disk. We indicate the position of $\lambda_{\rm circum,edge}$ on PSO J334's SED in Fig 3.2. If PSO J334 were consistent with the cavity accretion model, we would expect emission with energies higher than ∼NUV to be either (i) significantly lower than expected from a normal AGN disk or (ii) disappear entirely. However, if PSO J334 were consistent with a single-AGN system, we would expect UV emission from the inner-most part of the accretion disk that upscatters to X-rays via inverse-Compton interactions with the corona. Combining our 2–10 keV detection and the *GALEX* archival data, we can verify that the X-ray intensity is consistent with the expected

upscattered UV emission from a normal AGN disk, reflected by the considerable overlap between PSO J334's SED and the Shang et al. (2011) data in Fig. 3.2. We conclude that PSO J334 is incompatible with the cavity scenario.

3.6.2.2 "Notches" from a Minidisk

Regarding the minidisk model, the radiation that an ordinary disk would radiate between the inner edge of the circum-binary disk and the tidal truncation radii of the minidisks, $R_{\rm tidal}$, will be missing. In such a scenario, it is expected that the missing emission will produce a dip, or a "notch", in the thermal continuum spectrum, reflecting the missing emission between $R_{\rm circum,edge}$ and $R_{\rm tidal}$ (e.g. Roedig et al. 2012; Tanaka et al. 2012; Gültekin & Miller 2012; Kocsis et al. 2012; Tanaka & Haiman 2013; Roedig et al. 2014, however see Farris et al. 2015b for a simulation where notches become obscured). Thus, it is possible to use PSO J334's SED to search for evidence of minidisks. Specifically, Roedig et al. (2014) derive analytical calculations of the specific luminosity integrated from the cirum-binary disk and the two mini-disks, where the primary and secondary BHs are accreting material at rates $\dot{M}_1 = f_1\dot{M}$ and $\dot{M}_2 = f_2\dot{M}$. Here $\dot{M}_1$ and $\dot{M}_2$ are the mass accretion rates of the primary and secondary, and $\dot{M}$ is the circum-binary accretion rate. Further, they assume the circumbinary disk is in inflow equilibrium (i.e., $f_1 + f_2 = 1$) and take into account a hardening factor $g = 1.7$. The emergent spectrum may be hardened by a factor g due to the majority of the disk laying in a regime in which electron scattering opacity dominates absorption opacity (Shimura & Takahara 1995). Lastly, they assume that there is a sharp surface density cut-off at the inner edge of the circumbinary disk and the outer edges of the mini-disks. For this particular model, they find that a spectral depression tends to occur in the SED between $\sim kT_{\rm notch} - 15kT_{\rm notch}$, where $T_{\rm notch}$ is the characteristic temperature of the accretion disk at a radius $r_{\rm notch} \sim a$ and is approximately $2^{3/4}T_{\rm circum,edge}$ (see their equation 3). $T_{\rm notch}$ is evaluated at a radius that lies between the hottest point in the circum-binary accretion disk (which is truncated to $\sim 2a$) and the coldest point in the minidisk (which

extends to $\sim a/2$). We expect very little thermal radiation at the energy corresponding to the deepest point of the notch, which is centered at $E \simeq 4kT_{\rm notch}$.

For PSO J334, we calculate $T_{notch} \approx 19000 \pm 7000$ K, translating to an observable notch in the SED between 500–7000 Å, where the deepest point is predicted to occur at $\lambda_{\rm notch} \approx 1900^{+1200}_{-500}$ Å. In Fig. 3.2 we indicate the position of $\lambda_{\rm notch}$ with respect to PSO J334's SED. We use the analytical calculations in Roedig et al. (2014) to analyze how the SED shape is affected by the presence of a notch, for various parameters of q, f_1, and f_2. The continuum for the notch is estimated by approximating the Shang et al. (2011) SED between 500 Å and 7000 Å with a straight line. Three examples of notched SEDs are shown in Fig. 3.2. Our SED is reasonably resolved throughout the expected frequency range of a spectral notch, and the data appear nominally closer to the standard Shang et al. (2011) SED model.

We note that it is possible the mass ratio of PSO J334 falls much below $q \simeq 0.3$ (Liu et al. 2015). Specifically, for the case of $q \leq 0.1$ it is likely that any notch in the SED will have a different shape from the analysis above. We may expect $\lambda_{\rm notch}$ to occur at shorter wavelengths and the deepest portion of the notch to be even lower; this is a result of the primary BH's accretion flow barely contributing to the total SED (i.e., $f_2 \gg f_1$; Roedig et al. 2014). High S/N spectroscopy between 500 Å and 7000 Å, along with dense FUV observations, are required for a more robust analysis on possible notches in the SED.

3.6.2.3 Hard X-ray Emission from Minidisks

As a result of the expected supersonic motions of streams that are accreting onto the minidisks from the circum-binary disk, shocks are predicted as the streams hit the minidisk edges. It has been shown that these shocks should manifest in an excess of hard X-ray emission in the SED (Roedig et al. 2014; Farris et al. 2015b,a). Roedig et al. (2014) show that the post-shock temperature, $T_{\rm ps}$, of accreting streams is usually in excess of 10^9 K, with $T_{\rm ps} \propto (a/100R_G)^{-1}(1+q^{0.7})^{-1}$ (assuming the secondary is the main accretor). However, cooling is expected to rapidly set in such that the resultant emission is between 50 and 200

keV. These results agree with simulations presented in Farris et al. (2015a), where excess emission from stream shocking is ∼10 times higher than a normal AGN SED between 10 and 100 keV. Given that Farris et al. (2015a) assume a mass ratio $q = 1.0$, PSO J334 may be expected to have an excess of emission at an even energy higher if the mass ratio of the binary-AGN is much lower than unity.

Our rest-frame ∼ 0.9 to 24.5 keV *Chandra* spectrum shows no evidence of excess hard X-ray emission with respect to an absorbed power-law model. However, as argued above, it is likely that any excess X-ray emission would reside above our *Chandra* observation's energy range. We consider possible temperatures for the stream-shocking emission from PSO J334, given an assumed semi-major axis $a = 56R_G$ and a range of mass ratios $0.01 < q < 1.0$. Adopting the assumption from Roedig et al. (2014) that a mass ratio $q \simeq 1.0$ and semi-major axis $a = 100R_G$ will result in an additional Wien-like spectrum with peak energy $\simeq 100$ keV, we predict that any excess emission from stream-shocking in PSO J334 could peak between rest-frame 180–340 keV, or observed-frame 60–110 keV. Because of the approximate nature of these calculations, we can only make an estimate for detectability with *NuSTAR*. However, if we assume a similar photon index in the 60–110 keV energy range as found in our 2–10 keV spectral fit, and assume that stream-shocking will result in an excess of emission ∼10 times higher than a normal AGN SED in this energy range, the count rate in *NuSTAR* is expected to be close to $\sim 1 \times 10^{-5}$ counts per second. Thus, such emission will not be easily detected by *NuSTAR*. We note that a more detailed analysis on the post-shock temperature evolution, including relevant cooling mechanisms such as pair production, will be necessary in order to determine the resultant hard X-ray spectrum expected from stream shocking.

3.7 Conclusions

In this work, we present the first targeted X-ray observation of PSO J334, a candidate binary-AGN system, with the aim to uncover the true accretion nature of the quasar. If a binary-AGN system with a separation of $28R_S$ (Liu et al. 2016), PSO J334 is well into

the gravitational-wave dominated regime and should be undergoing circum-binary accretion. Simulations show that two main types of circum-binary accretion disk morphologies can be expected: a "cavity", where emission is truncated blueward of the wavelength associated with the temperature of the innermost ring due to a mostly empty accretion disk, or mini-disks, where there is substantial accretion onto one or both of the members of the binary, each with their own shock-heated thin disk. Cavities and minidisks are expected to exhibit different behavior in the high-energy regime. Specifically, if the accretion disk of PSO J334 contains a cavity it is very likely that no, or very little, X-ray emission is expected. Further, if PSO J334 is accreting via minidisks, we may expect to see a notch in the SED or an excess of hard X-ray emission above $\geq$ 100 keV. Our 40 ks *Chandra* observation allows for the opportunity to discern between a single- or binary-AGN system, and if a binary, can characterize the type of circum-binary accretion. The main results and implications of this work can be summarized as follows:

(1) We find that PSO J334's X-ray emission is best explained by a mildly absorbed power-law with intrinsic $N_H = 0.91^{+4.84}_{-0.89} \times 10^{22}$ cm^{-2} and $\Gamma = 2.02^{+0.83}_{-0.39}$, with an observed 2–10 keV flux of $3.20^{+0.9}_{-1.1} \times 10^{-14}$ erg cm^{-2} s^{-1}, or rest-frame 2–10 keV luminosity of $9.40^{+1.4}_{-1.1} \times 10^{44}$ erg s^{-1} at $z = 2.06$ (assuming isotropic emission). We fit a broken power-law model, which may originate from a binary system where both SMBHs are accreting with their own minidisk, and find at a 95% confidence level that the spectrum does not need an additional photon index to explain its shape.

(2) We construct a radio–X-ray SED for PSO J334, using new VLBA data (Mooley et al. 2017); archival *WISE*, UKIDSS, Pan-STARRS1 (Liu et al. 2015), and *GALEX* data; and our new *Chandra* data. We find the SED agrees well with the composite non-blazar AGN SEDs presented in Shang et al. (2011).

(3) Other analyses, such as comparing IR *WISE* colors to the empirical "AGN box" presented in Jarrett et al. (2011) and calculating the mass of the accreting system via the FP, further reflects the similarity of PSO J334 with respect to normal AGN.

(4) We calculate the temperature at the inner edge of a possible circum-binary disk and find that no, or very little, emission is expected beyond $\sim 2500^{+1600}_{-700}$ Å. However from our *Chandra* observation we can verify that the intensity at energies above 2500 Å is consistent with the expected upscattered UV emission from a normal AGN disk. We conclude that the X-ray emission of PSO J334 is incompatible with the cavity accretion mode.

(5) We find no gap in the SED expected from the missing emission between $R_{\rm circum,edge}$ and $R_{\rm tidal}$, predicted to be between 500–7000 Å, for mini-disk accretion models. We note that it is possible that a notch exists within the data but is undetected given the resolution of our SED.

(6) If PSO J334 is accreting via minidisks, then we may expect a detectable excess of hard X-ray emission above $E \geq 100$ keV, depending on the mass ratio of the system and the various time-dependent cooling processes of the post-shock photons. Our rest-frame $\sim$0.9 to 24.5 keV *Chandra* spectrum shows no evidence of excess hard X-ray emission with respect to an absorbed power-law model, however we predict that any excess emission from stream-shocking should peak between rest-frame 180–340 keV, or observed-frame 60–110 keV. Near-future observations are unlikely to detect a possible excess of emission at these higher energies.

We have shown through various analyses that there is an absence of evidence supporting PSO J334 as a binary-AGN system. Specifically, we find no compelling evidence supporting PSO J334 as a binary-AGN system containing a cavity, or a binary-AGN system with mass ratios $q \geq 0.1$. However, because of the small number of currently promising binary-AGN candidates, it is most likely that the best method to distinguish a binary-AGN from a single-AGN has yet to be identified. Regarding the true nature of PSO J334, a stronger argument in either direction can be made with i) a high S/N spectrum between 500–7000 Å to allow for a more robust analysis on whether PSO J334 agrees better with the standard AGN-model or a notched-SED, and ii) a FUV spectrum that will allow for a better analysis of a possible binary-AGN system with mass ratios much below $q = 0.1$. As well, hard X-ray observations

targeting excess emission expected from stream-shocking will be important for determining the accretion mode of the quasar.

We thank the referee for helpful and constructive comments. AF acknowledges support provided by the Rackham Graduate School Conference Grant and the National Space Grant Foundation's John Mather Nobel Scholarship Program. KG and MR acknowledge support provided by the National Aeronautics and Space Administration through Chandra Award Number GO6-17104X issued by the Chandra X-ray Observatory Center, which is operated by the Smithsonian Astrophysical Observatory for and on behalf of the National Aeronautics Space Administration under contract NAS8-03060. This research has made use of the NASA/IPAC Extragalactic Database (NED) which is operated by the Jet Propulsion Laboratory, California Institute of Technology, under contract with the National Aeronautics and Space Administration. This research has made use of NASA's Astrophysics Data System.

CHAPTER IV

Bayesian Analysis of SDSS J0914+0853, a Low-mass Dual AGN Candidate

4.1 Preface

Results in this chapter were published in: *Foord, A., et. al 2019. A Bayesian Analysis of SDSS J0914+0853, a Low-mass Dual AGN Candidate. The Astrophysical Journal, Volume 877, Issue 1, article id. 17* and are reproduced here with minor style revisions by permission of the American Astronomical Society under the non-exclusive right of republication granted to authors.

4.2 Abstract

We present the first results from `BAYMAX` (Bayesian AnalYsis of Multiple AGN in X-rays), a tool that uses a Bayesian framework to quantitatively evaluate whether a given *Chandra* observation is more likely a single or dual point source. Although the most robust method of determining the presence of dual AGN is to use X-ray observations, only sources that are widely separated relative to the instrument PSF are easy to identify. It becomes increasingly difficult to distinguish dual AGN from single AGN when the separation is on the order of *Chandra*'s angular resolution ($< 1''$). Using likelihood models for single and dual point sources, `BAYMAX` quantitatively evaluates the likelihood of an AGN for a given source.

Specifically, we present results from BAYMAX analyzing the lowest-mass dual AGN candidate to date, SDSS J0914+0853, where archival *Chandra* data shows a possible secondary AGN $\sim 0\farcs3$ from the primary. Analyzing a new 50 ks *Chandra* observation, results from BAYMAX shows that SDSS J0914+0853 is most likely a single AGN with a Bayes factor of 13.5 in favor of a single point source model. Further, posterior distributions from the dual point source model are consistent with emission from a single AGN. We find the probability of SDSS J0914+0853 being a dual AGN system with a flux ratio $f > 0.3$ and separation $r > 0\farcs3$ to be very low. Overall, BAYMAX will be an important tool for correctly classifying candidate dual AGN in the literature, and studying the dual AGN population where past spatial resolution limits have prevented systematic analyses.

4.3 Introduction

Given that almost all massive galaxies are thought to harbor nuclear supermassive black holes (SMBH; Kormendy & Richstone 1995) and that classical hierarchical galaxy evolution predicts that later stages of galaxy evolution are governed by mergers (e.g., White & Rees 1978), galaxy mergers provide a favorable environment for the assembly of active galactic nuclei (AGN) pairs (Volonteri et al. 2003). The role galaxy mergers play in triggering AGN and/or AGN pairs remains unclear (e.g. Hopkins & Quataert 2010a; Kocevski et al. 2012; Schawinski et al. 2012; Hayward et al. 2014; Villforth et al. 2014, 2017; Capelo et al. 2015), however both observations and simulations agree that AGN activity should increase with decreasing galaxy separation (e.g. Koss et al. 2012; Blecha et al. 2013; Ellison et al. 2013; Goulding et al. 2018; Capelo et al. 2017; Barrows et al. 2017a).

"Dual AGN" are usually defined as a pair of AGN in a single galaxy or merging system (with typical separations of $\sim$1 kpc), while a "binary AGN" is a pair of AGN that are gravitationally bound with typical separations $\lessapprox$100 pc (see Begelman et al. 1980 for a summary of the main merging phases of SMBHs). Understanding the specific environments where dual AGN occur provides important clues about black hole growth during the merging

process. Additionally, as progenitors to SMBH-binary mergers, the rate of dual AGN is intimately tied to gravitational wave events detectable by pulsar timing arrays and space-based interferometry (see Mingarelli 2019 and references within). Thus, dual AGN offer a critical way to observe the link between galaxy mergers, SMBH accretion, and SMBH mergers.

The frequency of galaxy mergers in our observable universe implies that dual AGN should be relatively common. In particular, assuming a dynamical friction timescale of $\sim$1 Gyr we expect the galaxy merger fraction with separations ≤ 1 kpc by $z = 0.1$ to be between $\sim$6–10% (Hopkins et al. 2010). However, these estimated merger fractions don't take into account the AGN duty cycle, and observations of nearby AGN have shown that at separations ≤ 1 kpc the fraction of *dual AGN* may be much higher (Barrows et al. 2017a). Yet, very few dual AGN with separations < 1 kpc have been confirmed. Such systems become difficult to resolve with *Chandra* beyond $z \geq 0.05$, where separations on the order of 1 kpc approach *Chandra*'s angular resolution (where the half-power diameter is $\sim$0.″8 at $\sim$1 keV). For example, the closest dual AGN candidate identified using two resolved point sources with *Chandra* is NGC 3393 (Fabbiano et al. 2011) with a projected separation of $\sim$150 pc ($\sim$0.″6; however see Koss et al. 2015 for a critical analysis of the X-ray emission). Thus, many indirect detection techniques have been developed to search for evidence of dual and binary AGN, primarily relying on optical spectroscopy and photometry.

Perhaps the most popular method of finding dual AGN candidates is via double-peaked narrow line emission regions (e.g., Zhou et al. 2004; Gerke et al. 2007; Comerford et al. 2009; Liu et al. 2010a; Fu et al. 2012; Comerford et al. 2012, 2013). Double-peaked narrow lines can be a result of a dual AGN system during the period of the merger when their narrow line regions (NLR) are well separated in velocity. The system can display two sets of narrow line emission regions, such as [O III], where the separation and width of each peak will depend on parameters such as the distance between the two AGN. However the optical regime alone is insufficient in confirming a dual AGN candidate because of ambiguity in interpretation of

the observed double-peaked narrow line regions. For example, bipolar outflows and rotating disks can also can produce the double-peaked emission feature (see, e.g., Greene & Ho 2005; Rosario et al. 2010; Müller-Sánchez et al. 2011; Smith et al. 2012; Nevin et al. 2016). Indeed, follow-up observations using high-resolution imaging and spatially resolved spectroscopy have found that many double-peaked dual AGN candidates are most likely single AGN (Fu et al. 2012; Shen et al. 2011; Comerford et al. 2015). Dual or binary AGN candidates can be confirmed using high resolution radio imaging (see Rodriguez et al. 2006; Fu et al. 2015; Müller-Sánchez et al. 2015; Kharb et al. 2017); however an absence of radio emission does not necessarily mean an absence of AGN (as only $\sim 10\%$ of AGN are radio-loud), while a detection of two radio nuclei can have multiple physical explanations (such as star-forming nuclei). Nuclei can only be classified as AGN at radio frequencies if they are compact and have flat or inverted spectral indices (see, e.g., Burke-Spolaor 2011; Hovatta et al. 2014).

4.3.1 X-ray observations of dual AGN candidates

The most robust method of confirming the presence of dual AGN is to use X-ray observations. Due to the relatively few possible origins of emission above 10^{40} erg s^{-1} besides accretion onto a SMBH (Lehmer et al. 2010), X-rays are one of the most direct methods of finding black holes, especially with *Chandra*'s superb angular resolution. Unlike the optical regime, X-rays are less sensitive to absorption from the dusty environments of merger remnants. Currently, many analyses searching for dual AGN candidates using *Chandra* observations implement the Energy-Dependent Subpixel Event Respositioning (EDSER) algorithm (Li et al. 2004). EDSER improves the angular resolution of *Chandra*'s Advanced CCD Imaging Spectrometer (ACIS) by reducing photon impact position uncertainties to subpixel accuracy, and in combination with *Chandra*'s dithering can resolve sub-pixel structure down to the limit of the *Chandra* High Resolution Mirror Assembly. However, thus far it has only been used to make images and qualitatively analyze them for dual point sources. In the absence of corroborating evidence from other data, the reliance on visual interpretation of dual AGN

with separations comparable to *Chandra*'s resolution leads to both false negatives and false positives. This issue is worse in the low-count regime (< 200 counts), where even dual AGN with larger separations ($> 0\farcs5$) but low flux ratios are not clearly distinct.

We have developed a `PYTHON` tool `BAYMAX` (**B**ayesian **A**nal**Y**sis of **M**ultiple **A**GN in **X**-rays) that allows for a quantitative and rigorous analysis of whether a source in a given *Chandra* observation is more likely composed of one or two point sources. This is done by taking calibrated events from a *Chandra* observation and comparing them to the expected distribution of counts for single or double source models. The main component of `BAYMAX` is the calculation of Bayes factor, which represents the ratio of the plausibility of observed data, given two different models. Values > 1 or < 1 signify which model is more likely (see Section 4.4 for explicit details). Further, `BAYMAX` returns the maximum likelihood values for the parameters of each model. In this chapter we introduce our tool `BAYMAX` and present its analysis on the *Chandra* observations of the lowest-mass dual AGN candidate SDSS J0914+0853. Here we specifically highlight `BAYMAX`'s capabilities with respect to the *Chandra* observations of SDSS J0914+0853. We are using a subset of `BAYMAX`'s full capabilities, i.e., analyzing an on-axis source, assuming identical spectra for both the primary and secondary AGN, and the background contribution is deemed negligible. As well, false positives are only analyzed for regions in parameter space (such as count number, separation, and flux ratio) that are specific to SDSS J0914+0853. Following studies will expand upon the explicit details of `BAYMAX`, including its capabilities of correctly identifying dual AGN as a function of observed flux, angular separations, off-axis angle, and flux ratios. In this chapter, we restrict our discussion to `BAYMAX`'s abilities on our observations of SDSS J0914+0853.

4.3.2 SDSS J0914+0853

SDSS J0914+0853 was originally identified by Greene & Ho (2007) as one of ∼200 low-mass SMBH based on "virial" black hole mass estimates, where the velocity dispersion and radius of the broad line region (BLR) were estimated from Hα emission line characteristics.

The system is at $z = 0.14$ ($D_L = 661$ Mpc and $D_A = 509$ Mpc for a ΛCDM universe, where $H_0 = 69.6$, $\Omega_M = 0.286$, and $\Omega_\Lambda = 0.714$) and is a low-mass ($M_{BH} = 10^{6.3} M_\odot$), low-luminosity AGN. SDSS J0914+0853 was observed by *Chandra* as part of a Cycle 13 program targeting low-mass AGN (Proposal ID:13858, PI:Gültekin). These data were taken to investigate the fundamental plane in the low-mass regime and thus are on-axis (Gültekin et al. 2014). Analyzing the 15 ks *Chandra* data with EDSER, the archival *Chandra* exposure shows a possible secondary source $0\farcs3$ away from the primary. The likelihood of contamination from an ultraluminous X-ray source (ULX) is very low; following the methodology in Foord et al. (2017a) we calculate the number of expected ULXs with $L_{\geq} 10^{41}$erg s^{-1} to be $< 10^{-3}$ within a radius of $0\farcs3$ from the center of the galaxy. If the emission is found to most likely originate from two point sources, it will be the lowest-mass dual AGN discovered, and analysis of this system paves the way for a better understanding of the role of mergers and AGN activity in low-mass systems. In particular, dual AGN in low-mass galaxies with low luminosities are the perfect testbed for discerning between competing models for the connection between galaxy mergers and AGN activity. It has been argued that mergers can trigger high-luminosity AGN but not low-luminosity AGN, which are triggered by stochastic processes (Hopkins & Hernquist 2009; Treister et al. 2012). A competing hypothesis is that there is no correlation between AGN luminosity and mergers (e.g.,Villforth et al. 2014). Since dual AGN most likely arise from mergers, the presence of a low-luminosity dual AGN in SDSS J0914+0853 would show that low luminosity AGN can arise from mergers. However, effects due to pileup and artifacts from the Point Spread Function (PSF) cannot be ruled out at a high statistical confidence for the low-count ($\sim$250 counts between 2–7 keV) image. At 10%, the pile-up fraction is relatively small, but combined with asymmetries in the *Chandra* PSF (Juda & Karovska 2010), it could produce a spurious dual AGN signature. Thus, a statistical analysis is necessary before a discovery can be confirmed.

We aim to unambigiously determine the true nature of SDSS J0914+0853. As stated above, the existing *Chandra* data cannot do this because (i) the pile-up introduces system-

atic uncertainties in the EDSER processing, (ii) the existing exposure is relatively shallow (15 ks), and (iii) potential PSF artifacts can produce spurious dual AGN signatures. To help determine the true nature of SDSS J0914+0853, we received a new observation (Proposal ID:19464, PI:Gültekin) that addresses all three of the above points. In particular, the observation (i) uses the shortest possible frame time with a subarray, thereby eliminating pileup, (ii) goes 3× deeper with a 50 ks exposure, and (iii) uses a substantially different roll angle so that any PSF artifacts will not appear in the same location on the sky. With a total of ∼723 counts between 2–7 keV (combining both datasets), `BAYMAX` is able to statistically analyze the likelihood that SDSS J0914+0853 is a dual AGN for separations $> 0\farcs3$ and flux ratios > 0.1.

The remainder of the chapter is organized into 5 sections. Section 4.4 introduces Bayesian inference, focusing on the specific components of Bayes factor and how `BAYMAX` calculates the likelihood and prior densities. In section 4.5 we analyze the *Chandra* observations of SDSS J0914+0853, including both a photometric and spectral analysis. In section 4.6 we present our results when running `BAYMAX` on the *Chandra* observations of SDSS J0914+0853, and in section 4.7 we discuss the sensitivity and limitations of `BAYMAX` across parameter space and how they affect our results. Lastly, we summarize our findings in Section 6. Please see Table 4.1 for a list of symbols used throughout this chapter.

4.4 Methods

4.4.1 Bayesian Inference

`BAYMAX` is capable of statistically and quantitatively determining whether a given observation is better described by a model composed of one or two point sources based on a Bayesian framework. A Bayesian approach combines all available information (using prior distributions and likelihood models) to infer the unknown model parameters (posterior dis-

Table 4.1: Symbols

Symbol (1)	Definition (2)
(x_i, y_i)	Sky coordinate of photon i
E_i	Energy of photon i, in keV
n	Total flux (counts) of given source
μ	Central position of given source in sky coordinates (2D; $\mu = [\mu_x, \mu_y]$)
k	Number of *Chandra* observations being modeled
Δx_K	Translational astrometric shift in x ($K = [1, \ldots, k-1]$)
Δy_K	Translational astrometric shift in y
Δr_K	Radial astrometric shift ($\Delta r_K = \sqrt{(\Delta x_K)^2 + (\Delta y_K)^2}$)
$\Delta\phi_K$	Rotational astrometric shift
f	Flux ratio between secondary and primary source ($0 < n_S/n_P < 1$)
M_j	Given model being analyzed by `BAYMAX`
θ_j	Parameter vector for M_j, i.e. [μ, f, Δx_K, Δy_K, $\Delta\phi_K$] .

Note. – Columns: (1) Symbols used throughout the text; (2) Definitions.

tributions). Bayes Theorem implies:

$$\underbrace{\frac{P(M_2 \mid D)}{P(M_1 \mid D)}}_{\text{Posterior odds}} = \underbrace{\frac{P(D \mid M_2)}{P(D \mid M_1)}}_{\text{Bayes factor}} \times \underbrace{\frac{P(M_2)}{P(M_1)}}_{\text{Prior odds}}, \tag{4.1}$$

where the posterior odds represents the ratio of the dual point source model (M_2) vs. the single point source model (M_1) given the data D; the Bayes factor ($\mathcal{B}$) quantifies the evidence of the data for M_2 vs. M_1, and the prior odds represents the prior probability ratio of M_2 vs. M_1. Specifically, the Bayes factor is the ratio of the marginal likelihoods:

$$\mathcal{B} = \frac{\int P(D \mid \theta_2, M_2) P(\theta_2 \mid M_2) d\theta_2}{\int P(D \mid \theta_1, M_1) P(\theta_1 \mid M_1) d\theta_1}, \tag{4.2}$$

representing the ratio of the plausibility of observed data D, given two different models, and parameterized by the parameter vectors θ_2 and θ_1. Values >1 or <1 signify whether M_2 or M_1 is more likely (see Jeffreys 1935 and Kass & Raftery 1995 for the historic interpretations of the strength of a given Bayes factor value; we analyze our data to define a "strong" Bayes factor value in Section 4.7.) In this chapter, we assume that M_2 and M_1 are equally probable, so that $P(M_2) = P(M_1) = 0.5$ and the Bayes factor directly represents the posterior odds. Thus

calculating the Bayes factor can be broken into two components — the likelihood density, $P(D \mid \theta_j, M_j)$, and the prior density, $P(\theta_j \mid M_j)$.

4.4.2 Data Structure and Modeling the PSF

In this section we will focus on the likelihood density implemented in `BAYMAX`. Each reprocessed *Chandra* level-2 event file tabulates the directional coordinates (x_i, y_i) and energy E_i for each detected photon, where i indexes each detected photon (See Table 4.1 for a summary of notation). The detector itself records the pulse height amplitude (PHA) of each event, which is roughly proportional to the energy of the incoming photon. In the reprocessed files, the energy E_i is calculated from the event's PHA value, using the appropriate gain table. Thus, `BAYMAX` takes calibrated events (x_i, y_i, E_i) from reprocessed *Chandra* observations and compares them to new simulations based on single and dual point source models.

We characterize the properties of the *Chandra* PSF by simulating the PSF of the optics from the High Resolution Mirror Assembly (HRMA) via ray tracing simulations. The two primary methods to simulate the HRMA PSF are `SAOTrace`[1] and the Model of AXAF Response to X-rays (`MARX`, Davis et al. 2012). While the `MARX` model uses a slightly simplified (and faster) description of the HRMA, differences between `SAOTrace` and `MARX` simulations are minimal for on-axis simulations. For our PSF analysis below, we find consistent parametric fits between an `SAOTrace` generated PSF and one generated by `MARX` – in particular the root-mean-square error between the two fits is on the order of $\sim 0.1\%$

Thus, our Likelihood models for single and dual point sources are created by parametrically modeling the *Chandra* PSF using high count simulations created by `MARX`-5.3.3. To translate the PSF model to an event file, the HRMA ray tracing simulations are projected on to the detector-plane via `MARX`. Ray tracing simulations generated by both `MARX` and `SAOTrace` will have roughly the correct total intensity, but small deviations in the overall shape. Specifically regarding `MARX` – the PSF wings are broader than observations while

[1] http://cxc.harvard.edu/cal/Hrma/Raytrace/SAOTrace.html

the PSF core is narrower than observed (Primini et al. 2011). These discrepancies can be reduced by blurring the PSF when projecting it to the detector-plane via the `AspectBlur` parameter. This parameter is used to account for the uncertainty in the determination of the aspect solution (such as effects from pixel quantization and pixel randomization), as well as the uncertainty in the instrument and dither models within `MARX`. The best value should be considered carefully for each unique observation[2]. For `MARX` generated simulations on ACIS-S, we expect the `AspectBlur` parameter to have values between $0\farcs25 - 0\farcs28$. For our PSF analysis we set `AspectBlur` to $0\farcs28$. We note that value used for `AspectBlur` does not represent the accuracy at which we can centroid.

For a given observation, a user-defined source model is input to `MARX` to generate X-ray photons incident from a single point source centered on the observed central position of the AGN (μ_{obs}, defined as the coordinates where the hard X-ray emission from the AGN is estimated to peak). Because we do not model the spectral parameters of the system (see Section 4.3), we are only interested in modeling the spatial distribution of a photon due to its energy E_i and our PSF does not depend on the spectral shape of our model. Each simulation uses the observation-specific detector position (`RA_Nom, Dec_Nom, Roll_Nom`) and start time (`TSTART`). We set the number of generated rays (`NumRays`) to 1×10^6 and the read-out strip is excluded by setting the parameter `ACIS_Frame_Transfer_Time` to 0.

We model the PSF as a summation of 2D Gaussians, where the amplitude and standard deviation of each Gaussian is energy-dependent. In general, the PSF may be any function which is unique to a given observation and can be quickly evaluated. For both the 15 ks and 50 ks observation, we fit a variety of possible functions to the PSF. Using the Bayesian Information Criterion as a diagnostic for model comparison, we find that a summation of three circular concentric 2D Gaussians yields the best-fit for both *Chandra* observations (specifically, we find the PSF wings are best-modeled by the broadness of a Gaussian component versus the addition of a Lorentzian component). We model the PSF for each observation

[2]http://cxc.harvard.edu/ciao/why/aspectblur.html

individually, however we find that the best-fit parameters for each PSF model are consistent with one-another within the 1σ error bars (which is not surprising, given that both sources were observed on-axis for ACIS-S albeit in different *Chandra* cycles).

Each photon is assumed to originate from a single or dual point source system. For example, for a single point source, the probability that a photon observed at location x_i,y_i on the sky with energy E_i is described by the PSF centered at μ is $P(x_i, y_i \mid \mu, E_i)$, i.e., the energy dependent PSF. For n total events, the total probability is the product of the probability for each detected photon, i.e., the likelihood density is:

$$\begin{aligned} \mathcal{L} = P(x, y \mid \mu, E) &= \prod_{i=1}^{n} P(x_i, y_i \mid \mu, E_i) \\ &= \prod_{i=1}^{n} \frac{M_{1,i}(\theta_1)^{D_i}}{D_i!} \exp(-M_{1,i}(\theta_1)), \end{aligned} \tag{4.3}$$

where we use the Poisson likelihood, appropriate given that *Chandra* registers each event individually. Here, $M_{1,i}(\theta_1)$ is the probability for event i given our PSF model, and D_i is the data value for event i. For a dual point source the total probability is $P(x, y \mid \mu_P, \mu_S, E, n_S/n_P)$, where μ_P and μ_S represent the location of the primary and secondary AGN. The ratio of the fluxes (or, total counts) between the secondary and primary is represented by $n_S/n_P = f$, where $0 \leq f \leq 1$. We note that our analysis on SDSS J0914+0853 does not include fitting for the spectral models. Using the archival data we find consistent hardness ratios between the candidate primary and secondary AGN, where we use circular and non-overlapping apertures centered on their apparent locations. Thus, we assume that the spectra are the same spectral shape as that for the entire system, but with different normalizations. Future analyses with `BAYMAX` will include fitting for different spectral shapes.

Because Bayes factor represents the *ratio* of likelihood densities, and we use the same data across both models, our calculations become simplified. We are left with:

$$\ln\mathcal{L} = \sum_{i=1}^{n} D_i \, \ln M_{j,i}(\theta_j) + \text{constant}, \tag{4.4}$$

where $M_{j,i}(\theta_j)$ is calculated for either a single ($j = 1$) or dual ($j = 2$) point source model via our parametrically-fit PSF, for each detected event i.

4.4.3 Prior Distributions

`BAYMAX` requires user input regarding (i) the number of datasets and (ii) the prior distributions for each parameter. Regarding point (i), SDSS J0914+0853 has $k = 2$ observations and thus the parameter vector $\theta_1 = [\mu, \Delta x_1, \Delta y_1]$ while $\theta_2 = [\mu_P, \mu_S, \log f, \Delta x_1, \Delta y_1]$. Here, $\mu = (\mu_x, \mu_y)$ is the central sky x,y positions of the AGN; Δx_1 and Δy_1 account for the translational components of the relative astrometric registration for the $k - 1$ observation; and $\log f$ is the log of the flux ratio where $f = n_S/n_P$. The relative astrometric registration adds an uncertainty that must be taken into account in order to avoid spurious dual AGN signals that can be generated from slight mismatches between two or more observations. We take this into account by including the astrometric registration of multiple observations as a set of parameters to be marginalized over. For SDSS J0914+0853, we find that the rotational component of the relative astrometric registration is expected to be very small ($\Delta\phi_1 < 1^\circ$) and including the parameter does not affect our results. Thus, we only include Δx_1 and Δy_1, which are analyzed for the shallower observation (i.e., relative to the 50 ks exposure).

Regarding point (ii), `BAYMAX` can incorporate any user-defined function to describe the prior distributions for each parameter. For SDSS J0914+0853, the prior distributions of μ for both M_1 and M_2 are described by a continuous uniform distribution[3]:

$$\mu = \mathcal{U}(a, b), \tag{4.5}$$

where we constrain all μ values to be between $a = \mu_{obs} - 2$ and $b = \mu_{obs} + 2$. Thus, the 2D parameter space for possible μ_x and μ_y is a 4×4 sky-pixel box ($\approx 1.98'' \times 1.98''$) centered on the observed central X-ray coordinates of SDSS J0914+0853. Further, the prior

[3]The continuous uniform distribution $\mathcal{U}(a, b)$ is a probability distribution where all values between the minimum a and maximum b are equally probable.

distributions of Δx_1 and Δy_1 are also described by a uniform distribution with $a = \delta\mu_{obs} - 3$ and $b = \delta\mu_{obs} + 3$, where $\delta\mu$ represents the difference between the observed central X-ray coordinates of the two observations (in practice, $\delta\mu$ is expected to be small; however because the most recent observation of SDSS J0914+0853 was taken in a subarray mode, the difference between the aimpoints of the two observations is ≈15 sky pixels). For M_2, the prior distribution for $\log f$ is also described by a uniform distribution (and thus f is described by a *log uniform* distribution), where $a = -2$ and $b = 0$. The range for the prior distribution of $\log f$ covers possible values expected for "major mergers" (with mass ratios $> 1/3$), while accounting for a large range of possible Eddington fractions between the two black holes. In general, informative priors can be incorporated if prior information is available. For example, we might set the prior distributions of μ_P and μ_S to Gaussian distributions centered on coordinates that are better constrained by other observations (such as spectroastrometric [O III] observations, or complementary IR photometry).

4.4.4 Calculation of Bayes Factor

Bayesian inference can be divided into two categories: model selection and parameter estimation. In this section we review how we address each component in `BAYMAX`.

Computing the marginal likelihood is challenging, as it involves a multi-dimensional integration over all of parameter space. Only over the last ∼20 years have the advances in computational power allowed Bayesian inference to become a more common technique for model selection. In addition, general numerical methods based on Markov chain Monte Carlo (MCMC; e.g., see Metropolis et al. 1953) have been developed, allowing one to conduct Bayesian inferences in an efficient manner, with few constraints on dimensionality or analytical integrability.

To calculate the marginal likelihood, `BAYMAX` implements a sampling technique called nested sampling (Skilling 2004). In nested sampling, the marginal likelihood is rebranded as the "Bayesian evidence", denoted by Z. Here, $Z = \int P(D \mid \theta_j, M_j) P(\theta_j \mid M_j) d\theta_j$.

Nested sampling transforms the multi-dimensional integral to a one dimensional integral by introducing the *prior mass* X, defined as $X = \int_{\mathcal{L}(\theta)>\lambda} P(\theta_j \mid M_j) d\theta_j$; here the integral extends over the regions of parameter space contained within the iso-likelihood contour $\mathcal{L}(\theta) = \lambda$ and at any given time has a value $0 < X < 1$. For a step-by-step explanation of nested sampling we refer the reader to Skilling (2004), Shaw et al. (2007), Feroz & Hobson (2008), and Feroz et al. (2009). A direct effect of the nested sampling methodology is sparsely sampling in low likelihood regions and densely sampling where the likelihood is high. To calculate the evidence, `BAYMAX` uses the `PYTHON` package `nestle`[4]. The package provides a pure-`PYTHON` implementation of nested sampling, where prior mass space can be sampled via different techniques. In particular, we use multi-ellipsoidal sampling (by setting `method`='multi'; see Mukherjee et al. 2006; Shaw et al. 2007; Feroz & Hobson 2008).

The two parameters that affect the accuracy of Z are the number of "active points" and the stopping criterion dlog$Z$. The number of active points represent how many points in prior mass space one is sampling at a given time (roughly analogous to the number of walkers in an MCMC run). The stopping criterion determines when the nested sampling loop terminates — when the current largest sampled likelihood does not increase by more than the stopping criterion value, the sampling will end[5]. For our analysis of SDSS J0914+0853, we use 500 active points (generally, a lower limit on the number of active points is $2N_{dim}$, and due to using the multi-ellipsoidal method we add additional points to characterize each mode well) and set the stopping criterion dlog$Z = 0.1$. By continually increasing the number of active points and decreasing the stopping criterion, the estimated evidence and its accuracy should converge. We find no significant difference in results when increasing our active points above 500 and using dlog$Z < 0.1$, and conclude that these values have properly sampled the likelihood space.

Lastly, for parameter estimation `BAYMAX` uses `PyMC3` (Salvatier et al. 2016), which uses

[4]https://github.com/kbarbary/nestle

[5]Specifically, at a given iteration i where the current evidence is Z_i and the estimated remaining evidence in the likelihood landscape is Z_{est}, if $\log(Z_i + Z_{est}) - \log(Z_i) <$ dlog$Z$, the sampling will terminate

gradient-based MCMC methods for sampling. Specifically, we use `PyMC3`'s built in Hamiltonian Monte Carlo (HMC) sampling method. HMC uses the gradient information from the likelihood to much more quickly converge than normal Metropolis-Hastings sampling. In general, HMC is more powerful for high dimensionality and complex posterior distributions (see, e.g., Betancourt et al. 2014).

In Figure 4.1 we show the results when we analyze two simulations with `BAYMAX`. The simulations have been reprocessed using EDSER, and binned by 2/3 of the native pixel size. We simulate a single and a dual AGN system via `MARX` using the same telescope configuration as our new 50 ks observation. Both simulations have $n = 700$ photons between 2–7 keV, and the same 2–7 keV spectrum as SDSS J0914+0853. We do not include a background contribution in our simulations (see Section 4.5). For the dual AGN simulation, each AGN has the same spectra but with normalizations such that the flux ratio $f = n_S/n_P = 0.8$ while the separation between the two AGN is $0\farcs4$. As evident, it is difficult to visually distinguish whether a given simulation is actually composed of one or two sources. Using the methodology presented above, `BAYMAX` favors the correct model for both simulations: for the single AGN simulation `BAYMAX` estimates $\mathcal{B} = 17 \pm 1.6$ in favor of the single point source model, while for dual AGN simulation `BAYMAX` estimates $\mathcal{B} = 25 \pm 1.5$ in favor of the dual point source model (error bars have been determined by running `BAYMAX` multiple times on each simulation, see Section 4.6). Although the hard X-ray emission appears quite similar between the two simulations, the joint posterior distributions are significantly different from one another. Specifically, for the dual AGN simulation the joint posterior distribution is more tightly concentrated around the true values. `BAYMAX` is able to recover the true separation and flux ratio within the 68% credible interval. However, for the single AGN, the separation and flux ratio are consistent with 0 at the 99.7% confidence level. We note that this particular joint-distribution shape ("L" shape) is consistent with a single AGN, where at very large flux ratios the dual AGN candidate is likely to have $r = 0$, and at very large separations the dual AGN candidate is likely to have $\log f = -2$. More specifically, the dual point source model

places each AGN at the same location and/or with arbitrarily low f, effectively consistent with one point source.

4.5 Data Analysis

4.5.1 X-ray Data

SDSS J0914+0853 was originally targeted to study low-mass AGN and their relation to the plane of black hole accretion. The quasar was placed on the back illuminated S3 chip of the Advanced CCD Imaging Spectrometer (ACIS) detector, with an exposure time of 15 ks (Obs ID: 13858). We received a new 50 ks exposure at a roll angle significantly different from the previous observation, and using the smallest subarray (1/8) on a single chip to get the shortest standard frame time (Obs ID: 19464). This was done to (1) place the PSF artifact in a different location, (2) avoid pileup, and (3) receive $\sim$ 2–3 times more counts. We re-reduced and re-analyzed the archival data to ensure a uniform analysis between the two datasets.

We follow a similar data reduction as described in previous X-ray studies analyzing AGN (e.g., Foord et al. 2017a,b), using the *Chandra* Interactive Analysis of Observations (`CIAO`) v4.8 (Fruscione et al. 2006). Both datasets are analyzed with the energy-dependent sub-pixel event repositioning algorithm (EDSER; Li et al. 2004), which can be included in the standard `CIAO` reprocessing command `chandra_repro` with the parameter `pix_adj=EDSER`. For each observation, we first evaluate the aspect solutions of the reprocessed level-2 event files to ensure the Kalman lock was stable at all times. Further, we inspect the event detector coordinates as a function of time and find that they followed the instrument's dither pattern, indicating no aspect-correction based degradation of the PSF.

We then correct for astrometry, cross-matching the *Chandra* detected point-like sources with the Sloan Digital Sky Survey Data Release 9 (SDSS DR9) catalog. The *Chandra* sources used for cross-matching are detected by running `wavdetect` on the reprocessed level-2 event

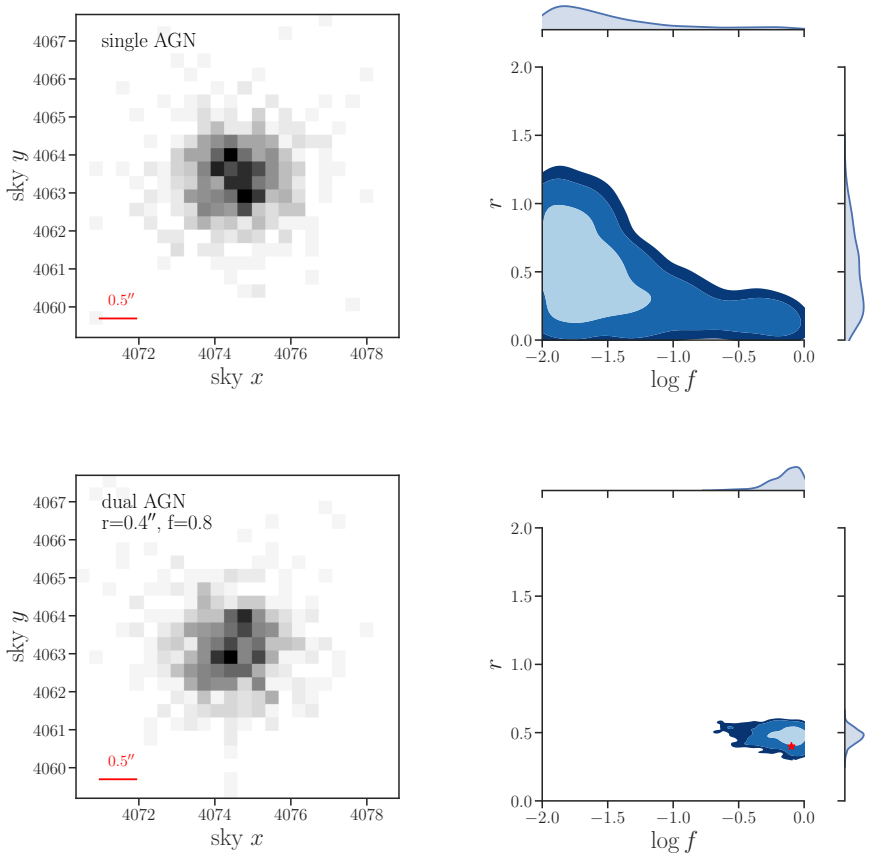

Figure 4.1: Simulated single and dual AGN, with their respective joint posterior distributions after being analyzed by BAYMAX. *Top*: A simulated single AGN (left) and the joint posterior distribution (right) for the separation (r, in arcsec)and flux ratio ($\log f$). The simulation has a total of $n = 700$ counts between 2–7 keV. The simulations have been reprocessed using the Energy-Dependent Subpixel Event Repositioning algorithm (EDSER; Li et al. 2004), and binned by 2/3 of the native pixel size. We do not include a background contribution from in these simulations. Using BAYMAX, we calculate a Bayes factor strongly in favor of the single point source model. The joint posterior distribution is shown with the marginal distributions along the top and right border. 68%, 95% and 99.7% confidence intervals are shown in blue contours. The separation and logarithm of the flux ratio are consistent with 0 and -2 at the 99.7% confidence level. We note that this particular joint-distribution shape is consistent with a single AGN, where at very large flux ratios the dual AGN candidate is likely to have $r = 0$, and at very large separations the dual AGN candidate is likely to have $\log f = -2$. *Bottom*: A simulated dual AGN (left) and the joint posterior distribution for the separation and flux ratio (right). The simulation has a separation $r = 0\farcs4$ and $f = 0.8$, and a total of $n = 700$ 2-7 keV counts. It is difficult to tell whether the observation is composed of one or two point sources from the hard X-ray emission alone. Using BAYMAX, we calculate a Bayes factor strongly in favor of the dual point source model. Further, using BAYMAX we retrieve the correct separation and flux ratio values within the 68% confidence level.

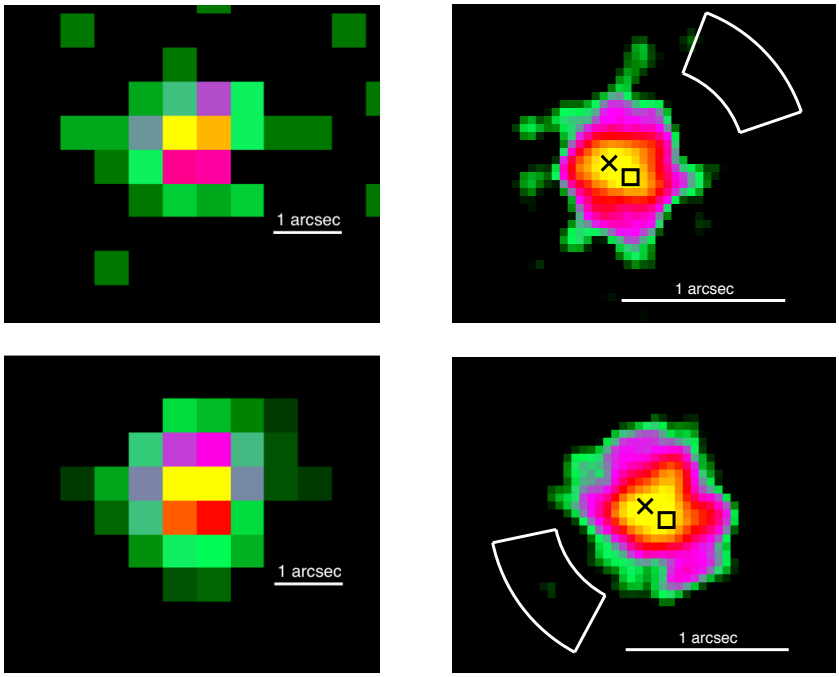

Figure 4.2: *Chandra* images of SDSS J0914+0853. *Top*: 2–7 keV raw (left) and smoothed (right) images of the 15 ks archival observation (Obs ID: 13858). The total number of 2–7 keV counts shown is 257. The smoothed image has been reprocessed using the Energy-Dependent Subpixel Event Repositioning (EDSER; Li et al. 2004) algorithm, and binned by a tenth of the native pixel size. The location of the asymmetry in the *Chandra* PSF is $\approx 0\farcs7$ from the central position of the AGN, and is outlined by a white polygon. For both datasets, we mask the photons from this region before running `BAYMAX`. There appear to be two regions of X-ray emission (denoted by a black "x" and a black square) separated by $\sim 0\farcs3$. *Bottom*: 2–7 keV raw (left) and smoothed (right) image of our new 50 ks observation (Obs ID: 19464). The total number of 2–7 keV counts is 484; the smoothed image has been reprocessed similarly to the archival dataset. We plot the spatial location of the primary (black "x") and secondary (black square) AGN, given the 15 ks observation. Although the archival dataset appears to have X-ray emission associated with two point sources, the new dataset has emission that more closely resembles a single point source.

file. We require each matched pair to be less than 2″ from one another and have a minimum of 3 matches. The 15 ks observation meets the criterion for an astrometrical correction; we find 8 matches between the *Chandra* observation and the SDSS DR9 catalog, resulting in a shift less than 0.″5. The 50 ks observation was taken in a subarray, and thus does not meet these criterion (however, because `BAYMAX` takes into account astrometric shifts between observations this step will not affect our final results, see Section 4.6). Background flaring is deemed negligible as neither dataset contain intervals where the background rate is 3σ above the mean level.

We then rerun `wavdetect` on filtered 0.5 to 7 keV data to generate a list of X-ray point sources. We use wavelets of scales 1, 1.5, and 2.0 pixels using a 1.5 keV exposure map, and set the detection threshold significance to 10^{-6} (corresponding to one false detection over the entire S3 chip). We identify the quasar as an X-ray point source 0.″4 (Obs ID: 13858) and 0.″7 (Obs ID:19464) from the SDSS-listed optical center (2″corresponds to 95% of the encircled energy radius at 1.5 keV for ACIS). Counts are extracted from a 2″ radius circular region centered on the X-ray source center, where we use a source-free annulus with an inner radius of 20″ and outer radius of 30″ for the background extraction. We compare the estimated background contribution from the datasets to the *Chandra* blank-sky files. Here, the blank-sky files are properly scaled in exposure time and have matching WCS coordinates, dimensions, and energies. We find consistent results, where within 2–7 keV we expect $\lesssim 1$ and 1.5 background counts within a 4×4 sky-pixel box ($\approx 1.98'' \times 1.98''$) centered on the quasar for the archival and new dataset, respectively.

Our reduced data are shown in Figure 4.2. Here, both exposures have been reprocessed using the EDSER algorithm and are binned by a tenth of the native pixel size. The archival data appear to have sub-pixel structure, indicating a possible secondary AGN $\sim 0.''3$ away from the primary, however our new observation is inconsistent with this picture. Although the X-ray emission may be slightly extended in the East-West direction (North is up, while East is left), we find minimal photometric evidence supporting the presence of a secondary

AGN.

4.5.2 Spectral Fitting

The quasar's net count rate and flux value are determined using XSPEC, version 12.9.0 (Arnaud 1996). All errors evaluated in this section are done at the 95% confidence level, unless otherwise stated, and error bars quoted are calculated with Monte Carlo Markov chains via the XSPEC tool `chain`. We implement the Cash statistic (`cstat`; Cash 1979) in order to best assess the quality of our model fits.

Both spectra have an excess of flux at soft X-ray energies (< 1 keV) with respect to the power-law continuum, while the 15 ks data appear to catch the source in a higher flux state in the soft X-ray band (see Fig. 4.3). Both of these behaviors are seen in AGN with a "soft excess" component (e.g., Lohfink et al. 2012, 2013; see Miniutti et al. 2009; Ludlam et al. 2015 for examples of soft X-ray excess in low-mass AGN candidates), an excess in emission above the extrapolated 2–10 keV flux that is detected in over 50% of Seyfert 1s (Halpern 1984; Turner & Pounds 1989; Piconcelli et al. 2005; Bianchi et al. 2009; Scott et al. 2012). The physical origin of the soft excess remains uncertain; the shape is suggestive of a low-temperature high optical depth Comptonization of the inner accretion disk, however the temperature of this component appears to be constant over a wide range of black hole masses (and thus inferred accretion disk temperatures; see Gierliński & Done 2004; Crummy et al. 2006). The two most popular explanations for the soft excess are blurred ionized reflection from the inner parts of the accretion disk (e.g., Fabian et al. 2002, 2005; Gierliński & Done 2004; Crummy et al. 2006) and Comptonization components (such as partial covering of the source by cold absorbing material, see Boller et al. 2002; Tanaka et al. 2004).

Indeed, we find a statistically better fit when including an absorbed redshifted blackbody component to account for this soft excess (`phabs`×`zphabs`×`(zpow + zbbody)`). We fix the Galactic hydrogen column density (the photoelectric absorption component `phabs`) to 4.21×10^{20} cm^{-2} (Kalberla et al. 2005), and the redshift to $z = 0.14$. In Figure 4.3, we show the X-

ray spectrum of both observations, along with the best-fit XSPEC models. For the archival dataset, we find best-fit values for intrinsic $N_H = 3.38^{+0.10}_{-0.10} \times 10^{20}$ cm^{-2}, power law component $\Gamma = 2.01^{+0.11}_{-0.12}$; and blackbody component $kT = 0.10^{+0.03}_{-0.05}$ keV. For our new dataset, we find best-fit values for intrinsic $N_H = 4.07^{+0.10}_{-0.10} \times 10^{20}$ cm^{-2}, power law component $\Gamma = 2.51^{+0.10}_{-0.12}$; and blackbody component $kT = 0.11^{+0.05}_{-0.04}$ keV.

However, because our analysis with `BAYMAX` is restricted to the 2-7 keV photons from SDSS J0914+0853, our results are not affected by the soft emission component in the spectrum. In particular, although we detect variability between the two observations in the low-energy band, the 2–10 kev fluxes are consistent with one another (at the 99.7% C.L.) when we fit each spectra independently between 2–7 keV with an absorbed redshifted power law. For the 15 ks observations we calculate a total observed 2–10 keV flux of $3.20^{+0.90}_{-0.80} \times 10^{-13}$ erg s^{-1} cm^{-2}, while for the 50 ks observation we calculate a total observed 2–10 keV flux of $2.23^{+1.0}_{-0.49} \times 10^{-13}$ erg s^{-1} cm^{-2} s^{-1}. This corresponds to a rest-frame 2–10 keV luminosity of $1.83^{+0.31}_{-0.40} \times 10^{43}$ erg s^{-1} and $1.25^{+0.35}_{-0.21} \times 10^{43}$ erg s^{-1} at $z = 0.14$ (assuming isotropic emission).

4.6 Results

When analyzing the 15 ks *Chandra* data with the EDSER option enabled, SDSS J0914+0853 appears to be an interesting dual AGN candidate. When binned, the data show a possible secondary source $0\farcs3$ away from the primary (see Fig. 4.2). Although a possibly interesting result, classifying the source based on a qualitative analysis runs the risk of a false positive. A statistical analysis is necessary before a discovery can be confirmed. With an abundance of photons, and a robust model of the *Chandra* PSF, in the following section we aim to unambigiously determine the true nature of SDSS J0914+0853. We first analyze each observation individually using `BAYMAX`, and then combine the two (yielding a total of $n = 723$ counts between 2–7 keV).

We restrict our analysis to photons with (i) energies between 2–7 keV and (ii) contained

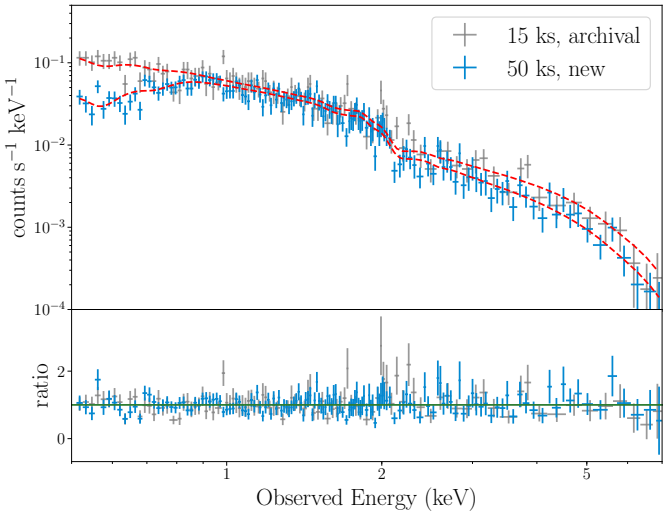

Figure 4.3: The observed 0.5–7.0 keV *Chandra* spectrum of SDSS J0914+0853 for both the 15 ks archival observation (grey points) and our new 50 ks observation (blue points), where the data have been folded through the instrument response. Both spectra appear to have a soft excess component, a feature seen in many narrow-line Seyfert 1 AGN. We fit the spectrum with the model `phabs`×`zphabs`×`(zpow+zbbody)`, fixing the Galactic absorption and redshift parameters at $N_H = 4.0\times\ 10^{20}$ cm^{-2} and $z = 0.14$. For each dataset, the best-fit models are shown in red. We list the best-fit values for each model in Section 4.5.2, defined as the median of the distribution. Because our analysis with `BAYMAX` is restricted to the 2–7 keV photons from SDSS J0914+0853, our results are not affected by the soft emission component in the spectrum. In particular, although we detect variability between the two observations in the low-energy band, the 2–10 keV fluxes are consistent with one another when we fit each spectra independently between 2–7 keV with an absorbed power law. The ratio of the data to the continuum model for SDSS J0914+0853 is shown in the bottom panel. The spectrum has been rebinned for plotting purposes.

within a 4×4 sky-pixel box (1.98″× 1.98″) centered on the nominal X-ray coordinates of the AGN. This corresponds to ∼95% of the encircled energy radius for the 2–7 keV photons. Because we expect $\lesssim 1$ and 1.5 background counts within this region for the archival and new dataset, each photon is assumed to originate from either one (M_1) or two (M_2) point sources, with no background contamination. The asymmetric PSF feature is within this extraction region, and sits approximately 0.″7 from the center of the AGN (see Fig. 4.2). Within 2-7 keV, there are 6 and 12 photons that spatially coincide with the feature for the 15 and 50 ks observations, respectively. We mask the feature in both exposures before running `BAYMAX`.

We run `BAYMAX` with the initial conditions for the parameter vectors θ_1 and θ_2 as stated in Section 4.4. When running `BAYMAX` on our 15 ks and 50 ks observation individually, $k = 1$ and thus we exclude the Δx_1 and Δy_1 from θ_1 and θ_2. Further, we run `BAYMAX` with the initializations for `nestle` as described in Section 4.4, with 500 active points and dlog$Z = 0.1$

Our 15 ks observation has a total of $n = 251$ counts between 2–7 keV, while our 50 ks observation has a total of $n = 472$ counts between 2–7 keV. Using `BAYMAX`, we calculate a Bayes factors (defined as the ratio of the evidence for the dual point source model to the single point source model) of $\frac{Z_2}{Z_1} = 0.154$ and $\frac{Z_2}{Z_1} = 0.102$ for the 15 ks and 50 ks observations, respectively. This represents a Bayes factor of ≈ 6.5 and ≈ 9.8 in favor of a single point source. The relative magnitudes of the Bayes factor values are not surprising – because the 15 ks observation has fewer counts than the 50 ks observation we expect there to be less evidence in favor of a given model. Indeed, using the definitions presented in Kass & Raftery (1995), both of these Bayes factor values are considered "positive" against the dual point source model. Further, the posterior distributions for θ_2 are consistent across both datasets: the best-fit locations for μ_P and μ_S are consistent with one-another at the 95% confidence interval, and the joint posterior distributions have shapes consistent with a single point source (consistent with the "L" shape seen in Fig. 4.1).

Given that the individual analyses on each dataset favor the same model, and that we can treat the two spectra as the same between 2–7 keV, we increase our statistical power and

combine both datasets. This yields a total of $n = 723$ counts between 2–7 keV. Although we analyze the two observations jointly, we emphasize that the likelihoods for each observation are calculated independently of one another, and are a function of their respective PSF models. Here, $k = 2$ and Δx_1 and Δy_1 are included in parameter vectors for each model. We use `BAYMAX` to calculate a Bayes factor $\frac{Z_2}{Z_1} = 7.40 \times 10^{-2}$. This represents a Bayes factor of $\approx$13.5 in favor of a single point source.

To test the impact of the MCMC nature of nested sampling, we run `BAYMAX` multiple times on the combined datasets. We find consistent results, with a spread in $\ln \mathcal{B}$-space well-described by a Gaussian distribution centered at $\ln \mathcal{B} = 2.6$ with standard deviation of 0.2. *This Bayes factor strongly supports that the single point source model best describes the X-ray emission from SDSS J0914+0853.* In Table 4.2 we list the best-fit values (defined as the median value of the posterior distributions) for parameter vector θ_1.

We examine the posterior distributions for θ_2 to better understand our results. In Figure 4.4 we show the combined 2–7 keV dataset ($\approx$ 65 ks, where the photons associated with the 15 ks exposure have been spatially shifted by the most-likely Δx_1 and Δy_1) with the best-fit x and y sky-coordinates for the primary and secondary AGN (μ_P and μ_S), as well as the joint posterior distribution for the separation, r, and log flux ratio, $\log f$, parameters. Here, $r = \sqrt{(\mu_{x,P} - \mu_{x,S})^2 + (\mu_{y,P} - \mu_{y,S})^2}$. Spatially, the best-fit locations for μ_P and μ_S are consistent with one-another at the 95% confidence interval. Further, the joint posterior distribution has a shape consistent with a point source — the median values of the marginal posterior distributions are $r = 0.15 \pm 0.5$ and $\log f = -1.6 \pm 0.4$, at very large flux ratios ($\log f \to 0$) the separation is consistent with 0, and at very large separations ($r \to 2''$) the flux ratio is consistent with 0. The best-fit values for all the parameters in parameter vector θ_2 are listed in Table 4.2.

We investigate the influence of our prior distributions on our results. In particular, the Bayesian evidence automatically implements Occam's razor — the simpler model will be more easily favored than the more complicated one, unless the latter is significantly better

at explaining the data. For our analysis, this means that the dual point source model needs enough data to overcome the inherent bias that BAYMAX has towards favoring the single point source model. Whenever the prior distribution is relatively broad compared with the likelihood function, the prior has fairly little influence on the posterior. Thus, we re-run BAYMAX with Gaussian prior distributions for μ, μ_P, and μ_S:

$$\mu = \mathcal{N}(\mu_m, \sigma^2), \tag{4.6}$$

where μ_m and σ^2 represent the mean and variance of the distribution. For μ_P and μ_S, we set μ_m to the nominal X-ray positions of the potential primary and secondary AGN and set σ to the observed separation between the two ($\sim 0\farcs3$), given the 15 ks archival observation. For μ we set μ_m to the nominal X-ray position of the AGN, and similarly set σ to $0\farcs3$. BAYMAX calculates a Bayes factor of 10.8 ± 1.2, consistent within the errors of our previous measurement. Further, the posterior distributions returned by BAYMAX are consistent with those listed in Table 4.2. We conclude that using sharper priors (comparable to the sharpness of our likelihoods), has no effect on our results.

4.7 Discussion

Our results support the hypothesis that the low-mass dual AGN candidate SDSS J0914+0853 is instead a single AGN. Individually, we find $\mathcal{B}$ =6.5 and 9.8 in favor of a single point source for the 15 ks and 50 ks observations. When we combine the two datasets for a joint analysis, we find a $\mathcal{B} \sim 13.5$ in favor of a single point source, and the posterior distributions are consistent with this model. Further, the prior distributions do not appear to have a great influence on our posteriors, reflecting that the data should be sufficient to favor the correct model, even when accounting for the Bayesian bias. In the following section we discuss the significance of our results by analyzing BAYMAX's capabilities across a range of parameter space for both the single and dual point source models. Assuming that SDSS J0914+0853

Table 4.2: Posterior Results for θ_1 and θ_2

Parameter (1)	Best-fit Value (2)
Single Point Source Model	
μ_x	4074.6 ± 0.1
μ_y	4063.6 ± 0.1
α	138.70
δ	+8.89
Δx_1	$-14.8'' \pm 0.''1$
Δy_1	$-25.8'' \pm 0.''1$
Δr_1	$29.8'' \pm 0.''1$
Dual Point Source Model	
$\mu_{x,P}$	4074.6 ± 0.1
$\mu_{y,P}$	4063.6 ± 0.1
$\mu_{x,S}$	4074.6 ± 1.5
$\mu_{y,S}$	4063.4 ± 1.5
α_P	138.70
δ_P	+8.89
α_S	138.70
δ_S	+8.89
r	$0.''15 \pm 0.''15$
$\log f$	-1.6 ± 0.4
Δx_1	$-14.8'' \pm 0.''1$
Δy_1	$-25.8'' \pm 0.''1$
Δr_1	$29.8'' \pm 0.''1$

Note. – Columns: (1) Parameters from θ_1: μ_x is the central x sky coordinate of the source, μ_y is the central y sky coordinate of the source, α is the central right ascension of the source in degrees, δ is the central declination of the source in degrees, Δx_1 is the translational astrometric shift in arcseconds, Δy_1 is the translational astrometric shift in arcseconds, and Δr_1 is the radial astrometric shift in arcseconds. Parameters α, δ, and Δr_1 are not fit for by `BAYMAX` but are calculated using μ_x, μ_y, Δx_1, and Δy_1. Parameters from θ_2 are the same as θ_1, where the underscore P refers to the primary and S refers to the secondary. Additionally: r is separation between the two point sources in arcseconds and $\log f$ represents the log of the flux ratio; (2) the best-fit values from the Posterior Distributions, defined as the median of the distribution. All Posterior distributions are unimodal, and thus the median is a good representation of the value with the highest likelihood. Error bars represent the 3σ confidence level of each distribution.

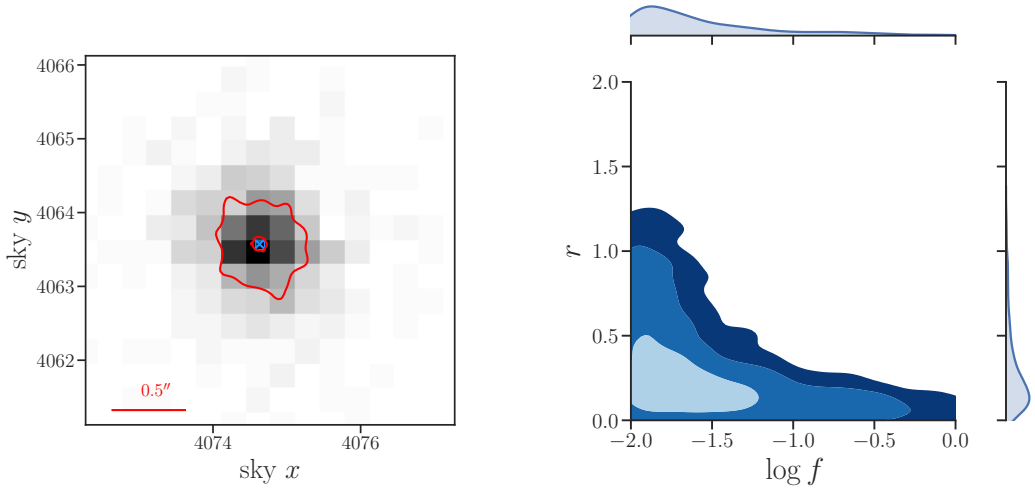

Figure 4.4: The combined 2–7 keV dataset (723 counts) for SDSS J0914+0853, with the best-fit sky x and sky y positions for a primary (μ_P, blue "x") and secondary (μ_S, blue square) AGN (*left*), and the joint posterior distribution (*right*) for the separation r (in arcseconds) and the flux ratio (in units of $\log f$), with the marginal distributions shown along the border. In the left panel, the respective 68% and 95% confidence intervals (red lines), while in the right panel the 68%, 95%, and 99.7% confidence intervals are shown in blue contours. The spatial positions of the primary and secondary AGN are consistent with one-another. At the 99.7% confidence level, SDSS J091449 has a separation and flux ratio consistent with zero. We note that this particular joint-distribution shape is consistent with a single AGN, where at very large flux ratios the system is likely to have $r = 0$, and at very large separations the system is likely to have $\log f = -2$.

is indeed a dual AGN system, we investigate how the Bayes factor determined by BAYMAX depends on parameters r and f. In particular, we aim to understand where in parameter space BAYMAX loses sensitivity for simulations with a comparable number of counts as our observations.

4.7.1 BAYMAX's Sensitivity Across Parameter Space

The first step is to investigate how well BAYMAX can classify a sample of simulated single AGN, i.e., our frequency of false-positives. This measurement will allow us to better define a range of Bayes factors that we can consider "strongly" support the dual point source model. We simulate 100 single AGN via MARX, assuming the same telescope configuration and spectrum as our new dataset. Further, each simulation has 700 photons between 2–7 keV. We analyze each simulation with BAYMAX and find that only 2 are misclassified as a dual AGN with $\mathcal{B} > 3$ (with the largest $\mathcal{B} = 3.5$). Thus, we define a $\mathcal{B} > 3$ in favor of a dual AGN as "strong evidence", while anything below this cut is classified as inconclusive.

We then run BAYMAX on a suite of simulated dual AGN systems, generated via MARX. The simulations were created with the same assumptions as listed above. Each simulation has 700 photons between 2–7 keV, and each simulated AGN has the same 2–7 keV spectrum as SDSS J0914+0853, but with normalizations proportional to their flux ratio. We simulated systems with separations that range between $0\farcs3$–$0\farcs5$ and flux ratios that range between 0.1-1.0. For each r–f point in parameter space, we evaluate 100 simulations with randomized position angles between the primary and secondary. Our results are shown in Figure 4.5, where we plot the logarithm of the mean Bayes factor for each point in parameter space. Consistent with expectations, BAYMAX favors the dual point source model more strongly as the separation and flux ratio of a given dual AGN simulation increases, where we can expect $\mathcal{B} \approx 10^7$ for systems with $r \geq 0\farcs5$. We enforce a cut of $\mathcal{B} > 3$, where only Bayes factors above this value are classified as strongly in favor of the dual point source model. We find that we are sensitive to most flux ratios where $r \geq 0\farcs35$, and for the smallest separations

($r \leq 0\farcs35$) BAYMAX is capable of identifying the correct model when $f \geq 0.8$

4.7.2 A Quasi-Frequentist Approach

Our analysis is intended to be a fully Bayesian inference, however some readers may find a frequenstist interpretation more intuitive. In the following section, we describe a potential interpretation of our results using a quasi-frequentist perspective.

On average, for separations below $0\farcs35$, BAYMAX will not necessarily favor the correct model for a dual AGN system. For SDSS J0914+0853, we estimate a possible separation of $0\farcs3$, given the shallower *Chandra* observation. However, the strength of the Bayes factor in favor of a single AGN has its own significance. From a frequentist perspective, we may ask what is the probability of measuring a $\mathcal{B} \geq 13.5$ in favor of a single AGN *if the system is dual AGN*. In this specific scenario, our "null hypothesis" is that SDSS J0914+0853 is a dual AGN system and our p-value represents the probability of measuring a $\mathcal{B} \geq 13.5$ in favor of a single AGN. Using our suite of dual AGN simulations, we analyze the probability of measuring a $\mathcal{B} \geq 13.5$, as a function of r and f. Across all of parameter space, we find $p \leq 0.05$ and thus reject the null hypothesis at a 95% confidence level. If we set our p-value threshold to $p < 0.03$, we find that only for the smallest flux ratios ($f < 0.2$) can the null hypothesis not be rejected for $r < 0.3$ (see Fig. 4.1). Thus, the probability of SDSS J0914+0853 being a dual AGN system with a (1) flux ratio $f > 0.3$, (2) separation $r > 0\farcs3$, and (3) measured $\mathcal{B} = 13.5$ in favor of a single AGN, is very low.

We find that for observations with 700 counts BAYMAX is sensitive to a large region of r–f parameter space, such that if SDSS J0914+0853 were a dual AGN, we expect different results. Our results and discussion highlight the importance of a robust, quantitative analysis of dual AGN candidates that are classified by their X-ray emission. Most candidate dual AGN are discovered via indirect detection methods, such as narrow-line optical spectroscopy or optical/IR photometry. However, directly detecting the X-ray emission unambigiously associated with a AGN is necessary for confirmation. For candidate AGN with separations

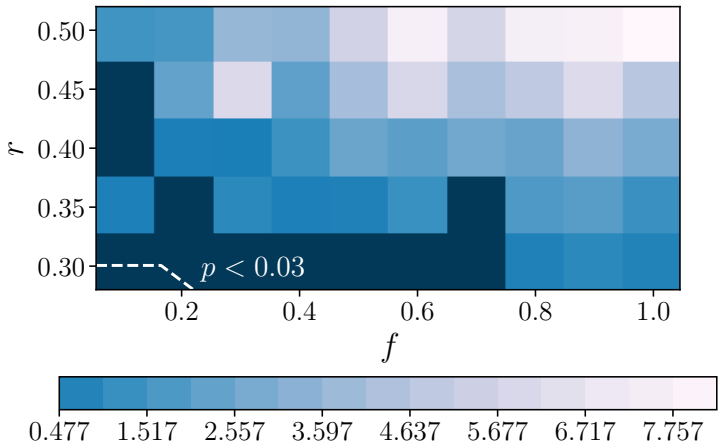

Figure 4.5: Bayes factor (defined as Z_2/Z_1) for simulated dual AGN with varying separation (r, in arcseconds) and flux ratios (f). For each point in parameter space we evaluated 100 simulations with randomized position angles (0-360°) between the primary and secondary AGN. Here we plot the logarithm of the mean Bayes factor for each point in parameter space. We enforce a cut of $\mathcal{B} > 3$, where above this value the Bayes factor is classified as strongly in favor of the dual point source model. Points in parameter space with a Bayes factor below this value are shown in dark blue. For a frequentist perspective, we add a contour (white dashed-line) where dual AGN with f and r values above the region have <3% chance of being classified as a single AGN with $\mathcal{B} \geq 13.5$, while all of parameter space has <5%. Assuming a null hypothesis that SDSS J0914+0853 is a dual AGN, we can reject the null hypothesis (with $p < 0.03$) at $f > 0.2$ for separations as low as $0\farcs3$.

on the order of *Chandra*'s resolution ($< 1''$), receiving observations with sufficient counts, paired with a robust model of the *Chandra* PSF will allow for the most accurate analysis. In particular, we may expect that most dual AGN candidates should have separations $< 1''$, as at a distance of 200 Mpc ($z \approx 0.05$) the physical-to-angular scale becomes 1.0 kpc/arcsec. Given the small number of currently confirmed dual and binary AGN, tools such as `BAYMAX` will be important for a precise measurement of the dual AGN rate, and as a result, an improved physical understanding of the evolution of SMBHs and their activity.

4.8 Conclusions

In this work, we present the first analysis by `BAYMAX`, a tool that uses a Bayesian framework to statistically and quantitatively determine whether a given observation is best de-

scribed by one or two point sources. BAYMAX takes calibrated events from a *Chandra* observation and compares them to simulations based on single and dual point source models. BAYMAX determines the most likely model by the calculation of the Bayes factor, which represents the ratio of the plausibility of the observed data D, given the model M_j and parameterized by the priors. We present the results of BAYMAX analyzing the lowest-mass dual AGN candidate SDSS J0914+0853, which was originally targeted as a dual AGN based on shallow archival *Chandra* imaging. The 15 ks exposure appears to have a secondary AGN $\sim 0\farcs3$ from a primary AGN We received a new 50 ks *Chandra* exposure, with (i) a shorter frame time to avoid pileup and (ii) a different roll angle, with the aim of unambiguously determining the true accretion nature of the AGN. The main results and implications of this work can be summarized as follows:

1. Analyzing our new 50 ks observation, we find (by visual analysis) that the 2–7 keV emission more closely resembles that of a single point source. Both spectra have an excess of flux at soft X-ray energies (< 1 keV) with respect to the power-law continuum, while the 15 ks observation appear to catch the source in a higher flux state in the soft X-ray band. Both of these behaviors are seen in AGN with a "soft excess" component, and we fit our spectra with an absorbed redshifted powerlaw and blackbody (`phabs×zphabs×(zpow + zbbody)`). For the archival dataset, we find best-fit values for intrinsic $N_H = 3.38^{+0.10}_{-0.10} \times 10^{20}$ cm^{-2}, power law component $\Gamma = 2.01^{+0.11}_{-0.12}$; and blackbody component $kT = 0.10^{+0.03}_{-0.05}$ keV. For our new dataset, we find best-fit values for intrinsic $N_H = 4.07^{+0.10}_{-0.10} \times 10^{20}$ cm^{-2}, power law component $\Gamma = 2.51^{+0.10}_{-0.12}$; and blackbody component $kT = 0.11^{+0.05}_{-0.04}$ keV.

2. We find that the 2–7 keV emission is consistent between the two observations, and fit the spectra in this energy-range with an absorbed redshifted powerlaw. For the 15 ks observations we calculate a total observed 2–10 keV flux of $3.20^{+0.90}_{-0.80} \times 10^{-13}$ erg s^{-1} cm^{-2}, while for the 50 ks observation we calculate a total observed 2–10 keV flux of $2.23^{+1.0}_{-0.49} \times 10^{-13}$ erg s^{-1} cm^{-2} s^{-1}. This corresponds to a rest-frame 2–10 keV

luminosity of $1.83^{+0.31}_{-0.40} \times 10^{43}$ erg s^{-1} and $1.25^{+0.35}_{-0.21} \times 10^{43}$ erg s^{-1} at $z = 0.14$ (assuming isotropic emission).

3. We use `BAYMAX` to analyze the 15 ks and 50 ks observations both individually, as well as combined, restricting our analysis to photons with energies between 2–7 keV. Using `BAYMAX` we calculate a Bayes factor in favor of the single point source model of ≈ 6.5 and 9.8 for the 15 ks and 50 ks observations, respectively. When combining the two observations, we calculate a Bayes factor of 13.5 in favor of a single point souce. To test the impact of the MCMC nature of nested sampling, we run `BAYMAX` multiple times on the combined datasets. We find consistent results, with a spread in $\ln \mathcal{B}$-space well-described by a Gaussian distribution centered at $\ln \mathcal{B} = 2.6$ with standard deviation of 0.2.

4. Our posterior distributions for both the single and dual point source model further support that SDSS J0914+0853 is a single AGN. Spatially, the best-fit locations from μ_P and μ_S are consistent with one-another within the 68% error level. Further, the joint posterior distribution has a shape expected from a single point source — the median values of the marginal posterior distributions are $r = 0.15 \pm 0.5$ and $\log f = -1.6 \pm 0.4$, at very large flux ratios ($\log f \to 0$) the separation is consistent with 0, and at very large separations ($r \to 2''$) the flux ratio is consistent with 0.

5. We investigate the influence of our prior distributions, by running `BAYMAX` with Gaussian prior distributions for μ, μ_P, μ_S. `BAYMAX` calculates a Bayes factor in favor of a single point source of 10.8 ± 1.2, consistent within the errors of our initial measurement. Further, the posterior distributions returned by `BAYMAX` are consistent with those listed in Table 4.2.

6. We investigate how the Bayes factor determined by `BAYMAX` depends on the separation and flux ratio of a given dual AGN system. We find that for *Chandra* observations with at least 700 counts between 2–7 keV, `BAYMAX` is capable of strongly favoring the correct

model for most flux ratios when $r \geq 0\farcs35$. For the smallest separations ($r \leq 0\farcs3$), `BAYMAX` is capable of identifying the correct model when the flux ratio $f \geq 0.8$.

7. From a quasi-frequentist perspective, we estimate the probability of measuring a $\mathcal{B} \geq 13.5$ in favor a single AGN, using a null hypothesis that SDSS J0914+0853 is actually a dual AGN. Across all of parameter space ($0\farcs3 < r < 0\farcs5$ and $0.1 < f < 1.0$), we find $p \leq 0.05$ and can reject the null hypothesis at a 95% confidence level. Thus, the probability of SDSS J0914+0853 being a dual AGN system with a (1) flux ratio $f > 0.3$, (2) separation $r > 0\farcs3$, and (3) measured $\mathcal{B} = 13.5$ in favor of a single AGN, is very low.

We have shown through various analyses that there is an absence of evidence supporting SDSS J0914+0853 as a dual AGN system. Specifically, `BAYMAX` estimates a Bayes factor strongly in favor of a single AGN and posterior distributions for a possible separation and flux ratio between a primary and secondary AGN are consistent with 0. Moving forward, statistical analyses with `BAYMAX` on *Chandra* observations of dual AGN candidates will be important for a robust measurement of the dual AGN rate across our visible universe. Lastly, our Bayesian framework will eventually be capable for more general analyses, such as evaluating binary active star systems.

A.F. and K.G. acknowledge support provided by the National Aeronautics and Space Administration through *Chandra* Award Number TM8-19007X issued by the *Chandra* X-ray Observatory Center, which is operated by the Smithsonian Astrophysical Observatory for and on behalf of the National Aeronautics Space Administration under contract NAS8-03060. We also acknowledge support provided by the National Aeronautics and Space Administration through *Chandra* Award Number GO7-18087X issued by the *Chandra* X-ray Observatory Center, which is operated by the Smithsonian Astrophysical Observatory for and on behalf of the National Aeronautics Space Administration under contract NAS8-03060. A.F. thanks Abderahmen Zoghbi for helpful discussion regarding `PyMC3`. This research has made use of

NASA's Astrophysics Data System.

CHAPTER V

A Second Look at 12 Candidate Dual AGN using BAYMAX

5.1 Preface

Results in this chapter were published in: *Foord, A., et. al 2020. A Second Look at 12 Candidate Dual AGN using* BAYMAX. *The Astrophysical Journal, Volume 892, Issue 1, id. 29* and are reproduced here with minor style revisions by permission of the American Astronomical Society under the non-exclusive right of republication granted to authors.

5.2 Abstract

We present an analysis of 12 optically selected dual AGN candidates at $z < 0.34$. Each candidate was originally identified via double-peaked [O III] λ5007 emission lines, and have received follow-up *Chandra* and *HST* observations. Because the X-ray data are low-count (< 100 counts) with small separations ($< 1''$), a robust analysis is necessary for classifying each source. Pairing long-slit [O III] observations with existing *Chandra* observations, we re-analyze the X-ray observations with BAYMAX to determine whether the X-ray emission from each system is more likely a single or dual point source. We find that 4 of the 12 sources are likely dual X-ray point source systems. We examine each point source's spectra via a Monte Carlo method that probabilistically identifies the likely origin of each photon.

When doing so, we find that (i) the secondary X-ray point sources in 2 of the systems have $L_{\rm X} < 10^{40}$ erg s^{-1}, such that we cannot rule out a non-AGN origin, (ii) one source has a secondary with $L_{\rm X} > 10^{40}$ erg s^{-1} but a spectrum that is too soft to definitively preclude being X-ray emitting diffuse gas that was photoionized by the primary AGN, and (iii) one system (SDSS J1126+2944) is a dual AGN. Additionally, using complementary *HST* observations, we analyze a sub-sample of systems that are visually identified as merging. Our results suggest that dual AGN may preferentially reside in mergers with small separations, consistent with both simulations and observations.

5.3 Introduction

Dual Active Galactic Nuclei (AGN) are systems comprised of two actively accreting supermassive black holes (SMBHs) whose host galaxies are in the process of merging. Given that all massive galaxies are likely to have a central supermassive black hole (Kormendy & Richstone 1995), dual SMBHs are thought to be a natural consequence of hierarchical galaxy formation (e.g., White & Rees 1978). Dual SMBH systems represent the earliest stages of the merger, where the SMBHs are at kiloparcsec separations and not yet gravitationally bound (see, e.g., Begelman et al. 1980). As the system loses energy through dynamical friction, the separation between the two SMBHs decreases with time as both sink towards the center of the gravitational potential-well.

Whether or not galaxy–galaxy interactions trigger accretion onto the central SMBHs remains a topic of debate. Similar-mass (with mass ratios >1:4), gas-rich galaxy mergers have been shown to provide a favorable environment for the assembly of AGN pairs (e.g., Volonteri et al. 2003; Hopkins et al. 2005; Di Matteo et al. 2005) and this hypothesis has been supported by studies of nearby galaxies (e.g., Koss et al. 2010; Ellison et al. 2017; Satyapal et al. 2014; Goulding et al. 2018). However, other studies that target higher-redshift ($z > 1$) galaxies over a wide range of AGN luminosity conclude there is no special relation between SMBH activity and host galaxy interactions (e.g., Cisternas et al. 2011; Kocevski et al. 2012;

Schawinski et al. 2012; Villforth et al. 2014). It is likely that these contradictory results are due to the variability of the AGN activity during the lifetime of the merger (Goulding et al. 2018), as the AGN may not be 'on' during the entire merger event. In this framework, the probability of AGN observability should increase as a function of decreasing separation, which has been supported by both simulations and observations (e.g. Koss et al. 2012; Blecha et al. 2013; Ellison et al. 2013; Goulding et al. 2018; Capelo et al. 2017; Barrows et al. 2017a).

Understanding which environmental factors are most important for dual SMBH activity allows for a better understanding about black hole growth and its relation (or lack thereof) to galaxy–galaxy interactions. Additionally, as progenitors to SMBH mergers, the rate of dual AGN has implications for the rate of expected gravitational wave events that will be detected by pulsar timing arrays (e.g., Mingarelli 2019) and future space-based interferometry.

There exist many multi-wavelength techniques to detect dual AGN candidates, each with their own caveats. The most popular technique is to use optical spectroscopy to search for double-peaked narrow line emission regions (which can sometimes be spatially resolved; see, e.g., Zhou et al. 2004; Gerke et al. 2007; Comerford et al. 2009; Liu et al. 2010a; Fu et al. 2012; Comerford et al. 2012, 2013; Barrows et al. 2013). Dual AGN systems can display two sets of narrow line emission regions, such as [O III] λ5007, during the period of the merger when their narrow line regions (NLRs) are well separated in velocity. Here, the separation and width of each peak will depend on parameters such as the distance between the two AGN. However, double-peaked emission features are known to originate from other processes, such as bipolar outflows and rotating disks (Greene & Ho 2005; Rosario et al. 2010; Müller-Sánchez et al. 2011; Smith et al. 2012; Nevin et al. 2016).

Thus, confirmation of dual AGN systems requires spatially resolving each individual AGN; beyond $z > 0.05$ high-resolution imaging is necessary, which can be accomplished with both radio or X-ray observations. Radio observations can resolve radio-emitting cores on the smallest spatial scales (see Rodriguez et al. 2006; Rosario et al. 2010; Tingay & Wayth

2011; Fu et al. 2011, 2015; Deane et al. 2014; Gabányi et al. 2014; Wrobel et al. 2014a,b; Müller-Sánchez et al. 2015; Kharb et al. 2017), however this technique is only efficient for radio-loud AGN ($\approx 15\%$ of the AGN population; Hooper et al. 1995), and AGN can only be differentiated from jet components at radio frequencies if they are compact and have flat or inverted spectral indices (see, e.g., Burke-Spolaor 2011; Hovatta et al. 2014). Indeed, this is further complicated by the fact that regions of intense starbursts can mimic both compactness and brightness temperatures of AGN; thus complementary IR data may be necessary to properly classify the source (see, e.g., Varenius et al. 2014)

A more efficient method is to use X-ray observations taken with the *Chandra X-ray Observatory* (*Chandra*). X-rays are one of the most direct methods of finding black holes, as AGN are one of the few sources that emit at X-ray luminosities above 10^{40} erg s^{-1} (Lehmer et al. 2010, 2019). However, the detection of the most closely separated pairs is limited by the instrument's Point Spread Function (PSF). Even with *Chandra*'s superior angular resolution (where the half-power diameter of *Chandra*'s Advanced CCD Imaging Spectrometer, ACIS, is $\sim 0\farcs8$ at $\sim$1 keV), systems with physical separations less than 1 kpc become difficult to resolve beyond $z \geq 0.05$.

Currently, many analyses on *Chandra* observations of dual AGN candidates implement the Energy-Dependent Subpixel Event Respositioning (EDSER) algorithm (Li et al. 2004). EDSER reduces photon impact position uncertainties to subpixel accuracy, and in combination with *Chandra*'s dithering can resolve sub-pixel structure down to the limit of the *Chandra* High Resolution Mirror Assembly. However, without a robust and statistical approach to analyze the *Chandra* observations, the interpretation of dual AGN with separations $< 1''$ can lead to false negatives and false positives, even after undergoing EDSER reprocessing. This issue is amplified in the low-count regime (< 100 counts), where even dual AGN with large separations are difficult to identify.

As a result, very few dual AGN have been confirmed to date, with the majority of systems at separations > 1 kpc. (see Deane et al. 2014). Thus, we have developed a `PYTHON`

tool BAYMAX (**B**ayesian **A**nal**Y**sis of **A**GNs in **X**-rays) that allows for a rigorous analysis of whether a source in a given *Chandra* observation is more likely composed of one or two X-ray point sources (see Foord et al. 2019). BAYMAX is capable of detecting dual X-ray point source systems for systems with low flux ratios between the primary and secondary, as well for systems with angular separations smaller than *Chandra*'s half-power diameter.

In this chapter we present an analysis of 12 optically selected dual AGN candidates that have existing archival *Chandra* data. The *Chandra* observations of these 12 targets were originally analyzed in Comerford et al. (2015), using a simpler PSF model and source identifier technique. Using this approach, one of the twelve systems was classified as a likely dual AGN (Comerford et al. 2015). We now re-analyze the *Chandra* observations using BAYMAX, with the goal of identifying other dual AGN systems using a robust statistical analysis. Combining the X-ray observations with archival *Hubble Space Telescope* (*HST*) and *Wide-field Infrared Survey Explorer* (*WISE*) observations, we aim to learn more about the preferential environments of each dual AGN candidate.

The remainder of the chapter is organized into 5 sections. In section 5.4 we introduce the sample and the existing multi-wavelength coverage. In section 5.5 we review Bayesian inference, Bayes factor and how BAYMAX calculates the likelihoods. In section 5.6 we present our results from running BAYMAX on the *Chandra* observations, review the best-fit parameters for each model, and quantify the strength of each result. In section 5.7 we discuss the nature of each dual AGN candidate by evaluating the spectral fits and discussing possible sources of contamination. In section 5.8 we discuss the sensitivity and limitations of BAYMAX across parameter space, and compare environmental properties between the dual AGN candidates and the single AGN candidates. Lastly, we summarize our findings in section 5.9. Throughout the chapter we assume a ΛCDM universe, where $H_0 = 69.6$, $\Omega_M = 0.286$, and $\Omega_\Lambda = 0.714$

Table 5.1: Galaxy Sample Properties

Galaxy Name	Redshift	D_A (Mpc)	*Chandra* Obs. ID	*Chandra* Exp. Time (s)	*HST*
(1)	(2)	(3)	(4)	(5)	(6)
SDSS J014209.01−005050.0	0.133	490.8	13959	19804	Yes
SDSS J075223.35+273643.1	0.069	273.8	12826	29650	No
SDSS J084135.09+010156.2	0.111	419.9	13950	19801	Yes
—	—	—	18199	21940	—
SDSS J085416.76+502632.0	0.096	369.4	13956	20078	Yes
SDSS J095207.62+255257.2	0.339	1007.0	13952	19807	Yes
SDSS J100654.20+464717.2	0.123	459.0	13957	19783	Yes
SDSS J112659.54+294442.8	0.102	389.8	13955	19798	Yes
SDSS J123915.40+531414.6	0.201	688.6	13953	19804	Yes
SDSS J132231.86+263159.1	0.144	524.9	13958	19807	Yes
SDSS J135646.11+102609.1	0.123	459.0	13951	19804	Yes
—	—	—	17047	34840	—
—	—	—	18826	42870	—
SDSS J144804.17+182537.9	0.038	156.4	13954	19807	Yes
SDSS J160436.21+500958.1	0.146	531.1	12827	29582	No

Note. – Columns: (1) SDSS galaxy designation; (2) redshift; (3) angular diameter distance; (4) *Chandra* Observation ID; (5) exposure time of *Chandra* observation; (6) *HST*/WFC3 data available.

5.4 Sample

The sample of galaxies studied in this chapter was created from a larger parent sample of 340 AGN, which all have double-peaked narrow emission lines identified via the Sloan Digital Sky Survey (SDSS; Wang et al. 2009; Liu et al. 2010b; Smith et al. 2010). Using follow-up long-slit spectroscopy with the Lick 3 m telescope; the Apache Point Observatory 3.5 m telescope; the Palomar 5 m telescope; the MMT 6.5 m telescope; and the Magellan II 6.5 m telescope, galaxies were chosen if their [O III] λ5007 emission components were separated by $\Delta x_{[\mathrm{O\ III}]} > 0\farcs75$ (Greene et al. 2011; Shen et al. 2011; Comerford et al. 2012), making them more easily resolved by *Chandra*. The sample was further filtered by enforcing a 2–10 keV flux limit of $F_{2-10} > 8 \times 10^{-15}$ erg cm^{-2} s^{-1}, where F_{2-10} was estimated using the [O III] λ5007 fluxes (Heckman et al. 2005). For more details regarding the [O III] λ5007 data analysis and sample cuts, we refer the reader to Comerford et al. (2015) and references therein.

Ultimately, the final sub-sample is composed of 13 galaxies, each of which received *Chan-*

dra observations over two separate programs (GO1-12142X, PI: Gerke; GO2-13130X, PI: Comerford). The analysis of one of these galaxies, SDSS J171544.05+600835.7, was presented in Comerford et al. (2011), where they confirm that the system is likely a dual AGN. The *Chandra* observations of the 12 remaining systems were analyzed in Comerford et al. (2015), where 1 of the 12 systems (SDSS J112659.54+294442.8, hereafter SDSS J1126+2944) was classified as a dual AGN. Here, we re-visit the 12 galaxies presented in Comerford et al. (2015); using `BAYMAX` we aim to (i) identify new dual X-ray point sources and (ii) re-evaluate the true nature of SDSS J1126+2944. The galaxies are located at redshifts $0.04 < z < 0.34$, and two of them are classified as Type 1 AGN by their SDSS spectra (SDSS J095207.62+255257.2 and SDSS J123915.40+531414.6, hereafter SDSS J0952+2552 and SDSS J1239+5314) while the others are classified as Type 2 AGN. In addition to *Chandra* data, 11 of the galaxies were also observed with multiband HST/WFC3 imaging to examine the host galaxies (see Comerford et al. 2015). For more information about each source, please see Table 5.1.

5.4.1 X-ray Data Analysis

For each galaxy, the *Chandra* exposure times were chosen such that both AGN in a given dual AGN candidate should have at least 15 counts. They were observed with over the course of two programs, GO1-12142X (PI: Gerke) and GO2-13130X (PI: Comerford). We looked for additional archival *Chandra* observations for these targets, and found them for SDSS J084135.09+010156.2 (hereafter SDSS J0841+0101; PI: Satyapal) and SDSS J135646.11+102609.1 (hereafter SDSS J1356+1026; PI: Greene). Incorporating these newer observations (see Section 5.5) increases the total number of counts to analyze and gives `BAYMAX` greater sensitivity across parameter space.

Each galaxy observation was on-axis and placed on the back-illuminated S3 chip of the ACIS detector. We follow a similar data reduction as described in previous *Chandra* analyses on AGN (e.g., Foord et al. 2017a,b, 2019), using *Chandra* Interactive Analysis of Observations

(CIAO) v4.8 (Fruscione et al. 2006). Further, all observations are reprocessed with EDSER.

We first correct for astrometry, cross-matching the *Chandra*-detected point-like sources with the SDSS Data Release 9 (SDSS DR9) catalog. The *Chandra* sources used for cross-matching are detected by running wavdetect on the reprocessed level-2 event file. We require each observation to have a minimum of 3 matches with the SDSS DR9, and each matched pair to be less than $2''$ from one another. Each galaxy meets the criterion for astrometrical corrections, and the resultant astrometric shifts are shift less than $0''.5$. Background flaring is deemed negligible for each observation, as there are no time intervals where the background rate is 3σ above the mean level. We then rerun wavdetect to generate a list of X-ray point sources. For each observation, wavdetect identifies an X-ray point source coincident with the SDSS-listed optical center.

5.5 Methods

BAYMAX uses a Bayesian approach to analyze a given *Chandra* observation and estimate the likelihood that is it better described by one or multiple point sources. In the following section we review BAYMAX's capabilities with regards to our 12 specific systems. In general, however, BAYMAX is flexible to include other models and/or prior distributions. For a more detailed review on the statistical techniques behind BAYMAX's calculations, please see Foord et al. (2019).

5.5.1 Bayesian Inference

In order to determine the likelihood of a dual X-ray point source, BAYMAX calculates the Bayes factor ($\mathcal{B}$). The Bayes factor represents the ratio of the marginal probability density of the observed data D under one model, to the marginal density under a second model. Here, each model is parameterized by a parameter vector, θ. For our analyses on dual AGN candidates, the two models are a dual point source model (M_2) vs. a single point source

Table 5.2: Symbols

Symbol (1)	Definition (2)
(x_i, y_i)	Sky coordinate of photon i
E_i	Energy of photon i, in keV
n	Total counts of given source
μ	Central position of given point source in sky coordinates (2D; $\mu = [\mu_x, \mu_y]$)
k	Number of *Chandra* observations being modeled
Δx_K	Translational astrometric shift in x ($K = [1, \ldots, k-1]$)
Δy_K	Translational astrometric shift in y
f_{BG}	Total count ratio between a given background component and the point source components
M_j	Given model being analyzed by `BAYMAX`
θ_j	Parameter vector for M_j, i.e. [μ, f, f_{BG}, Δx_K, Δy_K] .

Note. – Columns: (1) symbols used throughout the text; (2) definitions.

model (M_1):

$$\mathcal{B} = \frac{\int P(D \mid \theta_2, M_2) P(\theta_2 \mid M_2) d\theta_2}{\int P(D \mid \theta_1, M_1) P(\theta_1 \mid M_1) d\theta_1} \tag{5.1}$$

Because we are assuming that M_2 and M_1 are a priori equally probable, Bayes factor directly represents the posterior odds (see Foord et al. 2019 for a more rigorous mathematical proof). Bayes factor values >1 or <1 signify whether M_2 or M_1, respectively, is more likely (however, see Section 5.8 where we analyze false positive space to define a "strong" Bayes factor). Below we go into brief detail regarding the steps required to calculate two main components of the Bayes Factor: the likelihood densities ($P(D \mid \theta_j, M_j)$) and the prior densities ($P(\theta_j \mid M_j)$). In Table 5.2 we list important symbols that will be referenced in the following Section.

5.5.2 Modeling the PSF and Estimating the Likelihood Density

BAYMAX compares calibrated events (x_i, y_i, E_i) from EDSER-reprocessed *Chandra* observations to simulations of single and dual point sources that are based on the *Chandra* PSF. We simulate and model the PSF for each observation individually using the Model of AXAF Response to X-rays (`MARX`, Davis et al. 2012). `MARX` simulates the *Chandra* PSF of the optics from the High Resolution Mirror Assembly (HRMA), which is characterized by various parameters such as the source spectrum, the time of observation (`TSTART`), the nominal position of the detector during the observation (`RA_Nom, Dec_Nom, Roll_Nom`), and

the detector (ACIS-S). Thus, for any source with multiple observations (SDSS J0841+0101 and SDSS J1356+1026), the PSF is simulated and modeled for each observation individually.

For each observation, we use `MARX` to simulate X-ray photons incident from a single point source centered on the observed central position of the AGN, $\mu_{\rm obs}$. Although the shape of the PSF is energy-dependent, the x, y position of a photon with energy E does not depend on the spectral shape of a given source. Thus, our simulated PSF is independent of the spectral shape of our model. In order to robustly model the PSF, we generate 1×10^6 rays for each observation; here we exclude the simulated read-out strip provided by `MARX` by setting the parameter `ACIS_Frame_Transfer_Time` to 0. The PSF is modeled as a summation of three circular concentric 2D Gaussians, where the amplitude and standard deviation of each Gaussian is energy-dependent. In past analyses, we have found that this model is a good approximation of the on-axis *Chandra* PSF (Foord et al. 2019).

Each photon is presumed to originate from (i) a point source or (ii) a background component. Regarding the single point source model: given a PSF centered at μ, the probability that a photon is observed at sky coordinates x_i,y_i with energy E_i is $P(x_i, y_i \mid \mu, E_i)$. Similarly for the dual point source model, given the sky coordinates of a primary and secondary AGN (μ_P and μ_S), the probability that a photon is observed at sky coordinates x_i,y_i with energy E_i is $P(x, y \mid \mu_P, \mu_S, E, n_S/n_P)$. Here $n_S/n_P = f$, which represents the ratio of the total counts between the secondary and primary AGN, where $0 \leq f \leq 1$ (see Table5.2.)

There are several possible sources of X-ray contamination, including the Cosmic X-ray Background (CXB, which includes unresolved X-ray point sources such as background AGN), the non-X-ray background (NXB, caused by charged particles and γ-rays), and local, diffuse, X-ray emission. There are many possible origins of local diffuse emission, which should be individually determined for a given system (see Section 5.7.4). For the analysis presented in the chapter, `BAYMAX` fits for two different backgrounds: a lower count-rate component that represents the CXB and NXB, and a higher count-rate component that represents diffuse X-ray emission. This latter component is appropriate for merging systems, where extended

gas is frequently detected in both simulations and observations (see, e.g., Cox et al. 2006; Brassington et al. 2007; Sinha & Holley-Bockelmann 2009; Hopkins et al. 2013; Smith et al. 2018), and is evident in the *HST* observations of 2 of our 12 sources (see Fig. 5.1). We assume that photons originating from the background are uniformly distributed across a given region, such that the probability that a photon observed at location x_i,y_i on the sky with energy E_i is associated with a background component is $P(x_i, y_i \mid f_{BG}, E_i)$. Here, f_{BG} represents the ratio of counts between a given background component and the combined counts from all point source components. Because we assume that each background component is uniformly distributed, $P(x_i, y_i \mid f_{BG}, E_i)$ is always constant over a given region of interest.

As an example, given n observed events, the likelihood density for the single point source model is:

$$\begin{aligned} \mathcal{L} = P(x, y \mid \mu, f_{BG}, E) &= \prod_{i=1}^{n} P(x_i, y_i \mid \mu, E_i) + P(x_i, y_i \mid f_{BG}, E_i) \\ &= \prod_{i=1}^{n} \frac{M_{1,i}(\theta_1)^{D_i}}{D_i!} \exp(-M_{1,i}(\theta_1)), \end{aligned} \tag{5.2}$$

Here, the total probability is normalized by f_{BG}, such that the combined probability for each detected photon equals one. Given our PSF model, the probability for event i is $M_{1,i}(\theta_1)$, while D_i is the event's data value. Due to *Chandra* registering each event individually, we use Poisson likelihoods.

5.5.3 Prior Distributions

The parameter vectors for each model, for a given source, will depend on (i) the number of observations and (ii) the prior distributions for each parameter. Regarding point (i), 10/12 galaxies have $k = 1$ observations, while SDSS J0854+0101 has $k = 2$ and SDSS J1356+1026 has $k = 3$. Thus, for the majority of our sample the parameter vectors for M_1 and M_2 are $\theta_1 = [\mu, \log f_{BG}]$ and $\theta_2 = [\mu_P,\ \mu_S, \log f, \log f_{BG}]$. For SDSS J0854+0101 and SDSS J1356+1026, θ_1 and θ_2 also include $\Delta x_K, \Delta y_K$, which account for the translational

components of the relative astrometric registration for the $K = [1, ..., k-1]$ observation (see Table 5.2).

Regarding point (ii), any user-defined function can be used to describe the prior distributions for each parameter. We use continuous uniform distributions to describe the prior distributions of μ, where the bounds of the distribution are determined by the spectroastrometric [O III] λ5007 observations (see Section 5.6). The prior distribution for $\log f_{BG}$ is described by a Gaussian distribution, $N(\mu_{BG},\sigma^2_{BG})$, where μ_{BG} is estimated for each observation by selecting 10 random and source-free regions with a $2''$ radius and within a $20''\times20''$ region centered on the AGN. We set σ_{BG} to 0.5, allowing for `BAYMAX` to more easily move around parameter space.

For M_2, the prior distribution for $\log f$ is described by a uniform distribution, bound between -2 and 0. Regarding SDSS J0841+0101 and SDSS J1356+1026, the prior distributions of Δx_K and Δy_K are described by uniform distributions bound between $\delta\mu_{\rm obs} - 3$ and $\delta\mu_{\rm obs} + 3$, where $\delta\mu$ represents the difference between the observed central X-ray coordinates of the longest observation (Obs ID:18199 for SDSS J0841+0101 and Obs ID: 18826 for SDSS J1356+1026) and the $K = [1, ..., k-1]$ observation.

5.5.4 Calculation of Bayes Factor

In this section we briefly review how `BAYMAX` implements model selection and parameter estimation, but refer the reader to Foord et al. (2019) for more details.

For model selection, `BAYMAX` uses a sampling technique called nested sampling (Skilling 2004), which efficiently samples through likelihood space to estimate the marginal likelihood, usually referred to as the Bayesian evidence and denoted by Z (where $Z = \int P(D \mid \theta_j, M_j)P(\theta_j \mid M_j)d\theta_j$; see Skilling 2004, Shaw et al. 2007, Feroz & Hobson 2008, and Feroz et al. 2009 for more details.) In particular, `BAYMAX` uses the `PYTHON` package `nestle`,[1] which can estimate Z on the order of minutes for low-count (< 100) observations. For parameter

[1] https://github.com/kbarbary/nestle

estimation `BAYMAX` uses `PyMC3` (Salvatier et al. 2016), which uses a Hamiltonian Monte Carlo (HMC) sampling method to much more quickly converge than normal Metropolis-Hastings sampling.

The calculation of the Bayes factor and the estimations of the posterior distributions are separated into two different processes, allowing the user flexibility to only estimate posteriors for sources of interest (i.e., that have Bayes factors that favor the dual point source model). In general, nested sampling iterates through likelihood space in a coarser fashion and is a much faster calculation, as the maximum value in likelihood space only needs to be within the region where the points are sampled (as nested sampling is calculating an integral). While the Bayes factor calculations take on the order of minutes, PyMC3 calculations (where the main goal is indeed to find the maximum likelihood) will take on the order of hours (for > 100 counts).

For unimodal posterior distributions, the posterior distributions returned by nestle and PyMC3 are generally consistent. In particular, for each source in our sample that we analyze with PyMC3, we find that nestle returns posteriors with consistent median values (at the 68% confidence level), although the nestle posteriors are broader, a result of coarser sampling.

5.6 Results

For each observation, we restrict our analysis to photons with energies between 0.5–8 keV. We analyze the photons contained within square regions that are centered on the nominal X-ray coordinates of the AGN, $\mu_{\rm obs}$. The length of each square is defined as $l_{\rm box}$, where $l_{\rm box}$ varies between 10 and 32 sky-pixels for each observation ($4.95''$ and $15.84''$, respectively. See Figure 5.1). The known asymmetric *Chandra* PSF feature is within this extraction region (Juda & Karovska 2010), and sits approximately $0\farcs7$ from the center of the AGN. Because our PSF model does not take into account this asymmetry, we mask the feature in all exposures before running `BAYMAX`.

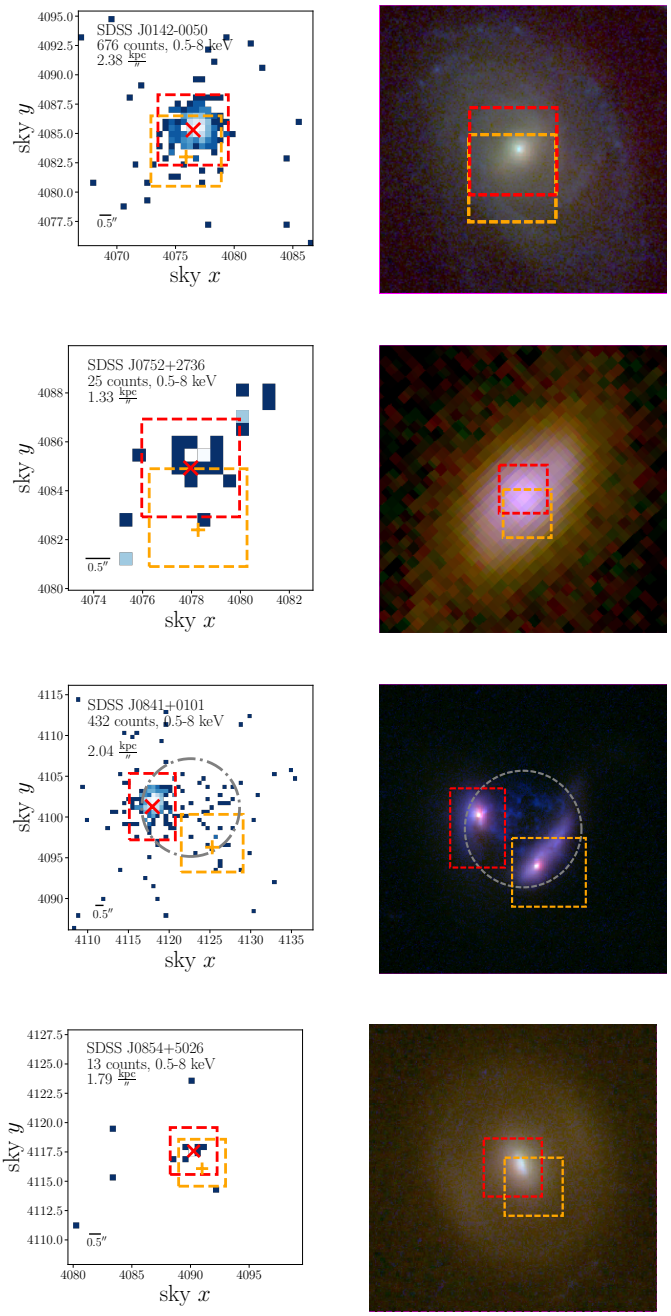

Figure 5.1: *Chandra* 0.5–8 keV observations of each candidate dual AGN (left) and corresponding combined optical observations of the same field-of-view (right). In each X-ray image we mark the location of each [O III] λ5007 emission component with a red "x" and an orange "+". We show the sky x, sky y region, within which the informative priors for μ are constrained to in red and orange boxes. When using non-informative priors, the central locations for the primary and secondary are allowed to be anywhere within the image. For SDSS J0841+0101 we denote the region within which the diffuse emission background component is restricted to with a gray box. Additionally, for SDSS J0841+0101 we show the combined X-ray emission for all *Chandra* observations, where we use the best-fit astrometric shift values as found by `BAYMAX`. The X-ray images have been binned to *Chandra*'s native pixel resolution; all images are scaled in log-space with minimum and maximum counts/bin as follows: SDSS J0142−0050 (min=1, max=92), SDSS J0752+2736 (min=1, max=3), SDSS J0841+0101 (min=1, max=24), SDSS J0854+5026 (min=1, max=2). All the optical images are combined *HST* images, with the exception of SDSS J0752+2736, which is an SDSS gri color composite image. For the *HST* images, we combine the F160W (red), F814W (green), and F438W (blue), with the exception of J1604+5009 (red: F105W; green: F621M; blue: F547M; GO 12521, PI: Liu). In all panels, north is up and east is to the left, and a 0.″5 bar is shown to scale.

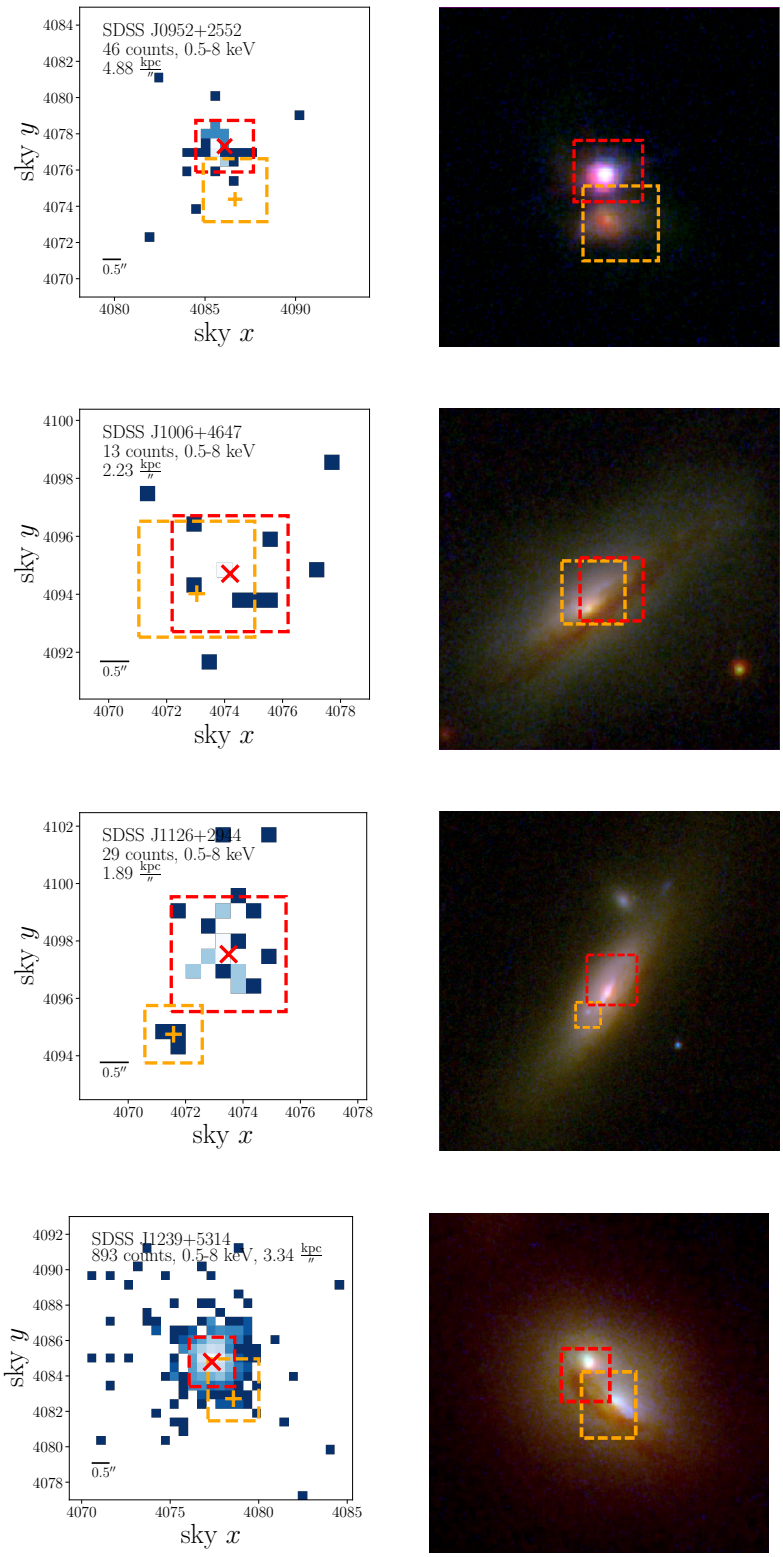

Figure 5.2: All images are scaled in log-space with minimum and maximum counts/bin as follows: SDSS J0952+2552 (min=1, max=8), SDSS J1006+4647 (min=1, max=3), SDSS J1126+2944 (min=1, max=3), SDSS J1239+5314 (min=1, max=147).

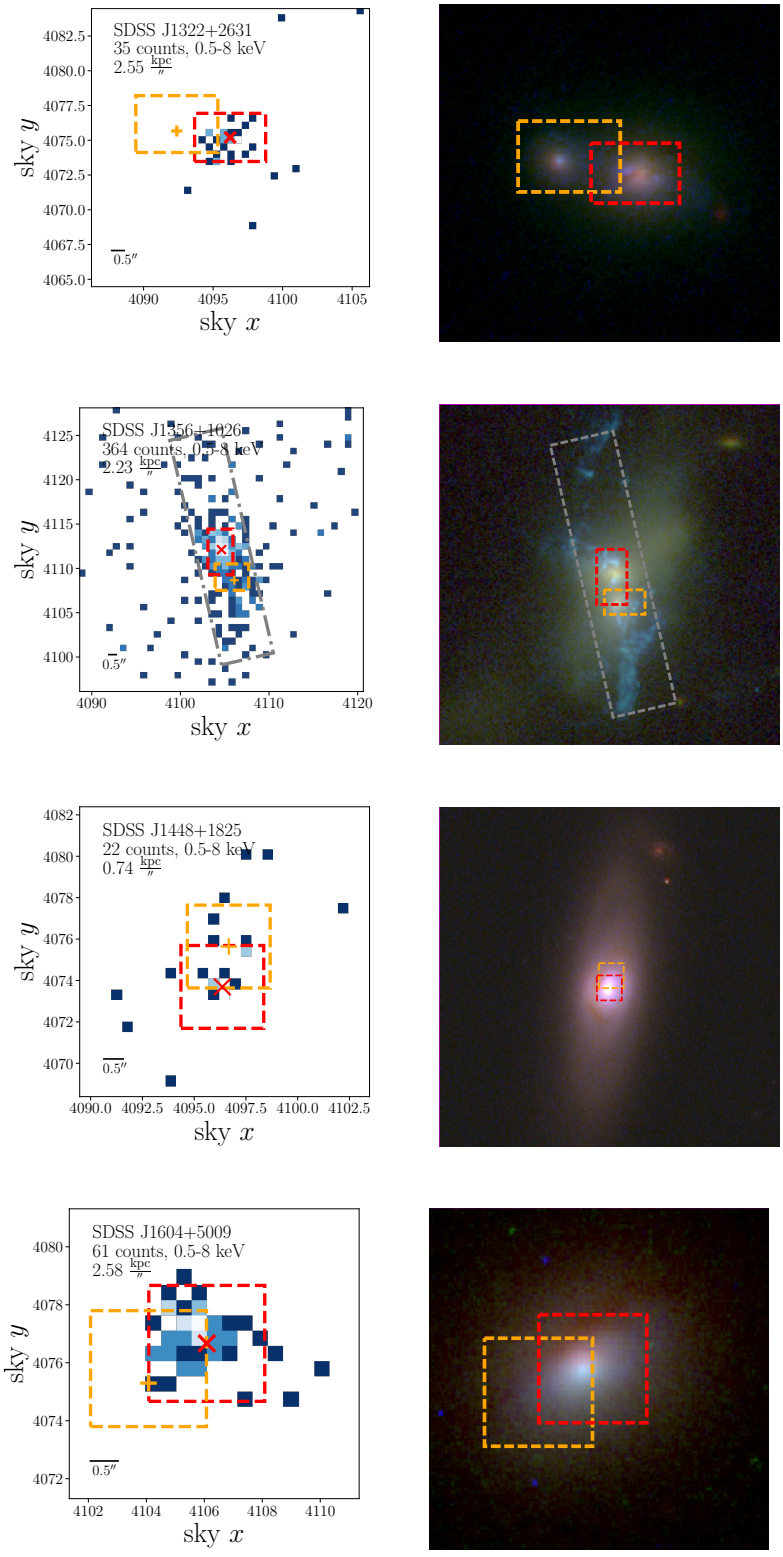

Figure 5.3: Similar to SDSS J0841+0101, for SDSS J1356+1026 we denote the region within which the diffuse emission background component is restricted to with a gray box. Additionally, we show the combined X-ray emission for all *Chandra* observations, where we use the best-fit astrometric shift values as found by `BAYMAX`. All images are scaled in log-space with minimum and maximum counts/bin as follows: SDSS J1322+2631 (min=1, max=4), SDSS J1356+1026 (min=1, max=24), SDSS J1448+1825 (min=1, max=3), SDSS J1604+5009 (min=1, max=6).

Table 5.3: Bayes Factor Results

Galaxy Name	non-informative $\ln \mathcal{B}$	informative $\ln \mathcal{B}$
(1)	(2)	(3)
SDSS J0142−0050	-3.14 ± 0.76	-1.46 ± 0.71
SDSS J0752+2736	4.90±0.51	0.25±0.43
SDSS J0841+0101	9.97±0.75	5.91±0.78
SDSS J0854+5026	0.26±0.59	0.18±0.37
SDSS J0952+2552	0.52±0.38	-0.83 ± 0.35
SDSS J1006+4647	0.47±0.40	0.41±0.63
SDSS J1126+2944	1.50±0.41	3.54±0.43
SDSS J1239+5314	-3.36 ± 0.85	-3.43 ± 0.50
SDSS J1322+2631	0.36±0.62	-0.91 ± 0.40
SDSS J1356+1026	41.65±0.65	34.78±0.70
SDSS J1448+1825	1.43±0.55	2.95±0.52
SDSS J1604+5009	-0.45 ± 0.50	-0.83 ± 0.49

Galaxy Name	$\ln \frac{Z_{1,\mathrm{D}}}{Z_1}$	$\ln \frac{Z_{2,\mathrm{D}}}{Z_2}$	$\ln \mathcal{B}_{\mathrm{D}}$
(1)	(2)	(3)	(4)
SDSS J0841+0101	139±0.75	148±0.71	-2.62±0.65
SDSS J1356+1026	264±0.75	238±0.79	8.70±0.70

Top. – Columns: (1) SDSS galaxy designation; (2) $\ln \mathcal{B}$ values, defined as Z_2/Z_1, using non-informative priors on the location of μ; (3) $\ln \mathcal{B}$ values, defined as Z_2/Z_1, using informative priors on the location of μ.
Bottom. – Columns: (1) SDSS galaxy designation; (2) $\ln \frac{Z_{1,\mathrm{D}}}{Z_1}$, using informative priors; (3) $\ln \frac{Z_{2,\mathrm{D}}}{Z_2}$, using informative priors; (4) $\ln \mathcal{B}_{\mathrm{D}}$, defined as $Z_{2,\mathrm{D}}/Z_{1,\mathrm{D}}$, using informative priors

5.6.1 Bayes Factor Results

For each galaxy, we first run `BAYMAX` using one background component (which accounts for the emission associated with the CXB and unresolved X-ray point sources) and non-informative priors, e.g., the prior distributions for μ are uniform distributions bound between $\mu_{\mathrm{obs}} - \frac{l_{\mathrm{box}}}{2}$ and $\mu_{\mathrm{obs}} + \frac{l_{\mathrm{box}}}{2}$. We then run `BAYMAX` using informative priors, where the distributions for μ are constrained by and centered on the spatial position of the [O III] λ5007 components (see Figure 5.1). Here, the sky x and sky y limits of each prior distribution were determined by visually identifying where one may expect a galactic nucleus via the optical observations. Lastly, we note that our prior distributions for μ are wide enough to account for the relative astrometric shifts between the *Chandra* and optical observations ($> 1''$, see Comerford et al. 2015).

To test the impact of the MCMC nature of nested sampling, we run BAYMAX 100 times on each dataset. The spread of the $\ln \mathcal{B}$ values are well-described by a Gaussian, and error bars are defined by the best-fit standard deviation. In Table 5.3 we list the various $\ln \mathcal{B}$ values for each of the 12 systems. Here $\ln \mathcal{B}$ is defined as the logarithm ratio of the evidence for the dual point source model to the single point source model (i.e., Z_2/Z_1). Thus, values that are less than 0 are systems that are better described by the single point source model.

5.6.2 Adding an Extended Background Emission Component

We more closely analyze the 5 systems that have $\ln \mathcal{B}$ greater than 0 in favor of the dual point source model. Two of these galaxies, SDSS J0841+0101 and SDSS J1356+1026, show evidence for extended emission in the *HST* F438W filter. Because our background model is spatially uniform, we are assuming a constant background rate across the entire image. With this current model, it is possible that a region of background with a higher count-rate can be mistaken for a resolved point source sitting among a background with a lower count rate. Although multiple analyses on SDSS J0841+0101 have concluded that the emission is consistent with two point sources (Comerford et al. 2015; Pfeifle et al. 2019a, in addition to our analysis of two point sources and uniform background without additional components), contamination from extended diffuse emission better explains why BAYMAX favors a dual point source more strongly using non-informative priors for SDSS J0841+0101. The "secondary" is most likely sitting in a region of X-ray emitting diffuse gas that is inconsistent with the spatial position of the nucleus of the merging galaxy. Similarly for SDSS J1356+1026, BAYMAX favors a dual point source more strongly using non-informative priors. The true nature of the extended X-ray emission has been studied extensively in the past (Greene et al. 2009, 2012, 2014) and was found to most likely arise from photoionization and/or shocks from a quasar-driven superwind.

Thus, for SDSS J0841+0101 and SDSS J1356+1026 we add an additional background component to our model. In Figure 5.1 we show these additional regions of background

components in gray dash-dotted regions, where the position and size of these regions are visually determined from the HST images. Within these regions, BAYMAX fits for a different background fraction, f_{BG}, than for outside these regions. We include the diffuse component when it is statistically favored, as determined by BAYMAX. In particular, for both the single and dual point source models, we compare the evidence of the original models (Z_1 and Z_2) to evidence the models that include a diffuse emission component ($Z_{1,\mathrm{D}}$ and $Z_{2,\mathrm{D}}$). We use informative priors for the locations of μ, as shown in Figure 5.1. For both SDSS J0841+0101 and SDSS J1356+1026, we find that including a diffuse emission component is strongly preferred for both the single and dual point source models ($\ln \frac{Z_{1,\mathrm{D}}}{Z_1}, \ln \frac{Z_{2,\mathrm{D}}}{Z_2} \gg 0$, see Table 5.3). With our updated model, SDSS J0841+0101 is no longer consistent with emission from two resolved point sources, and is instead better described by one point source with two background components ($\ln \mathcal{B}_{\mathrm{D}} < 0$). However, SDSS J1356+1026 remains better described by two point sources.

We analyze how the Bayes factor determined by BAYMAX depends on the shape and size of the additional background component. Specifically, because the diffuse emission surrounding SDSS J1356+1026 has an extreme spatial extension ($\approx$ 20 kpc) and is potentially driven by a superwind, the spatial distribution of extended gas is likely to be non-uniform within our square region ($l_{\mathrm{box}} = 32$ sky-pixels or $\approx$35 kpc at $z = 0.123$). However, we find that that our results do not change when constraining our analysis to counts within a smaller l_{box} values (i.e, a physically smaller area over which the diffuse emission is more accurately modeled as spatially uniform); given the low number of counts available, we conclude that the X-ray emission of the diffuse background component can be appropriately modeled with a spatially uniform distribution.

Similarly for SDSS J0841+0101, under the assumption that the region dominated by extended diffuse emission surrounds both optical nuclei, the model favored by BAYMAX remains a single point source, regardless of the shape. Naturally, as the size of the diffuse emission background component increases (and the size of the X-ray background region decreases)

$M_{j,\mathrm{D}}$ begins to resemble M_j, with one (dominant) background component. However, as long as the diffuse emission region is constrained to overlap with emission seen in the *HST* F438W filter (which represents a more informative model), the models favored by `BAYMAX` remain a single point source for SDSS J0841+0101 and a dual point source for SDSS J1356+1026. We conclude that SDSS J0841+0101 is most likely a single resolved point source, surrounded by extended diffuse X-ray emission while SDSS J1356+1026 is most likely a dual point source system, also surrounded by extended diffuse gas (for more details on the origin of this emission, we refer the reader to Section 5.7.4).

In general, the user should test various models that are considered appropriate for a given observation. For the 3 other sources in which BAYMAX favored the dual point source model (SDSS J0752+2736, SDSS J1126+2944, and SDSS J1448+1825), we do not see any evidence of an additional high-count background, in either the X-ray or complementary optical observations (and, on average, these observations had a low number of total counts), and thus we do not test for the significance of including additional high-count background for these observations. One may ask whether the emission is better described by (i) two point sources (M_2) or (ii) a single point source plus a compact region of diffuse emission (sitting at the location of the secondary; $M_{1+\mathrm{diff}}$). As an example, we can compare the Bayes factor between these two models for SDSS J1126+2944. Similar to M_{two}, for $M_{1+\mathrm{diff}}$ we parametrize the diffuse emission component by fitting for the count ratio between its emission and the emission of the primary (f). We use the same informative priors as shown in Fig. 5.1. We find $\mathcal{B} = 2.72$ ($\pm$ 1.55), in favor of $M_{1+\mathrm{diff}}$. The larger error bars are reasonable, given that there are only $\sim$3 counts associated with either the secondary point source / diffuse emission component. We stress, however, that a compact uniformly emitting region in this case is contrived and not physical; in such a case, we would assign prior odds that take this into account, keeping the Bayes factor in realistic territory. When doing similar tests using high-count simulations of dual point sources (where each point source is contributing >50 counts), the Bayes factor in favor of M_2 exceeds 10^{20}, a reflection of our robust PSF models.

Thus, we update our list of dual AGN candidates to four systems: SDSS J0752+2736, SDSS J1126+2944, SDSS J1356+1026, and SDSS J1448+1825. SDSS J0752+2736 has a Bayes factor value in favor of the dual point source model only when using non-informative priors, while the remaining three systems have Bayes factor values in favor of the dual point source model when using both informative and non-informative priors.

5.6.3 Strength of the Bayes factor

For each dual point source system, we analyze the strength of the Bayes factor. In the historical interpretation of the strength of the Bayes factor(see Jeffreys 1935 and Kass & Raftery 1995), values between $\approx 3 - 10$ were defined as "substantial", while values > 10 were defined as "strong". However, these $\mathcal{B}$ value bins were arbitrarily defined; of course, the interpretation of a "strong" Bayes factor value depends on the context. For each dual point source system we run false-positive tests to better, and uniquely, define a "strong" Bayes factor.

The false-positive tests are set-up as follows: we create single point source simulations based on each observation in `MARX`. We constrain our analysis to the counts contained within the same sky coordinates and energy cuts as the observations, use the same informative priors (or, non-informative in the case of SDSS J0752+2736), and add a uniform background contribution with a similar background fraction as each observation. This results in simulations with a similar fraction of background counts as well as total number of counts as the observation. For SDSS J1356+1026, we also add a synthetic diffuse emission component (or, a background component with a higher count-rate) that is constrained within the same region as shown in Fig. 5.1. For each system, we run `BAYMAX` on 1000 simulations and calculate what fraction have $\mathcal{B}$ values *in favor* of a dual point source. Besides defining a "strong" Bayes factor value for each source, this technique also allows us to measure the probability that each system is more likely two point sources versus one point source.

For the false-positive runs based on SDSS J0752+2736, SDSS J1356+1026, and SDSS

J1448+1825, 99% of the $\ln \mathcal{B}$ values are < 0.92 in favor of a dual point source system; while for SDSS J1126+2944 99% of the $\ln \mathcal{B}$ values are < 1.80 in favor of a dual point source system. Additionally, none of the 1000 simulations have $\ln \mathcal{B}$ values in favor of a dual point source model greater than what we measure (i.e., there is <99.9% chance that a single point source with a comparable number of counts would return a Bayes factor value, in favor of the dual point source model, greater than what we measure). Thus, we classify each Bayes factor value as "strong" in favor of the dual point source model.

5.7 Nature of the Dual Point Source Systems

We find that 4 of the 12 galaxies have strong Bayes factor values in favor of the dual point source model: SDSS J0752+2736, SDSS J1126+2944, SDSS J1356+1026, and SDSS J1448+1825. Generally, we find that the locations for a primary and secondary X-ray point source for SDSS J1126+2944, SDSS J1356+1026, and SDSS J1448+1825 using non-informative priors are consistent, at the 68% C.L, with those found using informative priors (albeit, with larger relative uncertainties). Further, because our informative priors are based on the locations of the spatially resolved O III emission components, as presented in Comerford et al. (2015), which were found to be consistent with the locations of the galactic nuclei, the best-fit `BAYMAX`-derived separations for SDSS J1126+2944, SDSS J1356+1026, and SDSS J1448+1825 are, by nature, consistent with the separations between the optical nuclei. The remaining 8 galaxies have $\ln \mathcal{B}$ that favor a single point source, or are consistent with 0 at the 99.7% confidence level (see Table 5.3).

Before we investigate the nature of each dual point source system, it is important to note the specific differences in our analysis versus the original analysis presented in Comerford et al. (2015): (i) in the original analysis the X-ray model contained two sources with a separation and orientation on the sky that were fixed at the measured separation and position angle of the two [O III] λ5007 emission components; and (ii) the significance of each of the two sources in the model were estimated individually, such that each system could be categorized

into three groups: no point source, 1 point source, or 2 point sources.

Regarding (i), because we run BAYMAX using both informative and non-informative priors, we are sensitive to detecting emission from a point source anywhere in the image. Regarding (ii), because BAYMAX is a *comparative* analysis, we can only conclude that each system is either better explained by a single or dual point source. Although the 8 systems with $\ln \mathcal{B}$ values < 0 are better explained by a single point source versus a dual point source, they require a specified model for comparison in order to better understand their true nature. For example, one could compare a single point source to a uniform background, in order to analyze whether the emission is consistent with a compact object versus the CXB. However, we note that the true origin of the X-ray emission of these 8 systems is outside the scope of this chapter.

In the following section, we aim to better understand the true nature of the 4 X-ray dual point source systems. In order to better determine the likelihood that each dual point source system is actually composed of two AGN, we analyze the posterior distributions and X-ray spectra. For each system, we determine the best-fit values of each fit parameter using the median values of their posterior distributions, which is appropriate given their unimodal nature. In Table 5.4 we list the best-fit values for r, $\log f$ and $\log f_{BG}$.

5.7.1 X-ray Spectral Analysis of Individual Point Source Components

The spectral fits and flux values are determined using XSPEC, version 12.9.0 (Arnaud 1996). For each point source component (2 per system, hereafter the "primary" and "secondary" point source), we create 1000 spectral realizations by probabilistically sampling from the full distribution of counts. Each spectral realization uses θ_2 values that are drawn from the posterior distributions as determined by BAYMAX. For each iteration, BAYMAX assigns each count to a specific model component (i.e, the primary, secondary, or background), based on the relative probabilities of being associated with each component. We then fit the spectra of the counts associated with the primary and secondary (and thus, they are background-

subtracted spectra), and create distributions of spectral parameters and flux values based on the best-fit values of each fit. This allows, for the first time, a spectral analysis of *individual* point source components in candidate dual AGN systems that are closely separated. This type of analysis is useful for measuring the fluxes of each source, as well as better constraining the flux ratio between the secondary and primary. Specifically, fitting 1000 spectral realizations for each point source allows for estimations on the flux ratio, whereas `BAYMAX` calculates the likely count ratio.

Each point source component is modeled as either a simple absorbed power-law: (`phabs`×`zphabs`×`pow`; hereafter $m_{\rm spec,1}$) or an absorbed power-law with Compton scattering: (`phabs`×(`pow` + `zphabs`×`pow`); $m_{\rm spec,2}$), where the power-law indices are tied to one-another. This latter model has been found to accurately describe the spectra of AGN in merger-environments (see, e.g., Pfeifle et al. 2019a). Although the Compton scattering component can be fit using a physically motivated model (such as BNTorus; Brightman & Nandra 2011b), doing so with a high statistical significance requires more counts than the observations contain. When using phenomenological models to describe our low-count spectra, the `zphabs` component in $m_{\rm spec,2}$ effectively accounts for the Compton scattering. We implement the Cash statistic (`cstat`; Cash 1979) in order to best assess the quality of our model fits. Specifically, the latter model is used if it results in a statistically significant improvement in the fit, such that $\Delta C_{\rm stat} > 2.71$ (see, e.g.,Tozzi et al. 2006; Brightman & Ueda 2012), corresponding to a fit improvement with 90% confidence (however, this is only valid if $C_{\rm stat}/{\rm dof}\approx1$, see Brightman et al. 2014 and references therein).

It has been found that the constraint on Γ is poor for low-count (<500) *Chandra* spectra (where the average uncertainty on Γ is > 0.5, Brightman & Ueda 2012). However, the large uncertainties introduced into the spectral fit can be reduced by fixing Γ. Thus, for those sources with an average of <10 counts (i.e., most of the secondary point sources), we assume the simpler spectral model, $m_{spec,1}$, and fix the power-law spectral index, Γ, to a value of 1.8 (Corral et al. 2011; Yan et al. 2015). For the primary point sources (where the average

number of 0.5–8.0 keV counts ranges from 15–177), if the best-fitting model where Γ is free is a significantly better fit than the best-fitting model where Γ is fixed (using the same criterion of $\Delta C_{\rm stat} > 2.71$) we choose the model with Γ as free as the best-fitting model. The exception to this is if nonphysical values were pegged for Γ (i.e., values greater than 3 or less than 1; see Ishibashi & Courvoisier 2010) or if the extragalactic column density N_H was pegged to values $> 10^{24}$ cm^{-2}. Only one primary point source, SDSS J1356+1026, met this criterion. For each model, we fix the column density to the Galactic value (Kalberla et al. 2005) as well as the redshift to that of the host galaxy.

We use the criterion of $L_{2-7\ \rm keV,unabs} > 10^{40}$ erg s^{-1}, as a first pass, to rule out possible non-AGN contributions. At X-ray luminositinies below this threshold, there are a handful of different possible sources of contamination, including a high-mass X-ray binary (HMXB) or an ultraluminous X-ray source (ULX). Although the most luminous ULXs may contain a black hole of intermediate ($> 100\ M_\odot$) mass, the compact object is still thought to be accreting matter from a massive donor star. Thus, these systems can be viewed as HMXBs in a broader sense. The majority of the high-mass X-ray binary population has 2–7 keV X-ray luminosities between 10^{38}–10^{39} erg s^{-1}, while the ULX population dominates at the highest luminosities, with $L_{2-7\ \rm keV} > 10^{39}$ erg s^{-1} (e.g., Swartz et al. 2011; Walton et al. 2011). The overall X-ray luminosity function of HMXBs and ULXs indicates a general cutoff at $L_{2-7\ \rm keV} = 10^{40}$ erg s^{-1} (e.g., Mineo et al. 2012; Sazonov & Khabibullin 2017; Lehmer et al. 2019), and previous studies on XRB contamination in both late- and early-type galaxies have concluded that the majority of nuclear (within $2''$ of the galactic nucleus) X-ray point sources with $L_{2-7\ \rm keV} > 10^{40}$ erg s^{-1} are highly unlikely to be emission associated with accretion onto XRBs (Foord et al. 2017a; Lehmer et al. 2019). We note, however, that such studies have yet to be carried out for a sample of merging systems, where merger-induced shocks and starbursts can amplify the surrounding X-ray emission. Particularly in the case of SDSS J1356+1026, which visibly has more complicated surroundings, we look at additional environmental aspects (see Section 5.7.4) before classifying the likely nature of the X-ray

Table 5.4: Posterior Results for θ_2

Galaxy Name	α_p	δ_p	α_s	δ_s	r (arcsec)	$\log f$	$\log f_{bkg}$
(1)	(2)	(3)	(4)	(5)	(6)	(7)	(8)
SDSS J0752+2736	7:52:23.341	+27:36:43.516	7:52:23.266	+27:36:44.562	1.50±0.30	−0.47±0.36	−0.72±0.40
SDSS J1126+2944	11:26:59.534	+29:44:42.573	11:26:59.602	+29:44:41.101	1.74±0.33	−1.00±0.44	−0.97±0.40
SDSS J1356+1026	13:56:46.123	+10:26:09.321	13:56:46.067	+10:26:07.502	2.00±0.62	−0.92±0.23	−0.16±0.10
SDSS J1448+1825	14:48:04.174	+18:25:37.925	14:48:04.177	+18:25:39.115	1.29 ± 0.52	−0.45±0.80	−0.40±0.34

Note. – Columns: (1) SDSS galaxy designation; (2) the central R.A. of the primary X-ray source; (3) the central declination of the primary X-ray source; (4) the central R.A. of the secondary X-ray source; (6) the central declination of the secondary X-ray source; (6) the separation between the two point sources in arcseconds; (7) the log of the count ratio between the secondary and primary; (8) the log of the count ratio between the background contribution. For SDSS J1356+1026, the background component is defined as the diffuse emission component. Each value is the best-fit value from the posterior distributions, defined as the median of the distribution. All posteriors distributions are unimodal, and thus the median is a good representation of the value with the highest likelihood (with the exception of r for J1356+1026, see Fig. 5.5). Error bars represent the 68% confidence level of each distribution.

emission.

In addition to $L_{2-7\text{ keV, unabs}}$, we analyze the hardness ratio of each, HR, defined as $HR = (H-S)/(H+S)$. Here, H and S are the number of hard and soft X-ray counts, where the threshold between the two is set to 2 keV. We list the best-fit values for each spectral parameter, $F_{0.5-8}$, $L_{2-7\text{ keV, unabs}}$, and HR, in Table 5.5 (we denote the values for the primary and secondary with subscripts p and s). For SDSS J1126+2944$_p$, SDSS J1356+1026$_p$, and SDSS J1448+1825$_p$ we quote the unabsorbed 2–7 keV luminosities from $m_{\rm spec,2}$. However, because the best-fit extragalactic column density will be systematically lower for the simpler model ($m_{\rm spec,1}$), we also list the best-fit parameters for $m_{\rm spec,1}$ for the purposes of comparison between the primary and secondary in a given system.

5.7.2 SDSS J0752+2736 and SDSS J1448+1825: A High Probability of Contamination from XRBs

5.7.2.1 SDSS J0752+2736

In the original analysis of SDSS J0752+2736, neither a primary or secondary point source were found to be statistically significant at the locations of each [O III] λ5007 emission

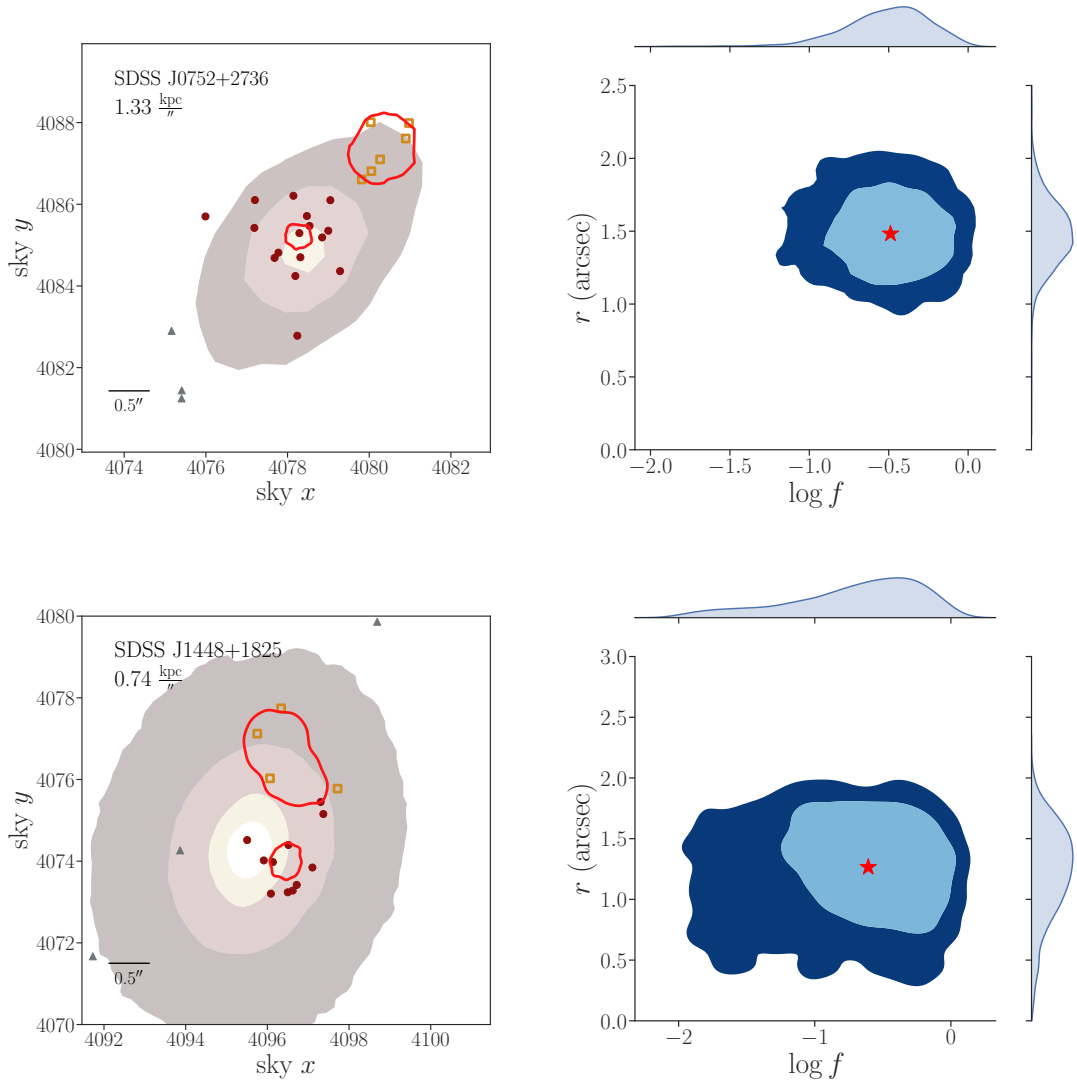

Figure 5.4: The 0.5–8 keV datasets for the two dual AGN candidates SDSS J0752+2736 and SDSS J1448+1825 (*left*) and the joint posterior distribution for the separation r (in arcseconds) and the count ratio (in units of $\log f$), with the marginal distributions shown along the border (*right*). In the left panels, we plot the 68% confidence intervals (red lines) for the best-fit sky x and sky y positions for a primary and secondary. Here, counts most likely associated with the primary are denoted by circles, counts most likely associated with the secondary are denoted by squares, counts most likely associated with background are shown as faded triangles. In order to more clearly see the results, we do not bin the data. Contours of the *HST* F160W observations of the host galaxies are overplotted (with the exception of SDSS J0752+2736, which are contours of the SDSS i-band observation). In the right panels, the 68%, and 95% confidence intervals are shown in blue contours. We denote the location of the median of the posterior distributions with a red star.

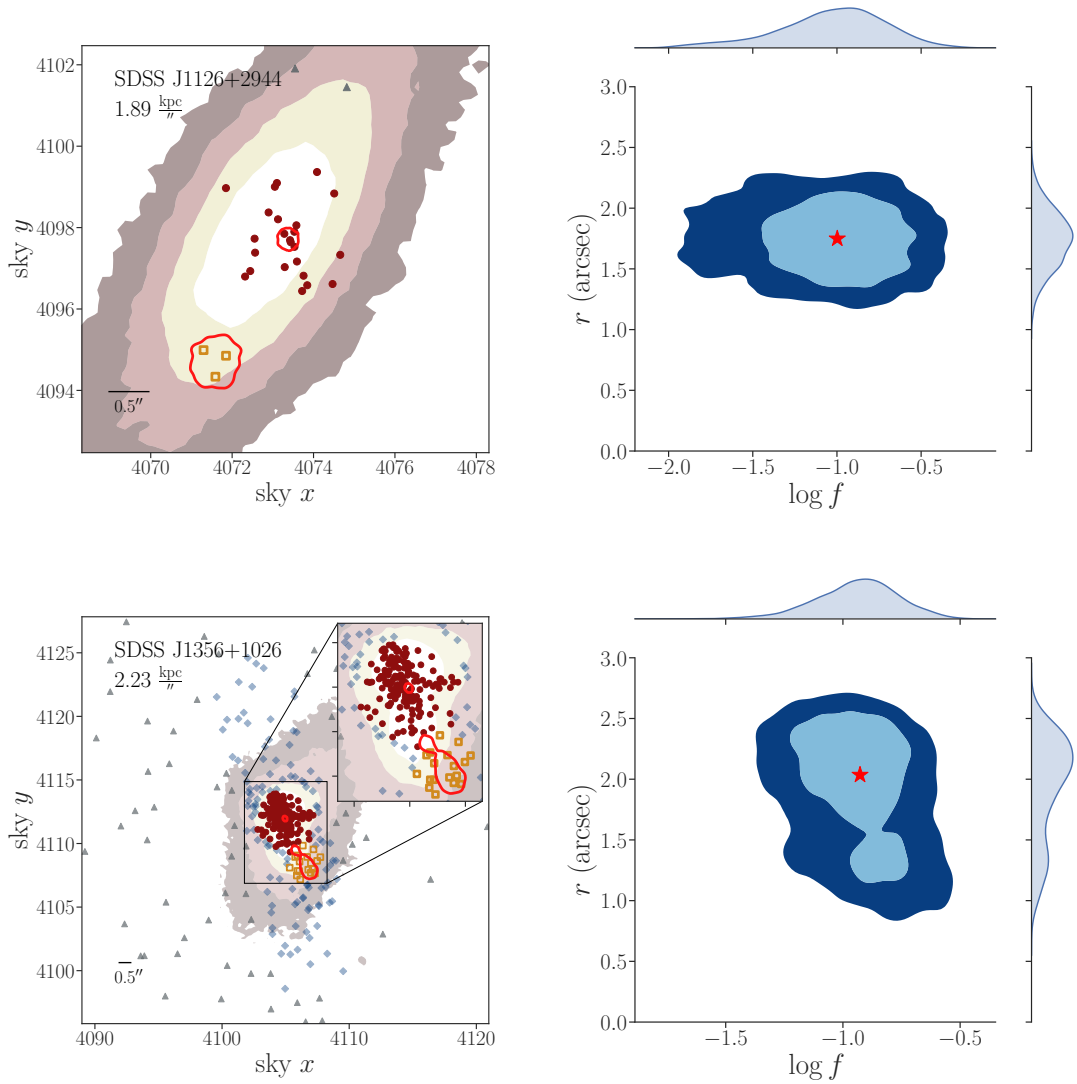

Figure 5.5: The 0.5–8 keV datasets for the two dual AGN candidates whose primary and secondary X-ray point sources meet our AGN luminosity criterion (left) and the joint posterior-distribution for the separation r and the count ratio (right). Symbols and contours follow the same guidelines as Fig. 5.4. For SDSS J1356+1026, we denote diffuse emission background with faded diamonds.

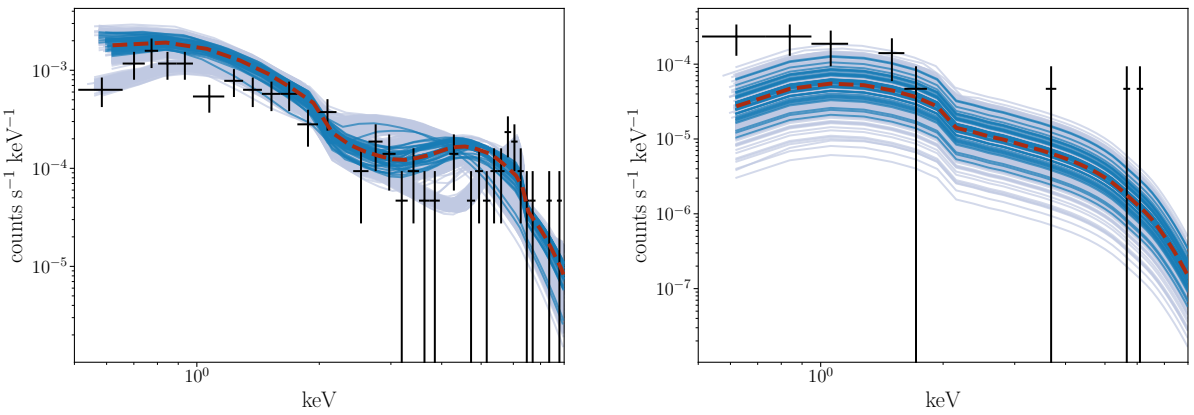

Figure 5.6: *Chandra* spectral fits for 1000 realizations for J1356+1026 (left: primary point source, where the median number of counts is 177; right: secondary point source, where the median number of counts is 20), where the data have been folded through the instrument response. We overplot one of the spectral realizations with black points and plot the median spectral fit in a red dashed line. We randomly select 50 of the 1000 spectral fits and plot them in dark blue to better highlight the density distribution of the lines. The spectra have been rebinned for plotting purposes. We fit J1356+1026$_p$ with the model `phabs`×(`pow` + `phabs`×`zphabs`×`pow`), while we fit J1356+1026$_s$ with the model `phabs`×`zphabs`×`pow`. For J1356+1026$_p$, Γ is allowed to vary, while for J1356+1026$_s$ we fix Γ to a value of 1.8. We investigate whether the emission of the secondary is consistent with the emission of the diffuse background component by allowing Γ vary. While $L_{2-7,\ \mathrm{keV}}$ remains $> 10^{40}$ erg s^{-1}, we can not differentiate this spectrum, at a statistical confidence level, from the diffuse emission component. We list the best-fit values for each model in Table 5.5, defined as the median of distribution of the best-fit values from the 1000 realizations.

Table 5.5: Best-fit Spectral Parameters

Galaxy Name	$m_{\rm spec,x}$	N_H (10^{22} cm^{-2})	Γ	$F_{0.5-8\ \rm keV}$	$L_{2-7\ \rm keV,\ unabs}$	HR
(1)	(2)	(3)	(4)	(5)	(6)	(7)
SDSS J0752+2736$_p$	1	$< 10^{-2}$	1.8	2.74±0.59	1.67±0.36	−0.24±0.1
SDSS J0752+2736$_s$	1	$< 10^{-2}$	1.8	0.46±0.10	0.71±0.16	−0.53±0.40
SDSS J1126+2944$_p$	2	34.20±2.00	1.8	33.50±2.90	284.50±55.90	0.32±.10
	1	0.23±0.1	1.8	11.80±0.90	19.00±1.70	
SDSS J1126+2944$_s$	1	14.30±7.70	1.8	4.64±2.00	28.80±15.80	0.30±0.2
SDSS J1356+1026$_p$	2	41.10±14.50	2.54±0.27	26.80±4.50	3.40±1.60×10^2	0.30±0.10
	1	$< 10^{-2}$	1.8	17.55±3.2	35.50±6.60	
SDSS J1356+1026$_s$	1	$< 10^{-2}$	1.8	0.90±0.41	1.80±0.80	−0.30±0.29
SDSS J1448+1825$_p$	2	56.30±14.5	1.8	12.80±5.20	17.50±10.00	-0.1 ± 0.20
	1	$< 10^{-2}$	1.8	4.20±1.00	0.75±0.2	
SDSS J1448+1825$_s$	1	$< 10^{-2}$	1.8	0.56±0.47	0.11±0.097	−0.98±0.1

Note. – Columns: (1) SDSS galaxy designation, we denote the primary and secondary with subscripts p and s; (2) the spectral model used; (3) the best-fit extragalactic column density; (4) the assumed or best-fit spectral index; (5); the measured 0.5–8 keV flux, in units of 10^{-15} erg s^{-1} cm^{-2}; (6) the rest-frame, unabsorbed, 2–7 keV luminosity in units of 10^{40} erg s^{-1}; (7) the hardness ratio, defined as $HR = (H - S)/(H + S)$. Each best-fit value is defined as the median of the full distribution. Error bars represent the 1σ confidence level of each distribution.

component (Comerford et al. 2015). Our analysis with informative priors does not refute this conclusion, as the Bayes factor disfavors the dual point source model. However, the dual point source model becomes favored when using non-informative priors, with $\ln \mathcal{B} = 4.90 \pm 0.51$.

Running `BAYMAX` using non-informative priors, we analyze the posterior distributions for the locations of the primary and secondary (μ), the count ratio (f), and the background fraction (f_{BG}). The best-fit position of each point source is shown in Figure 5.4, where the secondary appears to align with the position angle of the galaxy (see Fig. 5.1). We also show the joint posterior distribution for the separation between the two point sources, r, and the logarithm of the count ratio, ($\log f$). There are no *HST* data for this system, and thus it is not possible to resolve potential optical cores or smaller galactic disturbances on the same scale as the estimated separation ($< 2''$). We find the best-fit values for r and $\log f$ to be $1.5'' \pm 0.30''$ and -0.47 ± 0.36, respectively. At the 95% C.L., the separation between the two point sources is greater than $0''.5$.

We run our spectral analysis on SDSS J0752+2736, and find that, on average, the primary and secondary have 15 and 6 counts, respectively. We fit both the primary and secondary

point source with a simple absorbed power-law (`phabs×zphabs×pow`), with Γ fixed to a value of 1.8. For the primary, we calculate a total observed 0.5–8 keV flux of $(2.74 \pm 0.59) \times 10^{-15}$ erg s^{-1} cm^{-2}, while for the secondary we calculate a total observed 0.5–8 keV flux of $(4.60 \pm 1.00) \times 10^{-16}$ erg s^{-1} cm^{-2} s^{-1}. This corresponds to a rest-frame 2–7 keV luminosity of $(1.67 \pm 0.36) \times 10^{40}$ erg s^{-1} and $(7.1 \pm 1.60) \times 10^{39}$ erg s^{-1} at $z = 0.069$. Since we have fixed both point sources to have the same spectral shape, the count ratio that we calculate with `BAYMAX`, should represent the flux ratio between the two sources. We find that the flux ratio we calculate via `XSPEC` ($\approx$0.43) is consistent within the 68% error interval of the log f posterior (where the median value is $\approx$0.34).

Although the primary point source X-ray luminosity meets our $L_{2-7\ \mathrm{keV,\ unabs}}$ criterion, the secondary does not. With an X-ray luminosity below 10^{40} erg s^{-1}, we can not rule out contamination from possible XRBs or ULXs. Generally, the X-ray to optical flux ratio of most ULXs is very high (Tao et al. 2011), which is similar to low mass X-ray binaries and suggests that the optical emission arises from an accretion flow. This is consistent with the observation, as the secondary's position does not coincide with the measured bright [O III] λ5007 emission component, and has no obvious optical counterpart in the SDSS image.

Given the point-like emission, spatial position, and $L_{2-7\ \mathrm{keV,\ unabs}}$ value, the emission of the secondary point source in SDSS J0752+2736 is consistent with what is expected from a ULX. Thus, while the X-ray data are strongly indicative of a secondary point source, we can not conclude with a high certainty that SDSS J0752+2736 is a dual AGN system.

5.7.2.2 SDSS J1448+1825

In the original analysis of SDSS J1448+1825, neither a primary or secondary point source were found to be statistically significant at the locations of each [O III] λ5007 emission components (Comerford et al. 2015). However, we find that the dual point source model is favored when using both non-informative and informative priors, with a $\ln \mathcal{B} = 1.43 \pm 0.55$ and $\ln \mathcal{B} = 2.95 \pm 0.52$. When using informative priors, we find the best-fit values for r

and $\log f$ to be $1.29'' \pm 52''$ and -0.45 ± 0.80, respectively. However, at the 95% C.L., the separation between the two point sources is $< 0\farcs5$.

We run our spectral analysis on SDSS J1448+1825, and find that the primary and secondary have, on average, 14 and 3 counts. We fit the primary AGN with $m_{spec,2}$, fixing Γ to a value of 1.8. Here, we find that $\Delta C_{\rm stat} = 5.7$, such that the more complicated spectral model is a statistically better fit. For the primary, we calculate a total observed 0.5–8 keV flux of $(12.80 \pm 5.20) \times 10^{-15}$ erg s^{-1} cm^{-2}, while for the secondary we calculate a total observed 0.5–8 keV flux of $(5.60 \pm 4.70) \times 10^{-16}$ erg s^{-1} cm^{-2} s^{-1}. This corresponds to a rest-frame 2–7 keV luminosity of $(17.50 \pm 10.00) \times 10^{40}$ erg s^{-1} and $(1.10 \pm 0.97) \times 10^{39}$ erg s^{-1} at $z = 0.038$.

Although `BAYMAX` favors the dual point source model for J1448+1825, and the secondary's position is consistent with the secondary [O III] λ5007 emission component, the rest-frame unabsorbed X-ray luminosity is below our criterion and the X-ray spectrum of the secondary is very soft ($HR \approx -1$). Based on our MC spectral analysis, there is >50% chance that the count rate above 2 keV is 0. Given the average X-ray count-rate ($\approx 1 \times 10^{-4}$ cps) and assumed spectral shape ($\Gamma = 1.8$), this is consistent with what is expected from a possible low-luminosity AGN ($\approx$1 count between 2–8 keV), however we conservatively do not classify SDSS J1448+1825 as a dual AGN system. Deeper observations of SDSS J1448+1825 will allow for better constraints on the spectral shape.

5.7.3 SDSS J1126+2944: A dual AGN system with an ultra-compact dwarf galaxy candidate

SDSS J1126+2944 was the only confirmed dual AGN candidate found in the analysis of Comerford et al. (2015). Specifically, both the primary and secondary X-ray point sources were found to be statistically significant at the locations of each [O III] λ5007 emission component at a 5σ and 2.3σ confidence level, respectively. Our results agree with these conclusions, as we find $\ln \mathcal{B} = 3.54 \pm 0.43$ when using informative priors based on the

positions of the [O III] λ5007 emission components.

We analyze the posterior distributions for μ, f, and f_{BG} when `BAYMAX` is run using informative priors. We find the best-fit values for r and $\log f$ to be $1.74'' \pm 0.33$ and -1.00 ± 0.44. At the 95% C.L., the separation between the two point sources is greater than $1''$. The best-fit locations of the primary and secondary are shown in Figure 5.5.

We run our spectral analysis on SDSS J1126+2944, and find that primary and secondary, on average, have 25 and 3 counts. We fit the primary AGN with $m_{\rm spec,2}$, and fix the photon index of the power-law, Γ, to a value to 1.8. On average we find that $\Delta C_{\rm stat} = 39.6$, such that the more complicated spectral model is a statistically better fit. For the primary, we calculate a total observed 0.5–8 keV flux of $(3.35 \pm 0.29) \times 10^{-14}$ erg s^{-1} cm^{-2}, while for the secondary we calculate a total observed 0.5–8 keV flux of $(4.64 \pm 2.00) \times 10^{-15}$ erg s^{-1} cm^{-2} s^{-1}. This corresponds to a rest-frame 2–7 keV luminosity of $(2.84 \pm 0.55) \times 10^{42}$ erg s^{-1} and $(2.90 \pm 1.58) \times 10^{41}$ erg s^{-1} at $z = 0.102$.

We confirm that the location of the secondary coincides spatially with a faint point-like source discovered in the *HST* F160W, F814W, and F438W images (hereafter SDSS J1126+2944 SE ; Comerford et al. 2015). The merger ratio of the main host galaxy to SDSS J1126+2944 SE was found to be $\approx$ 460:1, and thus SDSS J1126+2944 SE was classified as a potential ultra-compact dwarf galaxy (Comerford et al. 2015). Indeed, the estimated upper-limit of the half-light radius of 280 pc agrees with other ultra-compact dwarf galaxies that host a supermassive black hole (e.g., M60-UCD1; see Seth et al. 2014). Specifically, M60-UCD1 is thought to be the remnant of a galaxy that was once more massive, but underwent tidal stripping via an encounter with the galaxy M60. Due to signs that SDSS J1126+2944 underwent some kind of tidal disruption itself in the *HST* images, this is a possible scenario.

As an additional step in the analysis of the true nature of the secondary point source, we compare the hard X-ray luminosity to the total, expected X-ray luminosity due to XRBs. Following a similar analysis to Foord et al. (2017a), we adopt an updated analytic prescription by Lehmer et al. (2019), to estimate the total, 2–7 keV luminosity expected from XRBs

($L_{\rm XRB}^{\rm gal}$). In particular, for a given stellar mass (M_*, which scales with the LMXB population; Gilfanov 2004) and star formation rate (SFR, which scales with the HMXB population; Mineo et al. 2012) the total, 2–7 keV luminosity from XRBs can be estimated (Lehmer et al. 2019). We use the values for M_* and the SFR as estimated in Barrows et al. (2017b), where they fit galaxy and AGN templates to the broadband photometric SEDs of a sample of dual AGN candidates, including SDSS J1126+2944 and SDSS J1356+1026. Since the values for M_* and the SFR have only been measured for the primary galaxies, we are assuming that the primary and secondary AGN are in galaxies with similar SFRs and stellar masses (and for SDSS J1126+2944 this is a conservative assumption, given the large mass ratio estimated by Comerford et al. 2015). We estimate a total 2–7 keV luminosity expected from XRBs $L_{\rm XRB}^{\rm gal} = 1.8^{+6.56}_{-1.58} \times 10^{40}$ erg s^{-1}, over a factor of 10 less than the measured X-ray luminosity of the secondary point source.

5.7.4 SDSS J1356+1026: A candidate dual AGN system among warm photoionized gas

Although SDSS J1356+1026 was originally found to have both a primary and secondary point source at a statistically significant confidence level (5σ and 4.4σ, respectively), it was conservatively categorized as a single AGN (Comerford et al. 2015), as the soft X-rays associated with an outflowing bubble (Greene et al. 2012, 2014) complicated the identification of a possible dual AGN. We take into account possible contamination from diffuse gas associated with photoionization by including an additional background component to our model (see Section 5.6). Further, our model for the additional background component is uniform over energy-space (i.e., a 2 keV photon is just as likely as a 7 keV photon), and thus conservative, as we expect most of the diffuse emission, regardless of its physical origin, to be <3 keV. We find that (i) the results from `BAYMAX` favor the model that includes the additional background component, for both the single and dual point source models, and (ii) the results from `BAYMAX` remain in favor of the dual point source model, even when accounting for the

diffuse emission.

However, if the extended emission in SDSS J1356+1026 is a result of extreme photoionization via feedback of the primary AGN (Greene et al. 2012, 2014), there is a possibility that the secondary X-ray point-source is instead associated with a luminous [O III] gas clump. Thus, analyzing our best-fit parameters for the location, as well as carrying out an X-ray spectral analysis, are imperative for a better understanding of the most likely origin of emission.

We find the best-fit values are $r = 2.00'' \pm 0.62''$ and $\log f = -0.92 \pm 0.23$. We note that the posterior distribution for r has a slight bimodality, due to a bimodality in the x, y position of the secondary X-ray point-source (see Fig. 5.5). This is likely due to the diffuse emission component contributing a large fraction of counts (69% of the counts emitted by both point sources, or ≈75% of the counts emitted by the secondary). However, at the 95% C.L., the separation between the two point sources remains $> 0\farcs5$, and the location of the secondary is consistent, within the errors, of the merging galaxy's optical nucleus.

Running our spectral analysis, we find that the primary and secondary have, on average, 177 and 20 counts. Here $\Delta C_{\rm stat} \approx 8$, such that $m_{\rm spec,2}$ is favored for the primary point source at a significant level. For the primary, we calculate a total observed 0.5–8 keV flux of $(2.38 \pm 0.16) \times 10^{-14}$ erg s^{-1} cm^{-2}, while for the secondary we calculate a total observed 0.5–8 keV flux of $(9.00 \pm 4.10) \times 10^{-16}$ erg s^{-1} cm^{-2} s^{-1}. This corresponds to a rest-frame 2–7 keV luminosity of $(5.60 \pm 2.00) \times 10^{43}$ erg s^{-1} and $(1.80 \pm 0.80) \times 10^{40}$ erg s^{-1} at $z = 0.123$. In Figure 5.6, we show the spectral fits for the 1000 realizations of both the primary and secondary point source.

Although we find that the position and luminosity of the secondary point source are consistent with what is expected from a central SMBH, there still exists the possibility of contamination from an [O III] gas clump. Thus, we compare the spectrum of the counts associated with secondary point source to that of the counts associated with the diffuse emission. When Γ is allowed to vary, with unconstrained values, we find that the spectrum

of the secondary point-source ($\Gamma \approx 3.0 \pm 0.64$) is consistent with spectrum of the diffuse emission ($\Gamma \approx 3.2 \pm 0.25$). We note that with the softer spectral fit, the total unabsorbed 2−7 keV luminosity of the secondary point-source still meets our AGN luminosity criterion ($L_{2-7,\ \mathrm{unabs}} = 1.1 \pm 0.60 \times 10^{40}$ erg s^{-1}). However, because we can not differentiate between the soft spectra of the secondary point source and diffuse emission at a statistical confidence level, we conservatively do not classify SDSS J1356+1026 as a dual AGN system.

Similar to SDSS J1126+2944, we compare the hard X-ray luminosity of the secondary point source to the total, expected X-ray luminosity due to XRBs. Using M_* and SFR values from Barrows et al. (2017b), we find $L_{\mathrm{XRB}}^{\mathrm{gal}} = 8.92^{+3.37}_{-2.29}$, such that the total, expected X-ray luminosity for XRBs is greater than the measured X-ray luminosity measured for the secondary point source. Of course, this is not a perfect comparison, as we do not expect that all of the X-ray luminosity from the XRB population is contained within a compact 2″radius centered on the location of the secondary point source. However, it further exemplifies the complexities when attempting to classify the true nature of the secondary in SDSS J1356+1026.

5.8 Discussion

Using `BAYMAX` on 12 dual AGN candidates, that were identified via [O III] λ5007 emission, we have found that 4/12 have a Bayes factor that favor the dual point source model, 2/12 have secondary point sources with X-ray luminosities consistent with an AGN, and 1/12 is likely true dual AGN system. Both SDSS J1126+2944 and SDSS J1356+1026 have strong Bayes factor values in favor of a dual point source and have primary and secondary X-ray point sources with X-ray luminosities consistent with emission from AGN. However, due to the extreme feedback associated with SDSS J1356+1026$_p$ (seen in both *Chandra* and *HST* observations) there is a probability that the X-ray emission of SDSS J1356+1026$_s$ is instead due to a luminous [O III] gas clump. Because we can not differentiate the spectrum of SDSS J1356+1026$_s$ from the background emission, we conservatively do not only classify

SDSS J1356+1026 as a dual AGN system. SDSS J0752+2736 and SDSS J1448+1825 have Bayes factor values that favor the dual point source model, however because of the large probability of contamination from XRBs, we additionally do not categorize them as dual AGN. The remaining 8 galaxies (SDSS J0142−0050, SDSS J0841+0101, SDSS J0854+5026, SDSS J0952+2552, SDSS J1006+4647, SDSS J1239+5314, SDSS J1322+2631, and SDSS J1604+5009) have Bayes factor values that do not favor the dual point source model. In the following section, we aim to better understand BAYMAX's sensitivity across parameter space, as well as characterize all 12 galaxies via a multi-wavelength analysis.

5.8.1 The Sensitivity of BAYMAX Across Count Ratio Space

We first discuss the significance of our results by analyzing BAYMAX's capabilities across a range of count ratio space for the dual point source model. In particular, we aim to understand where in parameter space BAYMAX loses sensitivity for simulations with a comparable number of counts as the 8 systems in which the Bayes factor value favored the single point source model. This is done by running BAYMAX on a MARX-generated suite of simulated dual AGN systems that closely match the observed data and expected dual configurations. The simulations have the same total number of counts between 0.5–8 keV as each observation, with a primary and secondary AGN located at the spatial locations of the measured [O III] λ5007 emission components. Further, each simulated AGN has the same 0.5–8 keV spectrum as the observation, but with normalizations proportional to their count ratio. We also add a spatially uniform background component to the simulations, where f_{BG} is determined from the best-fits returned by BAYMAX. For J0841+0101, we add an additional synthetic higher-count background to represent the diffuse emission component, which is constrained within the region shown in Fig. 5.1.

We simulate dual AGN systems with count ratios that range between 0.1–1.0, with the exception of the highest-count observations (SDSS J0142−0050 and SDSS J1239+5314), where we can probe lower count ratios (0.03–1.0). We analyze each simulation using the

same informative priors as used for the real datasets. For each f value in parameter space, we analyze 100 simulations, and evaluate the mean Bayes factor value. We enforce a cut of $\mathcal{B} > 3$, where only mean Bayes factor values above this threshold are classified as strongly in favor of the dual point source model.

For SDSS J0142−0050 and SDSS J1239+5314 we find that `BAYMAX` can correctly identify dual AGN systems with a strong Bayes factor value for all count ratio values (down to $f = 0.03$). This is not surprising, given that SDSS J0142−0050 and SDSS J1239+5314 have many counts (> 600 counts between 0.5–8 keV). At the lower-end of the count ratios probed, the secondary is, on average, contributing $\geq$20 counts.

For SDSS J1322+2631 and SDSS J0841+0101, `BAYMAX` is able to correctly identify the systems as a dual point source for the entire count-ratio range analyzed ($f = 0.1$–1.0). These results are not surprising, given that SDSS J1322+2631 has a large estimated separation between the [O III] λ5007 emission components ($> 2''$) and SDSS J0841+0101 has over 400 counts between 0.5–0.8 keV. For SDSS J0952+2552 and SDSS J1604+5009, `BAYMAX` is able to correctly identify systems as a dual point source for $f = 0.2$–1.0. Although these two systems have a comparable number of counts to SDSS J1322+2631 ($\approx$50), the projected separations between the [O III] λ5007 emission components are smaller ($\approx 1''$). We find that the strength of $\mathcal{B}$ in favor of the dual point source model increases as a function of the count ratio in the simulations, where the $\mathcal{B} > 10^2$ for systems with $f \geq 0.3$.

Regarding SDSS J0854+5026 and SDSS J1006+4647, given the small number of counts ($\approx$ 13 total counts between 0.5–8 keV) as well as smaller estimated separations between the [O III] λ5007 emission components ($< 1''$), `BAYMAX` is unable to favor the correct model, on average, for the entire range of f-values probed.

Using the count ratio thresholds determined by `BAYMAX`, we estimate the 2-7 keV luminosities of possible secondary point sources that we are sensitive to. Assuming a power-law spectral shape with $\Gamma = 1.8$, we find that `BAYMAX` is capable of detecting secondary point sources with $L_{2-7\ \mathrm{keV}} \geq 4 \times 10^{40}$ at the lower-luminosity end (SDSS J0841+0101, where

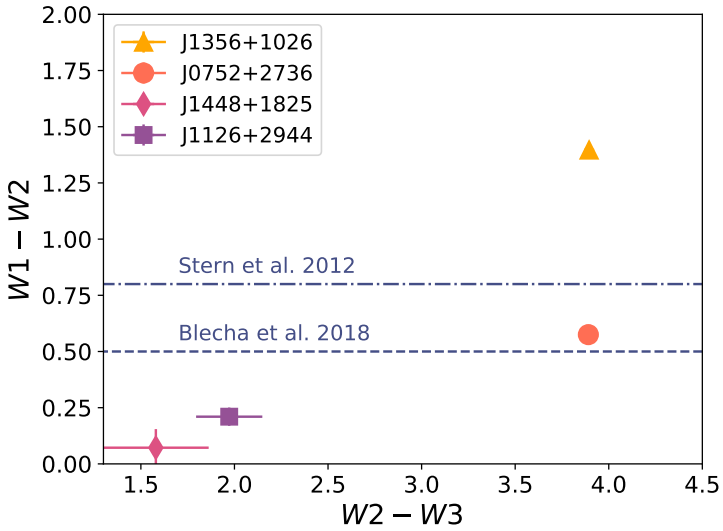

Figure 5.7: $W1 - W2$ vs. $W2 - W4$ color-color diagram for the four sources in the sample that have $\mathcal{B}$ that favor the dual point source model. We show various cuts, above which the majority of luminous AGN (Stern et al. 2012) and dual AGN (Blecha et al. 2013) should sit. We find that one of the sources, SDSS J1356+1026, has an AGN-dominated infrared flux. This is not surprising, given the overall lower X-ray luminosities of these systems.

$z = 0.096$) and $L_{2-7\ \mathrm{keV}} \geq 6 \times 10^{41}$ at the higher-luminosity end (SDSS J0952+2552, where $z = 0.339$). More data on each of these sources, especially SDSS J0854+5026 and SDSS J1006+4647, will be necessary in order for a more thorough analysis of their true nature.

5.8.2 Infrared Observations

We re-plot the mid-infrared colors from the *Wide-field Infrared Survey Explorer* (*WISE*) for the subsample of 4 systems with $\mathcal{B}$ in favor of the dual point source model (which were previously examined for all 12 systems in Comerford et al. 2015). Here we incorporate recent results from simulations of merging galaxies (Blecha et al. 2018a), where specific IR color-cuts in the *WISE* bands were found to select both merger-triggered AGN and dual AGN.

In general, IR colors are often used as a tool to identify AGN (Jarrett et al. 2011; Stern et al. 2012), as mid-IR-selected AGN are much less sensitive to attenuation by gas and dust than AGN selected in optical or soft X-ray bands. The standard single-axis color-cut (above

which, the source is likely an AGN) is $W1$-$W2 > 0.8$ (Stern et al. 2012), but multiple-axis cuts additionally using the $W3$ and $W4$ bands are used as well (see, e.g., Jarrett et al. 2011). However, such diagnostics are sensitive to only the most luminous AGN, that are contributing a considerable fraction of the total bolometric luminosity (Mateos et al. 2013). At lower luminosities, the selection is largely incomplete and strongly biased against AGN residing in massive and/or star-forming hosts.

Similar conclusions have been reached for more recent studies looking at the mid-IR colors of merger-triggered AGN (Blecha et al. 2018a), even in the late stages of gas-rich major mergers. More interestingly, however, Blecha et al. (2018a) find that a less stringent single-color cut not only selects merger-triggered AGN with a much higher completeness, but selects virtually all bright dual AGN (where each AGN have $L_{\rm bol} > 10^{44}$) throughout the merger.

Thus, we plot the $W1$–$W2$ vs. $W2$–$W3$ colors of the four systems with Bayes factor values in favor of the dual point source model in order to see if they lie in an interesting region of IR color-color space. We confirm the finding of Comerford et al. (2015) that only one of the four systems, SDSS J1356+1026, has an AGN-dominated mid-infrared flux. This is not surprising, given the overall lower luminosities of the sources (each point source has $L_{2-7\ \rm keV,unabs} < 10^{42}$ erg s^{-1}, besides SDSS J1356+1026). Additionally, both SDSS J1356+1026 and SDSS J0752+2736 lie above the less stringent single-color cut found in Blecha et al. (2018a). In the future, confirmation of dual-AGN via IR colors may be achieved with AO imaging in the near-/mid-IR bands, where the primary and secondary X-ray point sources can be analyzed individually.

5.8.3 Optical Narrow-line Ratio Diagnostics

We compare the classification of the central ionizing source via available optical spectroscopic data to the conclusions reached by our X-ray analysis. In particular, we analyze how the [O III]/Hβ and [N II]/Hα ratios compare to the line ratio BPT diagram ("Baldwin,

Phillips, & Terlevich"; see Baldwin et al. 1981; Kewley et al. 2006) for the four systems with Bayes factor values in favor of the dual point source model. These line ratio diagnostics can be used to classify the dominant energy source in emission-line galaxies.

With available long-slit spectroscopic data, we are capable of extracting BPT diagnostics individually for the primary and secondary X-ray point-sources. However, because the original long-slit spectroscopic analysis was designed to target the [O III]λ5007 emission, we do not have information regarding the [N II] or Hα emission. Thus, we compare these data-points to $\log [\mathrm{O\ III}]/\mathrm{H}\beta = 1$, above which the line ratios are consistent with emission from an AGN, at all reasonable $\log [\mathrm{N\ II}]/\mathrm{H}\alpha$ values. Such an analysis will allow us to better understand the true nature of the 4 systems with $\mathcal{B}$ that favor the dual point source model. In particular, because SDSS J1356+1026 is more complicated to classify, we are interested in whether this additional optical analysis classifies the secondary point source as an AGN.

We use available long-slit optical spectroscopic data for SDSS J0752+2736, SDSS J1126+2944, and SDSS J1448+1285 (Comerford et al. 2012); while we use archival Sloan spectral data for SDSS J1356+1026. SDSS J0752+2736 and SDSS J1126+2944 were observed with the Blue Channel Spectrograph on the MMT 6.5 m telescope ($0\farcs29$/pixel, Schmidt et al. 1989), while SDSS J1448+1285 was observed with the Kast Spectrograph on the Lick 3 m telescope ($0\farcs78$/pixel). In Figure 5.8 we plot pairs of line ratios for each system. Each long-slit observation used a 1200 lines mm^{-1} grating and was centered so that the wavelength range covered Hβ and [O III], given the various redshifts of each system. Due to the larger diameter of SDSS optical fibers ($3''$), the line ratio values calculated for SDSS J1356+1026 represent the line ratios for the primary and secondary AGN combined. In general, however, we find that the line ratios estimated with Sloan spectra are consistent with those estimated from long-slit spectra (see Fig. 5.8).

Each system with long-slit spectroscopic data (MMT and Lick) was observed twice, with the slit oriented along two different position angles on the sky. Here, the line ratios were estimated by collapsing the spectrum along the spatial direction (to increase the S/N), fitting

the spectra with either one or two Gaussians, and averaging the line ratios between the two position angles. For each system we identify whether the primary or secondary X-ray point source is spatially coincident with the red- or blue-shifted emission components using the spatial information provided by the long-slit observations.

Given that the locations of our informative priors for the primary and secondary X-ray point sources are based on the spatially resolved positions of red- and blue-shifted components of the [O III] long-slit observations (as determined in Comerford et al. 2012), we assume that each red- and blue-shifted component of a given spectrum represent emission from the primary and secondary X-ray point source (with the exception of SDSS J0752+2736, where no X-ray point source was found at a position consistent with a peak in the [O III] emission).

Another limitation of the original analysis targetting the [O III]λ5007 emission is that the Hβ emission is generally quite faint relative to the [O III]λ5007 emission lines. For SDSS J0752+2736 we are unable to fit a Gaussian to the red-shifted component of the Hβ emission line (which corresponds to the secondary X-ray point source) with any statistical confidence ($>1\sigma$). For SDSS J1448+1285 we are able to fit Gaussians to both the red- and blue-shifted Hβ components, however we note that the estimated Hβ flux values are statistically significant at $< 3\sigma$, and should be interpreted with skepticism. For SDSS J1126+2944, we are able to cleanly decompose the two X-ray point source components in Hβ velocity space (where the Hβ flux values are statistically significant at $> 3\sigma$); thus, we measure individual line ratios for the primary and secondary with high statistical confidence.

For SDSS J1126+2944, we find that the line ratios of each X-ray point source are consistent with AGN photoionization, in agreement with our X-ray analysis. Additionally, the line ratios of SDSS J1356+1026, and the primary X-ray point source in SDSS J0752+2736, are consistent with AGN photoionization. Lastly, both the primary and secondary X-ray point sources in SDSS J1448+1825 have [O III]/Hβ ratios consistent with AGN photoionization. This is surprising, given that the X-ray luminosity of the secondary X-ray point source is below our AGN luminosity criterion ($L_{2-7,\ \mathrm{unabs}} < 10^{40}$ erg s^{-1}). If SDSS J1448+1825 is

indeed a dual AGN, the low X-ray luminosity of the secondary AGN may be a result of the merger environment (see, e.g., Liu et al. 2013). Here, the X-ray emission is more susceptible to obscuration by the excess of gas at the galaxy center than the optical flux (which is emitted on larger physical scales than the X-ray flux). Indeed, in our spectral analysis we find that SDSS J1448+1825 has one of the largest extragalactic column densities ($> 50 \times 10^{22}$ cm^{-2}). These results confirm those in Comerford et al. (2015), where it was found that dual AGN have systematically lower X-ray luminosities, at a given [O III]λ5007 luminosity, than single AGN.

We note that our measurements of O III/Hβ are susceptible to possible amplification by other effects found in mergers, such as star formation and shocks (e.g., Rich et al. 2011; Kewley et al. 2013; Belfiore et al. 2016). In order to best separate AGN from shock-excited gas, follow-up observations, especially with integral field spectroscopy, will be necessary (D'Agostino et al. 2019). Deeper follow-up observations will also allow for a better spectral decomposition of the two X-ray point sources in SDSS J0752+2736 and SDSS J1448+1825; however due to the extreme spatial extent of the [O III]λ5007 emission in SDSS J1356+1026 (Comerford et al. 2015), cleanly decomposing the two X-ray point source components in O III velocity space is most likely not feasible, even with additional observations.

5.8.4 The Role of the Merger Environment

There is reason to believe that galaxy–galaxy interactions can trigger accretion onto central AGN. In particular, models show that tidal forces between the galaxies can cause gas to be subject to substantial gravitational torques, resulting in substantial gas flow towards the central SMBHs (Barnes & Hernquist 1991b; Mihos & Hernquist 1996; Di Matteo et al. 2008; Hopkins & Hernquist 2009; Anglés-Alcázar et al. 2017b). In this framework we may expect (i) the fraction of dual AGN increases as the separation between the two AGN decreases, and (ii) dual AGN may preferentially reside in gas-rich environments. Regarding (i), such a trend has been found in both simulations and observations. Simulations have been able

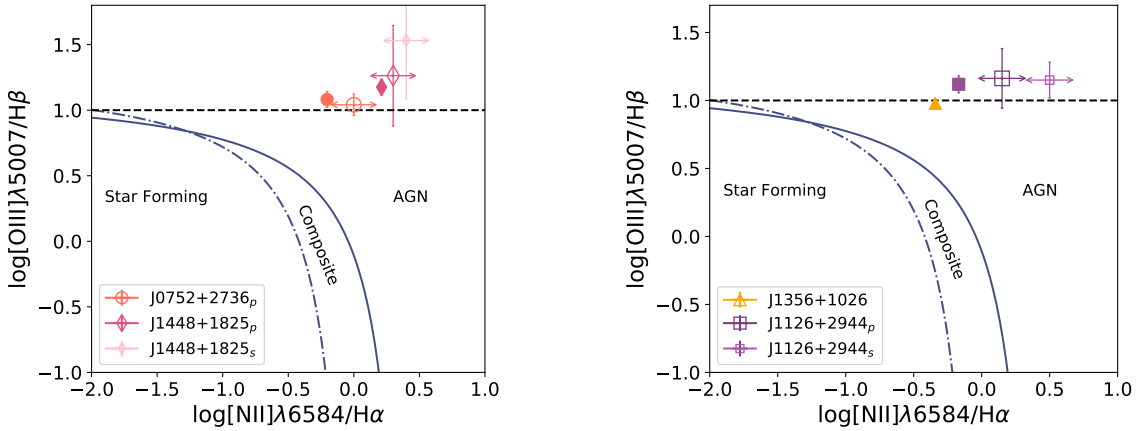

Figure 5.8: BPT optical spectroscopic line ratio diagrams, based on the [O III]/Hβ to [N II]/Hα emission line ratio. The blue lines represent the Kewley et al. (2001) (solid) and Kauffmann et al. (2003) (dot-dashed) demarcations, which separate different sources of photoionizaiton. We plot the line ratios for SDSS J075+2736 and SDSS J1448+1825 in the top panel and those for SDSS J1356+1026 and SDSS J1126+2944 in the bottom panel. We show the average [O III]/Hβ line ratio values for the long-slit data with open markers, where we note that values $\log$ [O III]/H$\beta > 1$ (black dashed line) are consistent with AGN photoionization, at all reasonable $\log$ [N II]/Hα values. Additionally, we show the [O III]/Hβ to [N II]/Hα ratios for each system using available Sloan spectra (filled markers). For each marker we include 1σ error bars. For SDSS J0752+2736$_p$ and SDSS J1356+1026, we find that the line ratios of each system are consistent with AGN photoionization. For SDSS J1448+1825, we find that the line ratios of the primary and secondary X-ray point sources are consistent with AGN photoionization; although the X-ray luminosity of this source is below our AGN luminosity criterion, it's possible that the X-ray emission of the secondary point source is highly obscured. For SDSS J1126+2944, we find that the line ratios of each point source are consistent with AGN photoionization, in agreement with our X-ray analysis. Because we have no N II/Hα for the long-slit data, we choose x-axis coordinates near the respective SDSS measurements.

to probe the smallest separations ($<$ 10 kpc; Blecha et al. 2013; Ellison et al. 2013; Capelo et al. 2017), while most observations have been constrained to the larger separations ($>$ 10 kpc, Koss et al. 2012; Goulding et al. 2018; however, Barrows et al. 2017a probes separations $<$10 kpc and also find that the fraction of dual AGN increases as a function of decreasing separation, including SDSS J1126+2944). Regarding (ii), numerical results from (Steinborn et al. 2016) have found that dual AGN are generally in more gas-rich systems; observationally, such a trend was found in Barrows et al. (2018), where the mean N_H value for a sample of dual AGN was found to be an order of magnitude higher compared to a sample of single AGN.

Taking the six merging galaxies in our sample, as determined visually from the *HST* observations (SDSS J0841+0101, SDSS J0952+2552, SDSS J1126+2944, SDSS J1239+5314, SDSS J1322+2631, and SDSS J1356+1026; note, this list includes two systems that have Bayes factor values strongly in favor of the dual point source model and secondary point sources that meets our AGN luminosity criterion), we plot the separation versus extragalactic column density in Figure 5.9. For SDSS J1126+2944 and SDSS J1356+1026, we plot separation and error between the X-ray point sources, as estimated by `BAYMAX`. For the single X-ray point source systems, we plot the separation and error between the stellar bulges, as measured by Comerford et al. (2015). We note that the two systems for which we are insensitive to any duality (SDSS J0854+5026 and SDSS J1006+4647) are not merging, and thus are not included. Here, N_H is found by fitting the *Chandra* observations of each system with both $m_{\rm spec,1}$ and $m_{\rm spec,2}$.

Because the spectroscopically determined extragalactic column density is model-dependent, the N_H values for $m_{\rm spec,1}$ and $m_{\rm spec,2}$ vary for a given system. By using the simpler spectral model, we are estimating the *average* extragalactic column density surrounding the AGN. Although the majority of these systems are found to have a statistically better spectral fit using $m_{\rm spec,2}$, partial covering and/or the Compton scattering fraction in the torus is difficult to estimate. Thus, the extragalactic column densities estimated with $m_{\rm spec,2}$ are useful for

understanding the magnitude of the column densities in gas clumps, while those estimated with $m_{\rm spec,1}$ are useful for understanding the average column densities across the system. The spectral fits are dominated by the emission of the primary X-ray point source, and thus the N_H measurements mostly pertain to the environments surrounding the primary X-ray point source. However, we interpret the N_H value as representative of the density of gas being torqued to the center of the gravitational potential well, as a result of the galaxy−−galaxy mergers

The placement of SDSS J1126+2944 on Fig 5.9 suggests that dual AGN may prefer systems with both the smallest separations (as previously confirmed by Comerford et al. (2015)) and low average gas-densities (as determined by $m_{\rm spec,1}$). Our measurement indicates that dual AGN activation could indeed be more common for merging galaxies with smaller separations, in agreement with both simulations and observations. However, our measurement of decreasing average N_H as a function separation is at odds with predictions, where dual AGN are expected to reside in environments with higher levels of gas. These results are most likely a result of selection bias; because these systems were originally selected based on their O[III] λ5007 emission, our sample of AGN may generally have lower average extragalactic column densities.

Taking the measured total $L_{\rm [OIII]}$ for each system (Comerford et al. 2015), we find that the systems with the largest N_H values tend to have lower [O III] λ5007 luminosities. Indeed, this confirms the findings of Comerford et al. (2015), where at a given [O III] luminosity, the hard X-ray luminosity of merging galaxies was found to be lower than non-merging AGN, likely due to the high N_H in dual AGN systems. In particular, SDSS J1356+1026 has both the lowest average measured N_H and the highest measured $L_{\rm [OIII]}$. All of these trends can be better understood using a larger sample of dual AGN candidates, selected via X-ray diagnostics. In particular, given our sparse data (and that only *one* of the six merging galaxies are confirmed dual AGN), future analyses with larger samples will be important.

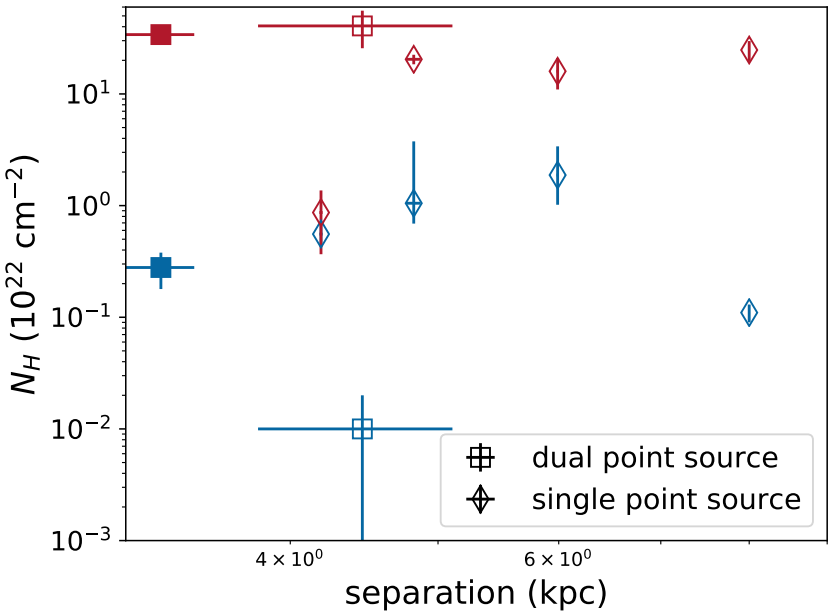

Figure 5.9: Extragalactic column density (N_H, 10^{22} cm^{-2}) vs. separation (kpc) of the six merging systems in our sample using $m_{\rm spec,1}$ (blue) and $m_{\rm spec,2}$ (red). We denote the two systems with Bayes factor values in favor of the dual point source model with squares (SDSS J1126+2944 and SDSS J1356+1026), where the one confirmed dual AGN in our sample (SDSS J1126+2944) is filled-in. The four other systems (with Bayes factor values that favor the single point source model) are denoted with diamonds. Our data suggest that dual AGN activation may be more common for merging galaxies with smaller separations. Although SDSS J1126+2944 has one of the highest N_H values in it's respective gas clump (i.e., N_H as determined by $m_{\rm spec,2}$), we find that the average N_H decreases as a function separation, at odds with predictions, and likely a result of selection bias. Given that only *one* of the six merging galaxies are confirmed dual AGN, future analyses with larger samples will be important to understanding the role of merger environments on SMBH activity.

5.9 Conclusions

In this work, we present our analysis using `BAYMAX`, a tool that uses a Bayesian framework to statistically and quantitatively determine whether a given observation is best described by one or two point sources. We present the results of `BAYMAX` analyzing a sample of 12 dual AGN candidates, originally targeted due to their double-peaked narrow emission lines. Each system received follow-up long-slit spectroscopy, targeting the [O III] λ5007 emission. Using existing *Chandra* data, we carry out a statistical analysis on the X-ray emission, to determine whether the emission is more likely consistent with a single or a dual point source system. The spatially resolved [O III] λ5007 emission components allow for informative priors on the location of the primary and secondary, while complementary *HST* data allow for further analysis on environments of each system. The main results and implications of this work can be summarized as follows:

1. When accounting for contamination from extended diffuse emission, we find that 4 of the 12 systems have Bayes factor values strongly favor of a dual point source: SDSS J0752+2736, SDSS J1126+2944, SDSS J1356+1026, and SDSS J1448+1825. For SDSS J0752+2736 we calculate $\ln \mathcal{B} = 4.90 \pm 0.51$; for SDSS J1126+294 we calculate $\ln \mathcal{B} = 3.54 \pm 0.43$; for SDSS J1356+1026 we calculate $\ln \mathcal{B} = 8.70 \pm 0.70$; and for SDSS J1448+1825 we calculate $\ln \mathcal{B} = 2.95 \pm 0.52$. One of these systems, SDSS J0752+2736, has $\mathcal{B}$ in favor of a dual point source system only when using non-informative priors, while the remaining systems have $\mathcal{B}$ in favor of a dual point source system when using both informative and non-informative priors on the location of the putative secondary. For the latter case, the Bayes factor values are all stronger when using informative priors, defined by the complementary [O III] λ5007 observations.

2. For the 4 dual AGN candidates, we analyze the strength of each Bayes factor value via false-positive tests. For each of the dual AGN candidates, we find there is a $> 99.9\%$ chance that the systems are composed of dual point sources. Based on these runs, we

conclude that each system has a "strong" Bayes factor.

3. We estimate the best-fit separation (r) and count ratio ($\log f$), as well as their uncertainties, for each dual AGN candidate. For SDSS J0752+2736 we find $r = 1.5'' \pm 0.30''$ and $\log f = -0.47 \pm 0.36$; for SDSS J1126+2944 we find $r = 1.74'' \pm 0.33''$ and $\log f = -1.00 \pm 0.44$; for SDSS J1356+1026 we find $r = 2.00'' \pm 0.62''$ and $\log f = -0.92 \pm 0.23$; and for SDSS J1448+1825 we find $r = 1.29'' \pm 0.52''$ and $\log f = -0.45 \pm 0.80$.

4. We investigate the nature of each dual AGN candidate by analyzing each point source's spectrum. Because `BAYMAX` assigns each count a probability of being associated with different model components, we are capable of fitting the spectrum of each individual X-ray point source in a given system. We find that the secondary X-ray point sources in SDSS J1126+2944 and SDSS J1356+1026 both meet our AGN luminosity criterion ($L_{2-7 \text{ keV,unabs}} > 10^{40}$ erg s^{-1}). However, because the softer spectrum of the secondary in SDSS J1356+1026 ($\Gamma \approx 3.0 \pm 0.64$) is consistent with spectrum of the diffuse emission ($\Gamma \approx 3.2 \pm 0.25$), we conservatively do not classify this system as a dual AGN. Lastly, although the X-ray emission from SDSS J0752+2736 and SDSS J1448+1825 are better described by dual point sources, the secondaries do not meet our AGN luminosity criterion and are most susceptible to contamination from XRBs.

5. For the 8 systems that have Bayes factor values that favor a single point source, we investigate how the Bayes factor determined by `BAYMAX` depends on the count ratio of simulated dual AGN systems with comparable counts, separations, and background fractions. For 2 of these systems, SDSS J0854+5026 and SDSS J1006+4647, we are unable to correctly identify that the emission is consistent with two X-ray point sources, for any count ratio between 0.1–1.0. This is a result of the low number of counts ($\approx$ 13 total counts between 0.5–8.0), as well as small angular separation ($< 1''$) assumed between the primary and secondary. However, for the remaining 6 systems, we are able to correctly identify a dual AGN system for the majority of count ratios analyzed.

This corresponds to an upper-limit luminosity threshold $4 \times 10^{40} < L_{2-7\mathrm{keV}} < 6 \times 10^{41}$ for the secondary AGN. Thus, our dual AGN fraction of 1/12 represents a lower-limit on the true dual AGN fraction of the sample.

6. We re-plot the *WISE* mid-infrared colors of the four systems with Bayes factor values in favor of the dual point source model to test whether our dual AGN candidates lie in an interesting region of IR color-color space. We confirm that only one of the four systems, SDSS J1356+1026, has an AGN-dominated mid-infrared flux. Additionally, SDSS J1356+1026 and SDSS J0752+2736 lie above a less-stringent color-cut that has been found to select both merger-triggered AGN and dual AGN.

7. We analyze how the [O III]/Hβ and [N II]/Hα ratios compare to the line ratio BPT diagram for the four systems with Bayes factor values in favor of the dual point source model. We use available long-slit optical spectroscopic data for SDSS J0752+2736, SDSS J1126+2944, and SDSS J1448+1285 (Comerford et al. 2012); while we use archival Sloan spectral data for SDSS J1356+1026. For SDSS J0752+27364$_p$ and SDSS J1356+1026, we find that the line ratios of each system are consistent with AGN photoionization. For SDSS J1448+1825, we find that the line ratios of the primary and secondary X-ray point sources are consistent with AGN photoionization; although the X-ray luminosity of this source is below our AGN luminosity criterion, it's possible that the X-ray emission of the secondary point source is highly obscured. For SDSS J1126+2944, we find that the line ratios of each point source are consistent with AGN photoionization, in agreement with our X-ray analysis.

8. Lastly, we investigate whether the merger environment plays a role in the triggering of dual AGN. Taking the six merging galaxies in our sample, we compare the separation and the extragalactic column density of each system. Our data suggest that dual AGN may prefer merger environments with both the smallest separations and N_H values. Thus, dual AGN activation may be more common for merging galaxies with smaller

separations, in agreement with both simulations and observations. However, given our sparse data (and that only one of the six merging galaxies are dual AGN), it will be important to study such trends in the future with larger samples.

Using a quantitative and statistical tool, we have confirmed one known dual AGN system (SDSS J1126+2944). Specifically, `BAYMAX` estimates a Bayes factor strongly in favor of the dual point source model for each system, and our spectral analysis has confirmed that emission from each point source is consistent with that expected from an AGN. In the future, we plan to use `BAYMAX` on larger samples of *Chandra* observations in order to constrain the rate of dual AGN across our visible universe. Additionally, using larger samples of dual AGN candidates we can begin to robustly measure the types of environments dual AGN prefer, allowing for a better understanding of black hole growth and its relation to galaxy–galaxy interactions.

We thank the referee for thorough and thoughtful comments that strengthened the chapter. A.F. and K.G. acknowledge support provided by the National Aeronautics and Space Administration through *Chandra* Award Number TM8-19007X issued by the *Chandra* X-ray Observatory Center, which is operated by the Smithsonian Astrophysical Observatory for and on behalf of the National Aeronautics Space Administration under contract NAS8-03060. We also acknowledge support provided by the National Aeronautics and Space Administration through *Chandra* Award Number GO7-18087X issued by the *Chandra* X-ray Observatory Center, which is operated by the Smithsonian Astrophysical Observatory for and on behalf of the National Aeronautics Space Administration under contract NAS8-03060. This research has made use of NASA's Astrophysics Data System.

CHAPTER VI

The True AGN Triality of Triple Mergers: An X-ray Perspective

6.1 Preface

Results in this chapter are a work in progress and will be published in *Foord, A. & Gültekin, K. in prep.*, to be submitted to the Astrophysical Journal.

6.2 Introduction

Systems with multiple supermassive black holes (SMBHs) are expected as a result of hierarchical galaxy formation (e.g., White & Rees 1978). In particular, if two massive galaxies are in the process of merging, it is expected that dynamical friction will drag their respective nuclear SMBHs toward the center of the gravitational potential well (see, e.g., Begelman et al. 1980). Through the process of merging, significant quantities of gas can be efficiently funneled down to physical scales at which the SMBHs can accrete – and the multiple SMBH systems can become multiple active galactic nuclei (AGN; Barnes & Hernquist 1991a; Di Matteo et al. 2008; Anglés-Alcázar et al. 2017a). Thus, multi-AGN systems are signposts of ongoing galaxy formation, and represent unique systems where the link between environment and activity (or, lack thereof) can be probed.

Studying the properties of multiple AGN systems, in a systematic manner, is especially important given the unknown magnitude that mergers play in SMBH growth and evolution. There is strong reason to believe that interplay between host galaxies and their respective SMBHs during mergers exist. Galaxy-mergers are thought to be a key process behind the various empirical SMBH-galaxy scaling relations, such as the relation between the supermassive black hole mass and host-galaxy bulge velocity dispersion ($M - \sigma$ relation) and luminosity ($M - L$ relation; Magorrian et al. 1998; Ferrarese & Merritt 2000; Tremaine et al. 2002; Gültekin et al. 2009b; McConnell & Ma 2013). These relations likely arise due to a combination of repeated mergers (Jahnke & Macciò 2011), triggered feedback processes from the AGN (Hopkins et al. 2006), and triggered star formation (Sobral et al. 2015). Yet, the connection between mergers and SMBH activity remains poorly understood; and it is currently unknown to what effect mergers are responsible for, or even correlated with, SMBH activity (Urrutia et al. 2008; Glikman et al. 2015; Treister et al. 2012; Fan et al. 2016; Schawinski et al. 2012; Villforth et al. 2014; Koss et al. 2010; Ellison et al. 2013; Satyapal et al. 2014; Weston et al. 2017; Barrows et al. 2018; Goulding et al. 2018). Past measurements were likely complicated by (1) AGN variability, (2) the difficulty in measuring higher-redshift mergers, and (3) the obscuration and merger-stage dependency of AGN activity. Thus, one of the best ways to analyze the possible ties between merger environments and SMBH activity is to study systems with unique observational flags of merger-driven SMBH growth - such as multi-AGN. Furthermore, studying the multi-AGN systems in X-rays, which are less affected by obscuration than optical diagnostics and represent a larger fraction of the AGN population than radio emitters, will result in the most complete study.

An important subset of the multi-SMBH population are triple SMBHs, and in particular, *nearby* triple SMBHs. Nearby triple SMBHs ($z < 0.3$) are theorized to play important roles in the coalescence of SMBHs and the stochastic gravitational wave background (GWB). For example, without additional interactions from a tertiary SMBH, two interacting SMBHs may not merge within the Hubble time due to an empty loss cone (Milosavljević & Merritt 2003a),

producing a stochastic GWB undetectable by pulsar timing arrays (PTAs; "the nightmare scenario", Dvorkin & Barausse 2017). Although triaxial potentials have been shown to prevent SMBH stalling (Vasiliev et al. 2015), it is not clear that triaxiality will sufficiently refill the loss cone in time (Merritt & Valluri 1996). More importantly, the process of two SMBHs becoming bound via dynamical friction may be far slower than initially thought (Tremmel et al. 2015), and it has recently been found that gas dynamics may cause the pair of SMBHs to stall at $\sim$1 kpc (Muñoz et al. 2019; Duffell et al. 2019). Interactions with a third SMBH can enhance the loss cone refilling rate by disturbing stellar orbits (Perets & Alexander 2008), shrinking the binary semimajor axis and increasing the eccentricity via the Kozai–Lidov mechanism (Blaes et al. 2002). All these effects can dramatically reduce the merger time of binaries by more than a factor of 10 (Blaes et al. 2002). On top of this, it is predicted that the SMBH binary population driving the detectable GWB signal comes from redshifts close to $z = 0.3$ (Kelley et al. 2017), and thus the rate of nearby triple AGN has significant implications for the GWB measurable with PTAs. Lastly, triple SMBH are expected to be common. A recent study on Illustris SMBH binaries found that >30% of AGN pairs have subsequent merger events, over a large range of redshift (Kelley et al. 2017), while analysis of the Millennium simulation found that 42% of massive ($10^{11} < M_\star < 10^{12}$) galaxies undergo more than one significant merger (Ryu et al. 2018).

However, to date, only one serendipitously discovered X-ray triple AGN has been identified (Pfeifle et al. 2019b). This is likely due to (i) observational constraints and (ii) the lack of systematic surveys searching for triple AGN. Regarding (i), confirmation of multi-AGN systems requires high spatial resolution X-ray observations. Although other wavelengths and techniques are useful for finding candidate multi-AGN systems, they are not enough on their own. For example, double-peaked optical emission lines are insufficient to confirm dual AGN due to ambiguity in interpretation, as single AGN spectra are known to also have double-peaked characteristics (Comerford et al. 2015; Nevin et al. 2016). On top of this, it is difficult to identify multi-AGN using optical line diagnostics as a result of optical extinction

and contamination from star formation (e.g., Koss et al. 2012). This is especially problematic for multi-AGN systems, as late-stage mergers tend to be highly obscured (Blecha et al. 2018b). X-rays are thus crucial to detecting closely separated triple AGN. Nuclear point sources with 2–10 keV X-ray luminosities $L_X > 10^{40}\,\mathrm{erg\,s^{-1}}$ are almost always SMBHs (Foord et al. 2017a; Lehmer et al. 2019), and *Chandra* can uniquely resolve them. Although various X-ray surveys targeting dual AGN exist, all X-ray confirmed dual AGN have large physical separations (Deane et al. 2014) and count ratios ($f \sim 1$, where f represents the ratio of the X-ray counts associated with the secondary to that of the primary AGN). We have developed `BAYMAX`, a code that quantitatively and rigorously analyzes whether a given *Chandra* source is more likely composed of one or multiple point sources (Foord et al. 2019, 2020). `BAYMAX` (i) takes calibrated *Chandra* events and compares them to the expected distribution of counts for single/multiple point source models; (ii) calculates a Bayes factor to determine which model is preferred, automatically taking into account model complexity; (iii) calculates likely values for separations (r) and count ratios (f); and (iv) fits spectra to each component. Analyses without `BAYMAX` are likely to lead to false negatives/positives (e.g., Koss et al. 2015; Foord et al. 2020), especially systems with small separations ($r < 1''$) and observations with low counts (≤ 200).

Regarding (ii), in this chapter we present the first targeted search for nearby triple AGN. In particular, we analyze a sample of 7 optically-identified, nearby ($z < 0.1$), triple galaxy-mergers, that have existing archival *Chandra* data. We analyze the *Chandra* observations using `BAYMAX`, with the goal of identifying closely-separated and faint multi-AGN systems that may otherwise go undetected. Combining the X-ray observations with archival *Wide-field Infrared Survey Explorer* (*WISE*) observations, we aim to learn more about the preferential environments of each multi-AGN candidate. The *Chandra* observations of 3 of these triple merger systems were previously analyzed in studies focusing on multi-AGN (Pfeifle et al. 2019b; Bianchi et al. 2013), which we now re-analyze via our robust statistical analysis. The remaining 4 have no existing analyses of their *Chandra* observations.

The remainder of the chapter is organized into 5 sections. In section 6.3 we introduce the sample and the existing multi-wavelength coverage. In section 6.5 we present our results from running `BAYMAX` on the *Chandra* observations and quantify the strength of each result. In section 6.6 we analyze the nature of each multiple AGN candidate by evaluating the best-fit parameters and spectral fits returned by `BAYMAX`, and discussing possible sources of contamination. In section 6.7 we classify the remaining single point source systems, and compare environmental properties between the single, dual, and triple AGN. Lastly, we summarize our findings in section 6.8. Throughout the chapter we assume a ΛCDM universe, where $H_0 = 69.6$, $\Omega_M = 0.286$, and $\Omega_\Lambda = 0.714$

6.3 Sample

Our sample was created by cross-matching the AllWISE AGN catalog (Secrest et al. 2015) with the Sloan Digital Data Survey Data Release 16 (SDSS DR16) catalog (Ahumada et al. 2019), for all AGN within $z < 0.3$. We visually identify systems composed of three interacting galaxies via the SDSS DR16 data, and we further filter the sample by enforcing that (i) a photometric or spectroscopic redshift measurement is available for each galaxy in a triple merger system and (ii) that the respective redshifts of each galaxy in a triple merger system are consistent with one another at the 3σ confidence level. While spectroscopic measurements of the redshift are generally well constrained (with fractional errors on the order of $\sim 10^{-3}$), photometric measurements of the redshift tend to have larger error bars and are estimated estimated by SDSS via the kd-tree nearest neighbor fitting procedure (see Csabai et al. 2007 for explicit details). Thus, because at least one galaxy member in each triple merger has a spectroscopic redshift measurement, we assume this value for all members (see Table 6.1). From this larger sample, 4 systems have existing, on-axis, archival *Chandra* observations: SDSS J1708+2153, SDSS J2356−1015, SDSS J1631+2252, SDSS J0849+1114. To this list, we add 3 triple galaxy mergers from the literature with archival *Chandra* and SDSS DR16 observations that meet our redshift criteria as described above: NGC 3341

Table 6.1: Triple Galaxy Merger Sample Properties

Galaxy Name	α	δ	Redshift	D_A (Mpc)	$\Delta\theta$ ($''$)	r (kpc)
SDSS J084905.51+111447.2	08:49:05.51	+11:14:47.26	0.078	306.4	–	–
SDSS J084905.51+111447.2 NW	08:49:05.43	+11:14:50.97	–	–	3.6	5.3
SDSS J084905.51+111447.2 SW	08:49:05.41	+11:14:45.94	–	–	2.3	3.4
SDSS J085837.67+182223.3	08:58:37.67	+18:22:23.35	0.059	236.9	–	–
SDSS J085837.67+182223.3 SW	08:58:37.52	+18:22:21.56	–	–	2.8	3.2
SDSS J085837.67+182223.3 SE	08:58:37.85	+18:22:22.43	–	–	2.8	3.2
SDSS J102700.40+174900.8	10:27:00.56	+17:49:00.38	0.066	262.9	–	–
SDSS J102700.40+174900.8 N	10:27:00.38	+17:49:02.89	–	–	3.6	4.6
SDSS J102700.40+174900.8 W	10:27:00.39	+17:49:00.95	–	–	2.4	3.0
NGC 3341	10:42:31.75	+05:02:52.82	0.027	112.6	–	–
NGC 3341 SW	10:42:31.47	+05:02:37.80	–	–	15.6	8.5
NGC 3341 NW	10:42:32.05	+05:02:41.95	–	–	9.6	5.2
SDSS J163115.52+235257.5	16:31:15.52	+23:52:57.51	0.059	236.9	–	–
SDSS J163115.52+235257.5 NE	16:31:15.62	+23:52:59.56	–	–	2.5	2.9
SDSS J163115.52+235257.5 NW	16:31:15.41	+23:53:08.44	–	–	11	12.6
SDSS J170859.12+215308.0	17:08:59.12	+21:53:08.08	0.072	284.8	–	–
SDSS J170859.12+215308.0 NE	17:08:59.42	+21:53:13.51	–	–	6.6	9.1
SDSS J170859.12+215308.0 SW	17:08:58.40	+21:53:05.12	–	–	10.5	14.5
SDSS J235654.30-101605.3	23:56:54.30	-10:16:05.31	0.074	292.0	–	–
SDSS J235654.30-101605.3 SE	23:56:54.49	-10:16:07.40	–	–	3.5	4.9
SDSS J235654.30-101605.3 NE	23:56:54.78	-10:16:01.06	–	–	8.2	11.6

Note. – Columns: (1) Galaxy name; (2) R.A. and (3) Dec. (J2000) from SDSS DR16; (4) spectroscopic redshift from SDSS DR16; (5) angular diameter distance; (6) angular separation from primary galaxy; (7) projected physical separation from primary galaxy.

(Bianchi et al. 2013), SDSS J0858+1822 (Liu et al. 2011b) and SDSS J1027+1749 (Liu et al. 2011a). Thus, while all of our triple mergers have *Chandra* and SDSS DR16 coverage, only 4 are included in the AllWISE AGN catalog.

The *Chandra* observations of 3/7 systems in our sample have been previously analyzed for the presence of multiple AGN: SDSS J0849+1114 (a triple AGN system; Liu et al. 2019; Pfeifle et al. 2019b), NGC 3341 (a single AGN system; Bianchi et al. 2013), and SDSS J2356−1016 (classified as a single AGN system; Pfeifle et al. 2019a). The remaining four systems have no existing analyses on the possible multiplicity of AGN in the *Chandra* observations, although SDSS J1027+1749 was claimed as triple AGN in Liu et al. (2011a) based on optical emission diagnostics. Re-visiting these galaxies using `BAYMAX`, we aim to identify new X-ray point sources, as well as re-evaluate the true nature of the previously

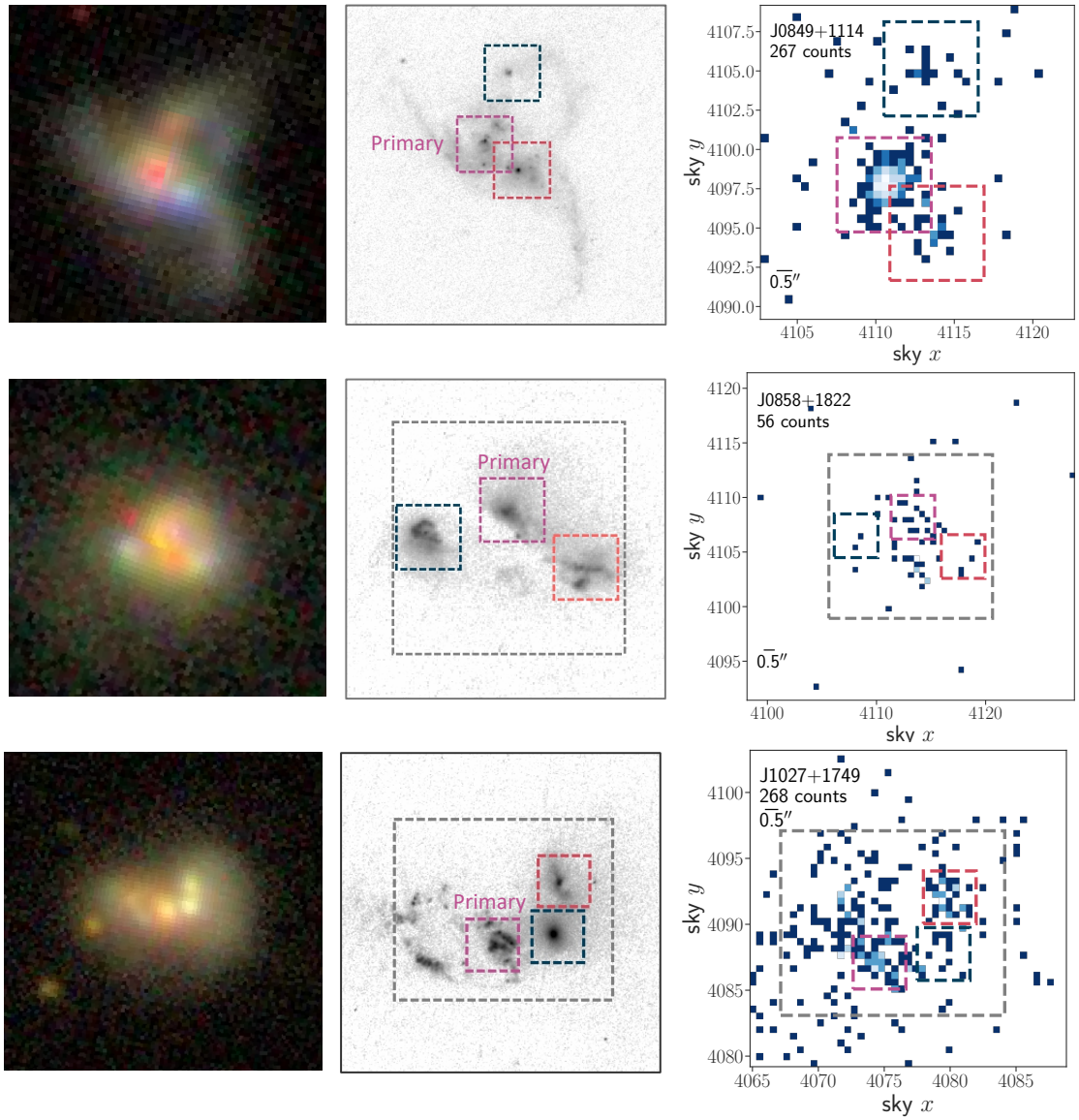

Figure 6.1: SDSS gri color composite observations (*left*), *HST* F366W observations (*center*), and *Chandra* 0.5–8 keV observations (*right*) of the triple mergers in our sample with *HST* observations. In the *HST* and *Chandra* datasets, we show the sky x, sky y region, within which the informative priors for μ are constrained to in purple, red, and blue boxes. When using non-informative priors, the central locations for the primary and secondary are allowed to be anywhere within the X-ray image. For SDSS J0858+1822 and SDSS J1027+1729 we denote the region within which the diffuse emission background component is restricted to with a gray box. Additionally, for SDSS J0849+1114 we show the combined X-ray emission for all *Chandra* observations, where we use the best-fit astrometric shift values as found by `BAYMAX`. The X-ray images have been binned to *Chandra*'s native pixel resolution. In all panels, north is up and east is to the left, and a 0.″5 bar is shown to scale.

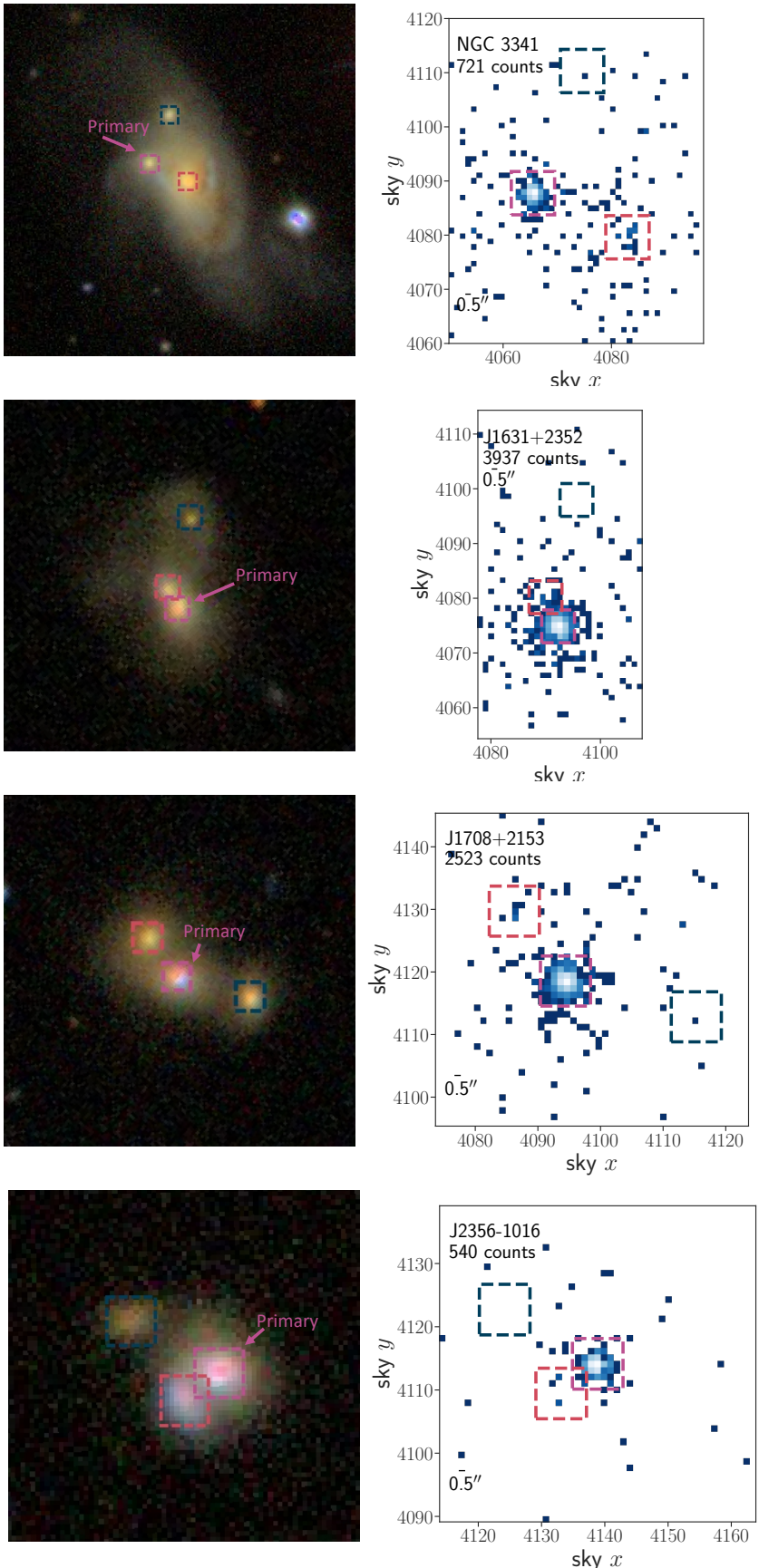

Figure 6.2: SDSS gri color composite observations (*left*), and *Chandra* 0.5–8 keV observations (*right*) of the triple mergers in our sample with no *HST* observations.

Table 6.2: *Chandra* Observation Information

Galaxy Name	*Chandra* Obs. ID	*Chandra* Exp. Time (s)
SDSS J084905.51+111447.2	14969	19800
–	18196	20980
SDSS J085837.67+182223.3	14970	19800
SDSS J102700.40+174900.8	14971	49410
NGC 3341	13871	49330
SDSS J163115.52+235257.5	13901	18150
SDSS J170859.12+215308.0	13903	18200
SDSS J235654.30-101605.3	18195	8620

Note. – Columns: (1) Galaxy name; (2) *Chandra* Observation ID; (3) exposure time of *Chandra* observation

claimed multi-AGN systems. The galaxies are located at redshifts $0.059 < z < 0.078$, and three (SDSS J0849+1114, SDSS J0858+1822, SDSS J1027+1749) have additional multiband HST/WFC3 (F506W and F5336W) imaging (PI: Liu, Proposal ID: 13112). In Table 6.1 we list the properties of each triple merger system, while in Table 6.2 we list the *Chandra* observation information.

6.3.1 X-ray Data Analysis

Each *Chandra* observation was on-axis and placed on the back-illuminated S3 chip of the ACIS detector. We follow a similar data reduction as described in previous *Chandra* analyses searching for AGN (e.g., Foord et al. 2017a,b, 2019, 2020), using *Chandra* Interactive Analysis of Observations software (`CIAO`) v4.12 (Fruscione et al. 2006).

We first correct for astrometry, cross-matching the *Chandra*-detected point-like sources with the SDSS Data Release 9 (SDSS DR9) catalog. The *Chandra* sources used for cross-matching are detected by running `wavdetect` on the reprocessed level-2 event file. We require each observation to have a minimum of 3 matches with the SDSS DR9, and each matched pair to be less than $2''$ from one another. Five of the seven systems meet the criterion for astrometrical corrections, while the remaining 2 observations were taken in sub-arrays and do not have enough X-ray point sources to match with the SDSS DR9 catalog. However, we note that the lack of astronomical corrections have no effect on our X-ray data analysis, as

the locations of each putative AGN are assumed to be relative to the primary X-ray point source, and our prior distributions for locations of each AGN are wide enough to account for the relative astrometric shifts between the *Chandra* and optical observations (see Section 6.4 for more details). Lastly, for each observation we find the background flaring contribution to be negligible, with no time interval containing a background rate 3σ above the mean level.

6.4 Methods

To analyze each *Chandra* observation for the presence of multiple X-ray point sources, we use `BAYMAX` (Bayesian AnalYsis of Multiple AGN in X-rays). `BAYMAX` is a tool designed to quantitatively evaluate whether a given *Chandra* observation is a single or multiple point source via a Bayesian framework (Foord et al. 2019, 2020). `BAYMAX` is especially powerful for systems with low count ratios between the AGN ($0.1 < f < 1.0$), and angular separations below $0\farcs5$. In particular, analyses on multi-AGN systems in the low-f and/or low-r regime without `BAYMAX` are likely to lead to false negatives/positives (e.g., Koss et al. 2015; Foord et al. 2020). With `BAYMAX`, we've analyzed many low count ratio dual AGN candidates, and are methodically expanding the small group of X-ray confirmed dual AGN (Foord et al. 2020).

In order to determine the likelihood of a given triple merger hosting multiple AGN, `BAYMAX` calculates the Bayes factor (hereafter denoted by $\mathcal{B}$). The Bayes factor represents the ratio of the marginal likelihood of two competing hypotheses. The value can be interpreted as a measure of the strength of evidence in favor of one hypothesis over the other. The Bayes factor can be defined mathematically as:

$$\mathcal{B}_{j/i} = \frac{\int P(D \mid \theta_j, M_j) P(\theta_j \mid M_j) d\theta_j}{\int P(D \mid \theta_i, M_i) P(\theta_i \mid M_i) d\theta_i} \tag{6.1}$$

Here, the marginal probability density of the observed data D under one model (M) is represented by $P(D \mid \theta, M)$, while each model is parameterized by a parameter vector, θ,

and thus the prior densities are represented by $P(\theta \mid M)$. Regarding our X-ray analysis on the triple galaxy mergers, we calculate the evidence for three different models: a single point source model (i.e., the data are consistent with the X-ray emission of a single AGN; M_1), a dual point source model (M_2), and a triple point source model (M_3). Thus, we calculate the Bayes factor twice, comparing the evidence of the dual point source model to that of the single point source model ($\mathcal{B}_{2/1}$), and the evidence of the triple point source model to the dual point source model ($\mathcal{B}_{3/2}$).

The main components of `BAYMAX` are as follows: (i) take calibrated *Chandra* events and compare them to the expected distribution of counts for single/multiple point sources models; (ii) calculate a Bayes factor to determine which model is preferred; (iii) calculate likely values for separations (r) and count ratios (f); and (iv) fit spectra to each model component. Regarding step (i), the probability densities of each model are estimated by comparing the sky coordinates (x, y) and energies (E) of each detected X-ray event to simulations based on single and multiple point source models. The properties of the *Chandra* PSF are characterized by simulating the PSF of the optics with `MARX` (Davis et al. 2012). For a source with multiple observations, `BAYMAX` first models the PSF of each observation and calculates the likelihoods for each observation individually (which is expected to depend on the detector position and start time of the observation), and then fits for astrometric shifts between different observations of the same source. Regarding step (ii) and (iii), `BAYMAX` uses nested sampling (Skilling 2004) to estimate the evidence of each model (and in particular, the tool uses the `PYTHON` package `nestle`[1]) and uses `PyMC3` (Salvatier et al. 2016) for parameter estimation. Below, we review the details of the prior densities used when running `BAYMAX` on observations of our triple galaxy merger sample. We refer the reader to Foord et al. (2019, 2020) for an in-depth review of the statistical techniques used to estimate likelihoods and posterior densities.

[1]https://github.com/kbarbary/nestle

6.4.1 Prior Densities

For all models, each photon is assumed to originate from either a point source component or the background. Thus, M_1 is parameterized by vector $\theta_1 = [\mu, \log f_{bkg}]$, while M_2 and M_3 are parameterized by vector $\theta_{2,3} = [\mu_N, \log f_n, \log f_{bkg}]$. Here, μ_N represents the location for N point sources ($N = [1, \ldots, N]$); f_{bkg} represents the ratio of counts between the background and the combined counts from all point source components; f_n represents the ratio of the total counts between a given point source and the primary point source ($n = [2, \ldots, N]$), and in Fig. 6.1 we show which X-ray point source we classify as the primary. For the one system with multiple observations (SDSS J0849+1114, see Table 6.2), the parameter vectors additionally include Δx_k and Δy_k, which account for the translational components of the relative astrometric registration for the $k = [1, ..., K-1]$ observation (where $K = 2$ for SDSS J0849+1114). For a single point source, the probability that a photon observed at sky coordinate (x, y) with energy E is described by the PSF centered at μ is $P(x, y \mid \mu, E)$, while for multiple point sources the total probability is $P(x, y \mid \mu_N, E, f_n, f_{\rm bkg})$.

We assume that events associated with the background are uniformly distributed across a given region, such that the probability that a photon observed at location x,y on the sky with energy E is associated with a background component is $P(x, y \mid f_{bkg}, E)$. Because we assume that each background component is uniformly distributed, $P(x_i, y_i \mid f_{bkg}, E)$ is always constant over a given region of interest. With this current model, it is possible that a spatially uniform background with a higher count-rate sitting among a spatially uniform background with a lower count-rate can be mistaken for a resolved point source. Specifically, 2 of the 7 triple merger systems (SDSS J0858+1822 and SDSS J1027+1749), show evidence in their *Chandra* observations for a a high-count, diffuse, emission surrounding the galactic nuclei (see Fig. 6.1). Extended, hot, gas is frequently detected in both simulations and observations of merging systems (see, e.g., Cox et al. 2006; Brassington et al. 2007; Sinha & Holley-Bockelmann 2009; Hopkins et al. 2013; Smith et al. 2018; Foord et al. 2020). For example, multiple analyses on dual AGN candidate SDSS J0841+0101 have found that the

emission is well-described by two point sources (Pfeifle et al. 2019a; Foord et al. 2020), but in Foord et al. (2020) we found that a uniform, high-count, distribution better explains the X-ray emission associated with secondary galactic nucleus, instead of point-like emission from an AGN. Thus, for SDSS J0858+1822 and SDSS J1027+1749 we add an additional background component to our model. In Figure 6.1 we show these additional regions of background components in gray dash-dotted regions, where the position and size of these regions are chosen such that they cover the majority of the optical emission of the triple galaxy merger, as determined from the SDSS DR16 observations. Within these regions, `BAYMAX` fits for a different background fraction, f_{diff} than for outside these regions.

All prior distributions of μ for all models are described by continuous uniform distributions. When using non-informative priors, the coordinates of each μ are allowed to be anywhere within a given region centered on the X-ray source centroid position; when using informative priors, the coordinates of each μ are defined by the locations of the galaxy nuclei as determined in the SDSS DR16 observations shown in Figure 6.1. We note that our informative prior distributions for μ are wide enough to account for the relative astrometric shifts between the *Chandra* and optical observations ($> 1''$). The prior distribution of $\log f_{bkg}$ is described by a truncated Gaussian distribution, $N(\mu_{bkg}, \sigma^2_{bkg})$, where μ_{bkg} is estimated by evaluating the count-rate in 10 random and source-free regions within a $20''$ radius of the X-ray source centroid position. We set σ_{bkg} to 0.5, allowing for `BAYMAX` to easily move in parameter space, and we truncate $\log f_{bkg}$ at -3 and 0. For M_2 and M_3, the prior distributions of $\log f_n$ are described by uniform distributions and are constrained between -4 and 4, accounting for a large range of possible count fractions between the X-ray emission of the AGN (and allowing for instances where the secondary or tertiary point source has more counts than the primary). For SDSS J0849+1114, the prior distributions of Δx_1 and Δy_1 are described by a uniform distribution constrained between $\delta\mu_{\rm obs} - 3$ and $\delta\mu_{\rm obs} + 3$, where $\delta\mu$ represents the difference between the observed central X-ray coordinates of two given observations. Here, we define Δx_k and Δy_k relative to the longest observation (ObsID:

18196). Lastly, for SDSS J0858+1822 and J1027+1749, the prior distribution of $\log f_{diff}$ is described by a uniform distribution constrained between -2 and 0.

6.5 Bayes Factor Results

For each observation, we restrict our analysis to photons with energies between 0.5–8 keV. We analyze the photons contained within rectangular regions that are centered on the midpoint of the nominal X-ray coordinates of the three point sources, $\mu_{\rm obs}$. The sky x- and and y-lengths of each rectangle are defined as l_x and l_y, where l_x and l_y vary between 20 and 60 sky-pixels for each observation ($9.9''$ and $29.7''$, respectively. See Figure 6.1). Most analyses use square regions with l_x=l_y, however we use a rectangular region for our analysis of NGC 3341 to avoid the inclusion of a nearby, bright, X-ray source (not associated with the triple merger) and our analysis of SDSS J1631+2532 due to the large ($\sim$4000) number of 0.5$-$8 keV counts in the observation. In the latter case, this helps to lower the computational time (as the probability densities are calculated by summing the log probability of each individual X-ray event, and thus the computational time increases as a function of X-ray events analyzed). The known asymmetric *Chandra* PSF feature is within this extraction region (Juda & Karovska 2010), and sits approximately $0\farcs7$ from the center of the AGN. Because our PSF model does not take into account this asymmetry, we mask the feature in all exposures before running `BAYMAX`.

For each galaxy, we run `BAYMAX` using non-informative priors — where the prior distributions for μ are uniform distributions bound between ($\mu_{\rm obs} - \frac{l_x}{2}$, $\mu_{\rm obs} + \frac{l_x}{2}$) and ($\mu_{\rm obs} - \frac{l_y}{2}$, $\mu_{\rm obs} + \frac{l_y}{2}$) — and informative priors — where the distributions for μ are constrained by and centered on each galaxy in the triple merger system (see Figure 6.1). Here, the sky x and sky y limits of each prior distribution were determined by visually identifying the possible extent of a galactic nucleus via the optical observations.

Of the seven triple mergers, using informative priors, we find 1 that favors the triple X-ray point source model (SDSS J0849+1114), 5 that favor the dual X-ray point source model

Table 6.3: Bayes Factor Results

Galaxy Name	$\ln \mathcal{B}_{2/1}$	$\ln \mathcal{B}_{3/2}$ (s)	$\ln \mathcal{B}_{2/1,\mathrm{inform}}$	$\ln \mathcal{B}_{3/2,\mathrm{inform}}$
SDSS J0849+1114	23.40 ± 1.90	22.40 ± 2.10	25.60 ± 1.40	19.40 ± 1.90
SDSS J0858+1822	-2.30 ± 3.60	2.10 ± 3.82†	0.63 ± 1.00	-0.76 ± 1.12
SDSS J1027+1749	28.50 ± 4.40	-4.50 ± 5.30	34.20 ± 1.80	-0.10 ± 1.90
NGC 3341	22.50 ± 1.80	...	2766.90 ± 1.60	-0.14 ± 1.40
SDSS J1631+2352	2.70 ± 1.90	2.31 ± 3.82†	6.20 ± 1.60	-0.81 ± 1.90
SDSS J1708+2153	16.60 ± 1.90	0.48 ± 3.90	18.40 ± 1.60	-1.90 ± 1.80
SDSS J2356−1016	0.70 ± 1.60	-0.95 ± 3.20	3.10 ± 1.30	-2.30 ± 1.40

Note. – Columns: (1) Galaxy name; (2) and (3) Bayes factor in favor of dual point source model and triple point source model, using non-informative priors on the locations (μ) of the point sources; (4) and (5) Bayes factor in favor of dual point source model and triple point source model, using informative priors on the locations (μ) of the point sources. Error bars represent the 99.7% confidence intervals. For NGCC 3341, the computational time required to estimate $\ln \mathcal{B}_{3/2}$ with the current models is on the order of months, however the data appear to favor the dual point source model over the triple point source model based on limited runs.
† – Although $\ln \mathcal{B}_{3/2}$ favors the triple point source model for these two systems, we emphasize that they are consistent with 0 at the 99.7% C.L. For SDSS J1027+1749, the triple point source model is *not* favored over the single point source model i.e, $\ln \mathcal{B}_{3/1} \approx -0.15$. These results are likely due to clumpy, diffuse, X-ray emission, see Section 6.7 for more details.

(SDSS J1027+1749, NGC 3341, SDSS J1631+2352, SDSS J1708+2153, SDSS J2356−1016) and 1 that favors the single point source model (SDSS J0858+1822). Here, if both $\ln \mathcal{B}_{1/2,\mathrm{inform}}$ and $\ln \mathcal{B}_{3/2,\mathrm{inform}}$ are consistent with 0, we classify the system as favoring the single point source model. In most cases where the Bayes factor favors a multi-point source model: (i) the Bayes factor favors the same model when using informative and non-informative priors, and (ii) the evidence for a given model is stronger when using informative priors. The one exception to this is SDSS J2356−1016, where the Bayes factor only favors the dual point source model when using informative priors. In Table 6.3 we list the various $\ln \mathcal{B}_{2/1}$ and $\ln \mathcal{B}_{3/2}$ values for each of the 7 triple merger systems. The error bars on the Bayes factor represent the 99.7% confidence intervals, as determined by `nestle`. We have found these errors to be consistent with the 3σ spread of the $\ln \mathcal{B}$ values when running `BAYMAX` multiple times on a single dataset.

6.5.1 Multiple X-ray Point Sources: Strength of the Bayes factor

For each triple merger that has a Bayes factor that favors either the triple or dual point source model, we run false-positive tests to better, and uniquely, define a "strong" Bayes factor. In particular, past analyses have defined arbitrary Bayes factor thresholds, above which values are deemed strong (Jeffreys 1935, 1961; Kass & Raftery 1995; Thrane & Talbot 2019). However, the interpretation of a strong Bayes factor value depends on the details of the dataset, and for our particular observations it depends on parameters such as the number of counts, count ratio, and separation.

Following the procedure outlined in Foord et al. (2019, 2020), for each system that has a Bayes factor favoring a model with multiple point sources, we simulate a suite of single point source simulations that are based on the *Chandra* observations. The simulations are created via `MARX` and use the same detector position, pointing, and exposure time of the *Chandra* observations (such that, on average, the point source will have the same number of counts as the primary point source). Additionally, the point source has the same spectrum as that of the primary point source. We only analyze the counts contained within the same sky coordinates and energy range as the observations, we use the same informative priors, and we add a uniform background contribution with a similar background fraction as each observation. For SDSS J1027+1749, we also add a synthetic diffuse emission component, constrained within the same region as shown in Fig. 6.1. For each system, we run `BAYMAX` on 100 such simulations and calculate what fraction have $\ln \mathcal{B}_{2/1} > 0$, or $\ln \mathcal{B}_{3/2} > 0$ (for the one triple point source system, SDSS J0849+1114).

For the false-positive runs based on SDSS J1027+1749, NGC 3341, SDSS J1631+2352, SDSS J1708+2153, 0/100 of the $\ln \mathcal{B}_{2/1}$ values are larger than the measured values of 34.20, 2766.90, 6.20, and 18.40; for SDSS J2356−1016, only 2/100 of the $\ln \mathcal{B}_{2/1}$ values are larger than the measured value 3.10; while for SDSS J0849+1114 0/100 of the $\ln \mathcal{B}_{3/2}$ values are larger than the measured value of 19.40. We interpret these results to mean that there is $\leq$99% (or, $<$ 98% for SDSS J2356−1016) chance that a single point source with a comparable

number of counts would return a Bayes factor value, in favor of a multiple point source model, greater than what we measure. Thus, we classify each Bayes factor value as "strong" in favor of the dual, or triple, point source model as indicated in Table 6.3.

6.6 Origin of X-ray Emission

In the following section we aim to identify the origin of X-ray emission for each triple merger with Bayes factors that favor multiple point source models. To better identify the true accretion nature, we analyze the X-ray spectra of each point source individually, as well as analyze the posterior distributions returned from `BAYMAX`. For each system, we determine the best-fit values of each model parameter using the median values of their posterior distributions, which is appropriate given their unimodal nature. In Table 6.4 we list the best-fit values for r, $\log f$ and $\log f_{bkg}$.

It is possible that additional X-ray point sources that either have low-luminosities within the *Chandra* energy band, and/or are highly-obscured will be undetected by `BAYMAX`. Thus, for systems with Bayes factors that favor the dual point source model, we estimate an upper-limit of the 2−7 keV luminosity of a possible tertiary X-ray point source. In particular, for a given set of parameter vectors θ_1, θ_2, and θ_3, `BAYMAX` assigns each count to a specific model component (i.e, the primary, secondary, tertiary, or background), based on the relative probabilities of being associated with each component. Taking the best-fit values for θ_2 as determined by `BAYMAX`, we mask the counts associated with the primary and secondary point source, and analyze the counts within a $2''$ radius extraction region centered on the optical coordinates of the galactic nucleus found to host no X-ray point source. We estimate the number of background-subtracted 0.5−8 keV counts associated with a possible tertiary, where the background contribution is estimated by evaluating the count-rate in 10 random and source-free regions, see Section 6.4. These count rates are then converted into 2−7 keV luminosities via the HEASARC tool WebPIMMS (v4.11), assuming a power-law spectrum with photon index $\Gamma = 1.8$

Below we go into brief detail outlining our spectral analysis, before reviewing the results for each system. In particular, with BAYMAX we can carry out a spectral analysis of *individual* point source components in candidate multi-AGN systems that are closely separated and/or have small count ratios. All errors bars reported in this section are evaluated at the 99.7% confidence level, unless otherwise stated.

6.6.1 X-ray Spectral Analysis

From our analysis in Section 6.5, we find 5 triple merger systems with Bayes factors that strongly favor the dual point source model: SDSS J1027+1749, NGC 3341, SDSS J1631+2352, SDSS J1708+2153, SDSS J2356−1016; while we find one triple merger system with a Bayes factor that strongly favors the triple point source model: SDSS J0849+1114. Following the technique outlined in Foord et al. (2020), we fit the individual spectra of each X-ray point source. The spectral fits are determined via XSPEC, version 12.9.0 (Arnaud 1996). Each system has either 2 or 3 point sources, hereafter the "primary" (as defined in Fig. 6.1), "secondary", or "tertiary". We create 100 spectral realizations of each point source component by probabilistically sampling from the full distribution of counts. Each spectral realization uses θ_2 or θ_3 values that are drawn from the posterior distributions as determined by BAYMAX. For each iteration, BAYMAX assigns each count to a specific model component, based on the relative probabilities of being associated with each component.

By fitting the 100 spectra of each point source component, we create distributions of the best-fit values for various spectral parameters, as well as the 0.5−8 keV flux and unabsorbed 2−7 keV luminosity. This additional analysis expands on the posterior distributions returned by BAYMAX, as fitting the spectral realizations for each point source results in estimates of the flux ratio, instead of the count ratio. Similar to Foord et al. (2020), each point source component is modeled as either a simple absorbed power-law (phabs×zphabs×zpow; hereafter $m_{\rm spec,1}$) or an absorbed power-law with Compton scattering (phabs×(pow + zphabs×zpow); $m_{\rm spec,2}$), where the power-law indices are tied to one-another. We implement the Cash statis-

tic (`cstat`; Cash 1979) in order to best assess the quality of our model fits. Specifically, the latter model is used if it results in a statistically significant improvement in the fit, such that $\Delta C_{\rm stat} > n{\times}2.71$ (where n represents the difference in number of free parameters between the models; Tozzi et al. 2006; Brightman & Ueda 2012), corresponding to a fit improvement with 90% confidence (Brightman et al. 2014). In particular, because we are evaluating distributions of spectral parameters, we require $\Delta C_{\rm stat} > n{\times}2.71$ at the 99.7% confidence level. For both $m_{\rm spec,1}$ and $m_{\rm spec,2}$, if the best-fitting model where Γ is free is a significantly better fit than the best-fitting model where Γ is fixed (fixed to a value of 1.8; Corral et al. 2011; Yan et al. 2015) we choose the model with Γ as free as the best-fitting model. Unsurprisingly, for point sources with a low number of average counts (< 20), the models where Γ is fixed tends to be a significantly better fit (Brightman & Ueda 2012). For each model, we fix the column density to the Galactic value (Kalberla et al. 2005) as well as the redshift to that of the host galaxy. We list the best-fit values for each spectral parameter, $F_{0.5-8}$, $L_{2-7\ \rm keV,\ unabs}$, and hardness ratio (HR) in Table 6.5. The HR is defined as $(H-S)/(H+S)$ where H and S are the number of hard (2−8 keV) and soft (0.5−2 keV) X-ray counts.

In our spectral analysis, bona fide AGN are classified as point sources with unabsorbed 2−7 keV luminosities $L_{2-7\ \rm keV,unabs} > 10^{41}$ erg s^{-1}, while likely AGN are classified as point sources with unabsorbed 2−7 keV luminosities $L_{2-7\ \rm keV,unabs} > 10^{40}$ erg s^{-1}. Any point source with $L_{2-7\ \rm keV,unabs} < 10^{40}$ erg s^{-1} is conservatively not classified as an AGN. Generally, for point sources with X-ray luminosities below $L_{2-7\ \rm keV,unabs} < 10^{40}$ erg s^{-1}, X-ray binaries (XRB) or ultraluminous X-ray sources (ULX) can explain the accretion nature. The majority of the high-mass X-ray binary (HMXB) population has 2–7 keV X-ray luminosities between 10^{38}–10^{39} erg s^{-1}, while the ULX population dominates at the highest luminosities, with $L_{2-7\ \rm keV} > 10^{39}$ erg s^{-1} (e.g., Swartz et al. 2011; Walton et al. 2011). The overall X-ray luminosity function of HMXBs and ULXs indicates a general cutoff at $L_{2-7\ \rm keV} = 10^{40}$ erg s^{-1} (e.g., Mineo et al. 2012; Sazonov & Khabibullin 2017; Lehmer et al. 2019), and previous studies on XRB contamination in both late- and early-type galaxies have concluded that the

majority of nuclear (within 2″ of the galactic nucleus) X-ray point sources with $L_{2-7\ \mathrm{keV}} > 10^{40}$ erg s^{-1} are highly unlikely to be emission associated with accretion onto XRBs (Foord et al. 2017a; Lehmer et al. 2019). However, these studies have yet to focus on a sample of merging galaxies, where amplified star formation rates can increase the surrounding X-ray emission. Thus, for each point source where $10^{40} < L_{2-7\ \mathrm{keV,unabs}} < 10^{41}$ erg s^{-1}, we compare the X-ray luminosities to the expected X-ray contribution from high-mass X-ray binaries. The high-mass X-ray binary X-ray luminosity function (XLF) traces recent start formation within the galaxy (Sunyaev et al. 1978; Grimm et al. 2003; Lehmer et al. 2010; Mineo et al. 2012; Lehmer et al. 2019) and should be the dominant source of contamination (with respect to low-mass X-ray binaries, whose XLF scales with the total stellar mass of the galaxy).

We estimate the total expected 2−7 keV luminosity from the high-mass X-ray binary population, $L_{\mathrm{HMXB}}^{\mathrm{gal}}$, using the analytic prescription presented in Lehmer et al. (2019): $L_{\mathrm{HMXB}}^{\mathrm{gal}} = \beta\mathrm{SFR}$, where $\beta = 39.71^{+0.14}_{-0.09}$ ergs s^{-1} $(M_{\odot}\ \mathrm{yr}^{-1})^{-1}$. Due to the likely obscured environments of these galaxies, we use the formalism presented in Bell et al. (2005), where the SFR is estimated from the total infrared luminosity of each triple galaxy merger, L_{TIR}. Here, we use the the 12 μm, 25 μm, 60 μm, and 100 μm flux density values from the IRAS Faint Source Catalog (Moshir & et al. 1990) to calculate L_{TIR} (as reviewed in Sanders & Mirabel 1996). If no IRAS data are available, we use archival *WISE* W3-band (12 μm) observations to estimate the 25 μm, 60 μm, and 100 μm flux density values (outlined in further detail in Section 6.6.4, see Terrazas et al. 2016). Given the angular resolutions of IRAS ($0.5' - 2'$) and *WISE* ($\approx$6.5″at 12 μm) we are unable to estimate the *individual* SFRs for each galaxy in the merger, and thus $L_{\mathrm{HMXB}}^{\mathrm{gal}}$ represents the expected X-ray luminosity from HMXBs across all three galaxies. For 1 dual X-ray point source system, where the separation between the two host galaxies are individually resolved by *WISE* (SDSS J1708+2153, see below), we estimate the total $L_{\mathrm{HMXB}}^{\mathrm{gal}}$ from each galaxy individually. Even in this best-case scenario, where each galaxy has its own SFR estimation, we stress that the calculated $L_{\mathrm{HMXB}}^{\mathrm{gal}}$ is the X-ray luminosity from HMXB contribution across the entire galaxy, whereas our X-ray detections are

contained within the central 2″ where the nuclear X-ray contribution from HMXB, $L_{\rm HMXB}^{\rm nucleus}$, can be an order of magnitude smaller than $L_{\rm HMXB}^{\rm gal}$ (Foord et al. 2017a).

6.6.2 SDSS J1027+1749

SDSS J1027+1749 was first identified as triple AGN candidate in Liu et al. (2011a). Optical [O III] λ5007 luminosities were individually measured for each galactic nucleus using the Dual Imaging Spectrograph (DIS) on the Apache Point Observatory 3.5 m telescope. Assuming each galaxy hosts an AGN, X-ray luminosities were estimated from the $\frac{L_{X,2-10\rm keV}}{L_{[OIII]}}$ relation for obscured AGN (Panessa et al. 2007). The estimated 2−10 keV luminosities for each AGN were all estimated to be greater than 10^{42} erg s^{-1}, representing a robust classification as a triple AGN system. However, the *Chandra* observation shows a more complicated scenario — a high-count, diffuse, emission is coincident with the primary galactic nucleus, and very little X-ray emission appears to coincide with the location of the western galaxy. Our analysis with `BAYMAX`, where we can include more complicated models that include various background regions, is necessary in order to understand whether the X-ray emission is consistent with three AGN.

`BAYMAX` finds the observation to have a Bayes factor that strongly favors the dual point source model, both with informative ($\ln \mathcal{B}_{2/1,\rm inform} = 34.20 \pm 1.80$) and non-informative ($\ln \mathcal{B}_{2/1} = 28.50 \pm 4.40$) priors. Furthermore, the locations of the primary and secondary point source are consistent between the informative and non-informative runs, and spatially coincide with the optical nuclei of the primary and northern-most galaxy. We find the best-fit values of separation and count ratio to be $r = 3.42^{''+0.40}_{-0.30}$ and $\log f = -0.05^{+0.45}_{-0.36}$. Thus, the separation is inconsistent with 0 at the 99.7% confidence level. In Figure 6.3 we show the best-fit locations of each point source and the joint posterior distribution for r and $\log f$.

Running our spectral analysis on the primary and secondary point source, we find that the primary and secondary have, on average, 37 and 35 counts. Both X-ray point sources are best-fit with $m_{\rm spec,1}$ where Γ is fixed to a value of 1.8. For the primary, we calculate a total

observed 0.5–8 keV flux of $5.73^{+1.4}_{-1.7} \times 10^{-15}$ erg s^{-1} cm^{-2}, while for the secondary we calculate a total observed 0.5–8 keV flux of $4.79^{+1.6}_{-2.0} \times 10^{-15}$ erg s^{-1} cm^{-2} s^{-1}. This corresponds to a rest-frame 2–7 keV luminosity of $3.23^{+0.78}_{-0.97} \times 10^{40}$ erg s^{-1} and $2.62^{+0.60}_{-1.21} \times 10^{40}$ erg s^{-1} at $z = 0.066$. Since we have fixed both point sources to have the same spectral shape, the count ratio that we calculate with `BAYMAX`, should represent the flux ratio between the two sources. We find that the log of the flux ratio calculated via `XSPEC` (≈ -0.07) is consistent with the posterior distribution of $\log f$ (where the median value corresponds to $\log f \approx -0.05$).

The $2-7$ keV luminosities of each point source are greater than 10^{40} erg s^{-1} at the 99.7% confidence level, which can be comfortably attributed to AGN emission. In order to better understand how these luminosities compare to the expected population of high-mass X-ray binaries, we estimate the total expected $2-7$ keV luminosity from the high-mass X-ray binary population, $L^{\rm gal}_{\rm HMXB}$. Using archival IRAS observations, we find the expected X-ray luminosity from the galactic HMXB population to be $2.95^{+1.1}_{-0.55} \times 10^{40}$ erg s^{-1}. Although this is consistent with X-ray luminosities measured for the secondary point source source, we emphasize that $L^{\rm gal}_{\rm HMXB}$ represents the expected X-ray luminosity across all three systems, whereas our X-ray detections with `BAYMAX` are estimates of the individual, *nuclear* X-ray emission. For example, if we assume that the individual IR luminosities for each galaxy scales as the measured SDSS i-band ratios ($\approx 26\%$ and 35% for the primary and secondary, respectively), we may expect $L^{\rm gal}_{\rm HMXB}$ for each galaxy to instead be $\approx 7.7 \times 10^{39}$ and $\approx 1.0 \times 10^{40}$ erg s^{-1}, confirming the AGN nature of each of the point sources.

Lastly, we estimate an upper-limit of the $2-7$ keV luminosity of a possible tertiary X-ray point source at the location of the western galaxy. We find 0^{+1}_{-0} background-subtracted $0.5-8$ keV counts within the nucleus of the SW galaxy, (where errors bars represent the 99% C.L. as determined by Poisson statistics, see Gehrels 1986). Assuming power-law spectra with photon index $\Gamma = 1.8$, we estimate an upper-limit of $L_X < 1.50 \times 10^{39}$ erg s^{-1} for a possible tertiary AGN in SDSS J1027+1749. Given our analysis, we conclude that the triple merger is composed of 2 AGN.

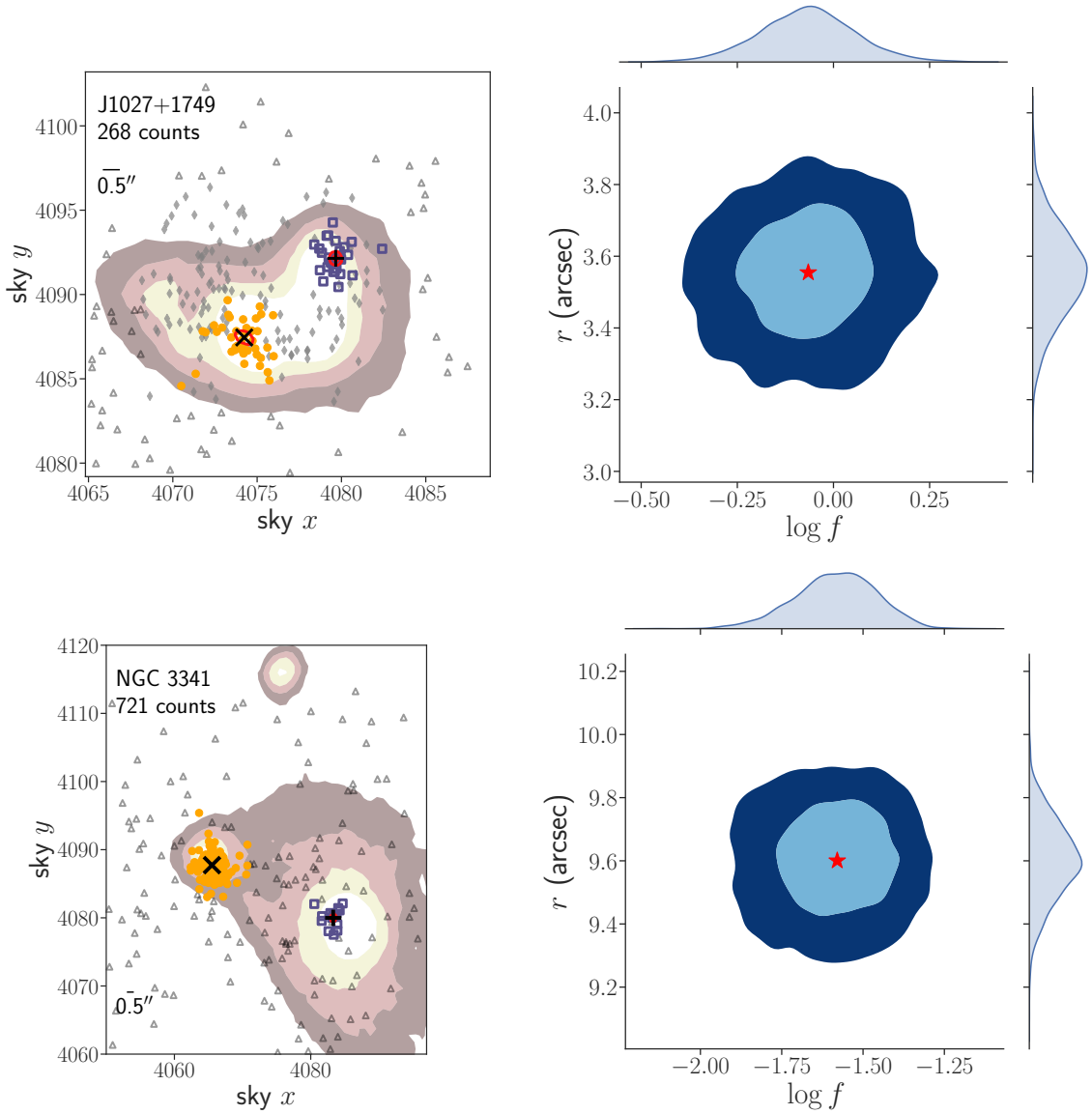

Figure 6.3: The 0.5–8 keV datasets for the two dual AGN candidates SDSS J1027+1749 and NGC 3341 (*left*) and their joint posterior distributions for r and $\log f$ (*right*). In the right panels, we plot the 68% confidence intervals (red lines) for the best-fit sky x and sky y positions for a primary and secondary (which are smaller than the symbol in most instances). Here, counts most likely associated with the primary are denoted by yellow circles, counts most likely associated with the secondary are denoted by open-faced purple squares, and counts most likely associated with background are shown as open-faced gray triangles. In order to more clearly see the results, we do not bin the data. Contours of the SDSS i-band observations of the host galaxies are overplotted. In the left panels, we show joint posterior distribution for the separation r (in arcseconds) and the count ratio (in units of $\log f$), with the marginal distributions shown along the border. The 68%, and 95% confidence intervals are shown in blue contours. We denote the location of the median of the posterior distributions with a red star.

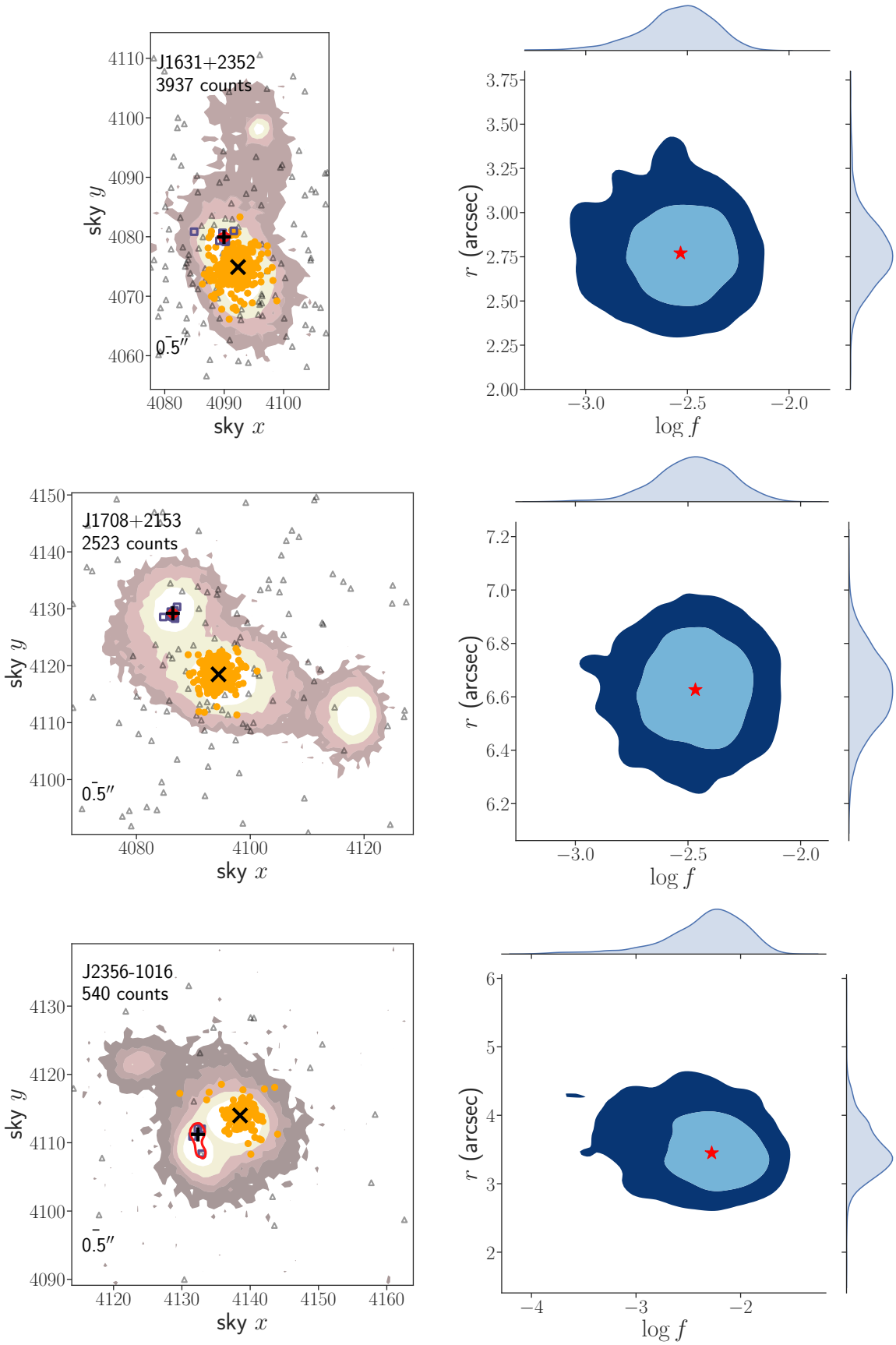

Figure 6.4: The 0.5–8 keV datasets for the three dual AGN candidates J1631+2352, SDSS J1708+2153 and SDSS J2356−1016 (*left*) and their joint posterior distributions for r and $\log f$ (*right*). Symbols and contours follow the same guidelines as Fig. 6.3

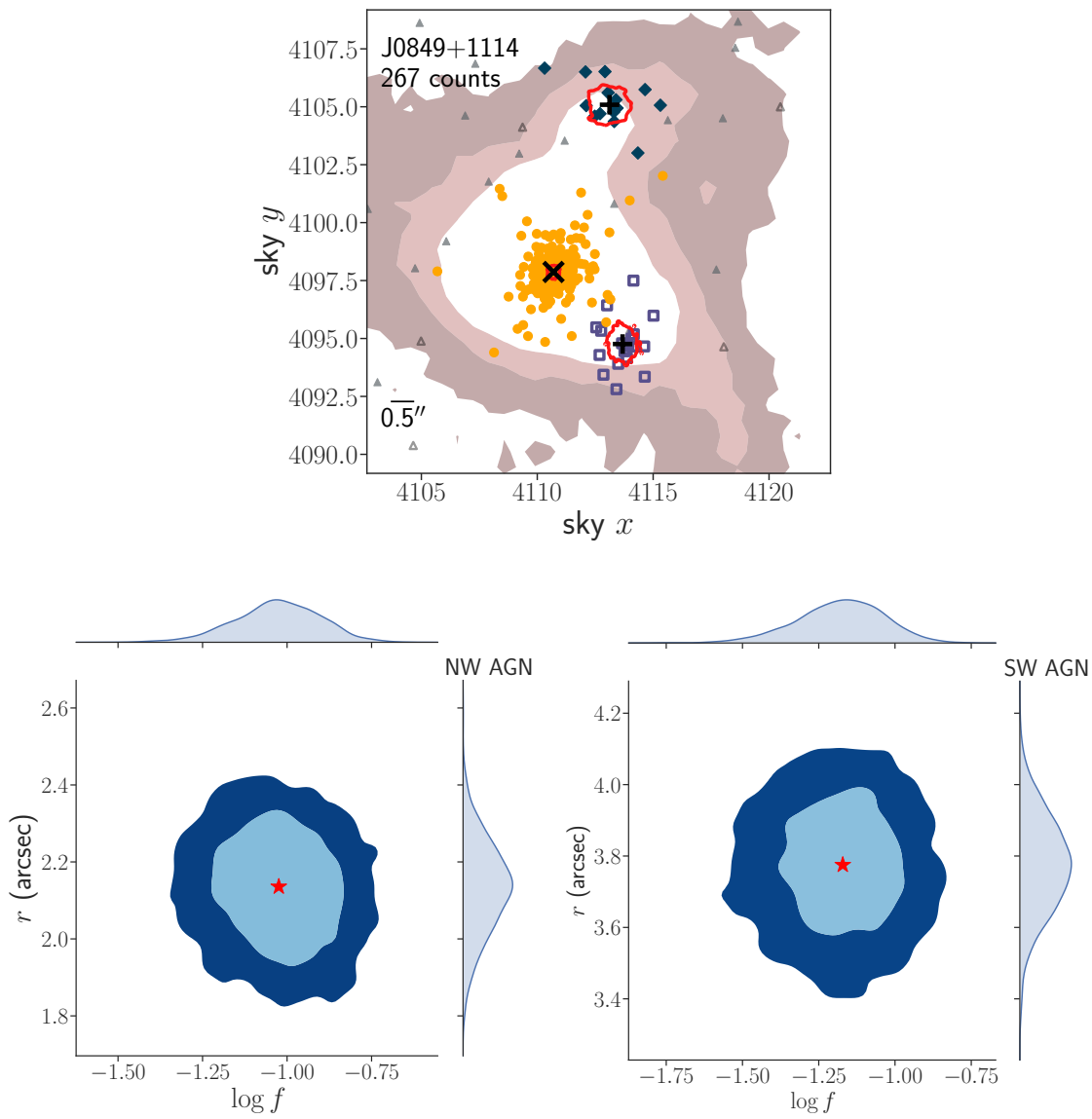

Figure 6.5: The 0.5–8 keV datasets for the triple AGN SDSS J0849+1114 (*top*) and the joint posterior distributions for r and $\log f$ for the secondary and tertiary X-ray point sources (*bottom*). Symbols and contours follow the same guidelines as Fig. 6.3, while we denote the counts most likely associated with the tertiary point source with green filled diamonds.

6.6.3 NGC 3341

The first analysis of NGC 3341 was presented in Barth et al. (2008), where SDSS data and new observations from the Keck Observatory were analyzed. Results from optical diagnostics were deemed too ambiguous for a proper classification of the AGN-nature of each galaxy. Expanding on this study via a multi-wavelength analysis that combined optical, X-ray, and radio data, Bianchi et al. (2013) concluded that the NE galaxy (classified as the primary in this study) showed evidence for AGN activity. Although the SW nucleus had emission detected in almost every wave-band, the emission was consistent with star-formation ($L_{2-7,\mathrm{keV}} \approx 4 \times 10^{39}$ erg s^{-1}, while there was no sign of any compact source at 5 GHz).

Our analysis with `BAYMAX` results in a Bayes factor that strongly favors the dual point source model, both with informative ($\ln \mathcal{B}_{2/1,\mathrm{inform}} = 2766.90 \pm 1.60$) and non-informative priors ($\ln \mathcal{B}_{2/1} = 22.50 \pm 1.80$). The locations of the primary and secondary point source are consistent between the informative and non-informative runs, and spatially coincide with the optical nuclei of the primary and SW galaxy. We find the best-fit values of separation and count ratio to be $r = 9.64^{''+0.31}_{-0.39}$ and $\log f = -1.61^{+0.38}_{-0.38}$. Thus, the separation is inconsistent with 0 at the 99.7% confidence level. In Figure 6.3 we show the best-fit locations of each point source and the joint posterior distribution for r and $\log f$.

Running our spectral analysis on the primary and secondary point source, we find that the primary and secondary have, on average, 566 and 16 counts. The primary X-ray point source is best-fit with $m_{\mathrm{spec},2}$, where Γ is free to vary; while the secondary X-ray point source is best-fit with $m_{\mathrm{spec},1}$ where Γ is fixed to a value of 1.8. For the primary, we calculate a total observed 0.5–8 keV flux of $3.63^{+0.07}_{-0.05} \times 10^{-13}$ erg s^{-1} cm^{-2}, while for the secondary we calculate a total observed 0.5–8 keV flux of $2.66^{+0.61}_{-0.76} \times 10^{-15}$ erg s^{-1} cm^{-2} s^{-1}. This corresponds to a rest-frame 2–7 keV luminosity of $8.54^{+0.41}_{-0.34} \times 10^{41}$ erg s^{-1} and $2.30^{+0.90}_{-0.70} \times 10^{39}$ erg s^{-1} at $z = 0.066$, at $z = 0.027$. The spectrum of the primary is measured to have extragalactic $N_H = 1.0^{+0.50}_{-0.62} \times 10^{23}$ cm^{-2}, with a relatively flat photon index of $\Gamma = 1.1^{0.14}_{-0.11}$. The high

level of N_H and flat spectral shape is consistent with an obscured environment. Although the primary has an X-ray luminosity consistent with accretion onto an AGN ($L_X > 1 \times 10^{41}$ erg s^{-1}), the SW galaxy does not ($L_X < 1 \times 10^{40}$ erg s^{-1}). These results agree with what was previously found in Bianchi et al. (2013).

NGC 3341 is not included in the IRAS All-Sky Survey, and the existing archival *WISE* observation is centered on the SW nucleus. However, given the primary point source's relatively high X-ray luminosity, and that standard diagnostics based on lines ratio unequivocally indicate that it is a Seyfert 2 galaxy (Barth et al. 2008; Bianchi et al. 2013), we conclude that the primary galaxy hosts an AGN. We estimate an upper-limit of the 2−7 keV luminosity of possible tertiary X-ray point sources at the location of the NW galaxy. We find 0^{+1}_{-0} 0.5−8 keV background-subtracted counts within the nucleus of the NW galaxy . Assuming power-law spectra with photon index $\Gamma = 1.8$, we estimate an upper-limit of $L_X < 1.80 \times 10^{39}$ erg s^{-1} for a possible tertiary AGN in NGC 3341.

6.6.4 SDSS J1631+2352

SDSS J1631+2352 is a triple merger system at $z = 0.059$, with no previous analysis on the *Chandra* dataset. Analyzing the archival *Chandra* observation with `BAYMAX`, we find that the data favor the dual point source model when using both informative ($\ln \mathcal{B}_{2/1,\mathrm{inform}} = 2.70 \pm 1.90$) and non-informative priors ($\ln \mathcal{B}_{2/1} = 6.20 \pm 1.60$). The best-fit value for the separation between the two point sources is $r = 2.84^{''+1.27}_{-0.63}$, inconsistent with 0 at the 99.7% confidence level; furthermore the best-fit location of the secondary point source is consistent with the location of the NE galaxy using both informative and non-informative priors. The best-fit value for count ratio is $\log f = -2.53^{+0.41}_{-0.50}$. We show the best-fit locations of each point source, and the joint posterior distributions for r and $\log f$ in Figure 6.4.

The spectral realizations of the primary (with an average of 3810 counts) and secondary (with an average of 11 counts) point source are best-fit with $m_{\mathrm{spec},2}$ and $m_{\mathrm{spec},1}$, with Γ fixed to a value of 1.8. When fitting the spectral realizations of the primary point source, we

identify a statistically significant Fe Kα fluorescent emission line, modeled by a Gaussian component (`zgaus`) fixed at 6.4 keV. We measure an equivalent width of $0.23^{+0.01}_{-0.02}$ keV for the Fe Kα line. The equivalent width of the Fe Kα line is strongly dependent on line-of-sight absorption, as well as other parameters such as geometry of the accretion disk, inclination angle at which the reflecting surface is viewed, and the elemental abundances of the reflecting matter (see, e.g., Brightman & Nandra 2011a). Although we measure a relatively mild line-of-sight hydrogen column density when fitting the 0.5−8 keV spectrum for the primary ($N_H = 1.10^{+0.01}_{-0.02} \times 10^{22}$ cm^{-2}), observations above 10 keV, such as with *NuSTAR*, may better constrain the spectral parameters (e.g., Marchesi et al. 2018). We calculate a total observed 0.5–8 keV flux of $2.29^{+0.01}_{-0.01} \times 10^{-12}$ erg s^{-1} cm^{-2}, and $5.26^{+4.84}_{-3.87} \times 10^{-15}$ erg s^{-1} cm^{-2} for the primary and secondary, respectively. This corresponds to a rest-frame 2–7 keV luminosity, at $z = 0.059$, of $1.32^{+0.01}_{-0.01} \times 10^{43}$ erg s^{-1} and $2.46^{+2.30}_{-1.84} \times 10^{40}$ erg s^{-1}. In Figure 6.6 we show our various spectral fits to the spectral realizations of the primary and secondary point source.

Both X-ray luminosities are above 10^{40} erg s^{-1}, while given the primary's 2−7 keV luminosity, we categorize it as a bona fide AGN. Due to no available IRAS data, we calculate $L^{\rm gal}_{\rm HMXB}$ using IR *WISE* W3 band (12 μm) observations. To convert the 12 μm flux to the equivalent FIR IRAS bands, we use the $f_{60\mu{\rm m}}/f_{12\mu{\rm m}}$, $f_{60\mu{\rm m}}/f_{25\mu{\rm m}}$, and $f_{60\mu{\rm m}}/f_{100\mu{\rm m}}$ flux ratios presented in Terrazas et al. (2016). To ensure the validity of this approach, we compare the estimated FIR IRAS-band flux values using the *WISE* W3 band detections to the actual IRAS-band flux values, for the triple mergers in our sample with both IRAS and *WISE* observations. We find that the estimated FIR IRAS-band flux values are consistent with the actual IRAS-band flux values.

For the primary and NE galaxy, we find $L^{\rm gal}_{\rm HMXB} = 2.79^{+1.06}_{-0.52} \times 10^{40}$ erg s^{-1}, which is consistent with the measured X-ray luminosity of secondary, at the 99.7% C.L. Similar to SDSS J1027+1749, if we assume that the individual IR luminosities for each galaxy scales as the measured i-band ratios (≈61% and 31% for the primary and NE galaxy), $L^{\rm NE\ gal}_{\rm HMXB} < 10^{40}$ erg s^{-1}, and the emission detected from the secondary point source can be safely attributed

to an AGN. For both SDSS J1631+2352 and SDSS J1027+1729, future observations with IFU spectroscopy will allow for a more detailed analysis of the individual SFRs of each galaxy in the merger systems.

We estimate the upper-limit of the 2−7 keV luminosities of a possible tertiary X-ray point source at the location of NW host-galaxy nuclei. We find 0^{+1}_{-0} 0.5−8 keV counts associated with a possible tertiary (NW galaxy) in SDSS J1631+2352. Assuming power-law spectra with photon index $\Gamma = 1.8$, we estimate an upper-limit of $L_X < 3.19 \times 10^{39}$ erg s^{-1}.

6.6.5 SDSS J1708+2153

SDSS J1708+2153 is a triple merger system at $z = 0.072$, with no previous analysis on the *Chandra* dataset. Analyzing the archival *Chandra* observations with `BAYMAX`, we find that the data strongly favor the dual point source model when using both informative ($\ln \mathcal{B}_{2/1,\mathrm{inform}} = 18.40 \pm 1.60$) and non-informative priors ($\ln \mathcal{B}_{2/1} = 16.60 \pm 1.90$). The best-fit value for the separation is $r = 6.61^{''+0.38}_{-0.38}$, inconsistent with 0 at the 99.7% confidence level, while the best-fit value for count ratio is $\log f = -2.52^{+0.44}_{-0.56}$. We show the best-fit locations of each point source, and the joint posterior distributions for r and $\log f$ in Figure 6.4. The best-fit location for the secondary is coincident with the location of the NE galaxy, using both informative and non-informative priors.

Analyzing the spectral realizations of each point source, we find that the primary and secondary have, on average, 2406 and 9 counts. Both the primary and secondary point sources are best-fit with $m_{\mathrm{spec},1}$, where Γ is allowed to vary for the primary. We calculate a total observed 0.5–8 keV flux of $1.46^{+0.01}_{-0.01} \times 10^{-12}$ erg s^{-1} cm^{-2}, while for the secondary we calculate a total observed 0.5–8 keV flux of $4.56^{+1.56}_{-0.19} \times 10^{-15}$ erg s^{-1} cm^{-2} s^{-1}. This corresponds to a rest-frame 2–7 keV luminosity of $1.17^{+0.01}_{-0.01} \times 10^{43}$ erg s^{-1} and $3.46^{+0.63}_{-1.22} \times 10^{40}$ erg s^{-1} at $z = 0.072$. The spectral fit of the primary point source shows low-levels of absorption, with $N_H = 0.10^{+0.01}_{-0.01} \times 10^{22}$ cm^{-2} and best-fit photon index $\Gamma = 1.37^{+0.01}_{-0.01}$.

Both the primary and second point sources have 2–7 keV luminosities above 10^{40} erg s^{-1}

at the 99.7% confidence level. Due to the larger angular separation between the two systems ($\approx$6.59″), we use resolved IR *WISE* W3 band (12 μm) observations of each galaxy to estimate their individual $L_{\rm HMXB}^{\rm gal}$. For the primary and NE galaxy, we find $L_{\rm HMXB}^{\rm pri\ gal} = 2.81^{+1.00}_{-0.50} \times 10^{40}$ and $L_{\rm HMXB}^{\rm NE\ gal} = 2.55^{+0.97}_{-0.47} \times 10^{40}$, inconsistent with the measured X-ray luminosities of the primary (at the 99.7% C.L.) and secondary (at the 95% C.L.) point source.

Lastly, we estimate an upper-limit of the 2−7 keV luminosity of a possible tertiary X-ray point sources at the location of the SW galaxy. Subtracting the expected background contribution, we find 0^{+1}_{-0} 0.5−8 keV counts associated with the nucleus of the SW galaxy. Assuming power-law spectra with photon index $\Gamma = 1.8$, we estimate an upper-limit of $L_X < 4.80 \times 10^{39}$ erg s^{-1} for a possible tertiary AGN in SDSS J1027+1749. Given our analysis, we conclude that the triple merger is composed of 2 AGN.

6.6.6 SDSS J2356−1016

SDSS J2356−1016 was analyzed in Pfeifle et al. (2019a), where they concluded that the X-ray emission was consistent with a single AGN. They find an X-ray detection at the location of the primary galaxy (at the 22.8σ C.L.), but they find no X-ray detection at the location of the SE galaxy, which is separated from the primary by 3.5″. However, source detection was determined using the `CIAO` package `wavdetect`, which is not always sensitive enough to detect both low-count and closely-separated multiple point source systems (see, e.g., Foord et al. 2020). Given that `BAYMAX` is powerful for low count-ratio systems, we re-analyze this triple merger to identify any previously missed detections. Analyzing the archival *Chandra* observations with `BAYMAX`, we find that the data strongly favor the dual point source model when using informative priors ($\ln \mathcal{B}_{2/1,\rm inform} = 3.10 \pm 1.30$). The Bayes factor does not strongly favor the dual point source model when using non-informative priors, likely due to the low number of counts associated with the secondary point source; however the best-fit locations of the primary and secondary point source are consistent between non-informative and informative runs, and spatially coincide with the primary and SE galaxy.

During our false positive tests, only 2 out of 100 simulations of single point sources analyzed by BAYMAX have $\ln \mathcal{B}_{2/1,\mathrm{inform}} > 3$, and thus we classify the merger as a dual X-ray point source system. The best-fit values of separation and count ratio are $r = 3.53^{''+1.60}_{-1.20}$ and $\log f = -2.37^{+0.73}_{-1.46}$. This separation is inconsistent with 0 at the 99.7% confidence level. We show the best-fit locations of each point source, and the joint posterior distributions for r and $\log f$ in Figure 6.4.

Analyzing the spectral realizations of each point source, we find that the primary and secondary have, on average, 516 and 4 counts. The primary point source source is best-fit with $m_{\mathrm{spec},2}$ while the secondary point source is best-fit with $m_{\mathrm{spec},1}$ where Γ is fixed for both models. We calculate a total observed 0.5–8 keV flux of $1.59^{+0.01}_{-0.01} \times 10^{-12}$ erg s^{-1} cm^{-2}, while for the secondary we calculate a total observed 0.5–8 keV flux of $7.33^{+7.04}_{-3.50} \times 10^{-15}$ erg s^{-1} cm^{-2} s^{-1}. This corresponds to a rest-frame 2–7 keV luminosity of $3.10^{+0.04}_{-0.04} \times 10^{43}$ erg s^{-1} and $8.06^{+9.57}_{-1.10} \times 10^{40}$ erg s^{-1} at $z = 0.074$. The spectral fit of the primary point source shows relatively high (with respect to the other dual X-ray point sources in the sample) levels of absorption, with $N_H = 7.83^{+0.18}_{-0.14} \times 10^{22}$ cm^{-2}.

Given the low number of counts associated with the secondary, the error bars are large relative to our other spectral analyses presented in this section. However, even accounting for the assumed error on our X-ray luminosity measurement, both X-ray point sources have 2–7 keV luminosities greater than 10^{40} erg s^{-1} at the 99.7% confidence level. SDSS J2356−1016 has no IRAS observations, and thus we use IR *WISE* W3 band observations of the entire triple merger system to estimate $L^{\mathrm{gal}}_{\mathrm{HMXB}}$. Following the procedure outlined in Section 6.6.5, we estimate the total HMXB X-ray contribution of the triple merger system to be $L^{\mathrm{gal}}_{\mathrm{HMXB}} = 2.97^{+1.1}_{0.56} \times 10^{40}$ erg s^{-1}. Although the primary X-ray point source is well above this luminosity, the secondary X-ray point source is consistent at the 99.7% C.L. with $L^{\mathrm{gal}}_{\mathrm{HMXB}}$. Thus, we aim to better understand the fractional contribution of $L^{\mathrm{gal}}_{\mathrm{HMXB}}$ to just the SE galaxy. In particular, Pfeifle et al. (2019a) calculated SFRs of each nucleus individually using the estimated, intrinsic, Hα line fluxes. These values were estimated from individually

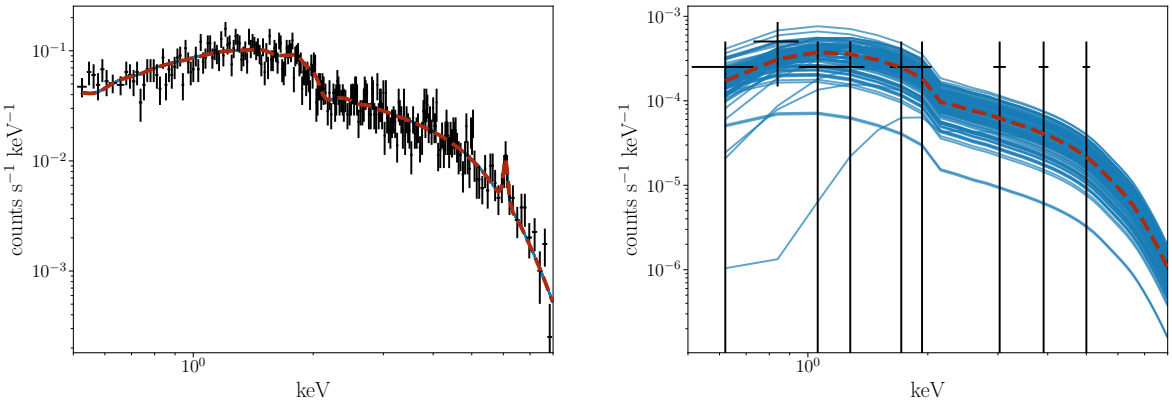

Figure 6.6: *Chandra* spectral fits for 100 realizations for the primary point source (*left*; where the median number of counts is 3810) and the secondary point source (*right*; where the median number of counts is 11) for SDSS J1631+2532. Data have been folded through the instrument response. We overplot one of the spectral realizations with black points and plot the median spectral fit in a red dashed line. The spectra have been rebinned for plotting purposes. We fit SDSS J1631+2532$_p$ and SDSS J1631+2532$_s$ with the spectral models (`phabs`×(`pow` + `zphabs`×`zpow`) and `phabs`×`zphabs`×`zpow`, where Γ is fixed to a value of 1.8 for both models. We identify a statistically significant Fe Kα fluorescent emission line in the spectra of the primary, modeled by a Gaussian component (`zgaus`) fixed at 6.4 keV. The emission of the primary and secondary point source are consistent with emission from AGN; in particular we find that the X-ray luminosities of each point source are greater than the estimated X-ray emission from all HMXBs in their respective host galaxy. We list the best-fit values for each model in Table 6.5, defined as the median of distribution of the best-fit values from the 100 realizations.

resolved Paα emission lines detected via near-IR longslit spectra of each nucleus from the Large Binocular Telescope (LBT). They find a SFR of 3.82 $M_\odot$ yr^{-1} for the SE nucleus, corresponding to $L^{\rm gal}_{\rm HMXB} = 6.4^{+0.4}_{-0.4} \times 10^{39}$erg s^{-1}. Thus, given the X-ray luminosities measured by `BAYMAX`, we classify both point sources as AGN.

We estimate an upper-limit of the 2−7 keV luminosity of possible tertiary X-ray point sources at the location of the NE galaxy. We find 0^{+1}_{-0} 0.5−8 keV background-subtracted counts associated with the nucleus of the NE galaxy. Assuming power-law spectra with photon index $\Gamma = 1.8$, we estimate an upper-limit of $L_X < 1.02 \times 10^{40}$ erg s^{-1} for a possible tertiary AGN in SDSS J2356−1016.

6.6.7 SDSS J0849+1114

SDSS J0849+1114 is a triple AGN candidate first published by Pfeifle et al. (2019a), and in-depth analyses followed in Pfeifle et al. (2019b) and Liu et al. (2019). In particular, Pfeifle et al. (2019a) conclude that the primary is detected at a 10.2σ level, while the SW and NE galaxy are detected at 2.2σ and 1.4σ, respectively. Given the lower significance of the SW and NE detections, we re-evaluate the system with `BAYMAX` to determine the likelihood that the merger is composed of three X-ray point sources. We find that `BAYMAX` strongly favors the triple point source system using both informative ($\ln \mathcal{B}_{3/2,\mathrm{inform}} = 19.4 \pm 1.9$) and non-informative priors ($\ln \mathcal{B}_{3/2} = 22.4 \pm 2.1$); furthermore the locations of each point-source are consistent between the informative and non-informative runs, and spatially coincide with the optical nuclei of each galaxy in the triple merger. The best-fit values for the separation and count ratio of the secondary (associated with the SW galaxy) X-ray point source are $r = 2.14^{''+0.32}_{-0.32}$ and $\log f = -1.04^{+0.36}_{-0.36}$; while the best-fit values for separation and count ratio of the tertiary (associated with the NW galaxy) X-ray point source are $r = 3.8^{''+0.35}_{-0.44}$ and $\log f = -1.22^{+0.40}_{-0.50}$. Here, the separation and count-ratio are defined relative to the position and number of counts associated with the primary point source. These separations are inconsistent with 0 at the 99.7% confidence level. We show the best-fit locations of each point source, and the joint posterior distributions for r and $\log f$ in Figure 6.5.

Creating 100 spectral realizations of each point source, we find that the primary, secondary, and tertiary have, on average, 189, 99, and 13 counts. The primary point source source is best-fit with $m_{\mathrm{spec},2}$ where Γ is fixed to a value of 1.8, while the secondary and tertiary point sources are best-fit with $m_{\mathrm{spec},1}$ where Γ is fixed to value of 1.8. Although Pfeifle et al. (2019a) find that adding an Fe Kα emission component into the primary's spectral model results in statistically significant better fit (using only one of the two *Chandra* observations), we find that the combined *Chandra* dataset results in spectral realizations that do not favor the addition of an Fe Kα emission component (and a similar conclusion was reached in Pfeifle et al. 2019b when combining both observations). We calculate a total

observed 0.5–8 keV fluxes of: $6.64^{+0.79}_{-0.63} \times 10^{-14}$ erg s^{-1} cm^{-2} for the primary; $4.0^{+1.6}_{-1.3} \times 10^{-15}$ erg s^{-1} cm^{-2} for the secondary; and $3.22^{+1.0}_{-1.3} \times 10^{-15}$ erg s^{-1} cm^{-2} for the tertiary. This corresponds to rest-frame 2–7 keV luminosities (at $z = 0.059$) of: $1.60^{+.21}_{-.10} \times 10^{42}$ erg s^{-1} for the primary, $1.90^{+0.57}_{-0.71} \times 10^{40}$ erg s^{-1} for the secondary, and $1.34^{+0.60}_{-0.48} \times 10^{40}$ erg s^{-1} for the tertiary. The spectral fit of the primary point source shows the highest-levels of absorption in our sample, with $N_H = 5.10^{+2.2}_{-1.3} \times 10^{23}$ cm^{-2}.

The nature of the three X-ray point sources has been extensively discussed in both Liu et al. (2019) and Pfeifle et al. (2019b). For the purposes of uniformity in our analysis, we use archival IRAS observations of the triple merger to estimate the total X-ray contribution from the galactic HMXB population and find $L^{\rm gal}_{\rm HMXB} = 2.97^{+1.13}_{-0.56} \times 10^{40}$ erg s-1. However, analyses carried out in Liu et al. (2019) and Pfeifle et al. (2019b) are more detailed than our approach. Liu et al. (2019) analyze radio, optical, and X-ray observations of the triple merger to best diagnose the accretion nature of each X-ray point source. Nuclear (within a $1''$ radius centered on each galaxy nucleus) star formation rates were estimated using dust-corrected U-band HST observations, and the X-ray emission of all three sources are greater than the expected X-ray emission of the nuclear HMXB population. This agrees with the findings in Pfeifle et al. (2019b), where using measured Paα emission from each nuclei, they estimate SFRs for each galaxy that result in an X-ray HMXB contribution an order of magnitude lower than the X-ray luminosity measured for each X-ray point source. Additional analyses in Liu et al. (2019) strengthen the evidence that each nucleus hosts an AGN: the primary and tertiary are detected as compact radio sources by the VLA at 9.0 GHz, and diagnostic emission-line ratios for all three nuclei (via long-slit spectroscopic observations using DIS on the Apache Point Observatory 3.5 m telescope) classify each as a type 2 Seyfert. Thus, we classify each X-ray point source as an AGN, and conclude that J0849+1114 is a triple merger with 3 AGN.

Table 6.4: Posterior Results for Multiple X-ray Point Sources

Galaxy Name (1)	α (2)	δ (3)	α_s (4)	δ_s (5)	r (arcsec) (6)	$\log f$ (7)	$\log f_{bkg}$ (8)
SDSS J1027+1749	10:27:00.39	+17:49:02.94	10:27:00.57	+17:49:00.63	$3.42^{+0.4}_{-0.3}$	$-0.05^{+0.45}_{-0.36}$	$-0.18^{+0.07}_{-0.09}$
NGC 3341	10:42:31.46	+05:02:37.94	10:42:32.05	+05:02:41.75	$9.64^{+0.31}_{-0.39}$	$-1.61^{+0.38}_{-0.38}$	$-0.70^{+0.09}_{-0.12}$
SDSS J1631+2352	16:31:15.52	+23:52:57.62	16:31:15.60	+23:53:00.10	$2.58^{+0.31}_{-0.30}$	$-2.53^{+0.41}_{-0.50}$	$-1.53^{+0.09}_{-0.09}$
SDSS J1708+2153	17:08:59.12	+21:53:08.06	17:08:59.41	+21:53:13.33	$6.61^{+0.38}_{-0.38}$	$-2.52^{+0.44}_{-0.56}$	$-1.35^{+0.11}_{-0.14}$
SDSS J2356−1016	23:56:54.36	−10:16:05.45	23:56:54.56	−10:16:06.77	$3.53^{+1.6}_{-1.2}$	$-2.37^{+0.73}_{-1.46}$	$-1.44^{+0.29}_{-0.36}$
SDSS J0849+1114	08:49:05.54	+11:14:47.94	08:49:05.44	+11:14:46.42	$2.14^{+0.32}_{-0.32}$	$-1.04^{+0.36}_{-0.36}$	$-0.77^{+0.17}_{-0.22}$
–	–	–	08:49:05.46†	+11:14:51.49†	$3.8^{+0.35\dagger}_{-0.44}$	$-1.22^{+0.40\dagger}_{-0.50}$	–

Note. – Columns: (1) SDSS galaxy designation; (2) the central R.A. of the primary X-ray source; (3) the central declination of the primary X-ray source; (4) the central R.A. of the secondary X-ray source; (6) the central declination of the secondary X-ray source; (6) the separation between the two point sources in arcseconds; (7) the log of the count ratio between the secondary and primary; (8) the log of the count ratio between the background and point source contribution. The dagger represents posterior results for the tertiary point source in SDSS J0854+1114. For SDSS J1027+1749, the background component is defined as the diffuse emission component, f_{diff}. Each value is the best-fit value from the posterior distributions, defined as the median of the distribution. All posterior distributions are unimodal, and thus the median is a good representation of the value with the highest likelihood. Error bars represent the 99.7% confidence level of each distribution.

6.7 Discussion

In the following section, we combine our results from the full sample of triple mergers to better understand the environments surrounding each AGN. We first aim to identify the origin of emission for the one system in our sample that has a Bayes factor that favors the single point source model, such that we have a classification for each triple merger as a single, dual, or triple AGN. We then combine our *Chandra* analysis with mid-IR *WISE* observations to gain insight on the preferential environments of multiple AGN systems.

6.7.1 SDSS J0858+1822: X-ray Emission Consistent with no AGN

SDSS J0858+1822 is a unique system within our sample, where there appears to be an excess of X-ray emission south of the primary galaxy (see Fig. 6.1), which does not spatially coincide with a galactic nucleus. Interestingly, when using non-informative priors, `BAYMAX` favors the single point source model, but with the best-fit location for the point source

Table 6.5: Best-fit Spectral Parameters

Galaxy Name	$m_{\rm spec,x}$	N_H (10^{22} cm^{-2})	Γ	$F_{0.5-8\ \rm keV}$	$L_{2-7\ \rm keV,\ unabs}$	HR
(1)	(2)	(3)	(4)	(5)	(6)	(7)
SDSS J1027+1749$_p$	1	$< 10^{-2}$	1.8	$5.73^{+1.29}_{-1.6}$	$3.23^{+0.78}_{-0.97}$	$0.12^{+0.18}_{-0.36}$
SDSS J1027+1749$_s$	1	$< 10^{-2}$	1.8	$4.79^{+1.1}_{-2.2}$	$2.62^{+0.6}_{-1.2}$	$-0.06^{+0.2}_{-0.4}$
NGC 3341$_p$	2	$10.1^{+0.50}_{-0.62}$	$1.1^{+0.14}_{-0.11}$	$363.0^{+7.1}_{-5.6}$	$85.4^{+4.1}_{-3.3}$	$0.78^{+0.03}_{-0.01}$
NGC 3341$_s$	1	$< 10^{-2}$	1.8	$2.66^{+0.61}_{-0.76}$	$0.23^{+0.09}_{-0.07}$	$0.48^{+0.24}_{-0.48}$
SDSS J1631+2352$_p$	2	$1.10^{+0.01}_{-0.02}$	1.8	$2.29^{+0.01}_{-0.01} \times 10^3$	$1.32^{+0.01}_{-0.01} \times 10^3$	$0.15^{+0.01}_{-0.01}$
SDSS J1631+2352$_s$	1	$0.13^{+2.26}_{-0.01}$	1.8	$5.26^{+4.84}_{-3.87}$	$2.46^{+2.30}_{-1.84}$	$0.03^{+0.34}_{-0.69}$
SDSS J1708+2153$_p$	1	$0.10^{+0.1}_{-0.01}$	$1.37^{+0.01}_{-0.01}$	$1.46^{+0.01}_{-0.01} \times 10^3$	$1.5^{+0.01}_{-0.01} \times 10^3$	$-0.02^{+0.01}_{-0.01}$
SDSS J1708+2153$_s$	1	$0.18^{+0.50}_{-0.14}$	1.8	$4.56^{+0.19}_{-1.56}$	$3.46^{+0.63}_{-1.22}$	$-0.44^{+0.17}_{-0.21}$
SDSS J2356−1016$_p$	2	$7.83^{+0.18}_{-0.14}$	1.8	$1.59^{+0.01}_{-0.01} \times 10^3$	$1.17^{+0.01}_{-0.01} \times 10^3$	$0.73^{+0.01}_{-0.01}$
SDSS J2356−1016$_s$	1	$3.2^{+1.10}_{-0.01}$	1.8	$7.33^{+7.04}_{-3.50}$	$8.06^{+9.57}_{-1.10}$	$0.55^{+0.40}_{-0.50}$
SDSS J0849+1114$_p$	2	$51.0^{+2.2}_{-1.3}$	1.8	$66.40^{+7.9}_{-6.3}$	$160.60^{+21.1}_{-10.0}$	$0.34^{+0.05}_{-0.04}$
SDSS J0849+1114$_s$	1	$< 10^{-2}$	1.8	$4.0^{+1.6}_{-1.3}$	$1.90^{+0.57}_{-0.71}$	$-0.23^{+0.31}_{-0.24}$
SDSS J0849+1114$_t$	1	$< 10^{-2}$	1.8	$3.22^{+1.0}_{-1.3}$	$1.34^{+0.60}_{-0.48}$	$-0.01^{+0.26}_{-0.21}$

Note. – Columns: (1) SDSS galaxy designation, we denote the primary, secondary, and tertiary with subscripts p, s, and t; (2) the spectral model used; (3) the best-fit extragalactic column density; (4) the assumed or best-fit spectral index; (5); the measured 0.5–8 keV flux, in units of 10^{-15} erg s^{-1} cm^{-2}; (6) the rest-frame, unabsorbed, 2–7 keV luminosity in units of 10^{40} erg s^{-1}; (7) the hardness ratio, defined as $HR = (H - S)/(H + S)$. Each best-fit value is defined as the median of the full distribution. We identify a statistically significant Fe Kα fluorescent emission line in the spectrum of SDSS J1631−1016$_p$, modeled by a Gaussian component (`zgaus`) fixed at 6.4 keV, with an equivalent width of $0.23^{+0.01}_{-0.02}$ keV (see Fig. 6.6). Error bars represent the 99.7% confidence level of each distribution.

corresponding to the location of the southern region of X-ray emission. This is consistent with our results when running `BAYMAX` with informative priors – the single point source model is favored, but the location of the point source is shifted to the southern-most edge of the spatial constraints placed on μ. We aim to better understand the accretion nature of the southern emission region (which, for example, may be explained by a background AGN or a recoiling SMBH), and do so by analyzing the spectrum.

We use the results from the non-informative run to create 100 spectral realizations of the point source south of the primary galaxy; this is done by sampling from the posterior distributions of θ_1 and probabilistically assigning counts to either the point source or background component. The spectral realizations of the point source are best-fit with $m_{\rm spec,1}$ where Γ is free to vary. We calculate a total observed 0.5–8 keV flux of $3.03^{+2.64}_{-1.32} \times 10^{-15}$ erg s^{-1} cm^{-2}, corresponding to a rest-frame 2–7 keV luminosity of $2.10^{+0.10}_{-0.07} \times 10^{39}$ erg s^{-1} at $z = 0.078$. Given the that the luminosity is below our AGN luminosity criterion of 10^{40} erg s^{-1}, we do not classify the X-ray point source as an AGN. The region is extremely soft, with best-fit $\Gamma = 8.48^{+0.68}_{-5.42}$ and $HR = -0.98^{+0.36}_{-0.0}$. It is likely that this point source represents a concentrated region (or, clump) of the surrounding diffuse emission, that is better modeled as a point-source sitting among a uniform background. Both the X-ray luminosity and the spectral shape are inconsistent emission associated with accretion onto a SMBH. Thus, we classify the ongoing triple merger in SDSS J0858+1822 as having no AGN.

Thus, from our full spectral analysis, we conclude that 1 triple merger in our sample has no AGN: SDSS J0858+1822; 1 triple merger system in our sample is composed of a single AGN: NGC 3341; 4 triple merger systems in our sample are dual AGN, all of which are new discoveries: SDSS J1027+1749, SDSS J1631+2352, SDSS J1708+2153, and SDSS J2356−1016; and we confirm one triple AGN system, SDSS J0849+1114.

6.7.2 X-ray and IR diagnostics

Our sample of X-ray observed triple merger systems gives us the unique opportunity to probe if and how the environments between single, dual, and triple r4jhAGN differ. Given that each of these triple merger systems are similarly separated on kilo-parsec scales, we are interested in (i) whether other environmental parameters differ between each system, and (ii) whether these differences are linked to the SMBH activity.

We analyze how the *WISE* $W1-W2$ colors vary as a function of the extragalactic hydrogen column density of the primary AGN. *WISE* color-color diagrams ($W2-W3$ versus $W1-W2$) are a standard diagnostic used to find obscured, luminous, AGN (e.g., Stern et al. 2005). AGN spectra are expected to be redder than star-forming galaxies between 1-10 μm, and as a result, sit in different locations on mid-IR color-color diagrams than inactive nuclei. Various color-cuts have been defined in the literature to define emission consistent with an AGN (Jarrett et al. 2011; Stern et al. 2005), and simulations of galaxy mergers are beginning to better identify the positions of *multiple* AGN systems on mid-IR color-color diagrams (Blecha et al. 2018b).

In the left panel of Figure 6.7 we show the mid-IR color-color plot for our sample of triple merger galaxies, excluding SDSS J0858+1822 (where we find no emission consistent with an AGN) and NGC 3341 (as the *WISE* aperture only includes the primary galaxy, where we find no emission consistent with an AGN). We note that the *WISE* colors account for all three galactic nuclei in all systems except SDSS J2356−1016 and SDSS J1631+2352, where the *WISE* aperture only covers the primary and secondary galaxy (however, the tertiary galaxies excluded in both cases were found to have no X-ray emission consistent with AGN). Thus, the numbers next to each marker represent the number of X-ray detected AGN within the *WISE* footprint. We find that 4 of 5 systems are identified as AGN via mid-IR color-color diagnostics, and that their $W1-W2$ colors are not correlated with the total AGN X-ray luminosity. Generally, these mid-IR color diagnostics are most useful for high-Eddington and luminous ($L_{\rm X} > 10^{43}$) AGN; thus accurate mass measurements of each system may give

more insight on possible trends between the X-ray measurements and $W1-W2$ colors.

We investigate a possible relation between the levels of gas obscuration and dust obscuration. In the right panel of Figure 6.7 we plot the measured N_H values from the primary AGN versus the measured $W1-W2$ colors of the system. We find a general trend where the N_H increases as a function of measured $W1-W2$. This is likely reflecting how the motions of gas and dust are coupled in merging environments, where large amounts can be siphoned into the active central region, and enshroud the central AGN. In particular, tidal forces between galaxies during mergers can cause gas and dust to be subject to substantial gravitational torques, where substantial amounts can be funneled towards the central SMBH (Barnes & Hernquist 1991b; Di Matteo et al. 2008; Anglés-Alcázar et al. 2017b). Interestingly, we find that the one triple AGN system in our sample has the highest levels of N_H and $W1-W2$ colors, while the dual AGN all have lower levels. Given that SMBHs grow, and ignite to AGN, through the accretion of cool gas, it is possible that triple merger systems with higher levels of nuclear gas (measured by N_H) will have more AGN. Investigating whether or not this trend varies with total number of AGN in a given merger will require a larger sample of multiple AGN systems.

6.8 Conclusions

In this study, the first targeted search for nearby triple AGN. We analyze 7 nearby ($0.059 < z < 0.078$) triple galaxy mergers with existing archival *Chandra* and SDSS DR16 observations. Each of these systems are confirmed as triple mergers with available spectroscopic and/or photometric redshift measurements. Running `BAYMAX` on these observations, we aim to detect low-count and closely-separated multiple AGN systems. Archival SDSS DR16 and/or *HST* observations allow for informative priors on the locations of each AGN, while `BAYMAX` allows for a statistical analysis on the presence of an X-ray point source at each galactic nucleus. Analyzing various parameters of each detected AGN, such as X-ray luminosity and levels of gas/dust obscuration, we further investigate differences in environments

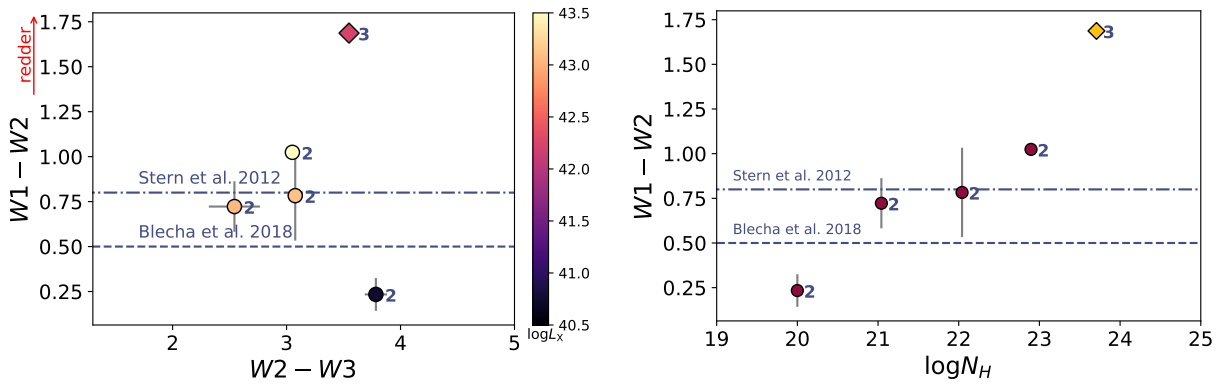

Figure 6.7: $W1-W2$ versus $W2-W3$ colors (*left*) and $W1-W2$ versus N_H associated with the primary AGN (*right*). We denote how many X-ray identified AGN are associated with each system with numbers next to each marker. Furthermore, we denote triple AGN with diamonds, dual AGN with circles, and single AGN with squares. In the left panel, we find that 4 of 6 systems are identified as AGN via mid-IR color-color diagnostics, and that their $W1-W2$ colors are not correlated with the total AGN X-ray luminosity. In the right panel, we find a trend of increasing N_H (associated with the primary) as a function of increasing $W1-W2$. Various AGN color-cuts, defined for single AGN by Stern et al. (2005), and multiple AGN by Blecha et al. (2018b), as shown in dash-dot and dashed blue lines.

associated with single, dual, and triple AGN. The main results of this study are summarized below:

1. We find that 1 triple merger system favors the single point source model (SDSS J0858+1822); 5 triple merger systems favor the dual point source model (SDSS J1027+1749, NGC 3341, SDSS J1631+2352, SDSS J1708+2153, and SDSS J2356−1016); and one triple merger system favors the triple point source model (SDSS J0849+1114). All of the multiple point source systems have Bayes factors that favor the same model when using both informative and non-informative priors, with the exception of J2356−1016, which has a Bayes factor that favors the dual point source model only when using informative priors.

2. We quantify the strength of the Bayes factor, by running false positive tests. We find that there is less than a 1% chance (or, $\leq$2% for SDSS J1631+2352) that the X-ray

emission of each system is actually described by a single point source.

3. The posterior distributions returned by `BAYMAX` show that the best-fit locations of each multiple AGN system coincide with the optical nuclei of galaxies within the merger (as determined by SDSS DR16) and all separations are inconsistent with 0 at the 99.7% C.L.

4. Running our spectral analysis on the multiple point source systems, we find that all point sources have unabsorbed $2-7$ keV luminosities greater than 10^{40} erg s^{-1}, and arguably greater than what is expected from nuclear (within $2''$) contamination from HMXBs, with the exception of the secondary point source in NGC 3341.

5. For the one system with a Bayes factor in favor of the single point source model, further investigation reflects that SDSS J0858+1822 likely hosts no AGN. Thus, we conclude that 1 triple merger system in our sample has no AGN (SDSS J0858+1822); 1 triple merger systems in our sample is composed of single AGN: NGC 3341; 4 triple merger systems in our sample are dual AGN, *all of which are new discoveries*: SDSS J1027+1749, SDSS J1631+2352, SDSS J1708+2153, and SDSS J2356−1016; and we confirm one triple AGN system, SDSS J0849+1114.

6. Analyzing the mid-IR emission of 5 of the mergers with archival *WISE* observations, we find that only 4 are identified as AGN via standard mid-IR color-color AGN diagnostics. Furthermore, there does not appear to be a link between $W1-W2$ colors (representing how red the environment is) and total X-ray luminosity of the AGN in each system. However, accurate mass measurements (and thus Eddington fraction measurements) of each system may give more insight on possible trends between the X-ray luminosities and $W1-W2$ colors.

7. We find a trend of increasing N_H (associated with the primary) as a function of increasing $W1-W2$ color. This is likely reflecting that the motions of gas and dust are

coupled in merging environments, and large amounts of both can be funneled into the active central region during mergers. Interestingly, we find that the one triple AGN system in our sample has the highest levels of N_H and $W1 - W2$ colors, while the dual AGN all have lower levels. Given that SMBHs grow, and ignite to AGN, through the accretion of cool gas, it is possible that triple merger systems with higher levels of nuclear gas (measured by N_H) will have more AGN. Investigating whether or not this trend varies with total number of AGN in a given merger will require a larger sample of multiple AGN systems.

CHAPTER VII

Conclusion

"Though I'm past one hundred thousand miles, I'm feeling very still. And I think my spaceship knows which way to go."

– David Bowie

In this dissertation, I have presented my contributions toward expanding the currently small confirmed population of AGN pairs, and learning more about the environmental impacts on SMBH activity. I've analyzed SMBH activity in nucleated galaxies (Chapter II), searched for a potential binary AGN in a high-redshift quasar (Chapter III), and created a tool that allows for X-ray detections of closely-separated, low-count, multi-AGN systems (Chapters IV, V, and VI).

The currently small population of confirmed dual AGN is a result of our limitations in spatially resolving closely separated, low count-ratio, systems in X-rays. With the development of `BAYMAX`, statistical and quantitative analyses of *Chandra* observations are resulting in the discovery of new dual AGN (Foord et al. 2020,b), a handful of which were previously analyzed and *missed* using alternative point source detection techniques. To date, I've detected at least 5 new dual AGN, a considerable fraction of the confirmed (~ 40) population. In addition to finding new dual AGN, multi-wavelength analyses resulted in identifying links between AGN activity and environment. Specifically, by combining results from `BAYMAX` with

optical observations, I showed the dual AGN may prefer closely-separated, gas-rich, environments (Foord et al. 2020); consistent with results from both numerical (Steinborn et al. 2016) and observational studies (Barrows et al. 2017a). Furthermore, using *WISE* mid-IR observations, I found that gas and dust levels appear to be linked in merger environments, and that larger levels of gas and dust may results in more AGN activation (Foord et al. 2020b). All of these measurements can be better confirmed as trends in the future using much larger samples of dual AGN.

Moving forward, analyses with `BAYMAX` will become much more powerful with (i) large, systematic X-ray surveys using archival *Chandra* observations and (ii) combining results from X-ray analyses with high-resolution NIR imaging or IFU spectroscopy. This latter point can be achieved in the future with the *James Webb Space Telescope*'s NIRSpec integral field unit, where each spatial element in the IFU data cube is $0\farcs1 \times 0\farcs1$. Within a year, `BAYMAX` is anticipated to be available for public use, where a multitude of astrophysical studies, beyond searching for AGN pairs, can make use of the code. In the following section, I briefly review the future directions of `BAYMAX`, and the impact these results will have on various fields.

7.1 `BAYMAX`: Analyzing jets, rings, and lensed systems

The Bayesian framework behind `BAYMAX` will be useful to a number of research fields beyond multiple AGN systems. Examples include binary active stars, or AGN with X-ray jets – any X-ray observation that is potentially composed of multiple X-ray point sources will benefit from the robust PSF modeling and statistical analysis provided by `BAYMAX`.

Most recently, `BAYMAX` was used in a study on 4C 63.20, which is a peculiar case of a high-redshift ($z = 4.261$), radio-bright quasar (Napier et al. 2020). There is a mismatch between the number of observed, luminous, radio-loud quasars and the predicted radio-loud quasar density (Ajello et al. 2009) for high-redshift AGN. For the redshift bin of $z = 3 - 4$ the observed number is close to factor of 3 times less than the prediction, while this jumps up to a factor > 10 for the redshift bin $z = 4 - 5$ (Volonteri et al. 2011). This conundrum is

often attributed to Cosmic Microwave Background (CMB) photons affecting the behavior of high-redshift jetted AGN; as the CMB energy density scales as $(1+z)^4$, at $z = 3$ it begins to dominate over the magnetic energy density (Celotti & Fabian 2004). The two main effects of this are that (i) synchrotron emission is suppressed and (ii) high-energy electrons will cool effectively via inverse Compton scattering off CMB photons, enhancing X-ray emission and further suppressing the radio emission (Ghisellini et al. 2014). The fact that 4C 63.20 has detected radio lobe emission, in spite of the strong assumed CMB energy density at the quasar's redshift, can be explained if the lobes are highly compact and/or magnetized. For such a system, CMB quenching models predict that the radio lobes should also be X-ray emitters and that the X-ray luminosity should be more luminous than for a comparably young and nearby radio galaxy.

Thus, deep observations with *Chandra* were obtained for 4C 63.20 over three epochs (Obs. IDs 20033, 19954, 18106; PI: Gallo), for a total of 100 ks with ACIS-S. One of the main goals of analyzing this dataset was to see if the individual radio lobes in 4C 63.20 were X-ray bright, which could only be resolved by *Chandra*. The stacked, 0.5−8 keV dataset was composed of less than 60 counts, making it difficult to measure the significance and location of any X-ray emission potentially coinciding with the radio lobes (see Figure 7.1). Thus, `BAYMAX` was incorporated into the analysis, to compare a single point source model (where X-ray emission is only consistent with the radio core) to a triple point source model (where the core and both radio lobes are emitting in X-rays). I found the Bayes factor strongly favored the triple point source model when using both non-informative ($\ln \mathcal{B}_{3/1} = 2.57 \pm 0.60$) and informative priors ($\ln \mathcal{B}_{3/1,\mathrm{inform}} = 4.85 \pm 0.64$).

Moving forward, `BAYMAX` has the ability to contribute to many fields beyond searching for and detecting multiple AGN systems. Current analyses include analyzing a dual AGN candidate with additional X-ray emission possibly associated with an Einstein ring from a background submillimeter galaxy[1]; future studies include using `BAYMAX` to analyze a pop-

[1]This project is being led by graduate student Sóley Hyman and Dr. Belinda Wilkes

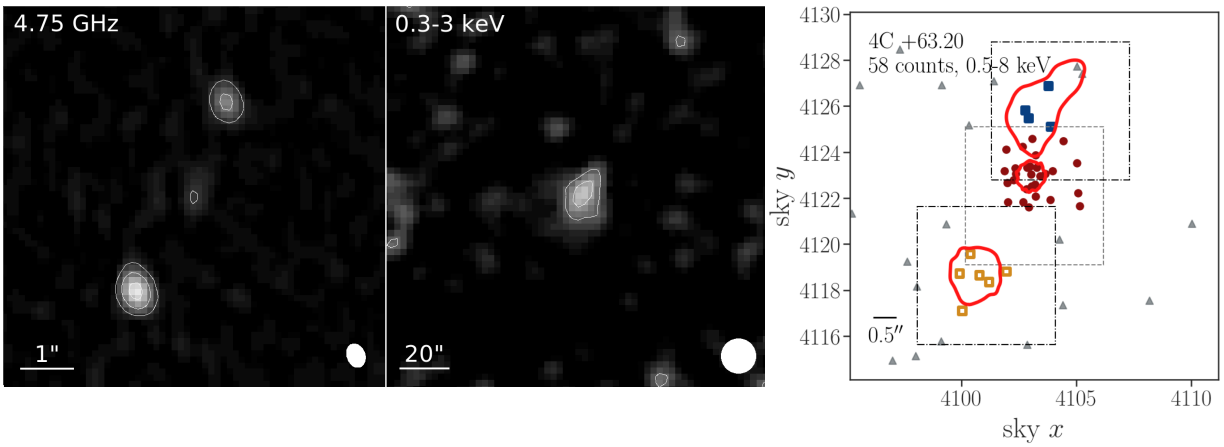

Figure 7.1: VLA (5 Ghz; *left*), *XMM-Newton* (0.3−3 keV; *center*), and *Chandra* (0.5−8 keV; *right*) images of 4C 63.20. Given the resolution of *XMM-Newton* (6″ FWHM at 1 keV), the X-ray image is consistent with a point source. *Chandra* observations show a spread of X-ray emission, consistent with position angle of the radio lobes. The system was analyzed with `BAYMAX`, where the triple point source model was strongly favored. Red circles, yellow open-faced triangles, and blue squared denote counts most likely associated with the core and two lobes (with red contours representing the error bars on their respective locations). In dashed boxes I show the sky x, y, priors used for the location of each point source. Figures taken from Napier et al. (2020).

ulation of high-redshift, massive, quasars to better measure the lensed fraction (Fan et al. 2019; Pacucci & Loeb 2019), which constrains the mass functions of the earliest populations of SMBHs, and thus black hole seed models[2].

7.2 Future X-ray Surveys with `BAYMAX`

Although the existence and evolution of SMBH pairs have been hypothesized for some time (Peters 1964; Begelman et al. 1980), the field of detecting and classifying AGN pairs remains relativity young. Large, systematic searches have mostly been carried out in the optical regime, taking advantage of large data releases associated with SDSS (Wang et al. 2009; Smith et al. 2010; Ge et al. 2012; Fu et al. 2012) or the W. M. Keck Observatory (Gerke et al. 2007; Comerford et al. 2009). In these instances, X-ray observations are mostly used as

[2]This project will be led by a summer CfA student, co-advised by myself, Dr. Fabio Pacucci, and Dr. Avi Loeb.

a follow-up confirmation step for dual AGN that are determined to be interesting. The X-ray regime remains relatively void of large, systematic, X-ray surveys searching for AGN pairs. The largest study to date is presented in Koss et al. (2012), where they use the Burst Alert Telescope (BAT) on the *Neil Gehrels Swift Observatory* in tandem with optical data to study the nuclear X-ray emission of over 150 merging systems. Given the angular resolution of BAT (FWHM of $6''$ at 1 keV), this study was sensitive to physical separations larger than 1 kpc. Moving forward, it will be important to carry-out large, systematic surveys where *Chandra* is the primary tool to discover AGN pairs, rather than a follow-up confirmation step. This will allow for true X-ray surveys, as well as a significant advancement of understanding in the rate of AGN pairs and their preferential environments. `BAYMAX` will play an important role in these future X-ray surveys, especially for low-count and/or closely separated systems, where the ability to estimate likelihoods using non-informative priors will be especially powerful.

7.2.1 Nearby X-ray Surveys with IR Follow-up

Recently, *Chandra* observations were taken for a sub-sample of the original BAT AGN sample from Koss et al. (2012). This sub-sample was composed of closely-separated merging systems, where the angular separation of the optical galactic nuclei were only resolvable with *Chandra*. Analyzing the *Chandra* observations with `BAYMAX` using non-informative priors, I found that one of the systems has a Bayes factor that strongly favors the dual point source model ($\ln \mathcal{B}_{2/1} > 5$). Analyzing high-resolution follow-up infrared observations (via the near-infrared camera, NIRC2, on the Keck 2 telescope at W. M. Keck Observatory; presented in Koss et al. 2018), it was determined that the system was composed of two nuclei, which coincide with the best-fit results returned from `BAYMAX` and which were previously undetected by optical imaging taken at the Kitt Peak Observatory (see Figure 7.2). This is just one example of the interesting results expected from pairing `BAYMAX` with a large X-ray survey of AGN.

In the future, I plan to carry out a multi-wavelength characterization of nearby ($z < 0.03$)

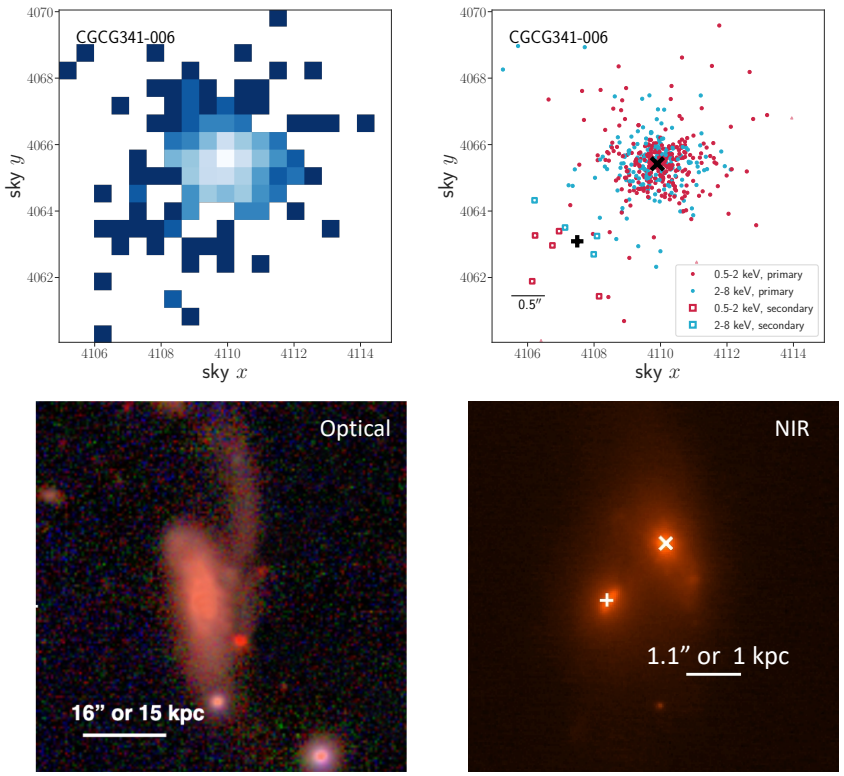

Figure 7.2: An example of a closely-separated, low count-ratio dual AGN system detected by `BAYMAX` (binned *Chandra* observations shown in the top left panel, unbinned *Chandra* dataset shown in the top right panel), undetected in optical observations (bottom left panel). Follow-up NIR imaging shows two nuclei (bottom right panel(, whose spatial positions coincide with the best-fit positions determined by `BAYMAX` (”$\times$” and ”+”). Both images in the bottom panels are taken from Koss et al. (2018) (with permission from Springer Nature Publishing, license number: 4827040195194).

dual AGN. Little is known about closely-separated (< 1 kpc) dual AGN, due to our inability to resolve the emission associated with each AGN. As a result, there is no well-constrained measurement of the fraction of dual AGN in this nearby, small-separation regime. For example, the rate of dual AGN at low redshifts has been estimated to be anywhere from $\sim 0.1\%$ (at ~ 1 kpc where AGN are defined using emission line ratios in a sample of merging galaxies; Liu et al. 2011b) to as high as 7% (for a sample of hard-X-ray-bright AGN; Koss et al. 2012). On top of this, AGN observability is expected to increase as a function of decreasing angular separation between the SMBHs (e.g. Goulding et al. 2018; Capelo et al. 2017; Barrows et al. 2017a). Recent observations of nearby ($z < 0.1$), moderately separated (< 5 kpc) systems find the fraction of dual AGN to be as high as 40% (Barrows et al. 2017a).

Constraining the rate of dual AGN in the small-separated regime is vital, as it will inform us of the role galaxy mergers play in triggering AGN (Villforth et al. 2017), timescales for post-merger SMBHs to sink to the center of the potential well (or, the effectiveness of dynamical friction; Antonini & Merritt 2012), as well as merger-related feedback physics (Hayward et al. 2014). I plan to use `BAYMAX` on a sample of 86 nearby ($z \leq 0.037$) AGN, in order to measure the dual AGN fraction in the small-separation regime. The sample was created using the AllWISE Catalog of AGN (Secrest et al. 2015, where AGN are identified using mid-IR color cuts presented in Mateos et al. 2012). There are 86 AGN within $\sim$155 Mpc ($z \leq 0.037$) and predicted $L_X > 10^{40}$ erg s^{-1}. Within this sample, 36/86 have archival *Chandra* observations, while 50/86 are proposed to receive new *Chandra* observations. The volume- and luminosity-limited sample will enable me to search for dual AGN with small separations, measure large-scale properties of the host galaxies (using complementary IR observations), and return a precise dual AGN fraction measurement (and the first *uniform* measurement of the nearby dual AGN fraction). More specifically, I will be sensitive to dual AGN with physical separations *as small as 14 pc and complete to separations larger than 250 pc*, two orders of magnitude smaller than the currently most-closely separated X-ray confirmed dual AGN (1.9 kpc; Comerford et al. 2011).

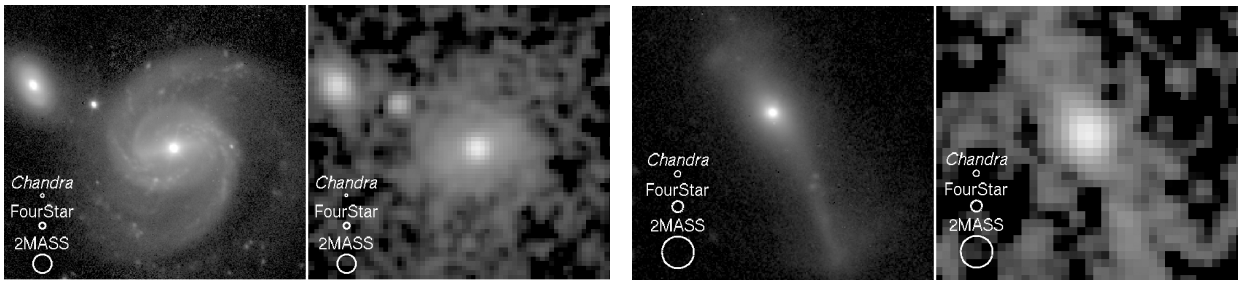

Figure 7.3: Images of 2 sample galaxies with FourStar (angular res. $\sim 0\farcs7$, left-hand side), compared against 2MASS (angular res. $\sim 2''$, right-hand side), which is frequently the highest resolution near/mid-IR available. With IR observations, I can probe structure down to hundreds of parsecs. Using only the archival 2MASS data, it would be possible to miss interacting pairs like NGC 7674 (left) and irregular/tidal features like ESO 543-G008 (right), which are both in my nearby AGN sample.

This homogeneous sample will allow for the first uniform measurement of the nearby dual AGN fraction. Taking the exceptionally conservative assumption that I find no new dual AGN, the archival sample alone will allow me to measure the dual AGN fraction to a precision of $5.5^{+3.8}_{-1.1}\%$ (at the 1σ C.L. using binomial intervals). This is based on the archival sample, where 2 of the 36 AGN (Mrk 739 and Mrk 273) have already been confirmed as dual (Koss et al. 2011; Liu et al. 2019). This value would already be inconsistent with some past theoretical predictions ($< 1\%$, Volonteri et al. 2016). Furthermore, the assumption of a dual AGN rate of 5.5% is conservative, as no previous observational study has been capable of probing such small separations as ours; in which case, the fractional uncertainties in the measurements will be proportionally smaller. Because galaxy merging simulations predict a large number of dual AGN at close (< 1 kpc) separations, finding no dual AGN within this sample (and tightly constraining the dual AGN fraction) will still yield important insights on the conditions associated with AGN triggering. Most interestingly, dynamical friction may be insufficient to decrease the separation of a dual SMBH system to $\sim$1 kpc with any regularity (Antonini & Merritt 2012); here, non-detections would suggest that the majority of dual AGN with separations $\geq$1 kpc are stalled. Other interpretations are that the AGN duty cycle is the main influence on activity during mergers (see Goulding et al. 2018), where AGN are only "on" earlier in the merger.

The X-ray analysis alone will advance understanding of AGN fueling mechanisms in merging systems vs. single AGN. In particular, an X-ray spectral analysis of detected dual AGN will allow for a measurement of the absorbing column toward the secondary AGN, and characteristics of any Fe Kα lines. I will combine my X-ray results with high-resolution, near-IR snapshots of each system to study merger-remnant features, such as dual stellar nuclei and faint tidal features, that are unidentifiable with other wavelengths. With these observations I will carry out qualitative (i.e., do the large-scale features show evidence of a past merger?) and quantitative (i.e., calculating the mass ratios from resolved small-scale features such as stellar nuclei) analyses on the environments for both single and dual AGN. Due to the large amount of dust in the nuclei, optical data are insufficient to identify dual nuclei on the scales of interest. H and K band data will be unaffected by the dust, such that I can relate dual AGN candidates in the X-rays to the near-IR morphology.

As a PhD candidate at the University of Michigan, I observed the Southern Hemisphere host galaxies ($\sim$ 50% of the sample) via high-resolution, near-IR snapshots using the FourStar instrument on the 6.5 m Baade telescope at Magellan. These observations probe structure down to $\sim$100 pc, where I searched for evidence of late-stage mergers or nuclei that have not yet completely merged in galaxies that otherwise look relaxed with existing data (see Fig. 7.3). Future, high-resolution IR observations of the Northern Hemisphere galaxies (which I am actively proposing to observe with the NIR Imager, NIRI, at the Gemini North telescope) will allow for the full sample of AGN environments to be analyzed in the IR-waveband. With NIRI, I will be able to observe each Northern Hemisphere host galaxy with a similar angular resolution ($\sim$0.″7, seeing limited) as my past observations with FourStar.

7.2.2 Quantifying the Rate of Dual AGN Across Cosmic Time ($0.5 < z < 3.5$)

Cosmological simulations predict that the fraction of dual AGN increases dramatically with redshift, however there is no well-constrained measurement of the fraction of dual AGN

at high-redshift. For example, at $z = 1$ the fraction of AGN that are dual is predicted to be anywhere between 0.06–1.0% (Yu et al. 2011; Steinborn et al. 2015), while at $z = 3$ the predicted range spans between 1–3% (Volonteri et al. 2016; Rosas-Guevara et al. 2015). In addition to this, observational constraints on the dual AGN fraction in the nearby universe ($z < 1$) have been found to be higher than predicted (Koss et al. 2012; Barrows et al. 2017a), reflecting that simulations may be underpredicting the true rate at all redshifts (see Fig. 7.4). Yet, an accurate measurement of the rate and evolution of dual AGN at high-redshifts ($1 < z < 3$) will inform us of the importance of feedback (or lack thereof) in merging galaxy systems (as measured in the simulations presented in Capelo et al. 2015) and the role galaxy mergers play in triggering AGN (Villforth et al. 2017) during the peak of galactic mergers and AGN activity.

I will carry out a large, uniform, archival search for dual AGN in distant galaxies (up to $z = 3.5$) found in wide and deep public *Chandra* surveys: COSMOS, AEGIS-XW, XUDS, AEGIS-XD, and CDF-S. Analyzing this large sample of archival AGN will lead to (i) a better understanding of the environments (and underlying physics) of dual AGN and (ii) a measurement of the merger rate history of AGN as a function of redshift. Regarding point (i), these surveys have coinciding archival *HST* observations, allowing for an optical analysis of each galaxy host. Optical imaging allows an analysis of possible galaxy morphology disturbances, and can help classify common characteristics of galaxies found with dual AGN vs. single AGN. Regarding point (ii), a quantitative analysis of the large number of archival AGN allows for a uniform study of the rate of dual AGN as a function of redshift.

The principal factor in whether `BAYMAX` can determine the duality of a given AGN with *Chandra* data is the number of background-subtracted net photon counts (N_c). I have found that with $N_c = 50$–200, there is good to excellent fidelity, depending on other factors such as count ratio (f), separation (r), and off-axis angle (OAA). Below $N_c = 50$, astrophysical background dominates the uncertainties; at the higher-end ($N_c \geq 200$), one can cover an extremely large range of parameter space (f, r) with high fidelity. In general, more counts

Table 7.1: Deep and Wide Archival *Chandra* Fields

Survey	Exposure time	Area	$L_{X,50}$ at $z = 2$	$N_{\rm AGN}$		
	ksec	deg^2	erg s^{-1}	$N_c > 50$	100	200
COSMOS	160	2.2	9.1×10^{43}	212	168	98
AEGIS-XW	200	0.67	7.2×10^{43}	137	68	34
X-UDS	200–600	0.33	2.8×10^{43}	36	23	10
AEGIS-XD	800	0.29	2.1×10^{43}	149	97	59
CDF-S	3500–5000	0.11	4.8×10^{42}	159	103	64

Note – A summary of the archival *Chandra* fields I aim to analyze with `BAYMAX`: COSMOS (Scoville et al. 2007; Elvis et al. 2009; Marchesi et al. 2016), AEGIS-XW (the wide X-ray portion of the All-wavelength Extended Groth strip International Survey; Laird et al. 2009), XUDS (*Chandra* coverage of the Subaru-XMM Deep / UKIDSS Ultra Deep Survey, Kocevski et al. 2018), AEGIS-XD (covers the central 0.29 deg^2 of AEGIS-XW to a depth of 800 ksec, Davis et al. 2007; Nandra et al. 2015), and CDF-S (Xue et al. 2011; Luo et al. 2017). For each survey, I list the effective exposure time, area of survey field, 0.5–10 keV X-ray luminosity of a source with 50 counts at $z = 2$ (assuming $\Gamma = 1.7$). The final 3 columns list the number of AGN with more than 50, 100, and 200 counts in the existing data. I only include sources with off-axis angles $\leq 5'$.

will allow for a higher sensitivity to lower separations and count ratios. Thus, I plan to analyze any AGN with $N_c > 50$ in each of the fields (with $OAA \leq 5'$, beyond which the PSF can not be accurately modeled by `BAYMAX`). All of these surveys have coinciding archival *HST* observations; additionally AEGIS-XW and AEGIS-UD are complemented by data from GALEX, Keck, CFHT, MMT, Subaru, Palomar, Spitzer, and VLA; while XUDS is additionally complemented by the Hyper Suprime-Cam Survey. The large amount of multiwavelength data for each of these surveys will allow for a better understanding of the environments and hosts of the dual AGN vs. single AGN systems — in particular I will search for possible merger-remnant features such as large-scale galactic disturbances, as well as features on smaller scales such as dual stellar nuclei.

Table 7.1 lists the number of sources with $N_c > 50$, 100, and 200 for each of the surveys (where I take into account the overlap between AEGIS-XW and AEGIS-XD); the total number of AGN with $N_c > 50$ is 693. Conservatively assuming the lower-end dual AGN fraction predicted by simulations (on average, $\sim 3\%$, see Fig. 7.4), I will be able to accurately determine the dual AGN rate (within 0.5%). *This study will find more dual AGN than are presently known.* Even more important than determining the global dual AGN rate is to

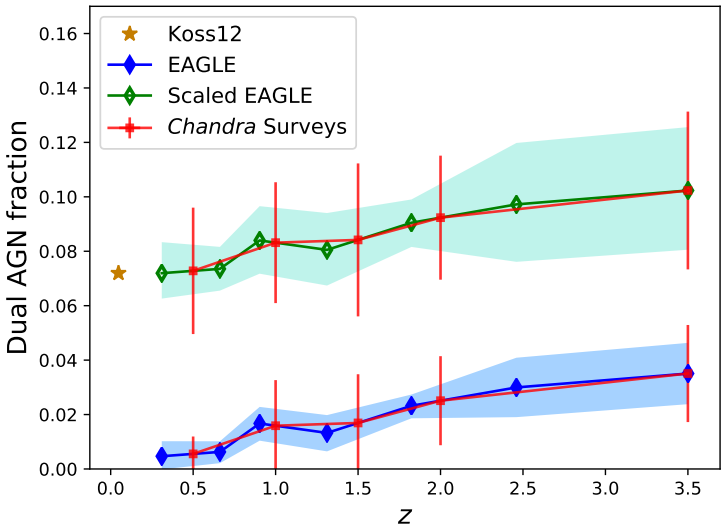

Figure 7.4: The dual AGN fraction as predicted by the hydrodynamical EAGLE simulations is shown in blue. The nearby dual AGN observational constraint (yellow star, Koss et al. 2012) is higher than predicted by EAGLE simulations. I scale the EAGLE simulations such that the predicted dual AGN fraction at $z \sim 0$ matches the observational constraints (green). In red I show how well I can constrain the dual AGN fraction using archival *Chandra* data (within 1σ, using binomial intervals) at both the low- and high-end of the predicted fraction. **My sample will allow for statistically differentiating between these two possible extremes, and my results will be a benchmark for future galaxy-evolution simulations.**

measure the rate as a function of redshift (spectroscopic identification is available for almost all of the X-ray detections across these surveys) — allowing for a quantitative measurement of the evolution of dual AGN across cosmic time. As shown in Fig. 7.4, by splitting the sample into 5 redshift bins (where each bin has 82, 160, 150, 156, and 145 AGN, respectively), I will be able to measure the dual AGN fraction between $z = 0$–3.5 to a precision of $< 2\%$. The tight constraint on the dual AGN fraction will allow me to statistically differentiate between the low- and high-end predictions for the fraction of dual AGN across cosmic time, where the simulations make reliable predictions at the separations (> 1 kpc) and luminosities ($L_X > 10^{43}$erg s^{-1}) that the analysis is sensitive to. These results will be a benchmark for all future galaxy-evolution simulations.

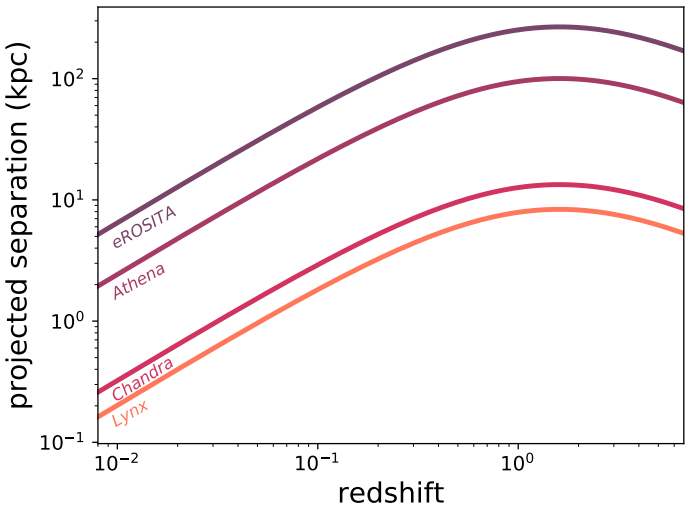

Figure 7.5: The resolving ability (in kpc) of current and future X-ray telescopes versus redshift. *eROSITA* and *Athena* will be able to resolve multiple AGN systems with separations of hundreds and tens of kiloparsec, while *Lynx* will be able to resolve multiple AGN with separations on the order of hundreds of parsec in the nearby Universe. Future versions of `BAYMAX` will include PSF models for X-ray telescopes beyond *Chandra*, optimizing AGN pair detection across many regions of parameter space.

7.3 AGN Pairs and Future Observatories

Looking forward, in the next few decades the number of known AGN, and AGN pairs, will massively grow due to X-ray observatories such as *eROSITA*, *Athena*, and possibly *Lynx*. These observatories represent key players in the future detection of AGN pairs across many interesting regions of parameter space (such as high-redshift and small separations) via both photometry and spectroscopy.

eROSITA is the main instrument on the Russian Spektrum-Roentgen Gamma (SRG) mission, sensitive to the 0.5−10 keV energy range, with a 0.83 deg^2 field of view, and an angular resolution of $\sim$16″ (on-axis). *eROSITA* is performing a 4 year survey of the X-ray sky, being about 20 more times sensitive in the 0.5−2 keV energy band than the *ROSAT* All-Sky Survey (Voges et al. 1999; Boller et al. 2016). The expected number of AGN to be detected from the survey is around 3 million, where tens of thousands will have redshifts

$z > 3$. Given the angular resolution, larger-separated AGN pairs (on the order of hundreds of kpc) will be resolved within $z < 0.3$; however because *eROSITA* will revisit most locations on the sky every 6 months, detection of AGN (as well as AGN pairs) via variability will be viable for relatively bright systems with large separations.

Athena is a X-ray observatory from the Cosmic Vision Program of the ESA (Nandra et al. 2013), due to launch in the early 2030s. *Athena*'s collective area at 1 keV will be more than one order of magnitude larger than any existing (or planned) X-ray observatory. The Wide Field Imager (WFI) has a large field-of-view ($40' \times 40'$), and $0.5-2$ keV sensitivity of $\approx 3 \times 10^{-17}$ erg s^{-1} cm^{-2}; it will detect over 400,000 AGN, where a few hundred are predicted to have $z > 6$! The WFI resolution of approximately $6''$ will allow for detection of AGN pairs down to separations of tens of kpc. Perhaps the most exciting instrument is the X-ray Integral Field Unit (X-IFU), with unprecedented spectroscopic capabilities ($\delta E/E \leq 10^{-3}$). It should be possible, in nearby AGN, to search for the presence of binary systems (down to relatively low mass ratios) by measuring radial velocity shifts of the broad iron Kα line, due to oscillations of a massive black hole around its barycenter (McKernan & Ford 2015). Here, multiple observations of a binary AGN will eventually provide the imprints of the presence of a binary system close to merger. On top of this, if *both* AGN in a binary system have their own respective fluorescence iron lines, with differences in systematic velocities of a few hundred km s^{-1}, it will be possible to spectrally resolve both iron line energy peaks.

Lynx is a concept study for consideration by NASA for the 2020 Astrophysics Decadal Survey. *Lynx* has the smallest PSF ($\approx 0\farcs5$) of any current or future X-ray observatory, making it the most powerful for discovering closely-separated AGN pairs over a wide redshift range. In Figure 7.5, I show the resolving abilities of *Lynx*, compared to other X-ray observatories, as a function of redshift. The PSF is maintained to an off-axis radius of at least 10 arcminutes, which is a large gain over Chandra's sub-arcsecond angular resolution (maintained out to only $\sim$2.5 arcminutes). This superb resolution well-matches that of *JWST* and the *Nancy Grace Roman Space Telescope* (*Roman*), which can provide IR counterparts

to faint and/or obscured AGN pairs detected by *Lynx*.

The future of X-ray astronomy is exciting, and the many new AGN that will be discovered will undoubtedly help us understand the population of AGN pairs, their evolution through time, and their environmental properties. In the future, I hope to adapt `BAYMAX` to include PSF models for other X-ray telescopes in addition to *Chandra*, optimizing AGN pair detection across many regions of parameter space, and gaining an understanding of the bigger picture of where dual AGN reside, and how they evolve, across the Universe.

BIBLIOGRAPHY

Abbott, B. P., Abbott, R., Abbott, T. D., et al. 2016, *Phys. Rev. Lett.*, 116, 061102

Ahumada, R., Allende Prieto, C., Almeida, A., et al. 2019, arXiv e-prints, arXiv:1912.02905

Ajello, M., Costamante, L., Sambruna, R. M., et al. 2009, *ApJ*, 699, 603

Alfvin, E. D., Miller, B. P., Haynes, M. P., et al. 2016, arXiv e-prints, arXiv:1606.04528

Alonso, M. S., Lambas, D. G., Tissera, P., & Coldwell, G. 2007, *MNRAS*, 375, 1017

Anglés-Alcázar, D., Davé, R., Faucher-Giguère, C.-A., Özel, F., & Hopkins, P. F. 2017a, *MNRAS*, 464, 2840

—. 2017b, *MNRAS*, 464, 2840

Antonini, F. 2013, *ApJ*, 763, 62

Antonini, F., Barausse, E., & Silk, J. 2015, *ApJ*, 812, 72

Antonini, F., & Merritt, D. 2012, *ApJ*, 745, 83

Arca-Sedda, M., Capuzzo-Dolcetta, R., Antonini, F., & Seth, A. 2015, *ApJ*, 806, 220

Arnaud, K. A. 1996, in Astronomical Society of the Pacific Conference Series, Vol. 101, Astronomical Data Analysis Software and Systems V, ed. G. H. Jacoby & J. Barnes, 17

Assef, R. J., Stern, D., Kochanek, C. S., et al. 2013, *ApJ*, 772, 26

Baade, W., & Minkowski, R. 1954, *ApJ*, 119, 215

Baker, J. G., Boggs, W. D., Centrella, J., et al. 2008, *ApJ*, 682, L29

Baldassare, V. F., Gallo, E., Miller, B. P., et al. 2014, *ApJ*, 791, 133

Baldwin, J. A., Phillips, M. M., & Terlevich, R. 1981, *PASP*, 93, 5

Bansal, K., Taylor, G. B., Peck, A. B., Zavala, R. T., & Romani, R. W. 2017, *ApJ*, 843, 14

Barnes, J. E., & Hernquist, L. E. 1991a, *ApJ*, 370, L65

—. 1991b, *ApJ*, 370, L65

Barrows, R. S., Comerford, J. M., & Greene, J. E. 2018, *ApJ*, 869, 154

Barrows, R. S., Comerford, J. M., Greene, J. E., & Pooley, D. 2017a, *ApJ*, 838, 129

Barrows, R. S., Comerford, J. M., Zakamska, N. L., & Cooper, M. C. 2017b, *ApJ*, 850, 27

Barrows, R. S., Sandberg Lacy, C. H., Kennefick, J., et al. 2013, *ApJ*, 769, 95

Barth, A. J., Bentz, M. C., Greene, J. E., & Ho, L. C. 2008, *ApJ*, 683, L119

Becker, R. H., White, R. L., Gregg, M. D., et al. 2001, *ApJS*, 135, 227

Begelman, M. C., Blandford, R. D., & Rees, M. J. 1980, *Nature*, 287, 307

Belfiore, F., Maiolino, R., Maraston, C., et al. 2016, *MNRAS*, 461, 3111

Bell, E. F., McIntosh, D. H., Katz, N., & Weinberg, M. D. 2003, *ApJS*, 149, 289

Bell, E. F., Papovich, C., Wolf, C., et al. 2005, *ApJ*, 625, 23

Berczik, P., Merritt, D., Spurzem, R., & Bischof, H.-P. 2006, *ApJ*, 642, L21

Berentzen, I., Preto, M., Berczik, P., Merritt, D., & Spurzem, R. 2009, *ApJ*, 695, 455

Betancourt, M. J., Byrne, S., Livingstone, S., & Girolami, M. 2014, arXiv e-prints, arXiv:1410.5110

Bianchi, S., Guainazzi, M., Matt, G., Fonseca Bonilla, N., & Ponti, G. 2009, *A&A*, 495, 421

Bianchi, S., Piconcelli, E., Pérez-Torres, M. Á., et al. 2013, *MNRAS*, 435, 2335

Binney, J., & Tremaine, S. 1987, Galactic dynamics

Blaes, O., Lee, M. H., & Socrates, A. 2002, *ApJ*, 578, 775

Blecha, L., Loeb, A., & Narayan, R. 2013, *MNRAS*, 429, 2594

Blecha, L., Snyder, G. F., Satyapal, S., & Ellison, S. L. 2018a, *MNRAS*, 478, 3056

—. 2018b, *MNRAS*, 478, 3056

Böker, T., Laine, S., van der Marel, R. P., et al. 2002, *AJ*, 123, 1389

Böker, T., Sarzi, M., McLaughlin, D. E., et al. 2004, *AJ*, 127, 105

Boller, T., Freyberg, M. J., Trümper, J., et al. 2016, *A&A*, 588, A103

Boller, T., Fabian, A. C., Sunyaev, R., et al. 2002, *MNRAS*, 329, L1

Brandt, W. N., & Alexander, D. M. 2010, Proceedings of the National Academy of Science, 107, 7184

Brassington, N. J., Ponman, T. J., & Read, A. M. 2007, *MNRAS*, 377, 1439

Brightman, M., & Nandra, K. 2011a, *MNRAS*, 413, 1206

—. 2011b, *MNRAS*, 413, 1206

Brightman, M., Nandra, K., Salvato, M., et al. 2014, *MNRAS*, 443, 1999

Brightman, M., & Ueda, Y. 2012, *MNRAS*, 423, 702

Burbidge, G. R. 1970, *ARA&A*, 8, 369

Burke-Spolaor, S. 2011, *MNRAS*, 410, 2113

Capelo, P. R., Dotti, M., Volonteri, M., et al. 2017, *MNRAS*, 469, 4437

Capelo, P. R., Volonteri, M., Dotti, M., et al. 2015, *MNRAS*, 447, 2123

Carollo, C. M., Danziger, I. J., Rich, R. M., & Chen, X. 1997, *ApJ*, 491, 545

Carollo, C. M., Stiavelli, M., & Mack, J. 1998, *AJ*, 116, 68

Carollo, C. M., Stiavelli, M., Seigar, M., de Zeeuw, P. T., & Dejonghe, H. 2002, *AJ*, 123, 159

Cash, W. 1979, *ApJ*, 228, 939

Celotti, A., & Fabian, A. C. 2004, *MNRAS*, 353, 523

Cisternas, M., Jahnke, K., Inskip, K. J., et al. 2011, *ApJ*, 726, 57

Comerford, J. M., Gerke, B. F., Stern, D., et al. 2012, *ApJ*, 753, 42

Comerford, J. M., Pooley, D., Barrows, R. S., et al. 2015, *ApJ*, 806, 219

Comerford, J. M., Pooley, D., Gerke, B. F., & Madejski, G. M. 2011, *ApJ*, 737, L19

Comerford, J. M., Schluns, K., Greene, J. E., & Cool, R. J. 2013, *ApJ*, 777, 64

Comerford, J. M., Gerke, B. F., Newman, J. A., et al. 2009, *ApJ*, 698, 956

Corral, A., Della Ceca, R., Caccianiga, A., et al. 2011, *A&A*, 530, A42

Côté, P., Piatek, S., Ferrarese, L., et al. 2006, *ApJS*, 165, 57

Côté, P., Ferrarese, L., Jordán, A., et al. 2007, *ApJ*, 671, 1456

Cox, T. J., Di Matteo, T., Hernquist, L., et al. 2006, *ApJ*, 643, 692

Crummy, J., Fabian, A. C., Gallo, L., & Ross, R. R. 2006, *MNRAS*, 365, 1067

Csabai, I., Dobos, L., Trencséni, M., et al. 2007, Astronomische Nachrichten, 328, 852

Cuadra, J., Armitage, P. J., Alexander, R. D., & Begelman, M. C. 2009, *MNRAS*, 393, 1423

Cutri, R. M., Wright, E. L., Conrow, T., et al. 2013, Explanatory Supplement to the AllWISE Data Release Products, Tech. rep.

D'Agostino, J. J., Kewley, L. J., Groves, B. A., et al. 2019, *MNRAS*, 485, L38

Davis, J. E., Bautz, M. W., Dewey, D., et al. 2012, in *Proc. SPIE*, Vol. 8443, Space Telescopes and Instrumentation 2012: Ultraviolet to Gamma Ray, 84431A

Davis, M., Guhathakurta, P., Konidaris, N. P., et al. 2007, *ApJ*, 660, L1

Deane, R. P., Paragi, Z., Jarvis, M. J., et al. 2014, *Nature*, 511, 57

Di Matteo, T., Colberg, J., Springel, V., Hernquist, L., & Sijacki, D. 2008, *ApJ*, 676, 33

Di Matteo, T., Springel, V., & Hernquist, L. 2005, *Nature*, 433, 604

Dickey, J. M., & Lockman, F. J. 1990, *ARA&A*, 28, 215

D'Orazio, D. J., Haiman, Z., & MacFadyen, A. 2013, *MNRAS*, 436, 2997

D'Orazio, D. J., Haiman, Z., & Schiminovich, D. 2015, *Nature*, 525, 351

Dotti, M., Colpi, M., Haardt, F., & Mayer, L. 2007, *MNRAS*, 379, 956

Drake, A. J., Djorgovski, S. G., Mahabal, A., et al. 2009, *ApJ*, 696, 870

Duffell, P. C., D'Orazio, D., Derdzinski, A., et al. 2019, arXiv, arXiv:1911.05506

Dvorkin, I., & Barausse, E. 2017, *MNRAS*, 470, 4547

Ellison, S. L., Mendel, J. T., Scudder, J. M., Patton, D. R., & Palmer, M. J. D. 2013, *MNRAS*, 430, 3128

Ellison, S. L., Secrest, N. J., Mendel, J. T., Satyapal, S., & Simard, L. 2017, ArXiv e-prints, arXiv:1705.05465

Elvis, M., Wilkes, B. J., McDowell, J. C., et al. 1994, *ApJS*, 95, 1

Elvis, M., Civano, F., Vignali, C., et al. 2009, *ApJS*, 184, 158

Eracleous, M., Boroson, T. A., Halpern, J. P., & Liu, J. 2012, *ApJS*, 201, 23

Escala, A., Larson, R. B., Coppi, P. S., & Mardones, D. 2005, *ApJ*, 630, 152

Event Horizon Telescope Collaboration, Akiyama, K., Alberdi, A., et al. 2019, *ApJ*, 875, L1

Fabbiano, G., Wang, J., Elvis, M., & Risaliti, G. 2011, *Nature*, 477, 431

Fabian, A. C., Ballantyne, D. R., Merloni, A., et al. 2002, *MNRAS*, 331, L35

Fabian, A. C., Iwasawa, K., Reynolds, C. S., & Young, A. J. 2000, *PASP*, 112, 1145

Fabian, A. C., Miniutti, G., Iwasawa, K., & Ross, R. R. 2005, *MNRAS*, 361, 795

Fan, L., Han, Y., Fang, G., et al. 2016, *ApJ*, 822, L32

Fan, X., Wang, F., Yang, J., et al. 2019, *ApJ*, 870, L11

Farris, B. D., Duffell, P., MacFadyen, A. I., & Haiman, Z. 2015a, *MNRAS*, 447, L80

—. 2015b, *MNRAS*, 446, L36

Fath, E. A. 1913, *ApJ*, 37, 198

Fazio, G. G., Hora, J. L., Allen, L. E., et al. 2004, *ApJS*, 154, 10

Feroz, F., & Hobson, M. P. 2008, *MNRAS*, 384, 449

Feroz, F., Hobson, M. P., & Bridges, M. 2009, *MNRAS*, 398, 1601

Ferrarese, L., & Merritt, D. 2000, *ApJ*, 539, L9

Ferrarese, L., Côté, P., Dalla Bontà, E., et al. 2006, *ApJ*, 644, L21

Filippenko, A. V., & Sargent, W. L. W. 1985, *ApJS*, 57, 503

Foord, A., Dylan, B., & Mercury, F. 2020b, in prep.

Foord, A., Gallo, E., Hodges-Kluck, E., et al. 2017a, *ApJ*, 841, 51

Foord, A., Gültekin, K., Nevin, R., et al. 2020, *ApJ*, 892, 29

Foord, A., Gültekin, K., Reynolds, M., et al. 2017b, *ApJ*, 851, 106

Foord, A., Gültekin, K., Reynolds, M. T., et al. 2019, *ApJ*, 877, 17

Fruscione, A., McDowell, J. C., Allen, G. E., et al. 2006, in Society of Photo-Optical Instrumentation Engineers (SPIE) Conference Series, Vol. 6270, Society of Photo-Optical Instrumentation Engineers (SPIE) Conference Series, 62701V

Fu, H., Myers, A. D., Djorgovski, S. G., & Yan, L. 2011, *ApJ*, 733, 103

Fu, H., Myers, A. D., Djorgovski, S. G., et al. 2015, *ApJ*, 799, 72

Fu, H., Yan, L., Myers, A. D., et al. 2012, *ApJ*, 745, 67

Gabányi, K. É., Frey, S., Xiao, T., et al. 2014, *MNRAS*, 443, 1509

Gallo, E., Treu, T., Jacob, J., et al. 2008, *ApJ*, 680, 154

Gallo, E., Treu, T., Marshall, P. J., et al. 2010, *ApJ*, 714, 25

Garmire, G., Feigelson, E. D., Broos, P., et al. 2000, *AJ*, 120, 1426

Ge, J.-Q., Hu, C., Wang, J.-M., Bai, J.-M., & Zhang, S. 2012, *ApJS*, 201, 31

Gehrels, N. 1986, *ApJ*, 303, 336

Georgiev, I. Y., & Böker, T. 2014, *MNRAS*, 441, 3570

Georgiev, I. Y., Böker, T., Leigh, N., Lützgendorf, N., & Neumayer, N. 2016, *MNRAS*, 457, 2122

Gerke, B. F., Newman, J. A., Lotz, J., et al. 2007, *ApJ*, 660, L23

Gezari, S., Martin, D. C., Forster, K., et al. 2013, *ApJ*, 766, 60

Ghisellini, G., Celotti, A., Tavecchio, F., Haardt, F., & Sbarrato, T. 2014, *MNRAS*, 438, 2694

Ghosh, P., & White, N. E. 2001, *ApJ*, 559, L97

Gierliński, M., & Done, C. 2004, *MNRAS*, 349, L7

Gilfanov, M. 2004, *MNRAS*, 349, 146

Glikman, E., Simmons, B., Mailly, M., et al. 2015, *ApJ*, 806, 218

Gnedin, O. Y., Ostriker, J. P., & Tremaine, S. 2014, *ApJ*, 785, 71

Gold, R., Paschalidis, V., Etienne, Z. B., Shapiro, S. L., & Pfeiffer, H. P. 2014, *Phys. Rev. D*, 89, 064060

Goulding, A. D., Greene, J. E., Bezanson, R., et al. 2018, Publications of the Astronomical Society of Japan, 70, S37

Graham, A. W., & Spitler, L. R. 2009, *MNRAS*, 397, 2148

Graham, M. J., Djorgovski, S. G., Stern, D., et al. 2015, *Nature*, 518, 74

Greene, J. E., & Ho, L. C. 2005, *ApJ*, 627, 721

—. 2007, *ApJ*, 670, 92

Greene, J. E., Pooley, D., Zakamska, N. L., Comerford, J. M., & Sun, A.-L. 2014, *ApJ*, 788, 54

Greene, J. E., Zakamska, N. L., Ho, L. C., & Barth, A. J. 2011, *ApJ*, 732, 9

Greene, J. E., Zakamska, N. L., Liu, X., Barth, A. J., & Ho, L. C. 2009, *ApJ*, 702, 441

Greene, J. E., Zakamska, N. L., & Smith, P. S. 2012, *ApJ*, 746, 86

Greenstein, J. L., & Matthews, T. A. 1963, *AJ*, 68, 279

Grimm, H. J., Gilfanov, M., & Sunyaev, R. 2002, *A&A*, 391, 923

—. 2003, *MNRAS*, 339, 793

Gualandris, A., Read, J. I., Dehnen, W., & Bortolas, E. 2017, *MNRAS*, 464, 2301

Gültekin, K., Cackett, E. M., King, A. L., Miller, J. M., & Pinkney, J. 2014, *ApJ*, 788, L22

Gültekin, K., Cackett, E. M., Miller, J. M., et al. 2009a, *ApJ*, 706, 404

Gültekin, K., & Miller, J. M. 2012, *ApJ*, 761, 90

Gültekin, K., Richstone, D. O., Gebhardt, K., et al. 2009b, *ApJ*, 698, 198

Haardt, F., & Maraschi, L. 1993, *ApJ*, 413, 507

Halpern, J. P. 1984, *ApJ*, 281, 90

Hayward, C. C., Torrey, P., Springel, V., Hernquist, L., & Vogelsberger, M. 2014, *MNRAS*, 442, 1992

Heckman, T. M., Ptak, A., Hornschemeier, A., & Kauffmann, G. 2005, *ApJ*, 634, 161

Heinis, S., Kumar, S., Gezari, S., et al. 2016a, *ApJ*, 821, 86

Heinis, S., Gezari, S., Kumar, S., et al. 2016b, *ApJ*, 826, 62

Hickox, R. C., Mullaney, J. R., Alexander, D. M., et al. 2014, *ApJ*, 782, 9

Ho, L. C., Filippenko, A. V., & Sargent, W. L. W. 1997, *ApJ*, 487, 591

Hooper, E. J., Impey, C. D., Foltz, C. B., & Hewett, P. C. 1995, *ApJ*, 445, 62

Hopkins, P. F., & Hernquist, L. 2009, *ApJ*, 694, 599

Hopkins, P. F., Hernquist, L., Cox, T. J., et al. 2005, *ApJ*, 630, 705

—. 2006, *ApJS*, 163, 1

Hopkins, P. F., Kereš, D., Murray, N., et al. 2013, *MNRAS*, 433, 78

Hopkins, P. F., & Quataert, E. 2010a, *MNRAS*, 407, 1529

—. 2010b, *MNRAS*, 405, L41

Hopkins, P. F., Bundy, K., Croton, D., et al. 2010, *ApJ*, 715, 202

Hough, D. H. 2013, in European Physical Journal Web of Conferences, Vol. 61, European Physical Journal Web of Conferences, 08009

Hovatta, T., Aller, M. F., Aller, H. D., et al. 2014, *AJ*, 147, 143

Humphrey, P. J., & Buote, D. A. 2008, *ApJ*, 689, 983

Ishibashi, W., & Courvoisier, T. J.-L. 2010, *A&A*, 512, A58

Ivezić, Ž., Menou, K., Knapp, G. R., et al. 2002, *AJ*, 124, 2364

Jahnke, K., & Macciò, A. V. 2011, *ApJ*, 734, 92

James, P. A., Shane, N. S., Beckman, J. E., et al. 2004, *A&A*, 414, 23

Jarrett, T. H., Cohen, M., Masci, F., et al. 2011, *ApJ*, 735, 112

Jeffreys, H. 1935, Proceedings of the Cambridge Philosophical Society, 31, 203

Jeffreys, H. 1961, Theory of probability, Clarendon

Jovanović, P., Borka Jovanović, V., Borka, D., & Popović, L. Č. 2016, *Ap&SS*, 361, 75

Juda, M., & Karovska, M. 2010, in Bulletin of the American Astronomical Society, Vol. 42, AAS/High Energy Astrophysics Division #11, 722

Kaiser, N., Burgett, W., Chambers, K., et al. 2010, in *Proc. SPIE*, Vol. 7733, Ground-based and Airborne Telescopes III, 77330E

Kalberla, P. M. W., Burton, W. B., Hartmann, D., et al. 2005, *A&A*, 440, 775

Kass, R. E., & Raftery, A. E. 1995, Journal of the American Statistical Association, 90, 773

Kauffmann, G., Heckman, T. M., Tremonti, C., et al. 2003, *MNRAS*, 346, 1055

Kellermann, K. I., Sramek, R., Schmidt, M., Shaffer, D. B., & Green, R. 1989, *AJ*, 98, 1195

Kelley, L. Z., Blecha, L., & Hernquist, L. 2017, *MNRAS*, 464, 3131

Kelly, B. C. 2007, *ApJ*, 665, 1489

Kewley, L. J., Dopita, M. A., Leitherer, C., et al. 2013, *ApJ*, 774, 100

Kewley, L. J., Dopita, M. A., Sutherland, R. S., Heisler, C. A., & Trevena, J. 2001, *ApJ*, 556, 121

Kewley, L. J., Groves, B., Kauffmann, G., & Heckman, T. 2006, *MNRAS*, 372, 961

Khan, F. M., Holley-Bockelmann, K., Berczik, P., & Just, A. 2013, *ApJ*, 773, 100

Kharb, P., Lal, D. V., & Merritt, D. 2017, Nature Astronomy, 1, 727

Kim, D.-W., & Fabbiano, G. 2004, *ApJ*, 611, 846

Kocevski, D. D., Faber, S. M., Mozena, M., et al. 2012, *ApJ*, 744, 148

Kocevski, D. D., Brightman, M., Nandra, K., et al. 2015, *ApJ*, 814, 104

Kocevski, D. D., Hasinger, G., Brightman, M., et al. 2018, *ApJS*, 236, 48

Kocsis, B., Haiman, Z., & Loeb, A. 2012, *MNRAS*, 427, 2680

Kormendy, J., & Ho, L. C. 2013, *ARA&A*, 51, 511

Kormendy, J., & Richstone, D. 1995, *ARA&A*, 33, 581

Koss, M., Mushotzky, R., Treister, E., et al. 2012, *ApJ*, 746, L22

Koss, M., Mushotzky, R., Veilleux, S., & Winter, L. 2010, *ApJ*, 716, L125

Koss, M., Mushotzky, R., Treister, E., et al. 2011, *ApJ*, 735, L42

Koss, M. J., Romero-Cañizales, C., Baronchelli, L., et al. 2015, *ApJ*, 807, 149

Koss, M. J., Assef, R., Baloković, M., et al. 2016, *ApJ*, 825, 85

Koss, M. J., Blecha, L., Bernhard, P., et al. 2018, *Nature*, 563, 214

Lacy, M., Petric, A. O., Sajina, A., et al. 2007, *AJ*, 133, 186

Lacy, M., Storrie-Lombardi, L. J., Sajina, A., et al. 2004, *ApJS*, 154, 166

Laird, E. S., Nandra, K., Georgakakis, A., et al. 2009, *ApJS*, 180, 102

Laplace, P. S. 1799, Allgemeine Geographische Ephemeriden, 4, 1

Lawrence, A., Warren, S. J., Almaini, O., et al. 2007, *MNRAS*, 379, 1599

Lehmer, B. D., Alexander, D. M., Bauer, F. E., et al. 2010, *ApJ*, 724, 559

Lehmer, B. D., Eufrasio, R. T., Tzanavaris, P., et al. 2019, *ApJS*, 243, 3

Lehto, H. J., & Valtonen, M. J. 1996, *ApJ*, 460, 207

Leigh, N., Böker, T., & Knigge, C. 2012, *MNRAS*, 424, 2130

Leighly, K. M., Terndrup, D. M., Gallagher, S. C., & Lucy, A. B. 2016, *ApJ*, 829, 4

Li, J., Kastner, J. H., Prigozhin, G. Y., et al. 2004, *ApJ*, 610, 1204

Liu, T., Gezari, S., Heinis, S., et al. 2015, *ApJ*, 803, L16

Liu, T., Gezari, S., Burgett, W., et al. 2016, *ApJ*, 833, 6

Liu, X., Civano, F., Shen, Y., et al. 2013, *ApJ*, 762, 110

Liu, X., Greene, J. E., Shen, Y., & Strauss, M. A. 2010a, *ApJ*, 715, L30

Liu, X., Shen, Y., & Strauss, M. A. 2011a, *ApJ*, 736, L7

Liu, X., Shen, Y., Strauss, M. A., & Greene, J. E. 2010b, *ApJ*, 708, 427

Liu, X., Shen, Y., Strauss, M. A., & Hao, L. 2011b, *ApJ*, 737, 101

Liu, X., Hou, M., Li, Z., et al. 2019, *ApJ*, 887, 90

Lodato, G., Nayakshin, S., King, A. R., & Pringle, J. E. 2009, *MNRAS*, 398, 1392

Lohfink, A. M., Reynolds, C. S., Miller, J. M., et al. 2012, *ApJ*, 758, 67

Lohfink, A. M., Reynolds, C. S., Mushotzky, R. F., & Nowak, M. A. 2013, *Mem. Soc. Astron. Italiana*, 84, 699

Lousto, C. O., & Zlochower, Y. 2013, *Phys. Rev. D*, 87, 084027

Ludlam, R. M., Cackett, E. M., Gültekin, K., et al. 2015, *MNRAS*, 447, 2112

Luo, B., Brandt, W. N., Xue, Y. Q., et al. 2017, *ApJS*, 228, 2

Magorrian, J., Tremaine, S., Richstone, D., et al. 1998, *AJ*, 115, 2285

Maness, H. L., Taylor, G. B., Zavala, R. T., Peck, A. B., & Pollack, L. K. 2004, *ApJ*, 602, 123

Marchesi, S., Ajello, M., Marcotulli, L., et al. 2018, *ApJ*, 854, 49

Marchesi, S., Civano, F., Elvis, M., et al. 2016, *ApJ*, 817, 34

Mateos, S., Alonso-Herrero, A., Carrera, F. J., et al. 2013, *MNRAS*, 434, 941

—. 2012, *MNRAS*, 426, 3271

Mayer, L., Kazantzidis, S., Madau, P., et al. 2007, Science, 316, 1874

McConnell, N. J., & Ma, C.-P. 2013, *ApJ*, 764, 184

McKernan, B., & Ford, K. E. S. 2015, *MNRAS*, 452, L1

Merritt, D., Milosavljević, M., Favata, M., Hughes, S. A., & Holz, D. E. 2004, *ApJ*, 607, L9

Merritt, D., & Valluri, M. 1996, *ApJ*, 471, 82

Messias, H., Afonso, J., Salvato, M., Mobasher, B., & Hopkins, A. M. 2012, *ApJ*, 754, 120

Metropolis, N., Rosenbluth, A. W., Rosenbluth, M. N., Teller, A. H., & Teller, E. 1953, *J. Chem. Phys.*, 21, 1087

Michell, J. 1784, Philosophical Transactions of the Royal Society of London Series I, 74, 35

Mihos, J. C., & Hernquist, L. 1996, *ApJ*, 464, 641

Miller, B., Gallo, E., Treu, T., & Woo, J.-H. 2012a, *ApJ*, 747, 57

—. 2012b, *ApJ*, 745, L13

Miller, B. P., Gallo, E., Greene, J. E., et al. 2015, *ApJ*, 799, 98

Miller, J. M. 2007, *ARA&A*, 45, 441

Miller, J. M., Fabian, A. C., Wijnands, R., et al. 2002, *ApJ*, 570, L69

Miller, J. M., Parker, M. L., Fuerst, F., et al. 2013, *ApJ*, 779, L2

Miller, M. C., & Davies, M. B. 2012, *ApJ*, 755, 81

Milosavljević, M., & Merritt, D. 2003a, *ApJ*, 596, 860

Milosavljević, M., & Merritt, D. 2003b, in American Institute of Physics Conference Series, Vol. 686, The Astrophysics of Gravitational Wave Sources, ed. J. M. Centrella, 201–210

Milosavljević, M., & Phinney, E. S. 2005, *ApJ*, 622, L93

Mineo, S., Gilfanov, M., & Sunyaev, R. 2012, *MNRAS*, 419, 2095

Mingarelli, C. M. F. 2019, Nature Astronomy, 3, 8

Miniutti, G., Ponti, G., Greene, J. E., et al. 2009, *MNRAS*, 394, 443

Mooley, K. P., Wrobel, J. M., Anderson, M. M., & Hallinan, G. 2017, ArXiv e-prints, arXiv:1703.10227

Mooley, K. P., Hallinan, G., Bourke, S., et al. 2016, *ApJ*, 818, 105

Moshir, M., & et al. 1990, IRAS Faint Source Catalogue, 0

Muñoz, D. J., Miranda, R., & Lai, D. 2019, *ApJ*, 871, 84

Mukherjee, P., Parkinson, D., & Liddle, A. R. 2006, *ApJ*, 638, L51

Müller-Sánchez, F., Comerford, J. M., Nevin, R., et al. 2015, *ApJ*, 813, 103

Müller-Sánchez, F., Prieto, M. A., Hicks, E. K. S., et al. 2011, *ApJ*, 739, 69

Muratov, A. L., & Gnedin, O. Y. 2010, *ApJ*, 718, 1266

Mushotzky, R. F., Done, C., & Pounds, K. A. 1993, *ARA&A*, 31, 717

Naiman, J. P., Ramirez-Ruiz, E., Debuhr, J., & Ma, C. P. 2015, *ApJ*, 803, 81

Nandra, K., Barret, D., Barcons, X., et al. 2013, arXiv e-prints, arXiv:1306.2307

Nandra, K., Laird, E. S., Aird, J. A., et al. 2015, *ApJS*, 220, 10

Napier, K., Foord, A., Gallo, E., et al. 2020, *MNRAS*, submitted

Neumayer, N., & Walcher, C. J. 2012, Advances in Astronomy, 2012, 709038

Nevin, R., Comerford, J., Müller-Sánchez, F., Barrows, R., & Cooper, M. 2016, *ApJ*, 832, 67

Nguyen, D. D., Seth, A. C., Reines, A. E., et al. 2014, *ApJ*, 794, 34

Pacucci, F., & Loeb, A. 2019, *ApJ*, 870, L12

Paczynski, B. 1977, *ApJ*, 216, 822

Panessa, F., Barcons, X., Bassani, L., et al. 2007, *A&A*, 467, 519

Pellegrini, S. 2010, *ApJ*, 717, 640

Perault, M. 1987, PhD thesis, -

Perets, H. B., & Alexander, T. 2008, *ApJ*, 677, 146

Peters, P. C. 1964, Physical Review, 136, 1224

Pfeifle, R. W., Satyapal, S., Manzano-King, C., et al. 2019a, *ApJ*, 883, 167

Pfeifle, R. W., Satyapal, S., Secrest, N. J., et al. 2019b, *ApJ*, 875, 117

Piconcelli, E., Jimenez-Bailón, E., Guainazzi, M., et al. 2005, *A&A*, 432, 15

Plotkin, R. M., Gallo, E., Miller, B. P., et al. 2014, *ApJ*, 780, 6

Popović, L. Č. 2012, NewAr, 56, 74

Primini, F. A., Houck, J. C., Davis, J. E., et al. 2011, *ApJS*, 194, 37

Raimundo, S. I., Fabian, A. C., Vasudevan, R. V., Gand hi, P., & Wu, J. 2012, *MNRAS*, 419, 2529

Reines, A. E., Sivakoff, G. R., Johnson, K. E., & Brogan, C. L. 2011, *Nature*, 470, 66

Rezzolla, L., Barausse, E., Dorband, E. N., et al. 2008, *Phys. Rev. D*, 78, 044002

Rich, J. A., Kewley, L. J., & Dopita, M. A. 2011, *ApJ*, 734, 87

Richards, G. T., Strauss, M. A., Fan, X., et al. 2006, *AJ*, 131, 2766

Richstone, D., Ajhar, E. A., Bender, R., et al. 1998, *Nature*, 385, A14

Rodriguez, C., Taylor, G. B., Zavala, R. T., et al. 2006, *ApJ*, 646, 49

Roedig, C., Krolik, J. H., & Miller, M. C. 2014, *ApJ*, 785, 115

Roedig, C., Sesana, A., Dotti, M., et al. 2012, *A&A*, 545, A127

Rosario, D. J., Shields, G. A., Taylor, G. B., Salviander, S., & Smith, K. L. 2010, *ApJ*, 716, 131

Rosas-Guevara, Y. M., Bower, R. G., Schaye, J., et al. 2015, *MNRAS*, 454, 1038

Rosati, P., Tozzi, P., Giacconi, R., et al. 2002, *ApJ*, 566, 667

Rubinur, K., Das, M., & Kharb, P. 2018, Journal of Astrophysics and Astronomy, 39, 8

Runnoe, J. C., Brotherton, M. S., & Shang, Z. 2012, *MNRAS*, 422, 478

Ryu, T., Perna, R., Haiman, Z., Ostriker, J. P., & Stone, N. C. 2018, *MNRAS*, 473, 3410

Salvatier, J., Wiecki, T., & Fonnesbeck, C. 2016, PeerJ Computer Science, 2, 1507.08050

Sanders, D. B., & Mirabel, I. F. 1996, *ARA&A*, 34, 749

Satyapal, S., Ellison, S. L., McAlpine, W., et al. 2014, *MNRAS*, 441, 1297

Sazonov, S., & Khabibullin, I. 2017, *MNRAS*, 466, 1019

Schawinski, K., Simmons, B. D., Urry, C. M., Treister, E., & Glikman, E. 2012, *MNRAS*, 425, L61

Schlafly, E. F., & Finkbeiner, D. P. 2011, *ApJ*, 737, 103

Schmidt, G. D., Weymann, R. J., & Foltz, C. B. 1989, *PASP*, 101, 713

Schmidt, M. 1963, *Nature*, 197, 1040

Schmidt, M., & Matthews, T. A. 1964, *ApJ*, 139, 781

Schödel, R., Merritt, D., & Eckart, A. 2009, *A&A*, 502, 91

Schwarzschild, K. 1916, Abh. Konigl. Preuss. Akad. Wissenschaften Jahre 1906,92, Berlin,1907, 1916, 189

Scott, A. E., Stewart, G. C., & Mateos, S. 2012, *MNRAS*, 423, 2633

Scoville, N., Aussel, H., Brusa, M., et al. 2007, *ApJS*, 172, 1

Secrest, N. J., Dudik, R. P., Dorland, B. N., et al. 2015, *ApJS*, 221, 12

Seth, A., Agüeros, M., Lee, D., & Basu-Zych, A. 2008, *ApJ*, 678, 116

Seth, A. C., van den Bosch, R., Mieske, S., et al. 2014, *Nature*, 513, 398

Shang, Z., Brotherton, M. S., Wills, B. J., et al. 2011, *ApJS*, 196, 2

Shaw, J. R., Bridges, M., & Hobson, M. P. 2007, *MNRAS*, 378, 1365

Shen, Y., Liu, X., Greene, J. E., & Strauss, M. A. 2011, *ApJ*, 735, 48

Shields, J. C., Walcher, C. J., Böker, T., et al. 2008, *ApJ*, 682, 104

Shimura, T., & Takahara, F. 1995, *ApJ*, 445, 780

Simić, S., & Popović, L. Č. 2016, *Ap&SS*, 361, 59

Sinha, M., & Holley-Bockelmann, K. 2009, *MNRAS*, 397, 190

Sivakoff, G. R., Jordán, A., Sarazin, C. L., et al. 2007, *ApJ*, 660, 1246

Skilling, J. 2004, in American Institute of Physics Conference Series, Vol. 735, American Institute of Physics Conference Series, ed. R. Fischer, R. Preuss, & U. V. Toussaint, 395–405

Slipher, V. M. 1917, Lowell Observatory Bulletin, 3, 59

Smith, B. J., Campbell, K., Struck, C., et al. 2018, *AJ*, 155, 81

Smith, K. L., Shields, G. A., Bonning, E. W., et al. 2010, *ApJ*, 716, 866

Smith, K. L., Shields, G. A., Salviander, S., Stevens, A. C., & Rosario, D. J. 2012, *ApJ*, 752, 63

Sobral, D., Stroe, A., Dawson, W. A., et al. 2015, *MNRAS*, 450, 630

Soifer, B. T., Helou, G., & Werner, M. 2008, *ARA&A*, 46, 201

Steinborn, L. K., Dolag, K., Comerford, J. M., et al. 2016, *MNRAS*, 458, 1013

Steinborn, L. K., Dolag, K., Hirschmann, M., Prieto, M. A., & Remus, R.-S. 2015, *MNRAS*, 448, 1504

Stern, D., Eisenhardt, P., Gorjian, V., et al. 2005, *ApJ*, 631, 163

Stern, D., Assef, R. J., Benford, D. J., et al. 2012, *ApJ*, 753, 30

Stocke, J. T., Morris, S. L., Weymann, R. J., & Foltz, C. B. 1992, *ApJ*, 396, 487

Stone, N. C., Küpper, A. H. W., & Ostriker, J. P. 2017, *MNRAS*, 467, 4180

Sunyaev, R. A., Tinsley, B. M., & Meier, D. L. 1978, Comments on Astrophysics, 7, 183

Swartz, D. A., Soria, R., Tennant, A. F., & Yukita, M. 2011, *ApJ*, 741, 49

Tanaka, T., Menou, K., & Haiman, Z. 2012, Monthly Notices of the Royal Astronomical Society, 420, 705

Tanaka, T. L. 2013, *MNRAS*, 434, 2275

Tanaka, T. L., & Haiman, Z. 2013, Classical and Quantum Gravity, 30, 224012

Tanaka, Y., Boller, T., Gallo, L., Keil, R., & Ueda, Y. 2004, *PASJ*, 56, L9

Tao, L., Feng, H., Grisé, F., & Kaaret, P. 2011, *ApJ*, 737, 81

Telfer, R. C., Zheng, W., Kriss, G. A., & Davidsen, A. F. 2002, *ApJ*, 565, 773

Terrazas, B. A., Bell, E. F., Henriques, B. M. B., et al. 2016, *ApJ*, 830, L12

Thrane, E., & Talbot, C. 2019, Publications of the Astronomical Society of Australia, 36, e010

Tingay, S. J., & Wayth, R. B. 2011, *AJ*, 141, 174

Tozzi, P., Gilli, R., Mainieri, V., et al. 2006, *A&A*, 451, 457

Treister, E., Schawinski, K., Urry, C. M., & Simmons, B. D. 2012, *ApJ*, 758, L39

Tremaine, S., Gebhardt, K., Bender, R., et al. 2002, *ApJ*, 574, 740

Tremmel, M., Governato, F., Volonteri, M., & Quinn, T. R. 2015, *MNRAS*, 451, 1868

Turner, M. L., Côté, P., Ferrarese, L., et al. 2012, *ApJS*, 203, 5

Turner, T. J., & Pounds, K. A. 1989, *MNRAS*, 240, 833

Urrutia, T., Lacy, M., & Becker, R. H. 2008, *ApJ*, 674, 80

Valtonen, M. J., Lehto, H. J., Nilsson, K., et al. 2008, *Nature*, 452, 851

Vanden Berk, D. E., Richards, G. T., Bauer, A., et al. 2001, *AJ*, 122, 549

Varenius, E., Conway, J. E., Martí-Vidal, I., et al. 2014, *A&A*, 566, A15

Vasiliev, E., Antonini, F., & Merritt, D. 2015, *ApJ*, 810, 49

Vaughan, S., Uttley, P., Markowitz, A. G., et al. 2016, *MNRAS*, 461, 3145

Villforth, C., Hamann, F., Rosario, D. J., et al. 2014, *MNRAS*, 439, 3342

Villforth, C., Hamilton, T., Pawlik, M. M., et al. 2017, *MNRAS*, 466, 812

Voges, W., Aschenbach, B., Boller, T., et al. 1999, *A&A*, 349, 389

Volonteri, M., Dubois, Y., Pichon, C., & Devriendt, J. 2016, *MNRAS*, 460, 2979

Volonteri, M., Haardt, F., Ghisellini, G., & Della Ceca, R. 2011, *MNRAS*, 416, 216

Volonteri, M., Haardt, F., & Madau, P. 2003, *ApJ*, 582, 559

Volonteri, M., Lodato, G., & Natarajan, P. 2008, *MNRAS*, 383, 1079

Walcher, C. J., Böker, T., Charlot, S., et al. 2006, *ApJ*, 649, 692

Walcher, C. J., van der Marel, R. P., McLaughlin, D., et al. 2005, *ApJ*, 618, 237

Walton, D. J., Roberts, T. P., Mateos, S., & Heard, V. 2011, *MNRAS*, 416, 1844

Wang, J.-M., Chen, Y.-M., Hu, C., et al. 2009, *ApJ*, 705, L76

Wang, J. X., Malhotra, S., Rhoads, J. E., & Norman, C. A. 2004, *ApJ*, 612, L109

Weston, M. E., McIntosh, D. H., Brodwin, M., et al. 2017, *MNRAS*, 464, 3882

White, S. D. M., & Rees, M. J. 1978, *MNRAS*, 183, 341

Wolter, H. 1952, Annalen der Physik, 445, 94

Wrobel, J. M., Comerford, J. M., & Middelberg, E. 2014a, *ApJ*, 782, 116

Wrobel, J. M., Walker, R. C., & Fu, H. 2014b, *ApJ*, 792, L8

Xue, Y. Q., Luo, B., Brandt, W. N., et al. 2011, *ApJS*, 195, 10

Yan, C.-S., Lu, Y., Dai, X., & Yu, Q. 2015, *ApJ*, 809, 117

Yang, G., Chen, C. T. J., Vito, F., et al. 2017, *ApJ*, 842, 72

Yu, Q. 2002, *MNRAS*, 331, 935

Yu, Q., Lu, Y., Mohayaee, R., & Colin, J. 2011, *ApJ*, 738, 92

Yuan, H. B., Liu, X. W., & Xiang, M. S. 2013, *MNRAS*, 430, 2188

Zhou, H., Wang, T., Zhang, X., Dong, X., & Li, C. 2004, *ApJ*, 604, L33